EVALUATING RECENT SEAT MODELS IN REAR-END IMPACTS ACCORDING TO CURRENTLY DISCUSSED CONSUMER TEST PROPOSALS

Kai-Uwe Schmitt
AGU Zürich, Switzerland, and
Institute for Biomedical Engineering,
University and ETH Zürich, Switzerland
Markus Muser
AGU Zürich, Switzerland
Paper Number 09-0116

ABSTRACT

To ensure a high safety standard of vehicle seats in rear-end collisions, consumer tests will include specific test standards. The prevention of soft tissue neck injuries is meant to be addressed by the introduction of such standards. To date particularly EuroNCAP has developed a detailed proposal how such seat tests should be conducted to assess the risk of whiplash associated disorders.
In this study the relevance of the different parameters included in the consumer test proposal for assessing seat performance under rear-end impact conditions was analysed. A series of sled tests according to the latest proposal were performed with different seats. The performance of the seats was assessed as suggested by the proposal. In a next step a sensitivity analysis was conducted to investigate the influence of the different parameters on the final score.

Based on our findings it is suggested to modify the test procedure such that criteria which are redundant or have a weak biomechanical foundation are omitted. The sensitivity analysis revealed that the final score and thus the discriminatory power of the evaluation scheme will persist such that the assessment procedure will still be able to rate the performance of the seats.

INTRODUCTION

To encourage car manufacturers to improve seat design such that it effectively reduces whiplash associated disorders (WAD), the inclusion of seat tests in consumer test procedures like EuroNCAP is discussed and corresponding proposals for test procedures were presented. Obviously, the crucial point in developing such test procedures is the choice of appropriate measures to assess seat performance. Also the final rating scheme that is used to combine different measures into a final score that is then used to classify the seats is of particular importance and therefore subject of several publications [e.g. 1, 2, 3].
The problem associated with the definition of a test procedure is two-fold. One the one hand it must be acknowledged that from a biomechanical point of view the WAD injury criteria and their respective biomechanical tolerance levels are associated with several uncertainties. For most criteria no widely accepted tolerance levels, let alone accurate injury risk curves, are available today. One of the often disregarded points in the tolerance limit discussions is the fact that most injury criteria values have a non-linear relation to injury risk. Many tolerance levels for criteria related to injuries other than WAD (such as HIC, Nij, TTI, Gambit, TI etc.) were derived using highly non-linear logistic regression curves. The biomechanical loads discussed in conjunction with WAD, e.g. accelerations, forces, moments of torque, are generally very low in comparison to loads acting in other crash situations. Therefore, even minor changes in a test set-up may result in significant changes in the loads measured.
In addition any test procedure must satisfy certain technical requirements that are essential to provide a powerful standard including e.g. repeatability and reproducibility. Generally, it was shown by several studies that sled tests seem a suitable method to investigate the behaviour of a seat in rear-impact [e.g. 2, 3]. However, with respect to the final rating of the results discussions are ongoing.
This study investigates a recent consumer test proposal by performing sled tests using different seats. Biomechanical aspects of the proposal are reviewed and the discriminatory power of the rating system is analysed.

MATERIALS & METHODS

A series of tests consisting of static as well as sled tests was performed. Table 1 summarizes the test series. Unless otherwise stated, the head restraint was positioned identically for all tests (head restraint was locked in the second-lowest position) and the seat back angle was always adjusted to a 25°± 0.2° torso line.

Table 1. Summary of the test series. A total of 21 sled tests were performed. 7 different seat models were used (A-G). In some tests more than one seat of the same model were used (e.g. A1, A2 and A3 are three seats of the same model). In some tests one specific seat was tested twice (marked with *).

Test no.	Seat	Re-active system	Pulse severity
MUS07001	A1	yes	medium
MUS07002	A2	yes	
MUS07014	B1	yes	
MUS07006	C1	yes	
MUS07007	C1*	yes	
AGU08001	D1	yes	
AGU08002	D1*	yes	
MUS07004	E1	no	
MUS07005	E1*	no	
MUS07012	E2	no	
AGU08004	E3	no	
AGU08005	E3*	no	
MUS07008	F1	no	
MUS07009	F2	no	
MUS07003	G1	no	
MUS07013	A3	yes	high
MUS07015	B2	yes	
MUS07011	C3	yes	
AGU08003	D2	yes	
MUS07010	E4	no	
AGU08006	E5	no	

Static tests

The head restraint height and the back set (i.e. the horizontal head to head restraint distance) was determined prior to each sled test. The data was acquired and recorded as described in the IIWPG geometry measurement technique [5] using a SAE H-point machine according to SAE J826 and the Head Restraint Measuring Device (HRMD).

Sled tests

Dynamic testing was performed using a HyperG220 sled to which the seats were rigidly mounted. All seats were adjusted in the same way. A BioRID-IIig dummy of the latest build level was used throughout this study. The dummy was seated and instrumented according to IIWPG/EuroNCAP procedures [1].

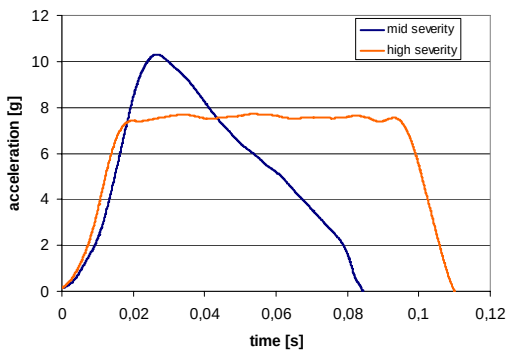

Figure 1. Crash pulses used in the sled tests.

Two different crash pulses were used in this study: a so-called medium severity pulse which represents a delta-v of 16 km/h and a high severity pulse that results in a delta-v of 24 km/h (Fig. 1).

For each test the following measures and neck injury predictors, respectively, were evaluated: NIC, Nkm, time until dummy head first contacts head restraint, T1-acceleration in x-direction, rebound velocity, neck shear force, and neck axial force.
For NIC the first 180ms were considered, i.e. NIC180. With respect to Nkm only the maximum Nkm is reported.

The results of the static and dynamic tests were scored in a system similar to the schemes currently discussed e.g. by EuroNCAP. The rating system considers both the static and the dynamic tests.
For the static tests, the backset and head restraint height were rated according to the limits given in Table 2. Scores range from -1 to +1; a sliding scale was used.
As for the results of the sled tests, Table 2 illustrates the higher and lower performance limits used for the rating. For results in between the higher and lower limits, a sliding scale was used to obtain the score. Each parameter in the dynamic tests can reach a maximum score of 0.5 points, i.e. for one pulse a maximum of 3 points is possible. Furthermore the capping limits as described in [1] were followed.

For the final rating, the worst score of the two static measurements is added to the score received for the corresponding sled test.

Table 2. Threshold values used for evaluating the static tests.

	Lower performance limit	Higher performance limit
Backset [mm]	40	100
Height [mm]	0	80

Table 3. Threshold values used for evaluating the dynamic tests.

	Lower performance limit	Higher performance limit
Medium severity pulse		
NIC [m2/s2]	11	24
Nkm [-]	0,15	0,55
Rebound velocity [m/s]	3,20	4,80
Fx (upper neck shear) [N]	30	190
Fz (neck axial) [N]	360	750
T1 x-acceleration [g]	9,3	13,1
Time to head restraint contact [ms]	51	76
High severity pulse		
NIC [m2/s2]	13	23
Nkm [-]	0,22	0,47
Rebound velocity [m/s]	4,10	5,50
Fx (upper neck shear) [N]	30	210
Fz (neck axial) [N]	470	770
T1 x-acceleration [g]	12,5	15,9
Time to head restraint contact THRC [ms]	48	75

To further investigate the sensitivity of the scoring scheme the dynamic results were scored according the current procedure, i.e. a maximum of 3 points was possible. The ranking of seats was determined and additionally the percentage of the maximum score was calculated (i.e. a seat that reaches 3 points has earned 100%). Afterwards, the number of parameters used to calculate the dynamic score was reduced. First the T1 acceleration and THRC were omitted, next the force measurements left out. To ensure that the test procedure accounts for criteria that are relevant in rearward as well as in the forward motion phase during a rear-end collision the final step included NIC and Nkm as well as the rebound velocity. Since the sliding scales and score system were not changed, the maximum score that could be reached changed accordingly. The changes in ranking were analysed.

RESULTS

Tables 4 and 5 (in the APPENDIX) present the results of the static and dynamic tests and also include the rating of the results according to the score scheme as described above.

The results of the sensitivity analysis of the rating system are shown in Tables 6 and 7 (both in the APPENDIX).

Table 4. Results for all static measures.

Test No.	Height [mm]	Score	Back set [mm]	Score	Total Score Static
MUS07001	30	0.25	30	1	0.25
MUS07002	33	0.18	26	1	0.18
MUS07014	49	-0.23	75	-0.17	-0.23
MUS07006	56	-0.4	40	1	-0.4
MUS07007	54	-0.35	45	0.83	-0.35
AGU08001	40	0	42	0.93	0
AGU08002	40	0	39	1	0
MUS07004	53	-0.33	79	-0.3	-0.33
MUS07005	51	-0.28	63	0.23	-0.28
MUS07012	29	0.28	61	0.3	0.28
AGU08004	32	0.20	60	0.33	0.20
AGU08005	30	0.25	65	0.17	0.17
MUS07008	88	-1.2	80	-0.33	-1.2
MUS07009	55	-0.38	74	-0.13	-0.38
MUS07003	56	-0.4	48	0.73	-0.4
MUS07013	34	0.15	26	1	0.15
MUS07015	53	-0.33	72	-0.07	-0.33
MUS07011	54	-0.35	49	0.7	-0.35
AGU08003	43	-0.08	41	0.97	-0.08
MUS07010	53	-0.33	70	0	-0.33
AGU08006	31	0.23	64	0.20	0.20

DISCUSSION

The results obtained in this test series are in the range of other similar test series as published in the literature. Generally the data shows a wide spread resulting in a corresponding final scores indicating that it included seats of different quality. It was observed that seats with re-active systems performed better than standard vehicle seats without such systems.

Reproducibility

As can be seen from the tests where the same seat was tested twice, the reproducibility of the results was acceptable and within limits described in the literature [e.g. 2]. However, in a more general view, reproducibility can be a problem in consumer tests where several test houses are involved. It should be kept in mind that reproducibility depends on different factors like the laboratory, the dummy, but also the seat and the procedure using the H-point machine. In our series we found that the latter aspect can especially be of importance for seats without lordosis restraint. Due to the straight back of the H-point manekin, a given curvature of the seat back can result in a higher variation when measuring the backset for example (see Fig. 2).

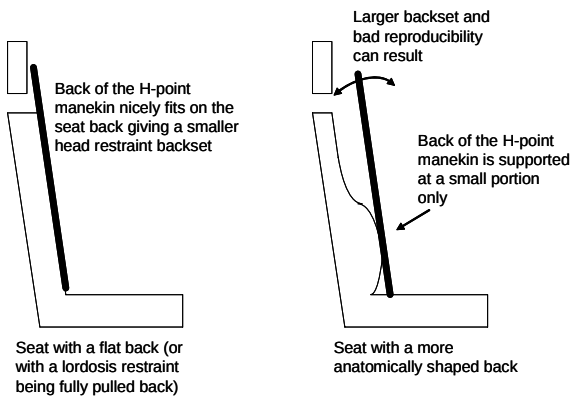

Figure 2. Illustrating the influence of a lordosis restraint on the measurement of the initial backset.

Sensitivity of the rating scheme

With respect to the score from the dynamic tests, it was found for the medium severity pulse the ranking is very robust. Even if some of the measures are omitted, the tendency of the ranking will not change significantly.

Looking at the percentage of the maximum scores, it can be seen that irrespectively of the actual maximum, the range is always between approx. 97% and 3%. Hence even when reducing the number of measures a wide spread of final scores can be expected, i.e the ability of the scoring system to differentiate the various seats is maintained. This can be relevant when designing a consumer test procedure. However, when reducing the number of criteria, the weighting of the different scores can be discussed. When solely regarding NIC, Nkm and the rebound velocity as relevant parameters to define the final score, it can be argued that criteria like NIC and Nkm that do show a link to the biomechanical background of neck injuries [6] should have a higher weight than the rebound velocity. For a future assessment procedure we therefore suggest to reduce the number of parameters but adjust the weight that a parameter has with respect to its biomechanical significance.

For the high severity pulse basically the same conclusions apply as for the medium severity pulse. However, it must be noted that the number of tests used for analysing the sensitivity of the high severity pulse is small. To assess whether the findings also hold true in a more general context, a larger number of test data is needed.

Threshold values and sliding scales

Questions arise concerning the biomechanical validity of a scoring system based on sliding scales. From a biomechanical point of view it seem fundamentally wrong to use a linear scale since it is to be expected that injury criteria values have a non-linear relation to injury risk.

Furthermore the use of performance limits and sliding scales that are different for the 16 km/h and the 24 km/h pulse is hard to understand biomechanically. One seat (model C, tests MUS07006, MUS07011), for instance, has reached exactly the same NIC value for both pulses, but obtains different scores. That the same NIC value was reached can be explained by the fact that the point in time when a maximum relative motion between head and torso occurs is more or less the same for both pulses. However, adjusting the limits that are used to score (i.e. the limit for NIC in the 16 and 24 km/h pulse, respectively) to different crash pulses by means of scaling seems wrong. From a biomechanical perspective, changing the limits means shifting the threshold on the underlying injury risk curve. In other words, a rating system with different injury threshold values accepts that the occupant is subjected to a different injury risk at a different pulse. Due to the lack of accurate injury risk curves today, the effect of such a shift can not be assessed. Facing a consumer test it might, however, become difficult to explain why an identical result as measured by a dummy is regarded less injurious at a high delta-v, i.e. a more severe accident.

T1 and THRC measurements

According to the proposal used here, the scores for T1 acceleration and THRC are linked. Only the worst of both scores is used to determine the final score. From a biomechanical standpoint, there seems no reason to link the criteria in the scoring system. Almost all research in the field of whiplash injuries is focused on the basic assumption that relative motion between head and thorax is responsible for whiplash injuries; this is taken into account explicitly by the NIC criterion, and implicitly also by all criteria using forces and moments. Neither a high T1 acceleration nor a high THRC must necessarily lead to excessive relative motion, as illustrated by the fact that low NIC values and high THRC and/or T1 measurements are observed in the tests (Tables X and X). Consequently also the correlation between e.g. NIC and THRC or T1 is bad. Hence, the inclusion of T1 and THRC appears to be questionable. As the sensitivity analysis indicated that the final score is not much influence by these two parameters we suggest omitting them.

Upper neck Fx

It has been hypothesised by various researchers that inter-vertebral shear forces are responsible for whiplash injuries [7]. Therefore, considering the upper neck Fx makes sense biomechanically. However, according the current proposal only the positive maximum of Fx is considered although volunteer tests have shown that the tolerance limits are almost identical in the positive and negative

direction [8]. For example, seat B in test MUS070014 showed only negative Fx values and thus obtained the maximum score of 0.5 for this criterion; if negative values would have been considered, the peak value of –173 N observed in this test would have led to a score of only 0.05 (!).
From a biomechanical consideration the inclusion of negative values for this criterion makes sense. If this is done, however, Fx is included already in the Nkm criterion and may, therefore, be left out altogether.

Upper neck Fz
The biomechanical significance of Fz with respect to whiplash injuries is not as clear as with Fx. Again, only the positive maximum (i.e. tension of the neck) is considered. Some researchers argue that a negative, i.e. compressive, loading of the spine is much more dangerous than a slight tensile loading, because by compressing the spine, the ligaments stabilising the vertebrae are relaxed and, thus, un-physiological inter-vertebral motion is made possible [7]. In contrast, a slight tensile loading might even be beneficial because the neck is stabilised. Thus, the relation between upper neck Fz and injury risk is not monotonous and does not cross the zero-point (Fig. 3).

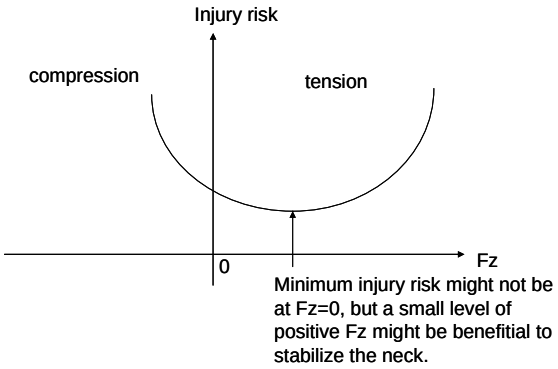

Figure 3. Schematic drawing of the relation between upper neck Fz and neck injury risk.

Furthermore, the BioRID dummy does not have compressible inter-vertebral discs that would allow for a certain damping of peak forces; the biofidelity of the Fz measurement is therefore unclear.

Static head restraint assessment
Comparing the outcome of the static and the dynamic parts of the test procedure, it is found that they conclude with a different ranking. Some seats even receive negative scores in the static tests. Generally, one must be aware that in the static measurement of the backset, i.e. the distance between head and head restraint, the actual contact point during impact is not necessarily the one which is used to measure the distance in the static case (see Fig. 4). In case of a rear-end collision the head of the person sitting on the seat will slightly rise relative to the head restraint due to a straightening of the spine and the rotation of the seat back. Hence the effective backset is to be expected higher than the one used in the static measurements. Consequently it depends very much on the design of the head restraint curvature whether this distance will increase in the dynamic case or not (Fig. 4). Additionally a re-active head restraint system will be able to bridge that gap such that a somewhat larger distance might be acceptable in the static case.
Therefore it is suggested using the static measurements as a pre-selection for the dynamic tests only. A seat that has a large backset in the static measurements and no re-active system intended to prevent whiplash injury, will most probably perform very bad in the dynamic tests. Hence there is no need to perform the dynamic part for seats with very poor static measurements. However, if a dynamic test is conducted, then the static measurements should be disregarded, i.e. if a seat manages to perform well in the dynamic tests, for instance, because of a well designed re-active system, the static measurement should not be part of the final scoring.

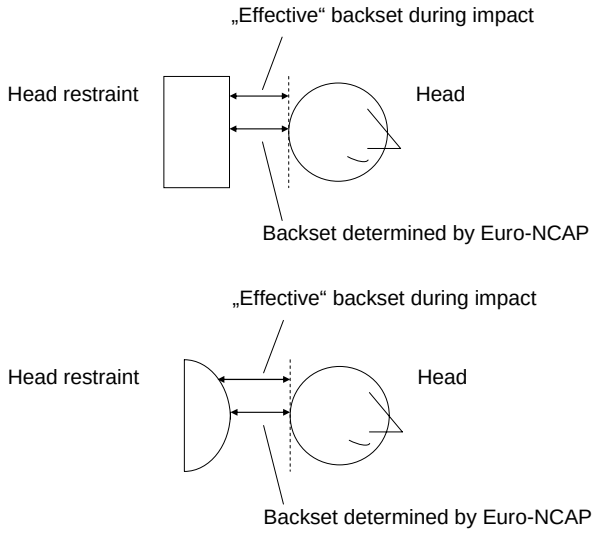

Figure 4. Backset situation for a’ theoretical’ block-shaped head restraint (top) and for a a more realistic head restraint showing a curved cross-section.

High severity pulse
Although WAD is primarily associated with low-speed impacts, it must be noted that a car manufacturer has additional seat design requirements to consider one of which is the seat performance in high speed impacts. Thus it can be argued that the 24 km/h pulse is of interest, for example, to ensure that the seat does not collapse in a high speed rear-end impact. But it has to be considered that in such crashes WAD is most

probably not the primary injury. Therefore it seems not reasonable to perform a 24 km/h sled test using the BioRID which was not designed for such high impacts and to determine criteria like NIC or Nkm that are not validated for such impacts. In order to assess whether a seat can withstand high loadings in rear-end impacts one can also perform a 24 km/h sled tests using a Hybrid III 95%ile dummy instead. In fact such a set-up seems suited to investigate the deformation characteristics of a seat. The Hybrid III 95%ile dummy is capable of performing such tests and by its anthropometry it represents a kind of worst case scenario. In such a dynamic test it can determined whether the seat collapses in case of a high speed rear-end impact. The determination of any neck injury criteria seems not necessary since the focus of such a test is the seat deformation rather than the neck injury risk. Although the seat stiffness could also be evaluated by other, probably much cheaper test set-ups, a sled test utilizing a crash test dummy seems the most illustrative way and thus particularly suited for consumer testing.

Rebound velocity

Generally it seems desirable that both the first phase of a rear-end impact as characterised by the backward motion of the occupant as well as the rebound phase are assessed in the test procedure.

The rebound velocity, although it has no direct correlation to biomechanics, seems a stable and reliable criterion for quantification of the rebound phase. All other criteria determined by dummy measurements might be dominated by the belt restraint phase. This can be problematic, because the belt system used for the sled tests does normally not correspond to the system used in the target vehicle, neither with respect to stiffness nor with respect to geometry. Thus it seems more appropriate to measure rebound velocity at a point in time before the belt restraint phase.

CONCLUSIONS

The test procedure that was used here intends to assess the performance of a seat with respect to its WAD injury risk. However, the proposal contains several factors that seem questionable from a biomechanics point of view. While the performance of sled tests with the set-up as proposed seem well suited, the evaluation scheme could be changed as follows:

- The number of criteria to be included in the rating system may significantly be reduced. By purely mathematical considerations, it was found that a reduced number of criteria does not sacrifice the accuracy of the assessment procedure. Some of the criteria are redundant, others not correlated to biomechanics (e.g. T1/THRC).
- It is proposed to reduce the parameters that determine the final score to be NIC, Nkm and the rebound velocity. If appropriate sliding scales are found, the moment My of the lower neck may be considered as well. There are few studies correlating this criterion to real-world accident data [6].
- The scoring system should be adjusted such that the kinematically more relevant phase of the occupant movement during rear-end impact is emphasized and a higher weight shall be put on the dynamic instead of the static parts of the test procedure.
- If more than one crash test pulse is used for the rating procedure, the same sliding scales should be used for all test pulses.
- A high speed pulse may be useful to ascertain seat back stability. In this case, however, a quasi-static test or a dynamic test where the seat back rearward deflection angle is measured as the only criterion would be sufficient.
- A harmonisation of the procedure how to position the head restraint is desired. The positioning of the head restraint prior to dynamic testing differs for tests that are conducted according to IIHS and EuroNCAP, respectively. Consequently also the results of the dynamic test are generally different. This can lead to quite different final scores
- An improvement of the currently straight back of the H-Point machine into a more anatomically shaped back should be envisaged.

ACKNOWLEDGEMENTS

The authors acknowledge the financial support by Toyota Motor Company. All tests were conducted at the facilities of DSD Linz (Austria).

REFERENCES

[1] EuroNCAP (2007) The dynamic assessment of car seats for neck injury protection, Version 2.6, Final Draft, Status 05/03/07

[2] Bortenschlager K et al. (2007) Review of existing injury criteria and their tolerance limits for whiplash injuries with respect to testing experience and rating systems, Proc. ESV Conf., Paper-No. 07-0486

[3] Adalin C, Sferco R, Ray P (2005) The repeatibility and reproducibility of proposed test procedures and injury criteria for assessing neck injuries in rear impact, Proc. ESV Conf., Paper No. 05-0340

[4] Bortenschlager K et al (2003) Comparison tests of BioRID II and RID 2 with regard to repeatability, reproducibility and sensitivity for assessment of car seat protection potential in rear-end impacts, Stapp Car Crash Journal, 47:473-488

[5] International Insurance Whiplash Prevention Group IIWPG (2006) Seat/head restraint evaluation protocol, version 2.5.
[6] Kullgren A, Krafft M, Lie A, Tingvall C (2007) The effect of whiplash protection systems in real-life crashes and their correlation to consumer crash test programmes, Proc. ESV Conf., paper no. 07-0468
[7] Yang, K., P. Begeman, et al. (1997) On the role of cervical facet joints in rear end impact neck injury mechanisms. SP-1226; SAE 970497.
[8] Goldsmith, W. and A. Ommaya (1984) Head and neck injury criteria and tolerance levels. The biomechanics of impact trauma (Eds. B. Aldman and A. Chapon). Amsterdam, Elsevier Science Publishers: 149-187..

APPENDIX

Table 5. Results for the dynamic tests.

Test No.	NIC		Nkm		Fx upper		Fz upper		T1 acceleration		THRC		Rebound velocity		Total Score Dynamic
	[m2/s2]	Score	[-]	Score	[N]	Score	[N]	Score	[m/s2]	Score	[ms]	Score	[m/s]	Score	
MUS07001	11	0.47	0.15	0.5	36.1	0.48	464	0.37	7.8	0.5	94	0	2.5	0.5	2.82
MUS07002	12.6	0.44	0.15	0.5	37.9	0.48	389.1	0.46	7.1	0.5	88	0	2.67	0.5	2.88
MUS07014	13.9	0.39	0.46	0.11	0	0.5	340.4	0.5	11.3	0.24	79	0	3	0.5	2.24
MUS07006	14.6	0.36	0.41	0.18	93.1	0.3	747.7	0	15.1	0	69	0.14	5.05	0	0.98
MUS07007	12.4	0.45	0.4	0.18	90.8	0.31	745.3	0.01	15	0	75	0.02	5.01	0	0.97
AGU08001	13.8	0.39	0.59	0	163.0	0.08	741.5	0.01	15.6	0	70	0.12	5.37	0	0.60
AGU08002	13.6	0.40	0.54	0.01	132.0	0.18	724.8	0.03	15.1	0	69	0.14	5.50	0	0.76
MUS07004	23.3	0.03	0.56	0	200.5	0	1057.8	0	12.1	0.13	98	0	4.34	0.14	0.3
MUS07005	21.3	0.1	0.57	0	231.2	0	1077.2	0	12.4	0.09	92	0	4.34	0.14	0.33
MUS07012	17.3	0.26	0.52	0.04	185.2	0.02	887.1	0	11	0.28	88	0	4.42	0.12	0.72
AGU08004	18.7	0.20	0.76	0	247.0	0	956.5	0	13.3	0	84	0	5.47	0.07	0.27
AGU08005	22.4	0.06	0.79	0	250.0	0	970.9	0	11.9	0.15	86	0	4.80	0	0.21
MUS07004	25.7	0	0.51	0.05	238.7	0	1332.8	0	15.5	0	93	0	4.63	0.05	0.1
MUS07009	21	0.12	0.51	0.05	179.3	0.03	899.9	0	10.6	0.33	89	0	4.6	0.06	0.59
MUS07003	19	0.19	0.36	0.24	121.9	0.21	1043	0	14.1	0	82	0	4.25	0.17	0.81
MUS07013	13.8	0.46	0.33	0.29	48.6	0.45	779.3	0	15.6	0.04	113	0	5.01	0.18	1.42
MUS07015	17.6	0.27	0.41	0.13	53.7	0.43	646.1	0.21	12	0.5	82	0	3.33	0.5	2.04
MUS07011	14.6	0.42	0.27	0.41	0	0.5	691	0.13	16.8	0	72	0.06	5.92	0	1.52
AGU08003	14.7	0.42	0.53	0	0	0.5	659.6	0.18	18.5	0	69	0.10	5.71	0	1.20
MUS07010	25.3	0	0.38	0.18	176.1	0.09	777.6	0	14.4	0.22	87	0	4.56	0.34	0.83
AGU08006	23.1	0	0.90	0	367	0	864.2	0	12.7	0.47	89	0	5.51	0	0.47

Table 6. Analysing the sensitivity of the dynamic score for the medium severity pulse.

Test no.	NIC Score	Nkm Score	Fx upper Score	Fz upper Score	T1 Score	THRC Score	Rebound velocity Score	Total Score	**rank**	**% of max. score**
MUS07001	0,44	0,5	0,48	0,46	0,5	0	0,5	2,88	**1**	**96,0**
MUS07002	0,47	0,5	0,48	0,37	0,5	0	0,5	2,82	**2**	**94,0**
MUS07014	0,39	0,11	0,5	0,5	0,24	0	0,5	2,24	**3**	**74,7**
MUS07006	0,36	0,18	0,3	0	0	0,14	0	0,98	**4**	**32,7**
MUS07007	0,45	0,18	0,31	0,01	0	0,02	0	0,97	**5**	**32,3**
MUS07003	0,19	0,24	0,21	0	0	0	0,17	0,81	**6**	**27,0**
AGU08002	0,4	0,01	0,18	0,03	0	0,14	0	0,76	**7**	**25,3**
MUS07012	0,26	0,04	0,02	0	0,28	0	0,12	0,72	**8**	**24,0**
AGU08001	0,39	0	0,08	0,01	0	0,12	0	0,6	**9**	**20,0**
MUS07009	0,12	0,05	0,03	0	0,33	0	0,06	0,59	**10**	**19,7**
MUS07005	0,1	0	0	0	0,09	0	0,14	0,33	**11**	**11,0**
MUS07004	0,03	0	0	0	0,13	0	0,14	0,3	**12**	**10,0**
AGU08004	0,2	0	0	0	0	0	0,07	0,27	**13**	**9,0**
AGU08005	0,06	0	0	0	0,15	0	0	0,21	**14**	**7,0**
MUS07004	0	0,05	0	0	0	0	0,05	0,1	**15**	**3,3**
MUS07001	0,44	0,5	0,48	0,46			0,5	2,38	**1**	**95,2**
MUS07002	0,47	0,5	0,48	0,37			0,5	2,32	**2**	**92,8**
MUS07014	0,39	0,11	0,5	0,5			0,5	2	**3**	**80,0**
MUS07007	0,45	0,18	0,31	0,01			0	0,95	**5**	**38,0**
MUS07006	0,36	0,18	0,3	0			0	0,84	**4**	**33,6**
MUS07003	0,19	0,24	0,21	0			0,17	0,81	**6**	**32,4**
AGU08002	0,4	0,01	0,18	0,03			0	0,62	**7**	**24,8**
AGU08001	0,39	0	0,08	0,01			0	0,48	**9**	**19,2**
MUS07012	0,26	0,04	0,02	0			0,12	0,44	**8**	**17,6**
AGU08004	0,2	0	0	0			0,07	0,27	**13**	**10,8**
MUS07009	0,12	0,05	0,03	0			0,06	0,26	**10**	**10,4**
MUS07005	0,1	0	0	0			0,14	0,24	**11**	**9,6**
MUS07004	0,03	0	0	0			0,14	0,17	**12**	**6,8**
MUS07004	0	0,05	0	0			0,05	0,1	**15**	**4,0**
AGU08005	0,06	0	0	0			0	0,06	**14**	**2,4**
MUS07002	0,47	0,5	0,48				0,5	1,95	**2**	**97,5**
MUS07001	0,44	0,5	0,48				0,5	1,92	**1**	**96,0**
MUS07014	0,39	0,11	0,5				0,5	1,5	**3**	**75,0**
MUS07007	0,45	0,18	0,31				0	0,94	**5**	**47,0**
MUS07006	0,36	0,18	0,3				0	0,84	**4**	**42,0**
MUS07003	0,19	0,24	0,21				0,17	0,81	**6**	**40,5**
AGU08002	0,4	0,01	0,18				0	0,59	**7**	**29,5**
AGU08001	0,39	0	0,08				0	0,47	**9**	**23,5**
MUS07012	0,26	0,04	0,02				0,12	0,44	**8**	**22,0**
AGU08004	0,2	0	0				0,07	0,27	**13**	**13,5**
MUS07009	0,12	0,05	0,03				0,06	0,26	**10**	**13,0**
MUS07005	0,1	0	0				0,14	0,24	**11**	**12,0**
MUS07004	0,03	0	0				0,14	0,17	**12**	**8,5**
MUS07004	0	0,05	0				0,05	0,1	**15**	**5,0**
AGU08005	0,06	0	0				0	0,06	**14**	**3,0**
MUS07002	0,47	0,5					0,5	1,47	**2**	**98,0**
MUS07001	0,44	0,5					0,5	1,44	**1**	**96,0**
MUS07014	0,39	0,11					0,5	1	**3**	**66,7**
MUS07007	0,45	0,18					0	0,63	**5**	**42,0**
MUS07003	0,19	0,24					0,17	0,6	**6**	**40,0**
MUS07006	0,36	0,18					0	0,54	**4**	**36,0**
MUS07012	0,26	0,04					0,12	0,42	**8**	**28,0**
AGU08002	0,4	0,01					0	0,41	**7**	**27,3**
AGU08001	0,39	0					0	0,39	**9**	**26,0**
AGU08004	0,2	0					0,07	0,27	**13**	**18,0**
MUS07005	0,1	0					0,14	0,24	**11**	**16,0**
MUS07009	0,12	0,05					0,06	0,23	**10**	**15,3**
MUS07004	0,03	0					0,14	0,17	**12**	**11,3**
MUS07004	0	0,05					0,05	0,1	**15**	**6,7**
AGU08005	0,06	0					0	0,06	**14**	**4,0**

Table 6. Analysing the sensitivity of the dynamic score for the high severity pulse.

Test no.	NIC Score	Nkm Score	Fx upper Score	Fz upper Score	T1 Score	THRC Score	Rebound velocity Score	Total Score	**rank**	**% of max. score**
MUS07015	0,27	0,13	0,43	0,21	0,5	0	0,5	2,04	**1**	**68,0**
MUS07011	0,42	0,41	0,5	0,13	0	0,06	0	1,52	**2**	**50,7**
MUS07013	0,46	0,29	0,45	0	0,04	0	0,18	1,42	**3**	**47,3**
AGU08003	0,42	0	0,13	0,5	0	0,1	0	1,15	**4**	**38,3**
MUS07010	0	0,18	0,09	0	0,22	0	0,34	0,83	**5**	**27,7**
AGU08006	0	0	0	0	0,47	0	0	0,47	**6**	**15,7**
MUS07015	0,27	0,13	0,43	0,21			0,5	1,54	**1**	**61,6**
MUS07011	0,42	0,41	0,5	0,13			0	1,46	**2**	**58,4**
MUS07013	0,46	0,29	0,45	0			0,18	1,38	**3**	**55,2**
AGU08003	0,42	0	0,13	0,5			0	1,05	**4**	**42,0**
MUS07010	0	0,18	0,09	0			0,34	0,61	**5**	**24,4**
AGU08006	0	0	0	0			0	0	**6**	**0,0**
MUS07013	0,46	0,29	0,45				0,18	1,38	**3**	**69,0**
MUS07015	0,27	0,13	0,43				0,5	1,33	**1**	**66,5**
MUS07011	0,42	0,41	0,5				0	1,33	**2**	**66,5**
MUS07010	0	0,18	0,09				0,34	0,61	**5**	**30,5**
AGU08003	0,42	0	0,13				0	0,55	**4**	**27,5**
AGU08006	0	0	0				0	0	**6**	**0,0**
MUS07013	0,46	0,29					0,18	0,93	**3**	**62,0**
MUS07015	0,27	0,13					0,5	0,9	**1**	**60,0**
MUS07011	0,42	0,41					0	0,83	**2**	**55,3**
MUS07010	0	0,18					0,34	0,52	**5**	**34,7**
AGU08003	0,42	0					0	0,42	**4**	**28,0**
AGU08006	0	0					0	0	**6**	**0,0**

MODELING AND PREDICTION OF OCCUPANT KNEE-THIGH-HIP INJURIES

Jialou Hu
Jay Z. Zhao
Amy Klinkenberger
TK Holdings Inc.
United States
Paper Number 09-0334

ABSTRACT

Although extensive modeling efforts have been made in the past decades to predict occupant/pedestrian knee-thigh-hip (KTH) injuries, prediction for the injuries at the tissue level for various loading conditions observed in automotive crashes is still challenging. This study develops model-based tissue injury criteria and a tool to predict occupant KTH injuries subject to different postures and loading rates.

An effective plastic strain based injury criterion with a defined universal threshold was developed for identification of the potential injury locations in the KTH body region. The published cadaver KTH low-rate impact tests at three postures of neutral, adduction, and flexion by UMTRI (University of Michigan Transportation Research Institute) have been simulated with the Takata 50th% male human model. Using the defined criteria, the model predicted the hip-bone and hip-joint fractures for the three postures, were well correlated to those observed from the tests. The KTH impacts were also simulated at two loading rates. The simulation results indicated a possible mode shift of the impact rate-associated injury with assumptions of viscous effects on hip-joint. A high rate impact more likely generates a fracture at the femur shaft; and the impact at a lower rate more likely fractures the hip-joint.

The validated KTH injury criteria and tool were thus applied for accident reconstruction of two vehicle crash cases (full frontal and offset frontal impacts) selected from the NASS/CDS & CIREN database, which caused occupant KTH injuries at AIS 2-3 scale. The simulations match the injury outcomes of the reported field observations.

INTRODUCTION

Lower extremities are the most injured body regions resulting from vehicle crashes. Their long term effect on societal "harm" due to permanent disability and impairment and associated cost is significant. The analysis of NASS-CDS database for the years 1990-1997 by Kuppa et al. [1] indicated that the risk of the AIS 2+ lower extremity injures in all frontal crashes was higher than any other body region. They estimated that the KTH complex injures accounted for ~55% of all the lower extremity injuries annually. Additional analysis of NASS-CDS database for the years 1993-2001 [2] concluded that the complex accounted for 18% of all AIS 2+ injuries sustained by frontal seat occupants involved in frontal automobile crashes and 23% of the associated Life-years Lost to Injury (LLI). Rupp et al. [3-4] estimated from 1995-2000 NASS-CDS database that about 30,000 KTH AIS 2+ injuries occurred annually in frontal crashes, of which approximately 47% were to the hip, and 30% to the thigh. Our latest analysis of NASS-CDS database confirm that lower extremities injuries in the years 2001-2005 remain the highest injured body region, accounting for ~21% of the total injuries and 17% of the AIS 3+ injuries.

Detailed investigations on the real-world automobile crash data indicate that the KTH injury locations and severity vary with crash severity. Although the risk of KTH injuries generally increase with increasing crash severity, quite a large number of the KTH injuries are occurring at crash severities of less than 35 mph [2]. The analysis of the UM CIREN database [5] indicated that the number and percentage of hip injures are particularly high in the 26-35 mph range, while the knee & thigh injuries are more frequent in the lower crash severity of less than 25 mph, which is less than current regulatory and consumer testing levels in FMVSS 208 and NCAP. The KTH injury locations and severity are also affected by other various factors, such as occupant seating posture, age and gender, the KTH contact object type and area, the lower leg/foot loading condition, vehicle crash modes and impact direction, etc. Some of these variables have been investigated in the laboratory PMHS (Post Mortem Human Subject) experiments [6-8].

To develop countermeasures for reduction of the KTH injuries in the real-world crashes, we need to fully understand why and how the KTH injuries occurred, especially in the low severity crashes of delta V less than 25 mph. Such injury mechanisms and outcomes could not be investigated and measured from physical laboratory tests for the anthropomorphic test devices such as Hybrid-III dummies, due to deficiencies in biofidelity of their lower extremities and associated measurable engineering parameter based injury criteria. Therefore, it is very important for us to conduct accident reconstruction for selected vehicle crash cases by computational simulation using a human body model. This requires fully validated human KTH and full body model and associated injury criteria for the tissue failures.

Many occupant/pedestrian KTH or full body models [9-16] have been developed in the past decades. The modeling work was mainly for the tissue material characterization and for the kinematics and response validation. However, few have attempted to develop an injury criterion for estimation of the KTH tissue injuries for various loading conditions observed in automotive crashes. To the our best knowledge none of the previous full body models have been applied to the accident reconstruction of car crash cases with KTH injuries at the tissue level. In previous research, we developed the Takata human body model [9-10] as a tool to evaluate the hard tissue injuries. Although the human model was previously validated at some extent in a series of sled tests simulations, an applicable injury criterion for the KTH tissues was not established, and the models applicability for accident case study and prediction of the occupant KTH injuries in car crashes were not verified.

This research pursued the following objectives:

1. to develop a better human KTH FEA (finite element analysis) model with associated tissue injury criterion applicable for identification of the potential injury locations in the KTH body region and for estimation of the KTH injury modes;
2. using Takata human full body model integrated with newly developed KTH sub-model to conduct accident reconstruction of two vehicle crash cases (full frontal and offset frontal impacts) caused the occupant hip or femur fractures.

KTH MODELING

Figure 1 shows the model of the KTH complex subtracted from the Takata 50th% male human model [9-10]. The hard tissues modeled in the pelvic region included the lumbar, sacrum and coccyx, ilium, ischium, pubis, symphisis pubica, and acetabulum, which have the trabecular bones modeled in solid elements and the cortical bones in shells. The sacroiliac joint was modeled as tied surfaces. The hip joints consisted of the hip joints ligaments (ligament of femur head, the capsular ligaments), the synovial membranes and contact between the femur head and acetabulum. In the thigh and knee regions, the cortical bones of the shaft of the long bones (femur, tibia and fibula) were modeled as solid elements, and those in the head/condyle region were modeled as shells with varying regional thickness. Two joints in each of the knee, the femoro-patellar joint and femoro-tibial joint, were modeled. The femoro-patellar joint consists of the patella, patellar and quadriceps tendons, and the patellar groove. The femoro-tibial joint consists of the femur condyle and articular cartilage, the tibia and fibula and meniscus, as well as the ligaments of ACL, PCL, MCL, LCL. The synovial membranes were modeled as surfaces for soft contact. Various tissue level correlations, such as the pelvis pendulum impact test, femur 3-point bending test, femur head and shaft impact tests, knee pendulum impact test have been implemented previously. The material properties of main tissues were provided [9-10]. In this study, we focus on 1) upgrading the hip joint model for KTH impact in neutral, adducted and flexed postures; and 2) investigating the impact rate effects to the KTH complex through an engineering approach.

1. Simulate the Effects of Hip Posture

The published UMTRI cadaver tests by Rupp, et al [3, 6] were used in upgrading the KTH model. The simulation setup for the impact is shown in Figure 1. The pelvis was held by fixed potting material in the top wing of the pelvis. The knee was impacted at 1.2 m/s and the response of the KTH complex was simulated.

In simulation, the model excluded the knee damage from the impact, as designed in the tests, with the material property management throughout the knee area. The impact loading pattern was measured through the total boundary force of the fixed potting material as well as the contact force of the impactor to the knee. The femur force was measured through the mid shaft of femur. After the KTH complex

model modification and the impactor stiffness management, the 300 N/ms impactor loading profile with the peak force about 6 KN at 40 ms, close to the defined by Rupp [3], was created, as shown in Figure 2.

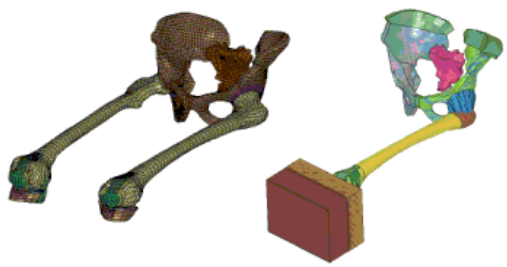

Figure 1. KTH complex and impact model setup.

At first, the responses of the KTH impact in a neutral position were analyzed. Figure 3 illustrates a Von-Mises stress distribution in the cortical bone of acetabulum. The maximum stress above threshold could indicate a potential fracture in the cortical bone. Comparing to the injury observed in the lab test [6], the FEA model reasonably correlates to the test in terms of the fracture location.

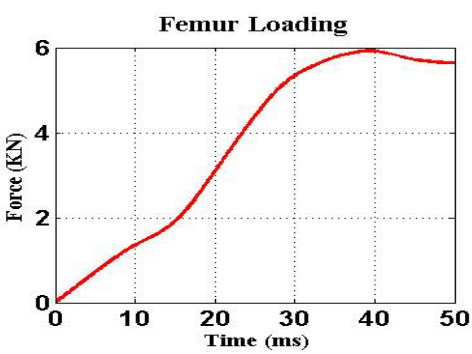

Figure 2. The 300N/ms impactor loading profile simulated.

Then a simulation was conducted of the KTH in three postures: neutral, 10 degree adducted and 30 degree flexed. Figure 4 shows the model top section views and side views of the three KTH postures. Figure 5 gives a typical shear stress distribution at 23 ms for the KTH impact at 30 degree flexed posture. In comparison to the neutral posture (Figure 3), the flexed posture generates a different injury pattern and the FEA indicates the vulnerable area for the flexed posture is at edge of the posterior wall of acetabulum.

Considering that different KTH postures yield different stress distribution patterns and it is difficult to find a unique fracture strength pattern and threshold for the cortical bone fracture of the hip joint, instead an engineering approach was developed to account for the posture variations with FEA feasibility in the strength evaluation, although the approach may reduce the precision in fracture sensitivity and location.

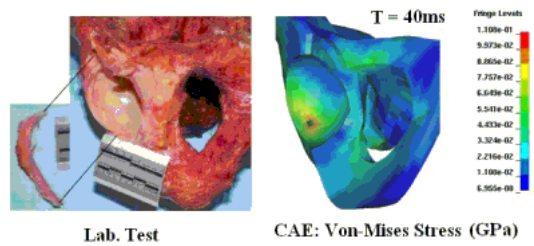

Figure 3. FE-evaluated acetabulum stress distribution vs. lab test injury observation (Lab test courtesy of Rupp).

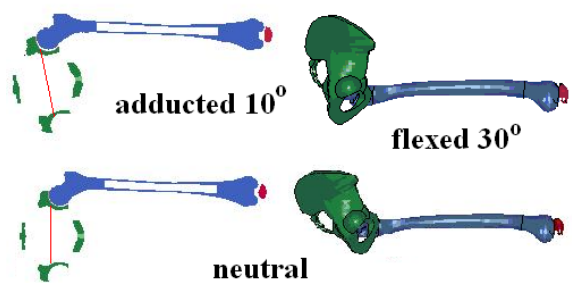

Figure 4. Modeling for the three KTH postures.

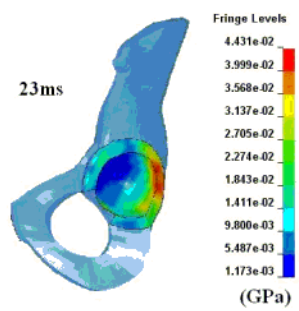

Figure 5. Shear stress yielded at flexed posture around a possible fracture time in acetabulum.

The often-used engineering strength measure in current FEA solvers is plastic strain. A plastic strain of 2.11% was applied to the three postures as a universal strength threshold to the hip fractures for the Takata 50th% KTH model. The forces at the fracture of the acetabulum were calculated, the results are provided as shown in Figure 6. These values match well to the laboratory test results observed by Rupp [3, 6]. Table 1 compares the hip fracture characteristics in the KTH impact to the neutral posture between the FEA and laboratory tests. Table 2 is the summary of the hip tolerance variation

with the other two postures to the neutral posture from the FEA and laboratory tests. In conclusion, the universal criterion of 2.11% plastic strain applied to the Takata 50th% male KTH model provides a reasonable assessment of the hip fracture tolerance for these postures.

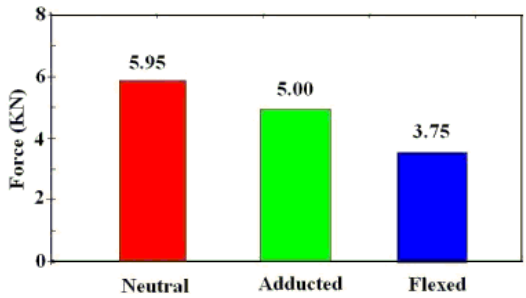

Figure 6. Hip tolerance evaluated with 2.11% plastic strain applied to the Takata 50th% male KTH model.

Table 1.
Hip tolerance from UMTRI test [4] and Takata FEA for KTH impact in neutral posture

Item	Lab. Test [4]		FEA
Test ID	Mean Value	sd	Value
Force at Fracture to all Subjects (KN)	5.70	1.38	
Force at Fracture to Male (KN)	5.96	0.61	5.95
Time to Peak (ms)	38.3	11.5	38
Loading Rate (N/ms)	193	114	198
KTH Stiffness (N/mm)	233	110	328

Table 2.
Hip tolerance percentage change of a given posture to the tolerance of neutral posture: Lab test [5] and FEA

	Neutral	Adducted 10 deg.	Flexed 30 deg.
Lab. Test	0	18 +/- 8%	34 +/- 4%
FEA	0	16%	37%

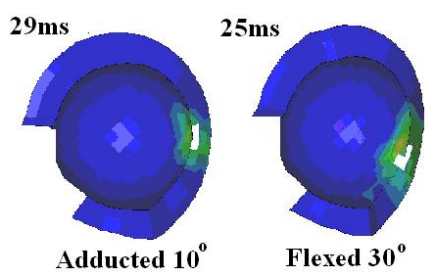

Figure 7. FE-evaluated injury location by element elimination at the time of fracture of acetabulum.

The LS-Dyna element elimination option, a computation method to eliminate those elements whose yielded plastic stains reach the defined threshold in the simulation, enables us to easily identify the injury locations in the KTH impact simulation. Figure 7 shows the fractures of the acetabulum in the KTH impact of the two different postures at the time of each fracture. As expected, the injury occurs at the posterior wall edge of the acetabulum to the adducted and flexed postures.

The above results demonstrate that the Takata 50th% male KTH model is successfully upgraded and applicable for KTH impacts of different postures with a universal strength threshold for injury estimation.

2. Explore Impact Rate Effects to KTH by FEA

As defined in the current Federal Motor Vehicle Safety Standard (FMVSS) 208, the force at mid femur of a midsize-male Hybrid III ATD shall not exceed 10KN in vehicle compliance crash testing. The 10KN force is established from the femur tolerance which is higher than that of the hip joint of the KTH impact studied above. In the KTH frontal impact, the knee contacts the impactor and the force is primarily transferred through the femur shaft to its proximal end. Then, the femoral head transfers the force through articular cartilage to the hip cup. If the acetabular tolerance is reached, the hip joint injures. However, in a significant amount of vehicle accidents with KTH impact, the occupant sustains a femur injury rather than a hip joint injury, one suspected reason is possibly due to the loading rate as mentioned in previous work by Rupp et al. [3].

Along with the Takata KTH modeling efforts, FEA was extended for a preliminary exploration to the impact loading rate effects. The knee damage concern was excluded in this particular study. The impact rate effects could be explored on the mechanical loading performance in the remaining parts of KTH complex: femur, articular cartilage, and hip cup.

Because of its anatomic geometry, the femur could experience a loading eccentricity when impacted resulting in bending. The FEA indicates that approximated uniaxial tensile stress and uniaxial compressive stress can be found along the sides of the shaft as shown in Figure 8. Figure 9 presents the two FEA measurements of the maximum stress. It is known that the bone tensile strength is significantly lower than the compressive strength (1/3 lower). The plot indicates that the vulnerable region of the shaft is at the lateral side with the approximated uniaxial tensile stress.

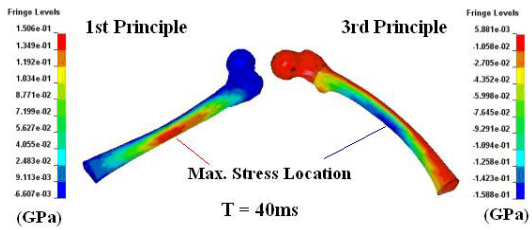

Figure 8. Stress yielded at the shaft during bending.

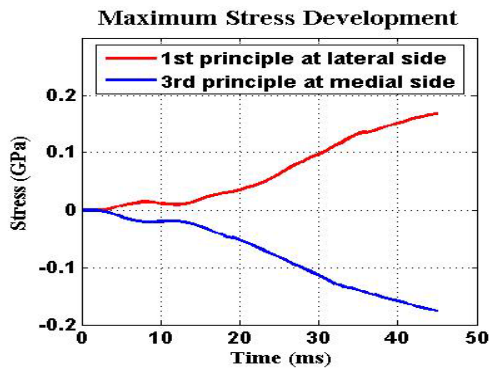

Figure 9. Maximum stress development at the location marked in Figure 8.

In contact with the femur proximal end, the articular cartilage has a biphasic structure, consisting of a solid phase and a fluid phase. Precise modeling of these structures can be challenging in FEA. Instead, a simplified modeling method for their mechanical characteristics was applied. An impact rate related viscous effect could be assumed as a hypothesis for the articular cartilage: the friction coefficient of the contact surface is a function of a relative velocity of the femur head to the acetabulum as shown in Figure 10. A tangential force is distributed at cartilage generated by the impact loading and becomes a part of the boundary conditions to the femur in bending. The boundary condition varies with the relative velocity.

Considered together with the femur bending feature and the assumed mechanical viscous effect of articular cartilage, FEA was conducted to investigate the responses of KTH impact at different rates. Two impact loading patterns, shown in Figure 11, were created in the KTH impact simulations, by varying the impact speed and adjustment of impactor stiffness. The slow rate impact peaked at 6 KN femur loading around 40 ms; and the fast rate impact peaked at 8 KN within 10 ms. The function of Figure 10 for the contact in the hip joint was used in simulations. Material strain-rate properties of the cortical bones of the femur and hip bone were previously implemented in the KTH model.

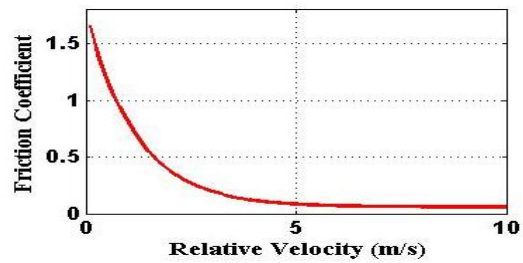

Figure 10. Assumed rate dependent mechanical viscous effect of articular cartilage.

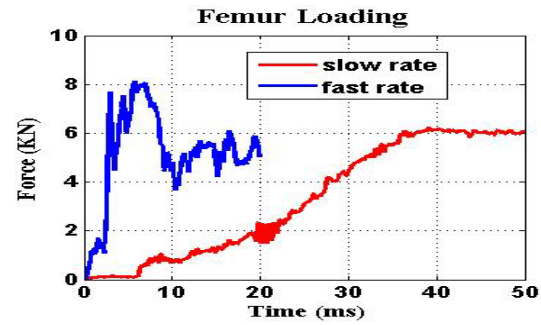

Figure 11. Two impact loading patterns created for impact rate effect study.

Three stress measurements were taken in the analyses: 1) the first principle stress at the maximum stress location on the lateral side femur, 2) the first principle stress at the maximum stress location at acetabulum 3) Von-Mises stress at the maximum stress location in acetabulum. The three locations are indicated in the picture shown in Figure 12.

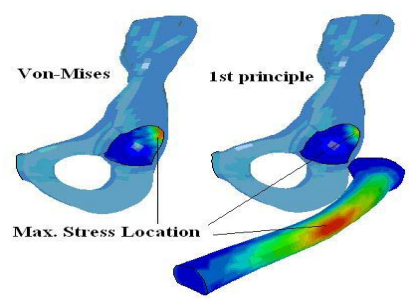

Figure 12. Three stress measurements for strength analysis.

Figure 13 presents the FEA results for the slow rate impact, and Figure 14 presents the data for the fast rate impact. In these plots, the red curve represents the measurement from acetabulum, and the blue represents the measurement from femur. In general, the different patterns of the stress status should not be put together for a direct strength comparison. However, in this particular situation, a fair assumption could be established for the strength

applications by considering that the uniaxial tensile strength to the cortical is the lowest of all.

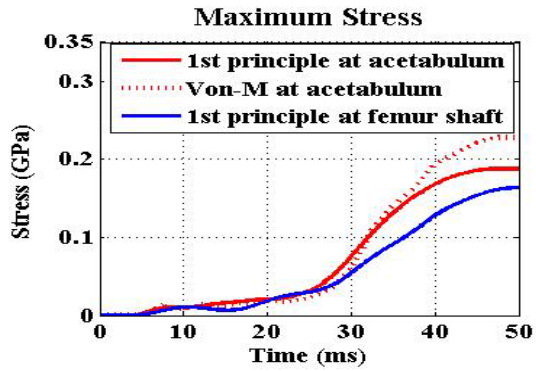

Figure 13. Stress measurements from a slow impact case.

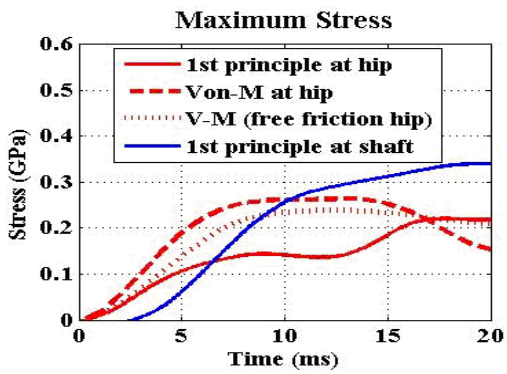

Figure 14. Stress measures from fast rate impact pattern.

For the slow rate impact, Figure 13 shows that the two stress measures of the acetabulum (red curves) are much higher than that of the femur (blue curve). Therefore, the slow rate impact most likely generates a hip joint injury, though the femur may still have a chance to fracture when the tensile stress is close to the acetabulum stresses. For the fast rate impact case in Figure 14, the plot in blue overlaps all the plots in red after 10 ms, which passes the peak time at 7 ms in this case. If the Von-Mises stress of the hip reaches its fracture strength around that time, it is possible to fracture the hip joint. However, tensile stress of the femoral bone with lower strength may also have a chance to fracture at the time. Along with the development of the bending mode, the femur stress continuously moves up; then the chance for the femur fracture would increase significantly. The femur could fracture during the unloading of the impact after the peak force. Figure 14 includes an additional fast rate impact case, presented by dense dot plot in red and marked as "free friction hip". This is a case of free tangential force inside the articular cartilage during the impact. The difference can be found between the two dot plots in red. It indicates the way of the friction influence to the maximum V-M stress level of acetabulum. It seems that the less viscous effect in the tangential plane of hip to a fast rate impact would increase the femur injury chance, because the acetabulum stress level moves down

The universal strength threshold was not tried for the two impact patterns from two kinds of impact rates because it could be strain rate dependence. The factors contributing to the effects of the impact rate in this model are biomaterial strain rate dependence characteristics of cortical bone, the assumption of the relative velocity of hip joint contact, and the strength of the cortical bone associated to the strain rate.

The assumption made for the articular cartilage is based on a physics concern that an easier bending of femur for a fast rate impact is throughout a less tangential restraint in the proximal femur head at the hip joint contact. In other words, an easily sliding of the femur proximal head may let a bending femur more easily reach an unstable condition than those with hardly sliding. Since the assumption needs test data for support, the function as the one in Figure 10 is only considered as an option for the Takata's KTH model.

The FEA offers a preliminary exploration to the KTH impact rate effects through a hypothesis concerned with a mechanical effect modeling of the hip joint. The viscous effect may not be limited to the articular cartilage. Other tissues, like muscle, could also be included.

KTH MODELING APPLICATION CASE 1

With the application of the upgraded Takata Human model from the above efforts, two vehicle accident field cases associated with KTH injury were studied to understand the injury development and injury mechanisms. All the vehicles involved in the cases studies are Honda Accords. A generic FE model of a 1994 Honda is publicly available in the NHTSA website. The model was downloaded and was improved by installing a generic frontal IP (instrument panel) model. The IP model was originally from a 2001 Taurus model available from NHTSA and its knee bolster geometry is modified to represent the Accord for the KTH study. A 1998 Honda Accord 30 mph Flat Frontal Barrier crash was taken from the NHTSA database for the knee bolster model correlation of both driver and passenger sides. The outlines of the vehicle correlation are addressed in Appendix.

Case 1: CIREN Case 830094706

Case 1 concerns an injured driver who was airbag restrained in a single vehicle crash with a relative low delta V impact. A 2003 Honda Accord, 4-door sedan was traveling west on a two-lane, two-way road. The driver of the Honda Accord reportedly fell asleep and crossed the eastbound lane, passed through an intersection and struck a guardrail at the southwest corner of the intersection. Figure 15 depicts the crash diagram of the scene. The impact was classified as a moderate 12 o'clock impact with a 10 degree PDOF (Principle Direction of Force). The WinSmash reconstruction program calculated an equivalent barrier speed of 35 kph (22 mph) which appears to be consistent with the vehicle damage. Figure 16 shows the left and right knee bolster contact.

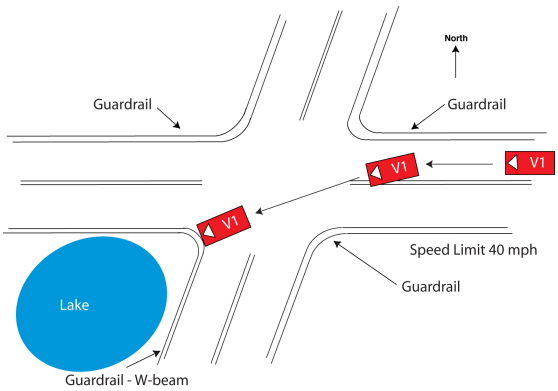

Figure 15. The crash diagram of the 2003 Honda Accord vs. Guardrail.

Figure 16. Left and right knee bolster contact.

Vehicle Crash Re-Construction Simulation

The case occupant: a 57-year-old male, 175 cm (5ft. 9in.), 95 kg (209 lb.), unbelted driver, restrained by the deployed steering-wheel airbag. The driver sustained fractures to the left anterior-lateral 5th and 6th ribs (AIS 2) and an OIS Grade III laceration of the spleen (AIS 3), these injuries are attributed to contact with the steering wheel rim as demonstrated by the rim deformation. The KTH injuries related to this investigation are the right acetabular fracture (AIS 3), right hip dislocation involving the articular cartilage (AIS 2), and right knee meniscus tear (AIS 2). These injuries are attributed to contact with the knee bolster as seen in Figure 16.

A vehicle at velocity 21.74 mph (35 kph) impact 80 degree to a flat barrier was simulated. The flat barrier was modeled with IIHS bumper honeycomb. Figure 18 shows the crash at 140 ms.

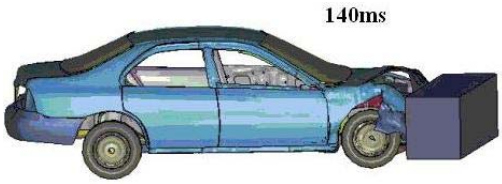

Figure 18. Vehicle impact simulation to a barrier crash in 80 degree at approximately 20 mph.

The vehicle motion profile obtained from the crash simulation is presented in Figure 19, where the positive side direction is from passenger side to driver side. The vehicle starts the impact at nearly 10 m/s speed, and rebounds at about 80 ms while the side velocity reaches highest level about 1m/s.

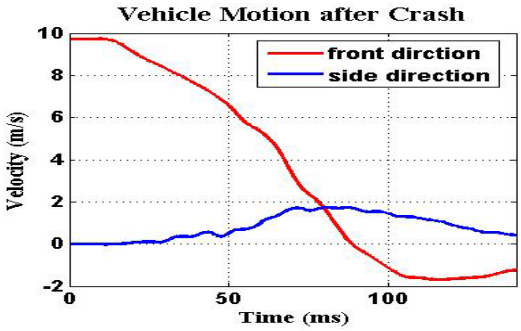

Figure 19. Vehicle velocity profile after crash.

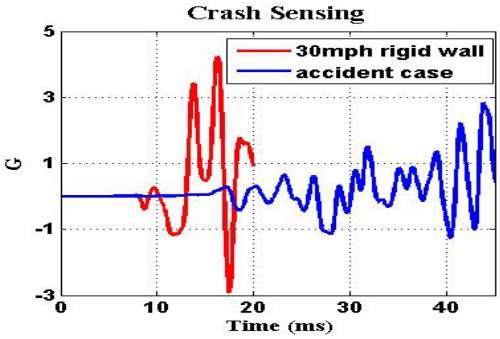

Figure 20. FE-evaluated vehicle frontal crash sensing signal of a rigid wall case and the reconstruction case.

To define the airbag deploying in the accident, crash sensing signals from the center radiator frame were measured through FEA to approach the TTF (time to fire). The signals, resulted from simulations of 30 mph frontal rigid wall impact and the accident case, are presented in Figure 20. The known TTF in the 30mph rigid wall crash is 12 ms. Depended on the algorithm aggressive level, the airbag could be deployed at a time between 26 ms and 38 ms in the crash. In the following addressed simulation, TTF=38ms is used.

During the low severity crash, the compartment entirety was kept without deformation. To simplify the occupant injury simulation in the next step, the vehicle crash can be moved into a simple sled protocol. The motion profile and airbag management were imposed to the sled model with a driver occupant.

Driver Occupant Injury Simulation

Simulation setup for the driver occupant at pre-crash is shown in Figure 21. The driver occupant is not restrained by belt, but by a frontal airbag (Figure 21). The male driver had the similar height but 20 kg more weight than that of the 50th% male human. The Takata 50th% male human model was scaled up without changing the stature in height but to match the total weight of the driver. The driver was assumed at a neutral posture; and initially at the same speed of the vehicle about to crash.

Figure 21. Simulation of unbelted driver in vehicle system.

The simulation showed the occupant moved obliquely forward to the passenger side and toward the windshield during the crash. As a result, the occupant's left side thorax contacts the steering wheel and the head contacts the windshield close to middle; as shown in Figure 22. The kinematics of the occupant is basically consistent with the contacts outlined in the accident case report. The oblique motion of the occupant results in uneven loading to the lower extremities during the crash. Figure 23 shows the FE-evaluated knee contact locations: the right knee impacts into the right corner of knee bolster and the left knee does the other end of the knee bolster of the generic model. Those basically match the contact points of knee bolster shown in Figure 16. Besides, knee meniscus tear (AIS 2) occurred in the right knee of the driver enable to be revealed from FEA for that the right knee was loaded from that contact. On the other hand, the shear stress was not observed in the left knee.

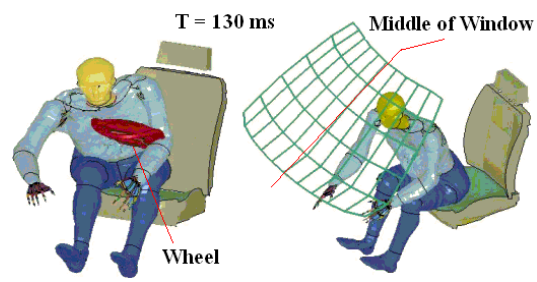

Figure 22. FE-evaluated occupant left thorax bending the wheel and head towards windshield.

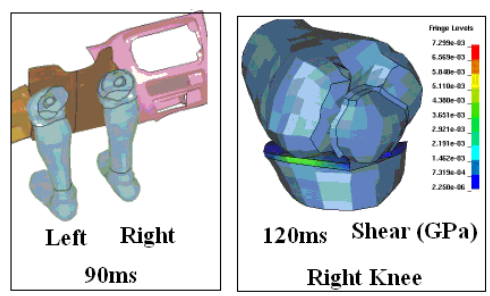

Figure 23. FE-evaluated knee impact location to bolster and right knee meniscus tear from the knee bolster contact.

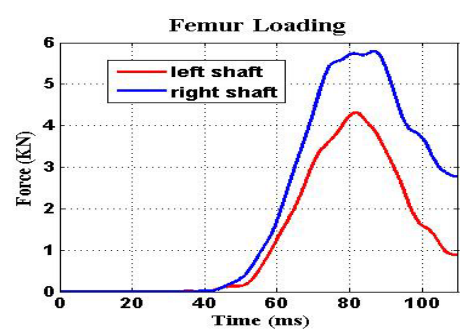

Figure 24. FE-evaluated occupant femur loading.

The femur loads were measured, as shown in Figure 24. Around 80ms, the left femur shaft experiences 5.8 KN and the right shaft experiences 4.2 KN. The loadings start at 40 ms. Therefore, both loading profiles can be categorized as a low rate impact. Figure 25 shows the KTH posture change with time. The occupant has his left KTH in abduction while flexion during the crash. In general, abduction

possesses a relative higher tolerance. The occupant's right KTH is in adduction and flexion with a higher femur loading.

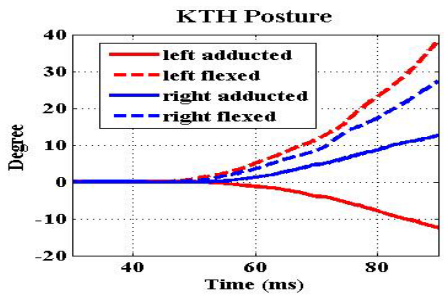

Figure 25. FE-evaluated occupant KTH posture.

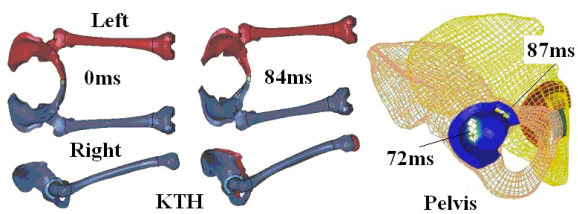

Figure 26. FE-evaluated occupant KTH posture in top and side view; and fracture in right hip joint.

The occupant KTH loading profile and posture status are inclined to a high chance of injury to the right hip joint. The snapshots of animations of the KTH are shown in Figure 26. Fractures were observed in the right acetabulum. The first fracture occurred at 72 ms when the right KTH at posture adducted 8 degree and flexed 10 degree with 5 KN femur loading.

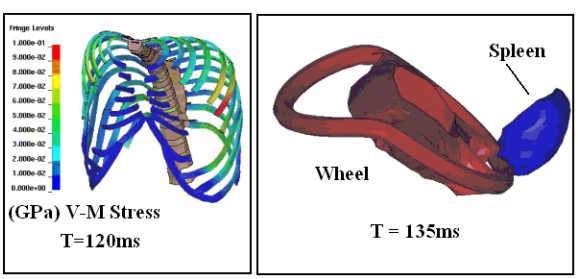

Figure 27. FE-evaluated stress distribution in rib cage, and wheel penetrates into spleen in simulation.

The KTH injury evaluated from the FEA is consistent with the related hip joint injuries reported in the case investigation. In addition to the lower extremity injuries, the FEA reconstructed the left anterior-lateral 5th and 6th ribs (AIS 2) and an OIS Grade III laceration of the spleen (AIS 3) that occurred in the accident due to the wheel rim impact are illustrated by the snapshots in Figure 27.

Overall, the Takata human model with the KTH modeling upgrade successfully predicts the KTH injury for the case application.

KTH MODELING APPLICATION CASE 2

Case 2 concerns an injured frontal passenger without airbag restraint in a two-car crash of a very low delta V impact. The delta V is less than 10 mph. The reported injuries to the front passenger are a left femur fracture (AIS 3) and left lower extremity skin contusion. The remaining two occupants, the driver and a rear-seat occupant, of the same vehicle have no reported injuries.

Case 2: NASS CDS Case 2000-049-268: Honda Accord vs. Honda Accord

A 1991 Honda Accord vs. 1991 Honda Accord: Vehicle 1 was traveling east in the first lane of a two lane undivided driveway, approaching a main cross street. Vehicle 2 was traveling south in the 3rd lane of a 3 lane divided road. Vehicle 1 began to make a left hand turn and contacted the front right corner and right rear side of Vehicle 2. Figure 28 depicts the crash diagram of the scene.

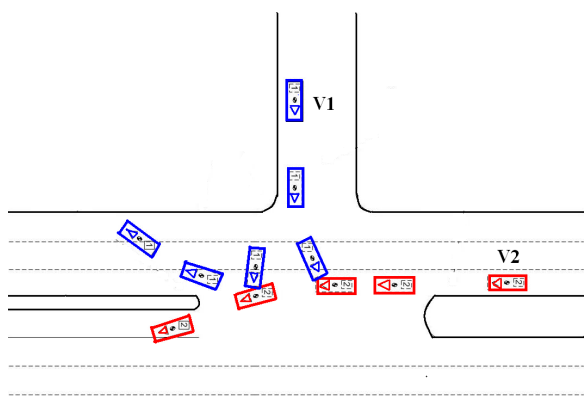

Figure 28. The crash diagram of the 1991 Honda Accord vs. 1991 Honda Accord.

Figure 29. Vehicle 1 damage.

WinSMASH computed a Delta V of 15 kmph/9mph which is consistent with the barrier equivalent speed of 15 kph (9 mph). Vehicle 1 sustained minimal damage as is seen in Figure 29. The case occupant: A 19 year old male 6 ft 0in. (183 cms) 170 lbs (77 kgs) was the right front passenger of Vehicle 1. The occupant sustained a left femur fracture (AIS 3) and left lower extremity skin contusion from apparent contact with the knee bolster.

As Vehicle 1 contacted the right front corner of Vehicle 2, the case occupant moved forward to the left, toward the point of impact. The occupant loaded the lower knee bolster, resulting in a femur shaft fracture. There were no other significant injuries.

Vehicle Crash Re-Construction Simulation

Figure 30 demonstrates the simulation model of a two-car crash in which the injured frontal passenger seated in Vehicle 1. Vehicle 1 impacted at 60 degree and 15 kph. Vehicle 2 moved forward at 45 kph. Vehicle 2 barely contacted the right frontal corner of Vehicle 1.

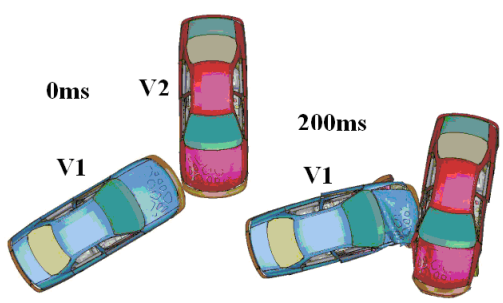

Figure 30. Two-car crash simulation.

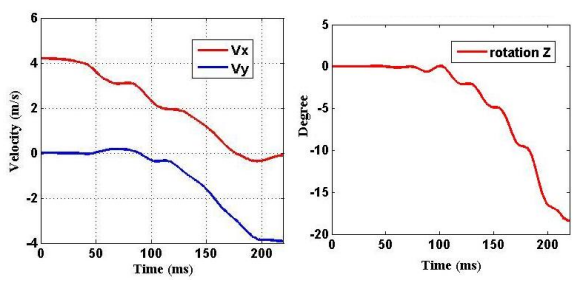

Figure 31. FE-evaluated motion profile including rotation of vehicle 1 post crash.

The motion profiles for Vehicle 1 evaluated from the FEA are presented as shown in Figure 31, where the positive x is from vehicle rear to front, and positive y from vehicle passenger side to driver side. Vehicle 1 at merely 4 m/s hits obliquely to Vehicle 2; and starts moving sideways and spinning toward the passenger side at around 100 ms. It is a very low delta V impact, and the deceleration is only about 4 G.

The occupant injury simulation can be simplified to a simple sled protocol simulation. The calculated motion profiles were imposed to the sled model with a passenger occupant

Passenger Occupant Injury Simulation

The injured frontal male passenger is close to a 50th% male human in weight and size, though he may be a little taller. So the Takata 50th% male human model in a neutral posture was directly applied to the system.

The vehicle was equipped with an automatic shoulder belt and manual lap belt. It is clear that the manual lap belt was not used from the final investigation report. No airbag was available in Vehicle 1. The occupant injury simulations were conducted for a condition of only automatic shoulder belt in use.

The accident happened when Vehicle 1 was making a left hand turn at the intersection. A crash of such low delta V indicates that the driver of Vehicle 1 was trying to stop the vehicle but initiated braking too late to fully stop. Assume the passenger, as a free motion body before the belt is active, possesses an initial velocity which is the same as the vehicle tuning speed before breaking. The passenger could be traveling at up to 30 mph just being about the crash. Therefore, an initial velocity of 12m/s (27mph) is defined for the passenger speed in the following simulation. The belt inertia management feature is triggered at 15ms when the vehicle reached 0.7G of deceleration for the motion profile.

First, the occupant was positioned in a normal seated posture. Under the belt condition for such a low delta V impact, simulation indicated the passenger's movement was restricted to all regions of his body except the knee. The only contact to the IP of the passenger is his knee to the knee bolster. Figure 32 demonstrates the most forward posture that the belted occupant could reach during the crash. The calculated femur loads are also presented and they are about 4KN at 10 to 20ms.

Though this is a fast rate impact, 4KN loading seems unlikely to fracture the femur. However, if the two equivalent loadings mainly act to just one leg, the

total force level then could fracture the shaft. Consider that the frontal passenger could have more flexibility in the posture and position, one candidate posture was defined for the simulation: the passenger abducted each of his thighs in about 5 degrees and turned his whole body 5 degrees toward the outboard side. At this posture, the left knee was closer to the knee bolster than the right knee. The human body model was positioned to replicate the assumed posture from pre-crash simulations. Figure 33 shows the occupant with the new posture in the system. After repeating the simulation, as expected, we have the calculated femur loading by the plots in Figure 34. The left femur experienced about 8KN at a fast rate loading while the right femur load was negligible.

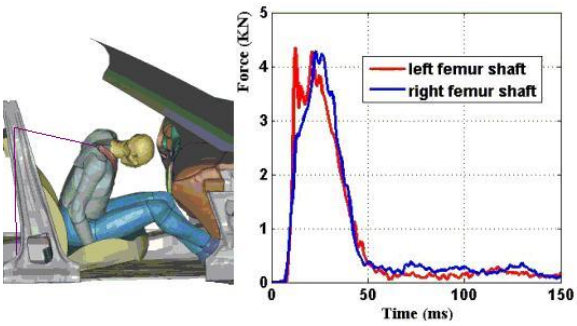

Figure 32. FEA evaluated belted occupant at 140ms and plots of the femur load.

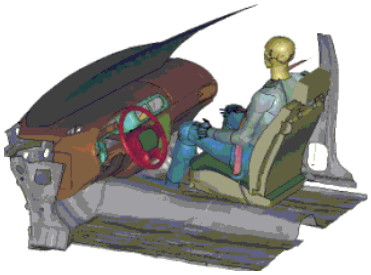

Figure 33. Occupant with one candidate posture leading a possible left femur fracture.

The case was once also evaluated for an unbelted condition as that could be a possible scenario in the field. Through simulation, FEA indicates the unbelted condition is unlikely because being unbelted would have lead to multiple injuries rather than just a single femur fracture.

The potential KTH fracture locations can be referenced to the maximum stress locations shown in Figure 35. The same as the previous strength analysis, the femur takes the first principle stress at the lateral side of the left femoral shaft; and the hip joint takes the Von-Mises stress. Figure 36 presents the time-histories of the stresses. It indicates that the femur has a higher chance of developing a fracture because the femur stress overlaps the acetabulum stress even before the KTH loading peak, and the stress reaches over a potential cortical bone strength tolerance level 125MPa after loading peak time at 22ms.

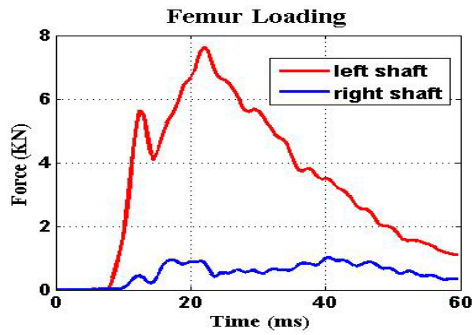

Figure 34. FE-evaluated femur loading profile to a belted occupant at a new posture.

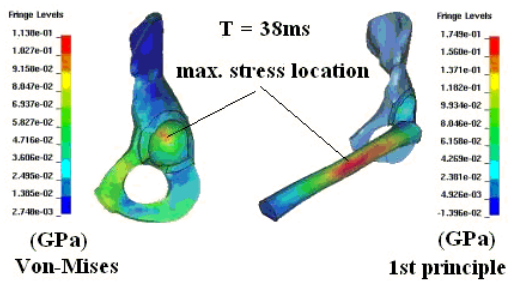

Figure 35. FE-evaluated the stress distribution in left femur and acetabulum at 38ms.

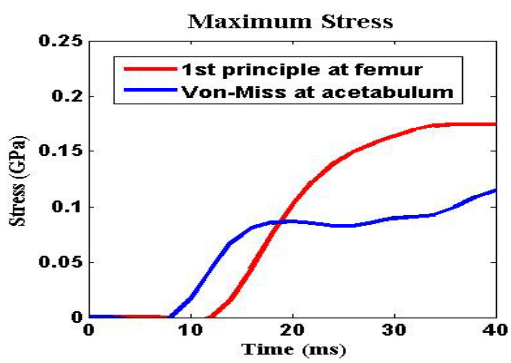

Figure 36. FE-evaluated stress development at the potential fracture locations of femur and acetabulum.

With the application of the Takata 50th% male human model, the field case is successfully investigated. The femur fracture mechanism of the belted occupant in a very low delta V impact is

explored, and the conditions leading to the injury is revealed.

DISCUSSION

Injury protection for KTH impact could be implemented by properly using the available restraint systems. For the first case, if the driver were belted, his kinematics would have managed to reduce the KTH adduction and flexion, and the lap belt would also share a part of knee loading. The driver would have had less chance of experiencing the acetabular fracture. Even if the driver failed to use the belt, if the vehicle was equipped with a knee airbag, it would also improve the KTH impact conditions.

In the knee airbag simulation the research indicates the knee bag is capable to manage the femur loading of less than 3KN for the unbelted heavy occupant. During the knee bag simulation the deploying knee bag did not affect the posture of the right KTH, however, the maximum plastic strain in the acetabulum was 1.548%, less than the threshold value of 2.11%. Therefore, the driver is less likely to have injury at the hip joint with the knee bag application. Figure 37 illustrates the performance.

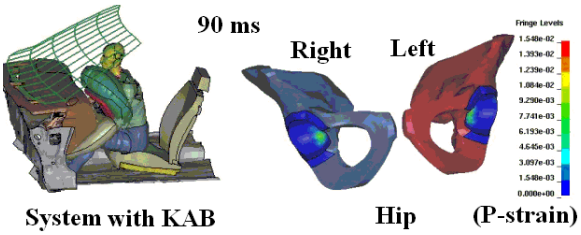

Figure 37. Driver in a system with knee airbag protection and the hip maximum plastic strain status in the protection.

For the second case, if a 3-point belt is equipped with a pretensioner, it would help to control the passengers initial velocity before knee impact and reduce the chance of fracture to the femur.

Though the upgraded Takata KTH model features three key posture of neutral, 10 degree adduction and 30 degree flexion, to be a "full" posture model, correlation to more posture variations may be needed. In the study, a posture computing post-processor tool, generating plots of Figure 25, is used with the universal strength threshold together for the assessment.

FE simulations for case reconstruction may operate with some uncertainties. Since the main target in the study is KTH injury, correlations were more focused on the crash environments directly related to KTH. The KTH injury in both cases occurs early in the crash sequence and later injury experienced in the crash were not concentrated on. To make a complete reconstruction simulation to study all injures in each case a vehicle crash simulation correlation for FMVSS 208 in the study could be further undertaken and some other components in the motion profile would not be ignored.

In this study, we only focused on the hip joint fractures and femur fractures from the PMHS laboratory tests and the real-field case studies. The modeling and model injury prediction capability verification should also be extended to the other body parts of the lower extremities, such as knee, ankle and foot, which are our continued effort for future work on the KTH injury mitigation.

CONCLUSION

The Takata 50th % male human model is upgraded especially for occupant KTH injury prediction or estimation. The model, with the effective plastic strain based injury criterion with a universal cortical bone fracture threshold developed in this study, is capable of predicting effects of occupant postures on the KTH injury patterns and severity under the conditions of UMTRI PMHS KTH impact tests for the neutral, 10 degree adducted, and 30 degree flexed postures.

The model is applied for a preliminary exploration of the effects of impact loading rate on the KTH fracture location and mode, with an assumed mechanical effect modeling for articular cartilage. An engineering approach is established through stress analyses of the femur and hip cup to judge the injury mode due to the rate effects. The engineering approach offers an option for Takata human KTH model applications.

The hip joint fracture and femur fracture are studied by simulating two vehicle crash cases at relative low delta V impacts. The simulations match the injury outcomes of the reported field observations. The occupant injury development and injury mechanisms in these two cases were explored.

ACKNOWLEGEMENT

The authors would like to gratefully acknowledge, to Dr. King Yang at Bioengineering Center of Wayne State University and Dr. Jonathan Rupp at UMTRI for their support for this research. Special thanks to

Gopal Narwani of TK Holdings Inc. for his valuable advice and support.

REFERENCES

[1] Shashi Kuppa, Jing Wang, Mark Haffner, Rolf Eppinger, "Lower Extremity Injuries and Associated Injury Criteria", 17th ESV Conference, Paper# 01-0457, 2001.

[2] Shashi Kuppa, Osvaldo fessahaie, "An Overview of Knee-Thigh-Hip Injuries in Frontal Crashes in The United States", 18th ESV Conference, Paper# 03-0416, 2003.

[3] Jonathan D. Rupp, Reed M.P. et al. "The tolerance of the human hip to dynamic knee loading", Stapp Car Crash Journal, Vol. 46, pp211-228

[4] Jonathan D. Rupp, Carl S. Miller, et al. "Characterization of Knee-Thigh-Hip Response in Frontal Impact Using Biomechanical Testing and Computational Simulations", Stapp Car Crash Journal, Vol. 52, pp. 421-474, 2008.

[5] Mark Sochor, Daniel Faust, Stewart Wang, and Lawrence Schneider, "Knee, Thigh and Hip Injury Patterns for Drivers and Right Front Passengers in Frontal Impacts", Stapp Car Crash Journal, Paper # 2003-01-0164, 2003.

[6] Jonathan D. Rupp, Reed M.P. et al. "Effects of hip posture on the frontal impact tolerance of the human hip joint", Stapp Car Crash journal, Vol. 47, p. 21-33, 2003.

[7] Eric Meyer, Michael Sinnott, etc. "The Effect of Axial Load in the Tibia on the Response of the 90° Flexed Knee to Blunt Impacts with a Deformable Interface", Stapp Car Crash journal, Paper # 2004-22-0003, 2004.

[8] Vijay Jayaraman, Eric Sevensma, etc., "Effects of Anterior-Posterior Constraint on Injury Patterns in the Human Knee During Tibial-Femoral Joint Loading from Axial Forces through the Tibia", Stapp Car Crash journal, Paper # 2001-22-0021, 2001.

[9] Jay Zhijian Zhao and Gopal Norwani, "Development of a Human Body Finite Element Model for Restraint System R&D Applications", 19th ESV Conference, Paper# 05-0399, 2005.

[10] Jay Zhijian Zhao and Gopal Norwani, "Biomechanical Analysis of Hard Tissue Responses and Injuries with Finite Element Full Human Body Model", 19th ESV Conference, Paper# 07-0354, 2007.

[11] Yuji Kikuchi, Yukou Takahashi, etc., "Development of a Finite Element Model for a Pedestrian Pelvis and Lower Limb", SAE Paper #2006-01-0683, 2006.

[12] Philippe Beillas, Paul Begeman, etc., "Lower Limb: Advanced FE Model and New Experimental Data" Stapp Car Crash journal, Paper #2001-22-0022, 2001.

[13] Yuichi Kitagawa, Junji Hasegawa, etc. "A Study of Knee Joint Kinematics and Mechanics using a Human FE Model", Stapp Car Crash journal, Paper #2005-22-0006, 2005.

[14] Costin Untaroiu, Kurosh Darvish, etc., "A Finite Element Model of the Lower Limb for Simulating Pedestrian Impacts", Stapp Car Crash journal, Paper #2005-22-0008, 2005.

[15] Chia-Yuan (Mark) Chang, etc., "Development of a Finite Element Model to Study the Effects of Muscle Forces on Knee-Thigh-Hip Injuries in Frontal Crashes", Stapp Car Crash journal, Paper #2008-22-0022, 2008.

[16] Jesse Ruan, etc., "Impact Response and Biomechanical Analysis of the Knee-Thigh-Hip Complex in Frontal Impacts with a Full Human Body Finite Element Model", Stapp Car Crash journal, Paper #2008-22-0022, 2008.

APPENDIX: VEHICLE IP CORRELATION

NHTSA Vehicle Database #V2836 of 1998 Honda Accord 30 mph into a flat frontal barrier is taken for vehicle system model correlation. The test in NHTSA was to evaluate the vehicle and occupant dynamics during a flat frontal barrier test at 30 mph. The vehicle was instrumented with 13 accelerometers to measure vehicle acceleration. Squib current was also collected to measure fire times of the airbag. The vehicle contained two instrumented Hybrid III 50th% percentile ATD, instrumented with head and chest accelerometers, chest deflection potentiometers, left and right femur load cells and upper neck load cells. The collected vehicle and occupant data was used to verify the vehicle model for simulation.

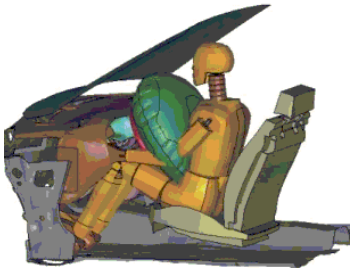

Figure 38. 30 mph flat frontal barrier FE simulation.

FEA was conducted to correlate the test for getting a reasonable mechanical property of knee boaster to use for the accident case simulation. The system model including Hybrid III 50th% dummy, airbag, and generic IP is shown as Figure 38. The dummy chest G is monitored in the simulation to make a basic assessment of correlation of the dummy kinematics to the test. The dummy femur loads are measured for the assessment of the mechanical properties of knee bolster.

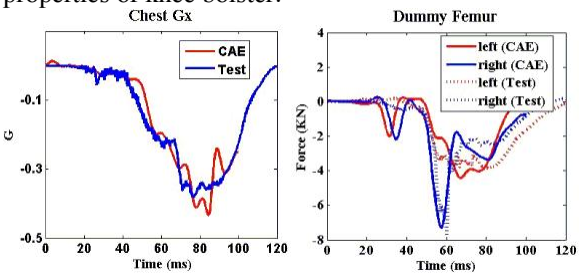

Figure 39. Driver performance correlation for chest G and femur loading of dummy.

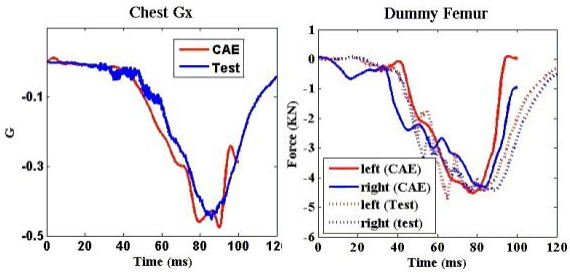

Figure 40. Passenger performance correlation for chest G and femur loading of dummy.

The correlations of the dummy performance to the both driver and passenger sides are obtained reasonably. The results for the driver side are presented in Figure 39, and passenger side at Figure 40. The FE correlations offer a fair base for the accident case simulation.

EVALUATION OF THE RISK OF INJURY CAUSED BY A KNEE AIRBAG IN OUT-OF-POSITION

Tiphaine Leport, Pascal Baudrit,
CEESAR, France
Philippe Petit, Xavier Trosseille,
LAB PSA Peugeot Citroën RENAULT, France
Guy Vallancien
Université René Descartes, France

ABSTRACT

As of today, active knee bolsters called knee airbags are available in some vehicles. However no assessment of the risk in Out-of-Position (OOP) conducted on Post Mortem Human Subject could be found in the literature. In total, 3 tests were performed in OOP on the Hybrid III 50th percentile dummy and 2 on two 50th percentile PMHS using a rigid subsystem based on the geometry of a commercially available mid-size European vehicle equipped with a knee airbag. The distance between the tibia and the airbag module ranged between 55 and 67 mm on the Hybrid III and was equal to 53 and 54 mm on the PMHS. The tests conducted on Hybrid III resulted in tibial drawer measurements in good agreement with the injury assessments since no injury was observed except bruises and abrasions (AIS 1). The results from the tests were compared to 36 real world frontal accident cases reported in France where drivers sustained only AIS 1 injuries (abrasion, contusion and bruise) during knee airbag deployment. The conclusions of this study are limited by the size of the sample (only 2 PMHS). However, the consistency between the outcome of the dummy and PMHS tests and the information from real world accidents provides a good confidence in the very low risk of injury associated with the knee airbag tested in OOP. Furthermore, the use of the Hybrid III dummy and the knee injury criteria based on the tibial drawer was appropriate in the tests conducted.

INTRODUCTION

Information on the different kinds of knee solicitations in car accidents is provided in the literature. Prior to the implementation of knee bolsters in the vehicles, the knee used to impact rigid elements such as the dashboard or the steering column, resulting in patella and femoral condyles injuries [1] [2] [3] [4] [5] [6]. Today, the knee bolsters have softened the contact between the knees and the vehicle and the solicitations are more distributed. Therefore, frequency of patella and femoral condyles injury occurrence has decreased and consequently, hip and knee ligament injuries have become of higher relative importance [7] [8] [9] [2] [5] [10] [11] [12] [13]. The development of active knee bolsters (knee airbag) brought a new type of loading, with an unusual range of impact. The literature does not report the existence of any tests on PMHS with such devices. Moreover, dummies have not been validated for this kind of tests [14] [15].

A study was performed on 36 real world frontal accident cases with knee airbags deployment reported in France between 2004 and 2008. The only injuries reported were abrasions, contusions and bruises (AIS1).

MATERIAL AND METHODS

As no assessment of the risk of knee airbag in Out-of-Position (OOP) conducted on Post Mortem Human Subject (PMHS) could be found in the literature, PMHS and dummy tests were performed. The tests were performed in a rigid subsystem based on the geometry of a commercially available mid-size European vehicle equipped with a knee airbag.

Specimen Preparation

For the dummy tests, the Hybrid III 50th percentile male was used. It was instrumented with a femur load cell (Fz), a knee ball slider assembly with linear potentiometer (Dx), a biaxial knee clevis load cell (Fz), a biaxial upper tibia load cell (Mx, My) and a three-axis lower tibia load cell (Fy, Fz, Mx).

The PMHS were obtained through the Body Donation to Science at the Saints Pères University of Medicine in Paris Vth after approval of the experimental procedure by the ethics committee of the university. The PMHS were tested for Cytomegalovirus (CMV), Human T cell Leukemia/lymphoma Virus (HTLV), Hepatitis C Virus (HCV), Hepatitis B Virus (HBV) and Human Immunodeficiency Virus (HIV), and a medical survey was documented. PMHS suspected of bone fragility (long bed stay, bone cancer, metastasis, etc.) were excluded. The PMHS were frozen and then thawed at ambient temperature during 48 hours before preparation. They were chosen to be as close as possible to a 50th percentile male. Their anthropometry, age and sex are reported in Table 1

Table 1 : PMHS Main Characteristics

PMHS #	586	588
Age	74	88
Sex	M	M
Total weight (kg)	77	69
height (m)	1.76	1.67
Thigh height (m)	0.46	0.46
Lower leg height (m)	0.55	0.52

A clinical examination of the knees was performed prior to and after the tests, to exclude the subjects presenting an abnormal laxity. In addition, prior to and after test, X-rays were taken while the thighs were fixed and a force was applied to the tibia by means of a weight of 4.5kg (Figure 1) in order to assess the range of anteroposterior tibial drawer laxity.

The effect of the test on the knee laxity was evaluated through the comparison of the range of laxity prior to and after testings. Finally, a dissection of the knees was performed to check the articular capsule and the knee ligaments.

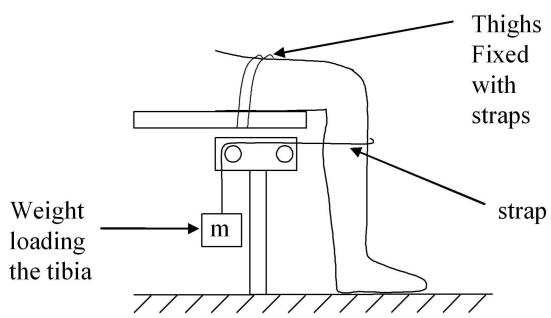

Figure 1 : Assembly for the radiographic examination

Test setups

A rigid subsystem based on the geometry of a commercially available mid-size European vehicle equipped with a knee airbag was used (Figure 3). The surrogate was seated in a standard car seat with the foot laying on a footrest. As in the car, the seat position was adjustable in height and in the antero-posterior direction. The angle of the backrest was 25° relative to the vertical plane. The knee airbag was fixed to a rigid plate placed in front of the knees and with an angle of 38° relative to the vertical plane. A rigid profile of the steering column was fixed to the plate with an angle of 35° with regard to the plane of the plate.

The coordinate system was defined as following: the YZ plane was the plane of the plate, the Z-axis corresponded to the lateral edge of the plate, the center was the left upper corner of the hole of the airbag. The X-axis was positive towards the subject, the Y-axis was positive towards the right and the Z-axis was positive upward.

Positioning procedure

The dummy was installed in the worst but realistic case of Out of Position. It was seated with the knees together, the feet on a rigid foot rest and the heels in contact with a fixed horizontal plan. The seat was initially adjusted in the lower vertical position and was then moved forward until the knees and the profile of the column were in contact. The left-right symmetry was verified. The femur and tibia angles and the distance between the plate and the tibias were used as guidelines for the PMHS positioning.

The PMHS were seated in the car seat with the knees together, the feet on a rigid foot rests and the heels in contact with a fixed horizontal plan. The heels were spread of 240 mm. The seat was positioned to obtain the following target position (Figure 2): the knees in contact with the profile of the column, a distance (D) of 55 mm between the tibias and the center of the airbag (measurement taken perpendicularly to the plate), the femur tilted by 22° and the tibia by 57° with regard to the horizontal plane.

A 3D measuring arm (Romer type 100) was used to digitize the targets and the bone landmarks during the specimen positioning

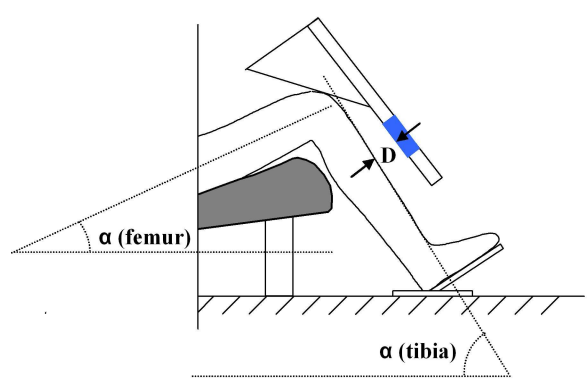

Figure 2 : Leg position

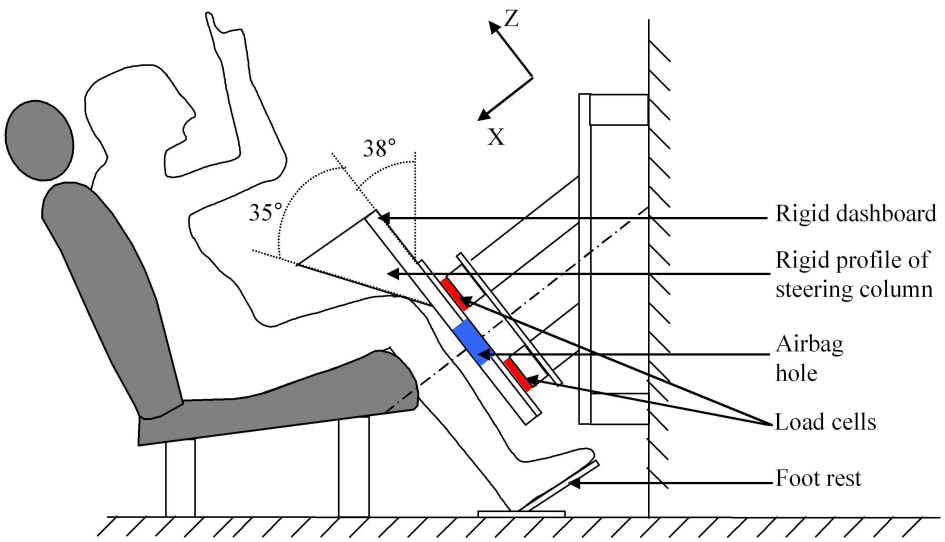

Figure 3 : test setup

Test matrix

The test configurations are described in Table 2. Two reference tests (HIII-C1 and HIII-C2) were performed with the dummy in the realistic OOP. A dummy test (HIII-F) was also performed by increasing the distance D while keeping the knees in contact with the profile of the column.

The PMHS were positioned to obtain the same position than for the dummy in the reference tests.

Table 2 : test matrix

Test #	Subject		D (plate -tibia) (mm)	Tibia angle (°)	Femur angle (°)
HIII-C1	HIII 50th	L	58	57	21
		R	57	58	23
HIII-C2	HIII 50th	L	55	58	23
		R	55	57	22
HIII-F	HIII 50th	L	66	57	20
		R	68	57	23
PMHS-1	MS586	L	51	55	23
		R	54	56	26
PMHS-2	MS588	L	54	55	24
		R	54	54	28

Instrumentation and data processing

Instrumentation. Four load cells were mounted between the airbag plate and a rigid fixed frame, to measure the forces applied onto the legs.

Filtering. The data were filtered CFC180.

High speed video. The tests were recorded using three high-speed cameras at 2000 frames-per-second (fps). The views consisted of a global view (right side), a zoom view centered on the left leg and a ¾ general view (back-above).

RESULTS

Deployment phases

The deployment of the airbag was composed by several phases, showing alternately falls and ascents of the plate forces. These phases are described below and illustrated by a sequence presented in Figure 4.

Phase 1 (F ↑): After the firing, the airbag fabric and the cover were expulsed.

Phase 2 (F ↓): the cover movement in X was stopped.

Phase 3 (F ↑): the airbag deployed against the tibias.

Phase 4 (F ↓): the airbag spread on sides.

Phase 5 (F ↑): the deployment on sides was ended, the airbag pushed on the knees backwards.

Phase 6 (F ↓): the upward unfolding and deployment of the bag. Vent holes opening.

Phase 7 (F ↑): the airbag continued to unfold and pushed on the knees.

Phase 8 (F ↓): the airbag passed over the knees and freely completed its upward deployment.

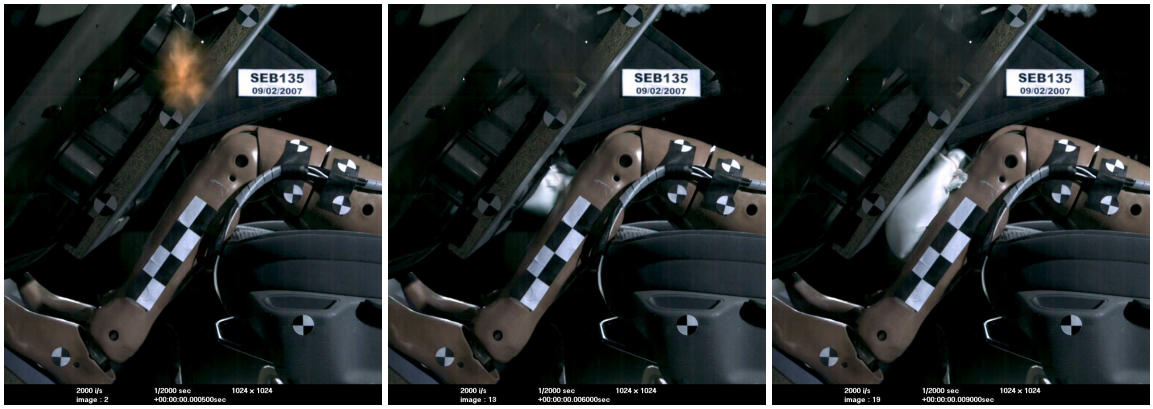

1- cover reaction

2- free deployment

3- unfolding against the tibias

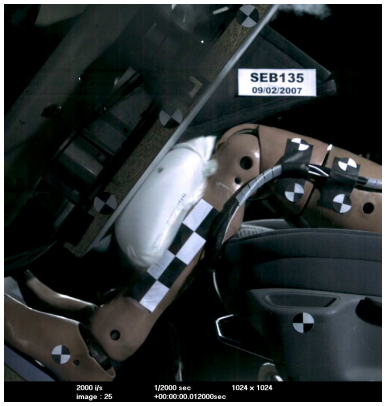

4- lateral deployment

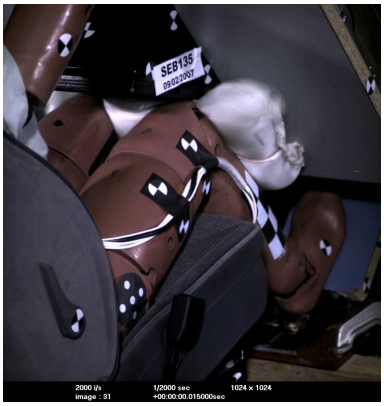

5- knee contact

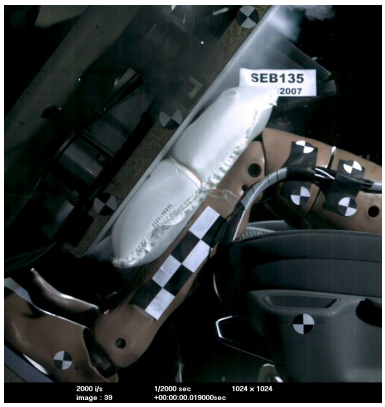

6- opening of the vent holes

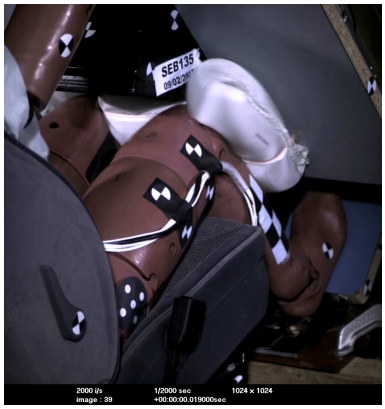

7- unfolding continuation and knee contact

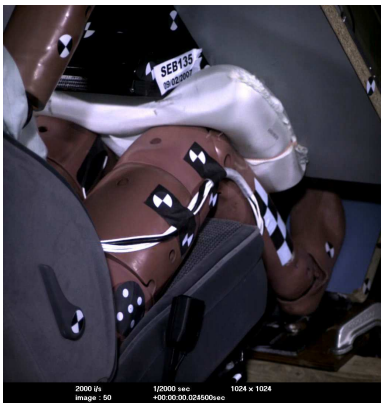

8- airbag over the knees

Figure 4 : Pictures of airbag deployment phases

Plate forces

As the plate was rigid and still, once the fabric was in contact with the lower leg, the plate reaction force can be assumed to be equal to the fabric/leg force. The forces are shown Figure 5. Eight phases of the deployment of the airbag are annotated in Figure 5.

The maximum plate forces and the impulse are presented in Table 3. The dummy tests HIII-C1 and HIII-C2 were very similar in amplitude and in profile. The oscillations observed at the various phases of the unfolding were synchronous. The forces of the PMHS-1 and PMHS-2 tests were also comparable in amplitude and in profile. The curve

profiles were also comparable between the dummy and the PMHS, with synchronous oscillations, but more marked for the PMHS tests. The maximum forces showed no significant difference between the PMHS and the dummy tests. The forces decreased more rapidly for the PMHS than for the dummy, so the total impulse was 30% lower for the PMHS, while at 22 ms, the impulses had the same order of magnitude.

Table 3 : Plate reaction

	Maximum plate force (X-axis) (kN)	Total plate impulse (N.s)	Impulse at 22ms (N.s)
HIII-C1	7.7	218	80
HIII-C2	8.4	240	85
HIII-F	7.0	219	67
PMHS-1	8.0	137	74
PMHS-2	7.6	168	69

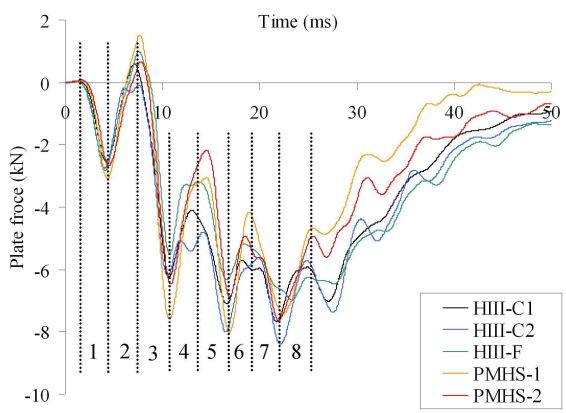

Figure 5 : Plate reaction forces

Injury assessments

The lower limbs of the subject MS586 and MS588 showed no bone or ligament injury. The ranges of knee laxity were not increased by the tests for none of the two specimens. Abrasions were found at the level of the third superior of the tibia or of the joint on each of the knees. (AIS1). The subject MS586 presented a bruise of the semi-membranous muscles at the lower level of the right and left femurs (AIS1). Abrasions and bruises were also observed in the real world accident cases.

Knee injury criterion

According to the bibliography, with the implementation of the knee bolsters in the vehicles, the injuries of the hip and the ligaments of the knee became dominant. It can reasonably be assumed that in OOP, the intrinsic aggressivity of the active systems concerns first the injuries of the ligaments of the knee. The dummy criterion associated with the knee injury is the tibial drawer. This translation was measured during the tests on the Hybrid III (Figure 6). The maximum values are presented in

Table 4 and ranged between 6.3 mm and 11 mm, while it was less than 5mm in the reference car. The threshold of the tibial drawer is 15 mm in the European regulation [16] and 6 mm for the EuroNCap. The translation is lower for the HIII-F test than for the two others where the dummy was positioned closer to the plate. The translation was systematically greater for the left than for the right knee. The femur forces are presented Figure 7.

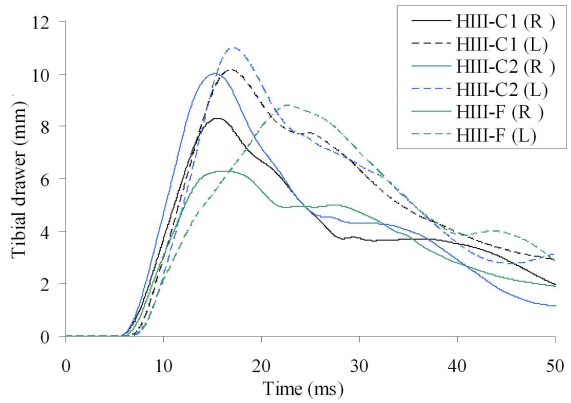

Figure 6 : Tibial drawers

Table 4 : Dummy tests results

	HIII-C1		HIII-C2		HIII-F	
	L	R	L	R	L	R
Max. plate force (kN)	3.9	2.6	4.3	4.1	3.8	3.2
	7.7		8.4		7.0	
Max. tibial drawer (mm)	10.1	8.3	11	10	8.8	6.3
Max. femur force (kN)	2.6	2.5	2.8	2.7	2.4	2.2

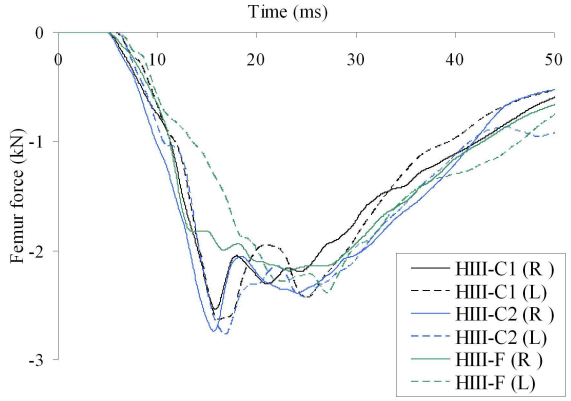

Figure 7 : Femur forces

Bibliographic comparison

Several studies on PMHS were performed to estimate tibial drawer injury threshold. Viano et al. [7], Balasubramanian et al.[12] and Meyer et al.[11] reported that the posterior crossed ligament (PCL) is damaged for an average translation of 16 mm of the tibia relative to the femur. This tibial drawer ranged between 9.5 mm and 30 mm depending on the specimen (Table 5). An injury risk curve for the posterior crossed ligament was calculated as a function of the tibial drawer using the data provided in the literature (Figure 8). Since the tibial drawer value is available at the injury occurrence, the survival method was used. Meyer et al. [11] performed tests with and without axial tibia loading. Balasubramanian et al. [12] performed tests on specimen with knees either intact or with the PCL only. As there is no statically significant difference of the tibia sliding in cases of PCL trauma between the different series of tests for each study, all the data were included to calculate the injury risk curve.

Table 5 : Tibial drawer for PCL injury – bibliographic data

Reference	PCL injury translation (mm)
Viano [7]	9.5
	10.7
	18
	30
Meyer [11]	19.9
	14.5
	17.9
	20.9
	16.1
	9.5
	10
	13.1
Balasubramanian [12]	16.3
	15.9
	21.5
	19.7
	15.3
	14.5

Balasubramanian et al. [12] compared the behavior of the Hybrid III 50th percentile and the PMHS. They found that apart from an initial higher stiffness, the overall response of the ball bearing knee slider of the Hybrid III dummy lay within the corridors for the PCL rupture.

Assuming the HIII dummy to be biofidelic, the tibia sliding of the HIII-C1 and HIII-C2 tests was associated to the PMHS, as the tests were performed in the same conditions and have shown plate forces similar in amplitude. The tibia sliding of the subjects was thus estimated to be equal to 10 mm. According to the injury risk curve, the risk associated with 10mm of tibia sliding is 11 %. It has to be noticed that the injury risk is overestimated compared to the reference car, as the subsystem was rigid, and then the force applied to the femur was higher than in real car tests.

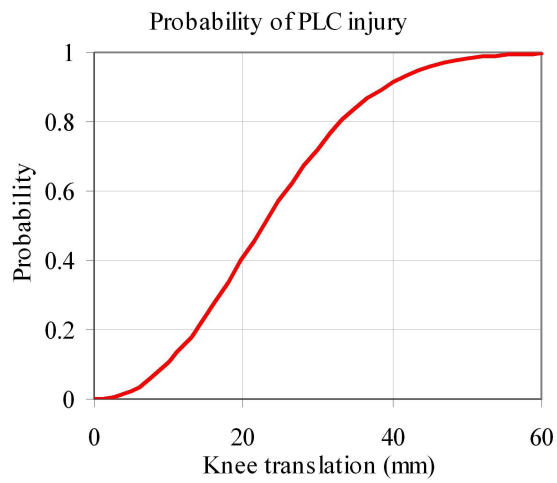

Figure 8 : Injury risk as a function of the tibial drawer

CONCLUSION

The objective of this study was to estimate the intrinsic aggressivity of the knee airbag in OOP. Based on the literature review, it was assumed that the risk due to the system in OOP concerns essentially the knee ligaments.

Three tests on HIII 50th percentile were performed in an Out-of-Position configuration using a rigid subsystem based on the geometry of a commercially available mid-size European vehicle equipped with a knee airbag. Two cadaver tests were performed in the same conditions. A 10mm translation was estimated for these tests. No bone or ligament injury was observed. This is in agreement with the literature tests, from which an injury risk curve was calculated. According to the injury risk curve, the risk associated with a 10mm translation is 11 %. Furthermore, this injury risk overestimated the real car performance since the subsystem was rigid, and then the force

applied to the femur was higher than in real car. Abrasions and bruises were observed on the cadavers. They were in agreement with the real world accident reports.

The conclusions of this study are limited by the size of the sample. However, the consistency between the outcome of the dummy and PMHS tests and the information from real world accidents provides a good confidence in the very low risk of injury associated with the knee airbag tested in OOP. Furthermore, the use of the Hybrid III dummy and the knee injury criteria based on the tibial drawer was appropriate in the tests conducted.

ACKNOWLEDGMENTS

The authors would like to thank the employees from CEESAR for their assistance: David Auffray, Gilles Corbin, Denis Dubois, Fréderic Loiseleux, Catherine Potier and Pascal Potier.

REFERENCES

[1] Viano, Stalnaker "Mechanisms of Femoral Fracture". J. of Biomechanics, 1980

[2] Hayashi, Choi, Levine, Yang, King. "Experimental and Analytical Study of Knee Fracture Mechanisms in a Frontal Knee Impact". 962423

[3] Atkinson, Garcia, Altiero, Haut. "The influence of Impact Interface on Human Knee Injury : Implications for Instrument Panel Design and the Lower Extremity Injury Criterion". 973327

[4] Atkinson, Mackenzie, Haut. "Patellofemoral Joint Fracture Load Prediction Using Physical and Pathological Parameters". 980358

[5] Atkinson, Atkinson, Haut, Eusebi, Maripudi, Hill, Sambatur. "Development of Injury Criteria for Human Surrogates to Address Current Trends in Knee-to-Instrument Panel Injuries". 983146

[6] Atkinson, Haut. "Impact Responses of the Flexed Human Knee Using a Deformable Impact Interface". J. Biomech Eng June 2001, Vol.123.

[7] Viano, Culver, Haut. " Bolster Impacts to the Knee and Tibia of Human Cadavers and an Anthropomorphic Dummy ". 780896

[8] Viano, Culver." Performance of a Shoulder Belt and Knee Restraint in Barrier Crash Simulation" . 791006

[9] Fukubayashi, Torzilli, Sherman, Warren. "An In Vitro Biomechanical Evaluation of Antero-Posterior Motion of the knee.Tibial Displacement, Rotation and Torque". J. Bone and Joint Surgery, 1982

[10] Rupp, Reed, Van Ee, Kuppa, Wang, Goulet, Schneider. "The Tolerance of the Human Hip to Dynamic Knee Loading". 2002-22-0011

[11] Meyer, Sinnott, Haut, Jayaraman, Smith. "The Effect of Axial Load in the Tibia on the Response of the 90° Flexed Knee to Blunt Impacts with a Deformable Interface". 2004-22-003

[12] Balasubramanian, Beillas, Belwadi, Hardy, Yang, King. "Below Knee Impact Responses using Cadaveric Specimens". 2004-22-0004

[13] Bartsch, Bolte IV, Litsky, McFadden. "Application of Anthropomorphic Test Device Crash Test Kinetics to Post Mortem Human Subject Lower Extremity Testing". 2006-01-0251

[14] Kuppa, Wang, Haffner, Eppinger. "Lower Extremity Injuries And Associated Injury Criteria". 17th ESV, 2001

[15] Rupp, Reed, Madura, Schneider "Comparison of Knee/Femur Force-Deflexion Response of the Thor, Hybrid III, and Human Cadaver to Dynamic Frontal-Impact Knee Loading". 18th ESV, 2003

[16] ECE/324 - Rev.1/Add.93/Rev.1
Agreement concerning the adoption of uniform technical prescriptions for wheeled vehicles, equipment and parts which can be fitted and/or be used on wheeled vehicles and the conditions for reciprocal ecognition of approvals granted on the basis of these prescriptions

COMPARISON OF ANTHROPOMORPHIC TEST DUMMIES WITH A PEDIATRIC CADAVER RESTRAINED BY A THREE-POINT BELT IN FRONTAL SLED TESTS

Joseph Ash
Yasmina Abdelilah
Jeff Crandall
Dan Parent
University of Virginia
Center for Applied Biomechanics
United States of America
Chris Sherwood
Insurance Institute for Highway Safety
United States of America
Dimitrios Kallieris
University of Heidelberg
Germany
Paper 09-0362

ABSTRACT

Validation data for assessing dummy child biofidelity are limited, especially with regard to whole-body kinematics. Therefore, the goal of this study was to assess the kinematic biofidelity of current child dummies relative to results obtained from analysis of a child cadaver sled test. The baseline data were obtained from a previously unpublished test performed with a 13-year old pediatric cadaver restrained by a three-point belt. The cadaver test conditions were reconstructed using two dummies with anthropometry closest to that of the cadaver, the HIII 10-year old and HIII 5th female dummies. Due to anthropometric and age-equivalent differences between the dummies and the child cadaver, geometric scaling was performed on the signals based on the seated height and material properties. Kinematic evaluations of head, hip, and knee trajectories were obtained from film analysis. Accelerations of the head, shoulder and lap belt loads were measured and compared among the dummy and child cadaver data. While this study shows that the HIII 10-year old, scaled HIII 5th female and scaled pediatric cadaver reasonably agree for the shoulder belt force, the resultant head acceleration, and the maximum head excursion, differences in kinematics were identified between the dummies and the cadaver. Some of these differences in dummy kinematics were attributed to nonbiofidelic motion of the rigid thoracic spine with extensive bending at the cervical and thoracic spine junction. In addition to new cadaver data, the study provides insight into the applicability of geometric scaling for dummy evaluation and suggestions for improved dummy biofidelity.

INTRODUCTION

The design and evaluation of current child restraint systems relies heavily on the biofidelity of current anthropometric test devices. Given the paucity of biomechanical data available for both development and validation of child dummies, child response targets have largely been achieved through geometric and material property scaling of adult responses. Dimensional scaling, however, involves a number of assumptions in terms of geometric similarity and loading of homologous structures that may not be justified with the differences in regional dimensions and mass distributions between children and adults (e.g., the child head comprises a disproportionate share of the overall body mass relative to the adult head). Furthermore, the scaling of response for material property from adults to children are usually limited to one tissue type (e.g., bone) within a body region whereas the actual response typically involves the composite response effects of a large number of soft and hard tissue types. Therefore, it is essential that dummies are evaluated under whole body loading conditions similar to the test environment in which they will be used to design restraint systems. While reconstructions of crashes involving children provides valuable injury data (c.f., Ash et al., 2009), the lack of information regarding initial occupant, restraint, and vehicle conditions introduces large uncertainties into reproducing these events in the laboratory for the purpose of dummy validation. For the validation of occupant kinematics, pediatric cadaver tests arguably provide the best condition for evaluation of dummy seat belt and booster seat restraint of children (Kallieris, 1976) despite some differences in muscular effects between dummies and cadavers. In the study presented here, data from a

sled test using a 13-year old cadaver was analyzed and compared to a series of tests conducted with dummies under identical test conditions to those of the pediatric cadaver. The two anthropomorphic test devices (ATD) that were closest in size to the pediatric cadaver were used including the Hybrid III (HIII) 10-year old and Hybrid III 5th percentile adult female (AF5) (~size of 12 year old). The tests and analysis in this paper compare the pediatric cadaver kinematic and kinetic data to the data obtained using the dummies.

METHODS

Pediatric cadaver

The pediatric cadaver data was taken from an unpublished test performed at the University of Heidelberg in 1976. Though the test analyzed in this study comes from an unpublished test, information about the general test setup can be found in Kallieris (1976). While the Kallieris (1976) study uses pediatric cadavers and child restraint systems which differ from this study, information regarding general testing methodology and cadaver preparation from the original study may provide additional information useful to the reader.

A 13-year old cadaver was positioned in a mid-1970's Volkswagen Golf Type 1 seat and restrained by a high elongation (17%) three-point belt. The impact velocity of the sled was 41 km/h and the pulse was trapezoidal with a median sled deceleration of 21 g. Black and white photos were taken before and after the test and high speed cameras acquired lateral and frontal views with frame rates of 1000 frames/s and 500 frames/s, respectively. Photo targets were placed on the head, shoulder, and pelvis of the cadaver (Figure 1).

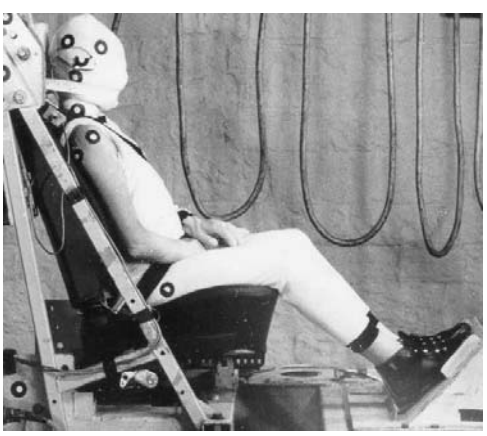

Figure 1. Seated position of the pediatric cadaver and placement of photo targets.

Their trajectories were subsequently analyzed using a commercial software package (Phantom Camera Control, Version 8.1.607 XP). The cadavers were instrumented with X and Z axis accelerometers fixed to the side of the head at the lateral projection of the head center of gravity (CG). In order to conform to the SAE J211 standard coordinate system (SAE, 2003), the Z axis component from the original data collection (Figure 2) was inverted to ensure it was positive in a downward direction.

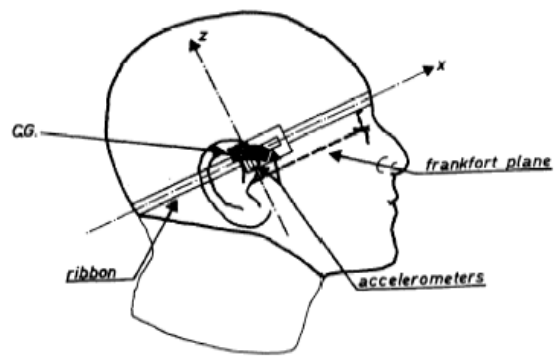

Figure 2. Mounting diagram of accelerometers in the pediatric cadaver test (from Kallieris, 1976).

In addition to the head and buck accelerations, forces were measured in the shoulder and lap belts.

Anthropometric test dummies

Subsequent to the pediatric cadaver test, tests with anthropometric dummies were designed to duplicate the experimental conditions of the cadaver using the UVA sled system (Via Systems Model 713). The test fixture, or "buck," consisted of the front passenger bucket seat of a 1975 Volkswagen Golf with matched anchorage locations for the seatbelts. The seat-adjustment mechanism was removed to make it more durable for repeated testing, and both the seat pan and seat back were rigidly fixed to the buck. The three-point belt was a custom-made, approximate replica of the original belt with 18% elongation webbing (Figure 3).

Figure 3. Hybrid III 10-year old dummy in rigidly fixed seat with replica seat belt.

The tests designed to duplicate the test conditions of the pediatric cadaver were three repeated tests with the HIII 10-year old tests and two repeated tests of the AF5. The dummies were calibrated prior to the testing, and all joints were adjusted to the relevant specification (1 g). The dummy was instrumented with accelerometers and angular rate sensors in the head (CG), accelerometers in the chest (CG) and pelvis, load cells in the upper and lower neck, femur, left and right ASIS, and clavicle. In addition, the dummies were modified to allow for attachment of instrumentation cubes containing accelerometers and angular rate sensors on the upper thoracic spine. Though the X, Y and Z components of the head CG acceleration were measured, only the X and Z were used in the calculation of the resultant acceleration since these were the only two channels collected for the pediatric cadaver.

Before placing the dummy in the seat, photo targets were attached to the dummy at the head CG, hip, knee, ankle, shoulder, and points along the thigh. Other photo targets were placed at measured distances on the test fixture in order to provide spatial resolution in various planes for the video analysis. The dummy was positioned in the Volkswagen seat according to the procedure developed by Reed (2006). This procedure made modifications to the specifications of FMVSS 213 in order to more accurately model real world child seated posture. After the dummy was centered, a force of 178 N was first applied to the pelvis and then to the thorax of the dummy to ensure it was properly seated. At this point, minor adjustments were made to ensure the dummy's position matched that of the cadaveric test using the pre-test photos of the pediatric cadaver . With the dummy firmly positioned in the seat, the three point belt was positioned and buckled. Belt tension load cells (Interface Model DK113523) were attached to the outboard lap and shoulder portions of the belt.

The tests were recorded using three high-speed (1000 frames/s) digital video imagers (Kodak RO) that were positioned to provide a perpendicular view from the driver's side of the sled track, an oblique view from the front/passenger side, and an overhead view. Photo target trajectories were tracked using video analysis software (Phantom Camera Control, Version 8.1.607 XP). To ensure test to test repeatability, a three dimensional positioning device (Faro arm) was used to confirm the initial condition of each dummy prior to launching the sled. In addition, photos were taken to record the pre-crash and post-crash position and the orientation of the dummies.

Geometric scaling

In order to compare the kinematics among the surrogates, the accelerations and loads of the dummies and the pediatric cadaver were scaled. The scaling methods take into account variations in subject anthropometry in order to calculate equivalent values between the two subjects and are based on dimensional analysis (Irwin, 1997 and Irwin, 2002). The nondimensional ratio used in the scaling analysis is the length scaling ratio (Equation 1),

$$\lambda_L = \frac{L_1}{L_2} \qquad (1)$$

where λ_L is the scaling factor, L_1 is the seated height of the reference subject (i.e.,the subject that will not be scaled) and L_2 is the seated height of subject to be scaled. The seated height was used in the length scaling factor since this information was directly measured for both the cadaver and the dummies. In addition to the length scaling factor the other fundamental nondimensional ratio used was the modulus of elasticity ratio λ_E. In order to scale the forces, accelerations and event times the following scale factors were used (Equations 2-4),

$$\lambda_A = \frac{1}{\lambda_L} \qquad (2),$$

$$\lambda_F = \lambda_K \lambda_L \qquad (3),$$

$$\lambda_T = \frac{\lambda_L}{\lambda_E^{0.5}} \qquad (4).$$

In the above equations, λ_A is the acceleration scaling factor (Equation 2), λ_F is the force scaling factor

(Equation 3) and λ_T is the time scaling factor (Equation 4) from Irwin (1997). The force scaling factor was based on the ratio of the stiffness of the subjects' chests, λ_K. This chest stiffness ratio takes into account the difference in stiffness of the subjects' ribs along with the contribution that the viscera and flesh have on the overall stiffness of the chest. The development of the chest stiffness ratio can be found in Appendix A.

The heights, elastic moduli, and masses used in this scaling approach along with the scale factors can be found in Table 1. The value of the Elastic Modulus for the HIII 10-year old was found in Irwin (2002) and the value of the elastic modulus for the 13-year old pediatric cadaver was estimated from interpolating between data points provided by Irwin (1997). Once the modulus scale factor was determined, it was used to determining the stiffness scale factor. The stiffness scale factor was then used in the force scaling factor development.

Once the values of the accelerations and forces were scaled the maxima, and minima in the case of the head CG X component, were found and compared. Since three repeat tests were performed with the Hybrid III 10-year old dummy, the average and standard deviations of responses were calculated.

Table 1.
Scale factors (compared to HIII 10-year old) and surrogate measurements

	HIII 10yo	HIII AF5	Pediatric Cadaver
Seated Height, [m]	0.72	0.79	0.81
Elastic Modulus, [GPa]	8.45	9.9	9.0
Mass, [kg]	35.0	49.1	50.0
λ_L	1	0.91	0.89
λ_E	1	0.85	0.94
λ_A	1	1.10	1.13
λ_K	1	0.85	0.89
λ_F	1	0.77	0.79
λ_T	1	0.99	0.92

For the pediatric cadaver and Hybrid III 5th female dummy, there were an insufficient number of tests (i.e., statistical degrees-of-freedom) to calculate standard deviations. Since direct comparison of point estimates (i.e., average response values at any time t) would not have accounted for test variability inherent even in controlled laboratory dummy tests, a methodology of generating estimates of confidence intervals was created. In order to compare dummy and cadaver responses, a normal distribution was assumed around the mean response. The upper and lower bounds of the 95% confidence interval were estimated using,

$$UB = (1 + COV * z)\mu$$
$$LB = (1 + COV * z)\mu \qquad (5).$$

In Equation 5, UB and LB are the upper bound and lower bound, respectively, COV is the coefficient of variation, z is the number of standard deviations to achieve the desired confidence interval, and μ is the mean of the quantity for which the boundaries are found. The COV that was used for the dummies was 10% because this was stated as the upper limit of acceptable values in the automotive safety field by Shaw (1994). Though 10% is considered the upper limit, a COV of 5% is considered good repeatability (Foster, 1977).

The length scaling factor was applied to the kinematic trajectories obtained from the video analysis. The lap and shoulder belt loads as well as the head center of gravity accelerations were scaled by the force and acceleration scaling factors, respectively. In order to scale the whole body kinematics of the various test subjects, a common reference origin was created to account for differences in local origins among the dummies of different sizes (Figure 4).

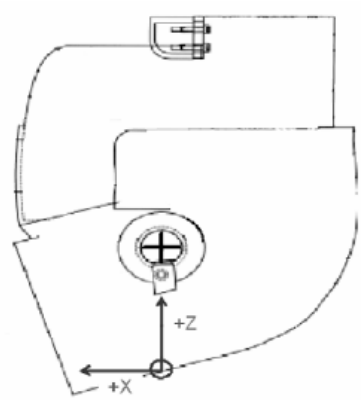

Figure 4. Location of common reference origin where the black cross represents the H-point of the dummy and the origin of the reference coordinate system is shown directly below H-point. (Adapted from NHTSA 2000)

The common point that was chosen for comparing these tests was the point directly below the H-point in the vertical direction to where the subject meets the

seat. This was done so that all trajectories would have a common reference point as the origin. For the dummies the H-point information was found from the technical specification drawings and the reference manuals for each dummy (HIII 10-year old: NHTSA 2005, AF5: NHTSA 2000). In order to determine an appropriate value of the vertical distance from the H-point in the pediatric cadaver, scaling was used. Since no measured value for this distance was included in the anthropometry, the known value of the vertical distance was taken for the HIII 6-year old and scaled, using the length scaling factor, to the approximate distance for the cadaver.

Video Analysis

To assess the kinematics of each surrogate, the points of interest from the videos were the head CG, the shoulder, the H-point, and the knee joint. Subsequently, the pixel trajectory values were converted to a quantitative measurement using the spatial resolution of the imager in the plane of the surrogate. Once the conversion into spatial dimensions was completed, the trajectories of the points of interest were filtered using the convention specified in ISO/DIS 13232-4 (ISO, 2004). This filter employs a four pass moving average designed to smooth the data.

The points of interest were tracked from the dummy tests using the photo targets that had been placed on the dummy at desired locations prior to testing. It was considerably more difficult to determine the location of these points in the cadaver test because the desired location was either not available for direct measurement (i.e., a photo target had not been placed at the location of interest) or the photo targets were placed on clothing that moved during the impact event. Therefore, several hybrid techniques were developed to account for either the lack of targets at a location or local movement of a target.

In the case of the head CG, the knee and the H-point, approximations of the point of interest had to be inferred. In order to account for out-of-plane rotations of the head that resulted in perceived movement of the head CG target on a planar projection, the location of the head CG points was determined by the head outline at the following locations: the highest point, the most leftward, the most rightward, and the lowest point. This method for approximating the location of the head CG by tracking the location of the centroid of the projected head area is shown in Figure 5.

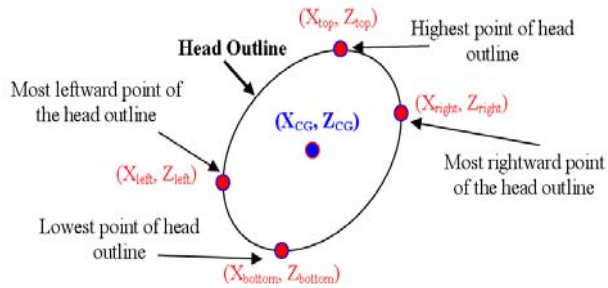

Figure 5. Approximation of the head CG of the pediatric cadaver by tracking the centroid of the head.

The head CG points (Equation 6) could then be approximated as

$$X_{CG} = \frac{X_{left} + X_{right}}{2}, Z_{CG} = \frac{Z_{top} + Z_{bottom}}{2} \quad (6).$$

In order to find an approximate location for the knee joint, points were taken where the leg meets the thigh anterior and posterior to the actual location of the knee center of rotation (i.e., the knee center). The location of these points and their practical placement can be seen in Figure 6.

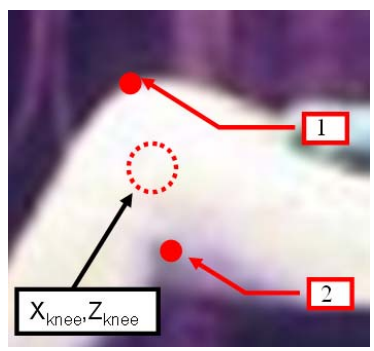

Figure 6. Determination of the location of the knee joint in the pediatric cadaver video analysis.

Once the location of these two points was determined, labeled 1 and 2 in Figure 6, the approximate location of the knee joint (Equation 7) was

$$X_{knee} = \frac{X_1 + X_2}{2}, Z_{knee} = \frac{Z_1 + Z_2}{2} \quad (7).$$

Once the location of the knee joint was determined, the approximate location of the H-point was calculated using the knee joint and femur length. This approach was taken because the location of the

hip marker was observed to move during the test as the cadaver's clothing moved. As shown in Figure 7, points are taken along the top of the thigh between the knee and hip.

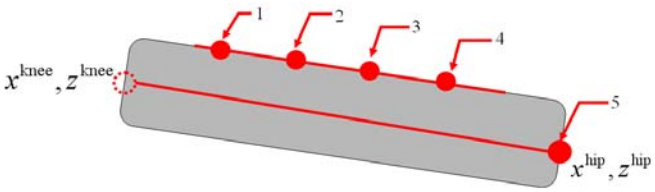

Figure 7. Method used for finding the approximate location of the H-point of the pediatric cadaver.

Using points 1, 2, 3, and 4 from Figure 7, which are four points along the top of the thigh, a least squares slope was found through those points. Since the femur could not be measured directly, it was assumed that the least squares slope was the same as the slope of the line connecting the knee and the hip. Validation of this technique was performed by overlaying the approximate hip points on the video of the test. It was observed that the approximate hip points predicted the location of the hip more accurately than the photo target, which moved considerably during interaction of the clothes with the seat and belt. The length of the femur was not listed in the cadaveric anthropometric data so its length was estimated (Snyde, 1977). By matching the known measurements of body weight, body length, and seated height with average measurements in the database, an age range based on the cadaver's anthropometry was determined based on those measurements rather than the subject age. With the assumed femur length and thigh angle, the approximate location of the H-point was determined based on the previously calculated knee joint location.

RESULTS

Scaling accelerations and forces

Before using scaling (Equations 2, 3, and 4) was used to qualify the performance of the dummies relative to the cadaver, the applicability of scaling techniques for this particular sled environment was evaluated. We determined the extent of the violations of the assumptions related to geometric similarity (i.e., the assumption that the dummies responses are scaled versions of each other) and homologous loading points (i.e., the assumption that if the belt loads a particular point in one sized dummy it loads the same point in another) by assessing the effectiveness of scaling the dummy responses to each other. Since the dummies were developed with the same dimensional analysis scaling procedures utilized in our analysis (Mertz, 2001), we reasoned that a dummy's response should be scalable to that of another dummy if the assumptions of geometric similarity and homologous loading are not drastically violated. In order to test this assumption, the responses of the HIII 10-year old were compared to the scaled responses of the Hybrid III 5th female. It was observed that the scaled acceleration and seat belt forces produced comparable results (see Appendix C).

After determining that the scaling method was capable of providing comparable results between the two dummies, the seat belt load and head CG acceleration were scaled (Figure 8 and Figure 9). Additional graphs of the scaled lap belt load and X and Z components of the head CG acceleration are included in Appendix B.

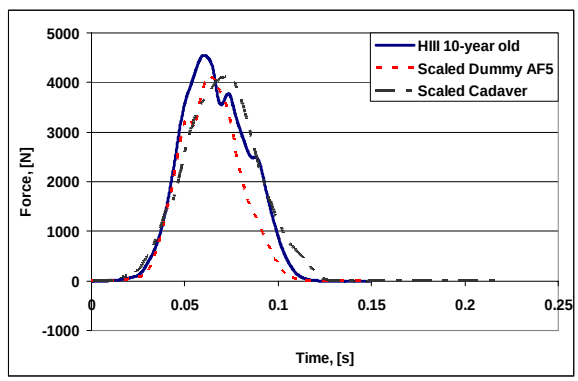

Figure 8. Scaled values of the AF5 and pediatric cadaver graphed with the values of the HIII 10-year old for the shoulder belt.

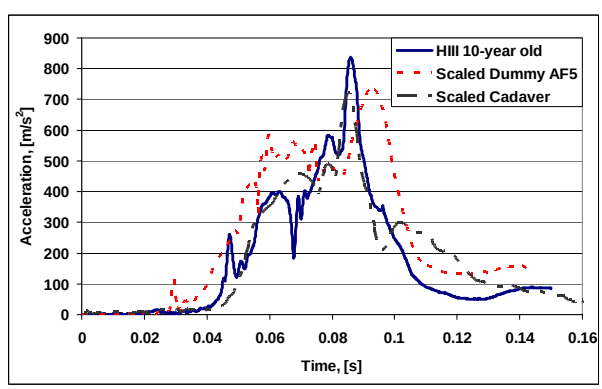

Figure 9. Scaled values of the AF5 and pediatric cadaver graphed with the values of the HIII 10-year old for resultant head CG acceleration.

Table 2.
HIII 10-year old, Scaled AF5, and Scaled pediatric cadaver values

		HIII 10-year old					Scaled AF5			Scaled Pediatric Cadaver
		Average	St. Dev.	COV	Upper bound	Lower bound	Average	Upper bound	Lower bound	Value
Belt Forces, [N]	Lap	3999	325	0.081	4782	3215	4119	4926	3312	2886
	Shoulder	4545	64	0.014	5436	3654	3976	4756	3197	4119
Head CG, [m/s^2]	X	-1085	267	-0.246	-1298	-872	-715	-855	-575	-352
	Z	551	81	0.147	659	443	542	649	436	663
	Resultant	1086	266	0.245	1299	873	739	884	594	720
Pre-strike Head CG, [m/s^2]	X	-189	3	-0.018	-226	-152	-235	-281	-189	-352
	Z	404	29	0.070	484	325	542	649	436	296
	Resultant	427	39	0.092	511	343	569	681	457	456
Chest CG, [m/s^2]	X	-459	12	-0.026	-549	-369	-553	-661	-445	
	Y	71	41	0.574	85	57	53	64	43	
	Z	-401	134	-0.333	-480	-323	-127	-152	-102	
	Resultant	501	72	0.144	599	403	573	685	461	

In Figure 8 and Figure 9 it is seen that the general trend of the data along with the peak value are similar between the scaled values of the AF5, scaled pediatric cadaver, and the HIII 10-year old.
The upper and lower bounds found in Table 2 were calculated using Equation 5 with the average values and 95% confidence intervals (z = 1.96). To find the upper and lower bounds for the scaled AF5, a coefficient of variation of 10% was assumed since the sample size was insufficient (n = 2) to determine a standard deviation.

Table 3.
Percent Difference between dummies and pediatric cadaver in head excursion

	Cadaver Scaled to:	
	HIII 10-year old	AF5
Cadaver, [cm]	16.5	24.6
Dummy, [cm]	15.8	22
% Difference	4.4%	11.8%

Kinematic scaling

In order to validate the technique of length scaling for kinematic factors, the trajectories of the HIII 10-year old and the Hybrid III 5th were compared. It was found that scaling between the dummies provided good agreement of the kinematic trajectories (see Appendix B for more detail). Scaling the pediatric cadaver trajectories to the HIII 10 and AF5 dummy sizes (Figure 10 and Figure 11) resulted in similar maximum head excursion values (Table 3.) and H-point trajectories.

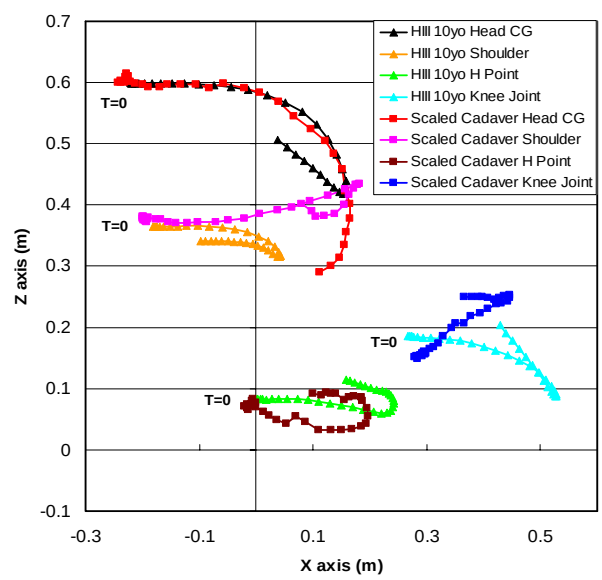

Figure 10. HIII 10-year old and scaled pediatric cadaver kinematic trajectories

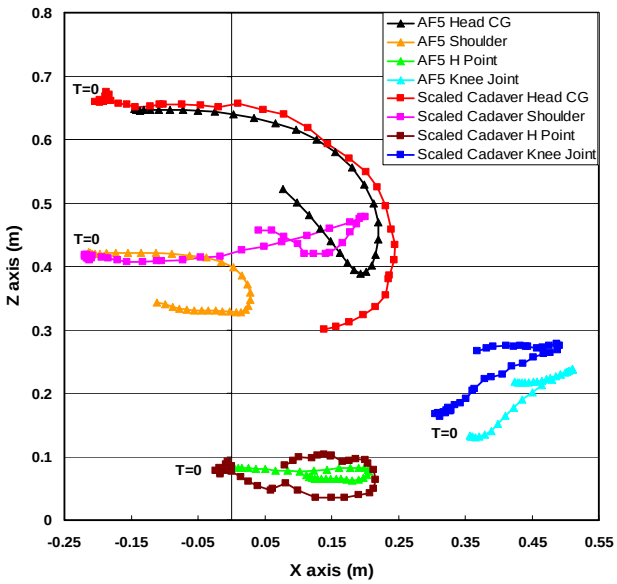

Figure 11. AF5 and scaled pediatric cadaver kinematic trajectories.

The head excursion values in Table 3 are the maximum distance that the head CG traveled past the origin in the +X direction. The percent difference calculation is based on this distance relative to the excursion of the pediatric cadaver. The differences in the knee joint trajectories for the cadavers (Figure 10) occurred because the HIII 10-year old foot not contact the floor of the buck. The differences in the shoulder trajectories in Figure 10 and Figure 11 were due to the rigid spine and shoulder assembly that are part of the HIII dummies. As the cadaver engaged the seat belt, the shoulder and upper body bent over the shoulder belt, causing a larger travel distance of the shoulder.

Differences in Kinematics

Though the head excursions of the dummies and the scaled cadaver produced similar results, the mechanism in which these excursions were achieved was quite different. In order to determine the way in which the dummies and the pediatric cadaver reached their points of maximum excursion, points were digitized along the approximate location of the spine and head using the video analysis software. These points along the spine to the base of the skull, to the most posterior point of the skull or and ending with the most superior point of the skull will be referred to as the spinal contour. The spinal contours were taken in 10 ms intervals back from the time of maximum excursion, labeled t = 0 ms, for 70 ms and included one contour after the time of maximum excursion for both the pediatric cadaver (Figure 12) and HIII dummy (Figure 13).

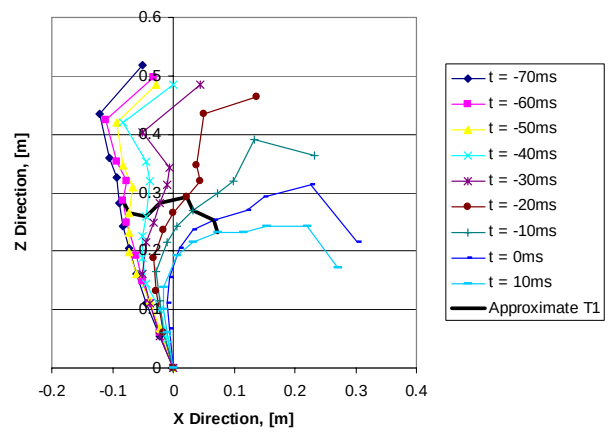

Figure 12. Spinal contours of the pediatric cadaver with approximate T1 location shown during motion

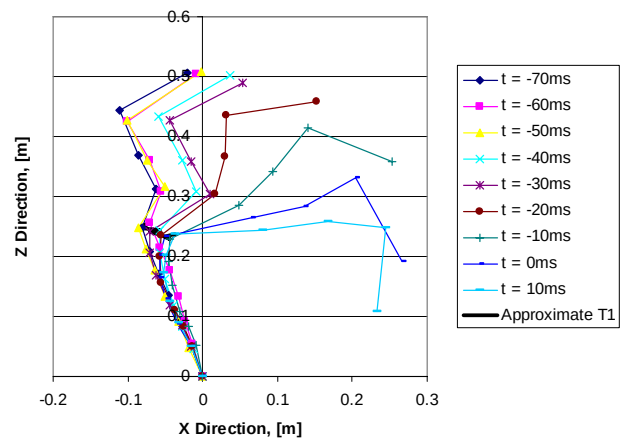

Figure 13: Spinal contours of HIII dummy with approximate T1 location shown during motion

The equivalent location of the T1 vertebra was tracked along with other points along the spine and head to form the spinal contour for the HIII dummy (Figure 12 and Figure 13). It was observed that the T1 location travels further in the test with the pediatric cadaver, which is to be expected given the rigid nature of the HIII spine. In order to compare the relative horizontal displacement of T1 between the surrogates the displacement relative to the initial position of the approximate location of T1 was found when the most distal point of the spine is held fixed. The T1 displacement of the cadaver is much larger

than that of the HIII dummy, as seen in Figure 12 and Figure 13, caused by noticeable bending of the thoracic region of the pediatric cadaver's spine. This result is consistent with observations made by Sherwood (2002), where it was found that the non-biofidelic thoracic spine of the HIII 6-year old produced unrealistically high flexion moments in the dummy's lower neck. Additionally shown by Sherwood (2002) in crash simulations was that additional thoracic spine flexibility decreases all forces and moments in the neck and improves the dummy's kinematics relative to the cadaver's.

LIMITATIONS

A limitation of this study is that there is only one pediatric cadaver was used in the analysis. The approximations used in determining the head CG location, knee joint and H point location all provide reasonable estimations, but are still approximate methods for determining the desired location. It is also possible that the seat that was used for the test was worn and that this affected the response of the dummy. Additionally, scaling procedures will introduce some error into the study due to violations of geometric similarity. The process of video analysis used in this study is a potential source of error.

CONCLUSION

This study found that scaling techniques provided reasonable results when scaling between the dummies. When comparing between the dummy and the pediatric cadaver, the scaling techniques reasonably predicted the shoulder belt force, head CG resultant acceleration and occupant head kinematics. Though the scaling techniques for the occupant kinematics produced comparable results between the cadaver and the HIII 10-year old and AF5, this does not necessarily indicate that the cadaver could be scaled to the any size child dummy. Violations in geometric similarity (i.e. different loading locations of the belt on the dummies of different size and seating position between subjects) would likely have a large influence on the scaling results. This study showed that the rigid spine of the dummy greatly influences the biofidelity of head CG and torso kinematics. As shown in the Sherwood (2002) and this study in the lack of non-biofidelic head movement, increasing the flexibility of the spine of the dummies would produce more accurate dummy head CG kinematics. With the information gained in this study, additional data into the kinematics and kinetics of children are obtained, that, in turn, may be used in the further development of child dummies. Areas where the dummy responses are shown to be non-biofidelic, the rigid thoracic spine for example, can be improved.

ACKNOWLEDGMENTS

We would like to thank NHTSA for their support of the dummy tests although the opinions expressed in this paper are solely those of the authors. In addition, we would like to thank Shashi Kuppa, Steve Ridella, and Erik Takhounts for their technical guidance. The authors would also like to thank TRW for providing the high elongation webbing for the dummy tests.

REFERENCES

Ash, J., Sherwood, C., Crandall, J., Parent, D., Arbogast, K. (2009). Reconstruction of a real world crash involving a child using Hybrid III 10-year old and 5th percentile adult female ATDs. 21st International Technical Conference on the Enhanced Safety of Vehicles (ESV). Stuttgart, Germany

Foster, J.K., Kortge, J.O., Wolanin, M.J. (1977) Hybrid III – A biomechanically-based crash test dummy. SAE Paper No. 770938, Society of Automotive Engineers.

Irwin, A. L. and Mertz, H. J., (1997) Biomechanical basis for the CRABI and Hybrid III child dummies. Paper SAE 973317. Proc. 41st Stapp Car Crash Conference, pp. 1-12. Society of Automotive Engineers, Warrendale, PA.

Irwin, A. L., Mertz, H. J., Elhagediab, A. M., Moss, S. (2002) Guidelines for assessing the biofidelity of side impact dummies of various sizes and ages. Paper SAE 2002-22-0016. Stapp Car Crash Journal, Vol. 46, Nov. 2002, pp. 297-319. Society of Automotive Engineers, Warendale, PA.

ISO TC 22/SC 22/WG 22. Motorcycles—test and analysis procedures for research evaluation of rider crash protective devices fitted to motorcycles—Part 4: Variables to be measured, instrumentation and measurement procedures. ISO/DIS 13232-4, August 31, 2004, Copyright ISO, 2004.

Kallieris, D., Barz, J., Schmidt, G., Heess, G., Mattern, R. (1976). Comparison between child cadaver and child dummy by using child restraint systems in simulated collisions. Paper SAE 760815. Proc. 20th Stapp Car Crash Conference, pp 511-542. Society of Automotive Engineers, Warrendale, PA.

Kent, R., Murakami, D., Kobayashi, S. (2005) Frontal thoracic response to dynamic loading: The role of superficial tissues, viscera, and the rib cage. 2005 International Conference on the Biomechanics of Impacts (IRCOBI) Prague, Czech Republic.

Ku, H.H., (1969) Statistical concepts in metrology. In Precision Measurements and Calibration: Statistical Concepts and Procedures, Special Publication 300, Vol. 1. pp. 296-330. Edited by Ku, H.H., United States Department of Commerce, National Bureau of Standards, Washington, D.C.

Mertz, H.J., Jarrett, K., Moss, S., Salloum, M., Zhao, Y. (2001) The Hybrid-III 10-year old dummy. Proc. Stapp Car Crash Journal, 45:319-328.

National Highway Traffic Safety Administration (NHTSA). (2000) U.S. DOT/NHTSA - Report - Hybrid III 5th Percentile Small Adult Female Crash Test Dummy - Drawings. Document NHTSA-2000-6940-16.

National Highway Traffic Safety Administration (NHTSA). (2005) US DOT/NHTSA - HIII-10C drawing package. Document NHTSA-2005-21247-4.

Reed, M. P., Schneider, L. W., Klinich, K. D., Manary, M. A., Ebert-Hamilton, S. M. Improved positioning procedures for 6YO and 10YO ATDs based on child occupant postures. Paper SAE 2006-22-0014. Stapp Car Crash Journal, Vol 50, Nov. 2006, pp. 337-388. Society of Automotive Engineers, Warrendale, PA.

SAE (2003) SAE J211/1 Instrumentation for Impact Test. Part 1. Electronic Instrumentation. Society of Automotive Engineers, Warrendale, PA, 2003.

Shaw, G., Roy, P., Schneider, L. W., Scavnicky, M., Lapidot, A. (1994) Interlaboratory study of proposed compliance test protocol for wheelchair tiedown and occupant restraint systems. Paper SAE 942229. Proc. 38th Stapp Car Crash Conference, Nov. 1994, pp. 355-370. Society of Automotive Engineers, Warendale, PA.

Sherwood, C. P., Kallieris, D., Eichelberger, M. R., Orzechowski, K. M., Cradall, J. R., Gupta, P. K., Kent, R. W., van Rooj, L., Shaw, C. G. (2002) Prediction of cervical spine injury risk for the 6-year-old child in frontal crashes. Proc. Association for the Advancement of Automotive Medicine, 46th annual conference. Association for the Advancement of Automotive Medicine, 2002, pp. 231-247.

Snyder, R. G., Schneider, L. W., Owings, C. L., Reynolds, H. M., Golomb, D. H., Sckork, M. A., (1977) Anthropometry of infants, children and youths to age 18 for product safety design. UM-HSIR-77-17, Consumer Product Safety Commission http://ovrt.nist.gov/projects/anthrokids/

APPENDIX A

Stiffness Scaling Development

This Appendix provides a discussion and shows the development of the chest stiffness scaling that is used in scaling the shoulder and lap belt forces. Since scaling the forces by the modulus scaling factor alone would seem to neglect the effect of the flesh and the viscera on the magnitude of the scaled belt forces, an alternative way was developed.
Dimensional analysis scaling techniques state that forces are scaled by modulus and length as shown in Equation A1

$$\lambda_F = \lambda_E \lambda_L^{\ 2} \qquad \text{(A1).}$$

Since it is also known that stiffness would scale by modulus and length (Equation A2) as,

$$\lambda_F = \lambda_K \lambda_L \qquad \text{(A2).}$$

It is shown that force can also be scaled (Equation A3) as

$$\lambda_F = (\lambda_E \lambda_L)\lambda_L = \lambda_K \lambda_L \qquad \text{(A3)}$$

The reason that the chest stiffness cannot be scaled simply by the modulus and length, as was shown above, is that there are differences in the child and adult thorax. These differences are not accounted by scaling only by the elastic modulus of the ribs and therefore another approach was taken. Using normalized stiffness information from Kent et al. (2005), the development of the chest stiffness scaling was possible. The intact thorax had a value of 1, the denuded thorax had a value of 0.87 and the eviscerated thorax had a value of 0.69.
The model of the thorax was assumed to be three springs in parallel. This assumption is made because it is observed that as additional elements are added to the eviscerated case, i.e. the flesh and viscera, the stiffness increases. Since the normalized total stiffness, k_T, is known to be 1 and the stiffness of the ribs, k_R, is known to be 0.69, the stiffness of the viscera, k_V, and flesh, k_F, are also known from the following relations:

$$k_F + k_V + k_R = k_T = 1$$

and,

$$k_V + k_R = 0.87$$

and,

$$k_R = 0.69$$

The relative contributions of the flesh, the viscera and the ribs are known to be:

$$k_F = 0.13$$
$$k_V = 0.18$$
$$k_R = 0.69$$

A stiffness ratio can be found between the child and the adult, represented as 1 and 2, respectively,

$$\frac{k_1}{k_2} = \frac{k_{T1}}{k_{T2}} = \frac{k_{F1} + k_{V1} + k_{R1}}{k_{F2} + k_{V2} + k_{R2}}$$

It was assumed that the stiffness of the flesh and the viscera is constant between the adult and the child and that the ribs themselves are geometrically similar their stiffness values can be scaled as done in Equation A2.
The stiffness ratio is then known to be

$$\lambda_K = \frac{k_1}{k_2} = \frac{k_{F1} + k_{V1} + \lambda_E \lambda_L k_{R2}}{k_{F2} + k_{V2} + k_{R2}}$$
$$= \frac{0.13 + 0.18 + 0.69\lambda_E \lambda_L}{0.13 + 0.18 + 0.69} = 0.31 + 0.69\lambda_E \lambda_L$$

Since the stiffness ratio is known the force scaling ratio is also known (Equation A4)

$$\lambda_F = \lambda_K \lambda_L = \left(0.31 + 0.69\lambda_E \lambda_L\right)\lambda_L \qquad \text{(A4).}$$

APPENDIX B

Comparison of HIII 5th Female to HIII 10-year old dummies

In the comparison of the belt forces and head CG accelerations between the HIII 10-year old and the scaled Hybrid III 5th female (Figure B1 - Figure B5 , the general trends as well as the approximate magnitudes of the data peaks are similar. Since data obtained from the HIII 10-year old and the scaled AF5 appeared to be an approximately equivalent, the scaling method will be used to scale between the dummies and the pediatric cadaver.

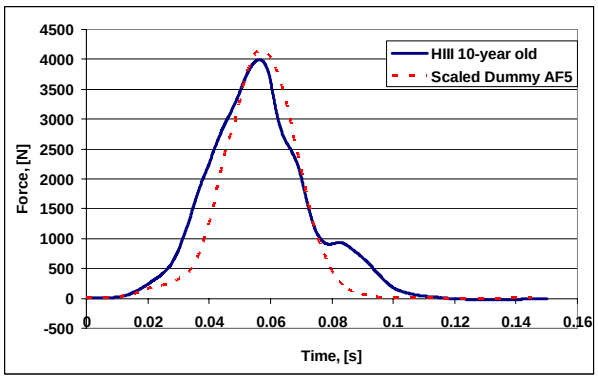

Figure B1. Lap belt load of the scaled AF5 Dummy and HIII 10-year old.

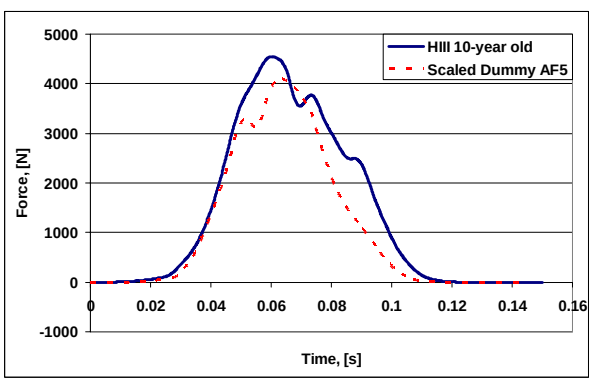

Figure B2. Shoulder belt load of the scaled AF5 Dummy and HIII 10-year old.

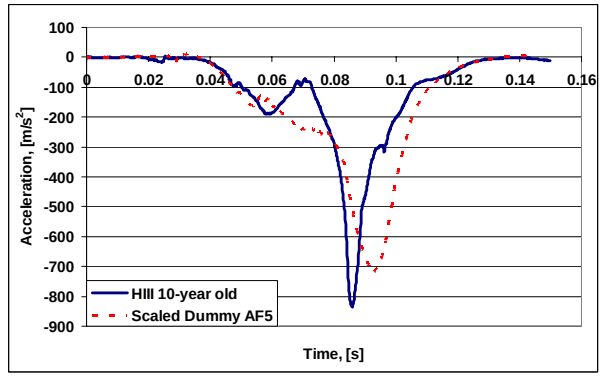

Figure B3. Head CG acceleration (X component) of the scaled AF5 Dummy and HIII 10-year old.

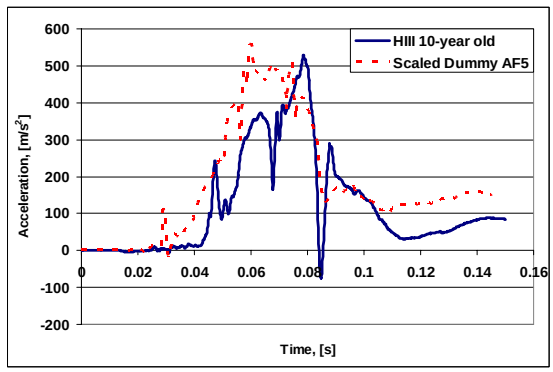

Figure B4. Head CG acceleration (Z component) of the scaled AF5 Dummy and HIII 10-year old.

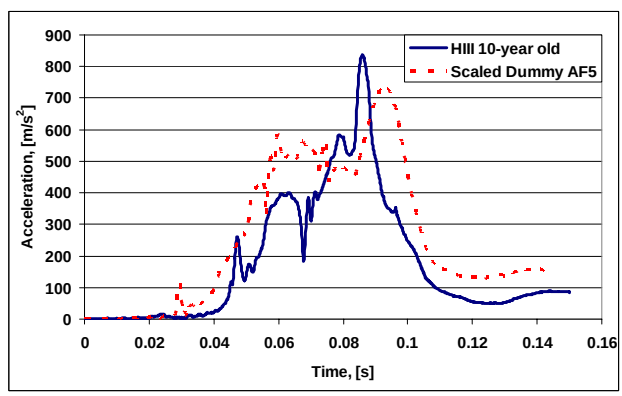

Figure B5. Head CG acceleration (resultant) of the scaled AF5 Dummy and HIII 10-year old.

Kinematic Scaling

The kinematic trajectories scaled between the HIII 10-year old and the AF5 shown in Figure B6 show that the trajectories can be scaled between the dummies and that the excursion of the head, which is

particularly important when analyzing child dummy kinematics, differed by less than 3 cm.

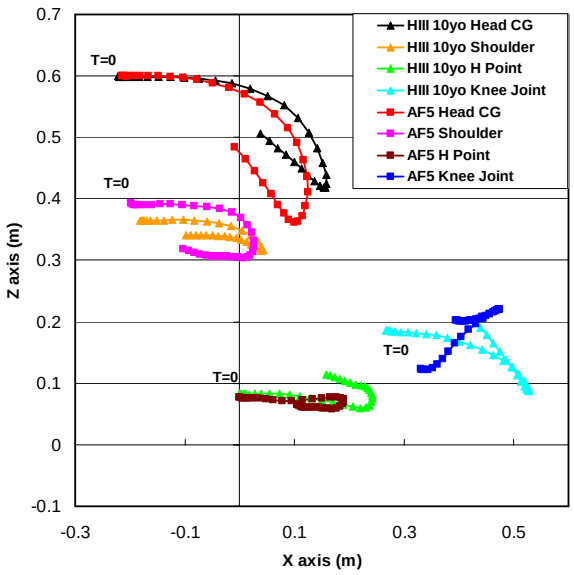

Figure B6. HIII 10-year old and AF5 kinematic trajectories

All other points showed similar kinematics between the dummies with the exception of the knee joint. The reasons for the differences in the knee joint trajectories between the dummies were due to violations in geometric similarity, more specifically the violation of homologous points. These violations were seen in the seating positions of the two dummies (Figure B7).

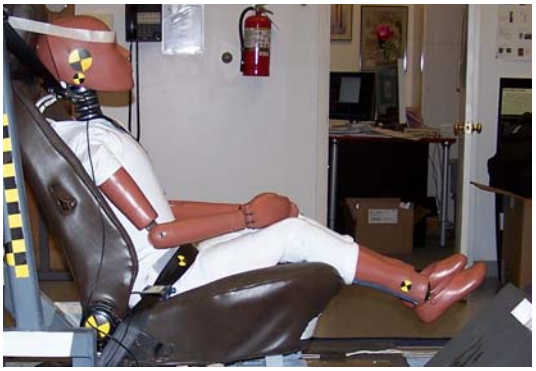

Figure B7. HIII 10-year old seated position.

Figure B8. AF5 dummy seated position.

Since the foot of the Hybrid III 5th resides on the footrest of the buck, the knee joint was forced upward as the entire dummy translated forward. This motion was not seen in the HIII 10-year old where the knee would sink into the seat padding as the dummy was restrained by the belt system. The neck assembly of the HIII 10-year old dummy, seen in Figure B7, was in a more posterior position than the AF5 dummy. To correct this, the initial position of the HIII 10-year old was adjusted to begin at a similar X position as the AF5.

APPENDIX C

Scaled pediatric cadaver and AF5 graphed with HIII-10 year old acceleration and belt load

The shoulder belt loads and head CG accelerations of the pediatric cadaver and AF5 were scaled to the HIII 10-year old (Figure C1 - Figure C3).

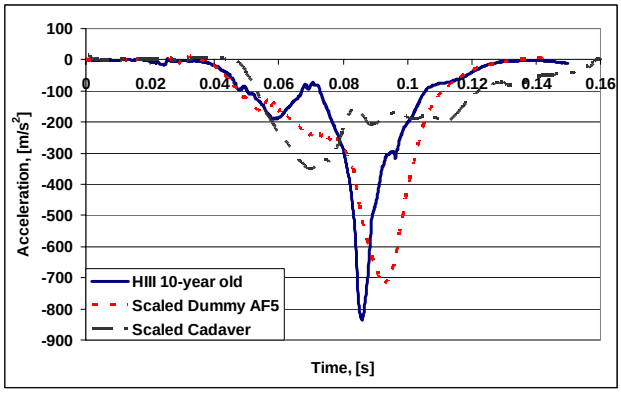

Figure C1: The scaled X component of the head CG acceleration.

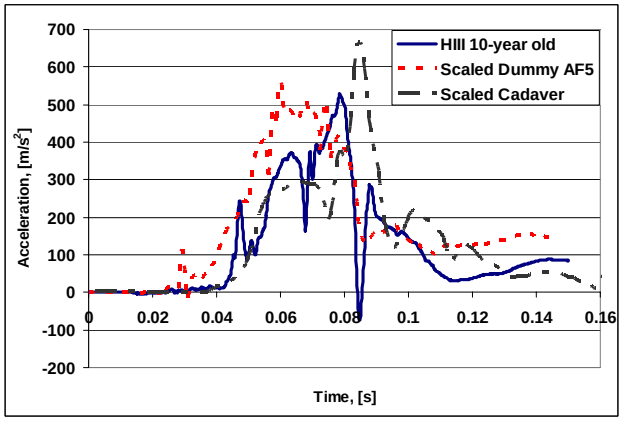

Figure C2: The scaled Z component of the head CG acceleration.

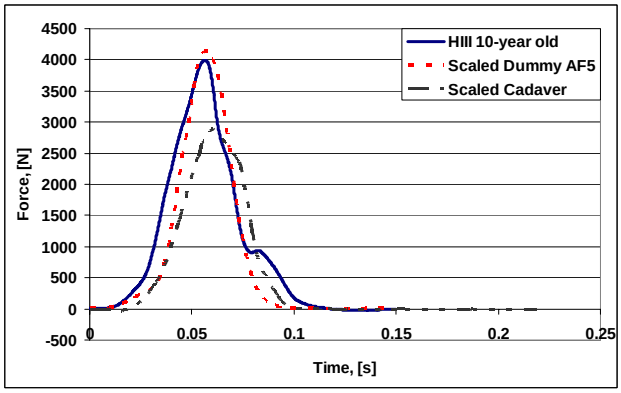

Figure C3: The scaled shoulder belt force.

THREE YEARS OLD CHILD HEAD-NECK FINITE ELEMENT MODELING. SIMULATION OF THE INTERACTION WITH AIRBAG IN FRONTAL AND SIDE IMPACT.

Meyer F., Roth S., Willinger R.

Mechanical Institute of Fluids and Solids, FRE3240 STRASBOURG UNIVERSITY-CNRS, 2 rue Boussingault 67000 Strasbourg FRANCE.

Paper Number : 09-0392

ABSTRACT

This study proposes to assess the interaction between the 3 years old child Head-Neck system and a typical airbag, a protective system frequently used in the automotive field. Two separated models (Head and Neck) developed at the Strasbourg University (UDS) were coupled in order to estimate the injury risk during this type of impact. The first model developed is a three years old child Finite Element neck Model (FEM) based on a realistic geometry (Meyer et al. 2008). This FEM was validated in four directions against an original method based on scaling method (Irwin et al. 1997). The second FEM is a 3 years old Head FE model published by Roth et al. in 2008. This model proposed an injury criterion in terms of Von Mises stress in the brain for moderate neurological injuries. After a coupling of these two FE models two impacts a frontal and lateral impact configuration is simulated. These impacts consisted of an airbag deployment at different gaps in order to calculate and estimate child brain injury risks.

INTRODUCTION

The growing demand for greater mobility in Europe has made individual transportation an essential and even inevitable feature of modern leaving. Children are more and more often conveyed in cars or other modes of road transportations. With this increased travels, the risk for children, of becoming involved in an accident as occupant has consequently increased. Based on the above accident data, it is obvious that in spite of the significant improvements in recent years in vehicle safety, the current number of deaths and casualties added to the social and economic costs is still unacceptable. Fatalities and injuries, especially to children, shall be reduced by all the available ways: public regulation, prevention/education of road users, road infrastructure, compatibility between vehicles, active, passive and tertiary safety devices.

As regards children, it is very difficult to obtain figures for fatalities or severely injured children in the 27 European Countries, but if we consider the EU 15 countries, where the use of child restraint is mandatory since a long time, approximately 600 children are killed in cars on the European roads and 80 000 are injured (data source: IRTAD).If there has been a hudge effort on human adult FE modeling only very few attempts exist as long as children are concerned.

Due to ethical reasons, there is paucity in experimental data concerning the child's head and neck characterization. As a consequence, there is a considerable difficulty for the validation of children FE models. For the neck validation one solution is to use the Scaling method's established by Irwin's and Mertz 1997. This method permits to calculate a theorical experimental corridor based on on the adult experimental data, in terms of displacement and acceleration. The mechanical properties such as the mass density of the cervical vertebrae, the rigidity both for the intervertebral discs and the ligament are calculated with this scaling method.

One way to investigate child Head injury criteria using numerical models is to simulate real world head trauma. Well documented accidents can help to understand child injuries in comparing numerical mechanical parameters with what really happened, distinguishing biofidelic behavior of a child numerical head and the ability to have an injury predicting tool. Indeed, even if the biofidelic behavior of child models cannot be checked, based on classical experimental versus numerical validation process, investigations of child injury mechanisms can be performed by developing an injury predicting tool, studying numerical

simulation of a large number of real accidents and to correlate mechanical parameters outputs with observed injuries. In the present work these previous published Head and Neck models are coupled to a simplified thorax in order to investigate child Head-Neck response under frontal and lateral airbag deployment as a function of initial distance between airbag and Head.

MATERIALS AND METHODS

Three years Old Child's Neck FE model

The neck model used in the present study has been previously published (Meyer et al. 2008) and will therefore be presented very shortly.

A three year old male child head and neck was scanned (figure 1) in order to base this study on a realistic human geometry, and to integrate the detailed vertebrae anatomy. The surfaces were reconstructed, so that the cervical vertebrae could be completely meshed.

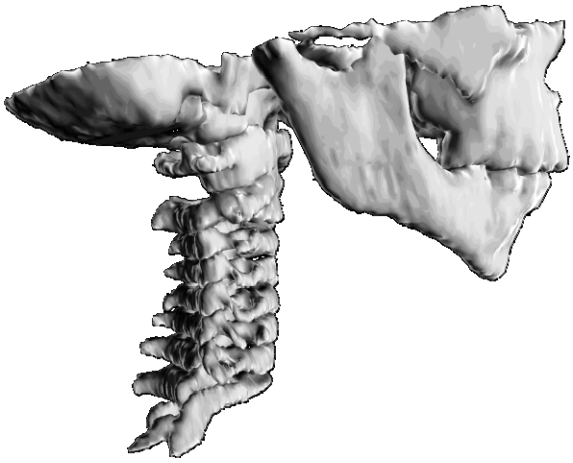

Figure 1. Reconstruction of the cervical spine based on scanner section.

For the cervical vertebrae, shell elements offer the possibility of strictly respecting the anatomical surface. The upper and the lower ligamentary system were reproduced with springs elements and the intervertebral discs with bricks elements (3 layers).

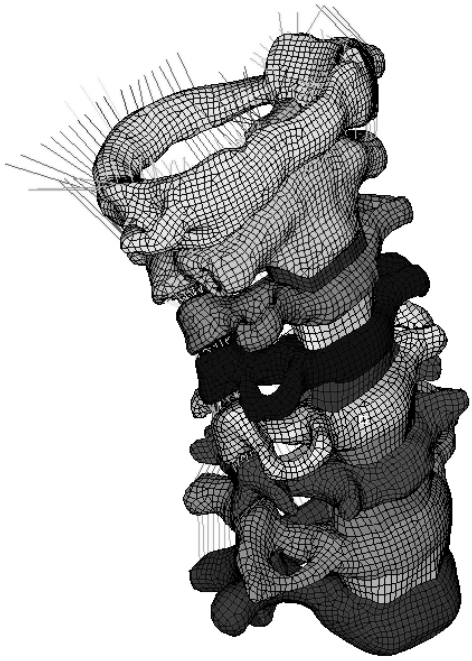

Figure 2. Surface meshing of the cervical column (C1-T1) with its ligamentary system. (See also Meyer et al. 2008 for further details).

Finally the model of the three year old child neck contains a total of 2 826 brick elements and 44 758 shell elements and 712 springs.

Finite element models of adult neck are typically validated against experimental data carried out by the N.B.D.L (Van der Horst M.J. 2002, Meyer et al. 2004), with frontal, oblique, lateral impacts (Ewing et al. 1968, Ewing et al. 1977). Unfortunately, for ethical reasons, it is not possible to perform similar tests on children so no data exist in the literature for dynamic validation of a paediatric neck model. In the present study, inputs for the three-year-old-child model correspond to those used in the NBDL tests (Frontal, Lateral, Oblique) but outputs, i.e., head accelerations and displacements ' corridors , are scaled down in accordance with Irwin's method (1997). An example of the frontal validation is illustrated in figure 3 where the superimposition of experimental response corridors obtained with the scaling method, and numerical curves obtained with the finite element model of the child neck is reported.

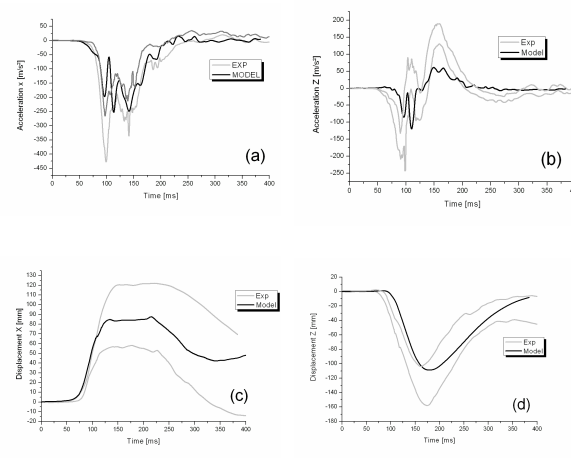

Figure 3. Results under frontal impact: X-axis (a), Z-axis (b) linear head acceleration, X-axis (c), Z-axis (d) head displacement and kinematic response of the whole head/neck system (e).

Child's head model and injury criteria.

The head model wich will be coupled to the neck was published by Roth et al. in 2008. Hereafter a short presentation is re-called.

As illustrate in figure 4, the developed three years old head model takes into account the main anatomical features of a three year old child. It includes the scalp, the skull, the sutures (sagittal, coronal, lambdoid), the face, the cerebro spinal fluid (CSF), the falx, the tentorium and the brain. Finally, the whole model of the three year old child head (a) contains a total of 23000 brick elements and 3500 shell elements.

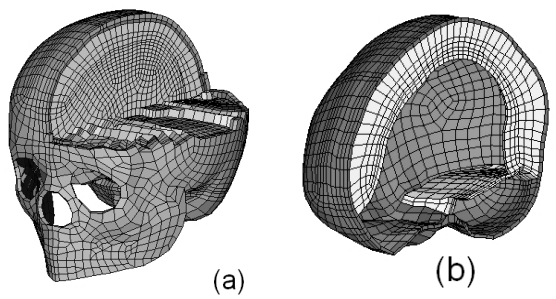

Figure 4. Meshing description of the detailed three year old child head finite element model (a) Cross section of the HEAD FEM (b) Membranes Falx & tentorium. (See also Roth et al. 2008)

In order to investigate child injury criteria with the finite element model, 25 real world accidents involving child aged from 2.5 to 3.5 year old were collected. These accidents are free fall from different heights and are simulated with the 3YOC head in order to extract the best mechanical parameter able to predict injury occurrence. From medical files, several data are available: gender, age, height of fall, type of impacted surface, type of injury. Injuries are classified into two categories: Moderate neurological injuries (2 in the AIS scale, unconsciousness limited to few hours after impact) and severe neurological injuries (>3 in the AIS scale, with a >24hours coma). Among these 25 cases, 15 accidents induced with no neurological injuries, 8 lead to moderate neurological injuries, and 2 to severe neurological injuries.

The determination of the head injury risk curves for specific injury mechanisms is based on a correlation study between the values of the proposed candidate criteria and the neurological lesions occurrences. Maximum values of mechanical parameters are used to build a histogram. The accident cases are finally sorted according to the injury classification, *i.e.* moderate or absence of neurological injuries. When the injury predictor candidate is adequate, a distinction is visible between the low values of the uninjured cases and the high values of the computed for the injured cases. This threshold can accurately be calculated since it is the value leading to a 50% risk an injury. For the statistical approach, the modified maximum likelihood method is chosen. It is a logistic regression method developed and described by Nakahira et al. (2000). The quality of the regression is thereby given by the negative estimator *EB* which should be as close to zero as possible. For each of these parameters: Von Mises stress, peak linear acceleration , maximum pressure, peak angular acceleration and HIC value, EB were calculated in order to identify the most relevant injury parameter (figure 5).

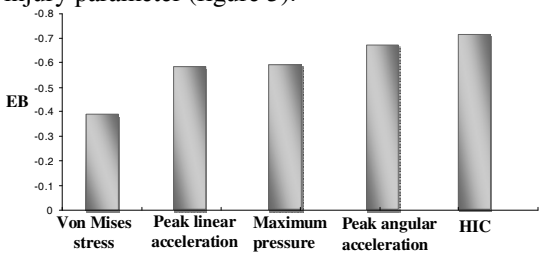

Figure 5. EB regression parameters for several candidates for moderate neurological injury criterion.

As a result of numerical reconstructions of real world cases, shear distribution in term of stress appear to be an interesting predicting candidate for neurological lesions. These parameters had also been used for prediction of neurological injuries in adult head finite element model by Deck et *al*. (2008). As a conclusion a Von Mises brain shearing stress of 48 Kpa will be retained for neurological injuries.

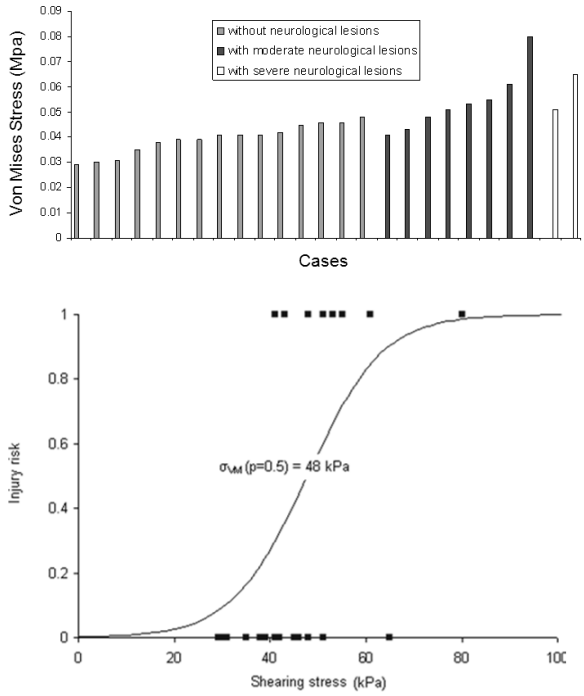

Figure 6. Histogram illustrating the correlation between the best mechanical parameter candidate (brain Von Mises stress) computed with 3 YOC FE model and corresponding injury risk curves.

Coupled three years child Head-Neck-Thorax model under impact.

In the framework of the present study the Neck FE model was coupled to the Head FE model. The connection between the Head and the Neck is made through the ligamentary system. The existing upper ligaments were connected to the Head FEM and the contact between the atlas and the occiput was reproduced with a sliding interface. The objective of the coupling between the Neck and the Thorax was to take into account the mass and inertia effect of the thorax in case of an airbag impact. The geometry was taken from an adult thorax and scaled down in accordance with Irwin's method. As the thorax has only an inertial effect in the context of this study a very simplified thorax model is proposed. The whole three years old coupled model is illustrated in figure 7.

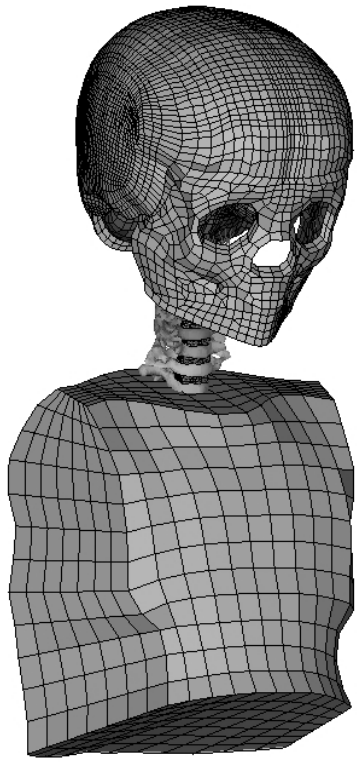

Figure 7. Coupling of the three years old Head-Neck FEM to a simplified thorax model.

In order to provide realistic inertia, the thorax was meshed with bricks elements and the density was adjusted in order to have a mass of 6.61 Kg (Irwin et al 1997) and an inertia of Ixx=3.15*10^7g.mm², Iyy=2.73*10^7g.mm², Izz=2.36*10^7g.mm². Finally T1 vertebra was associated to the thorax as a key element for the coupling of this segment to the head-neck complex.

In order to simulate child airbag interaction during airbag deployment two impacts conditions are suggested, a frontal and a lateral one. For each case the child is supposed to be seated statically without seat back, i.e. without any restrain of his thorax and with no initial velocity. For the frontal impact five distances between the chin and the airbag are proposed i.e. 6, 8, 10, 12 and 13.5 cm. For the lateral impact five distances between ear and airbag are suggested as well, being 6, 8, 10, 12 and 13.5 cm. For these ten impacts the injury parameters at head will be computed in order to express the injury risk for each case. Figure 10 presents more details relatively to the initial conditions of this impact simulation for the frontal configuration, as the

airbag center of mass is set at 4.2 cm below the child head center of mass.

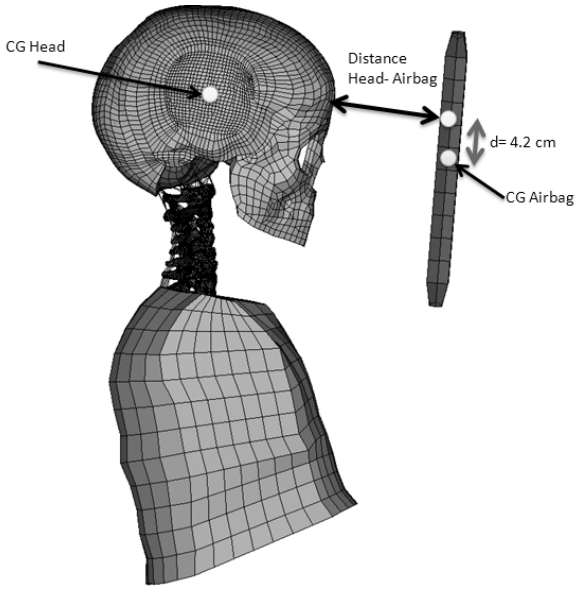

Figure 8. Child under airbag deployment under frontal configuration.

RESULTS

In this section results are reported separately for the frontal airbag deployments as the lateral ones.

Frontal Impact

Figure 9 represents the maximum of forces calculated per head/airbag distances. It can be observed that there is no significant correlation between head/airbag distance and calculated maximum interaction force.

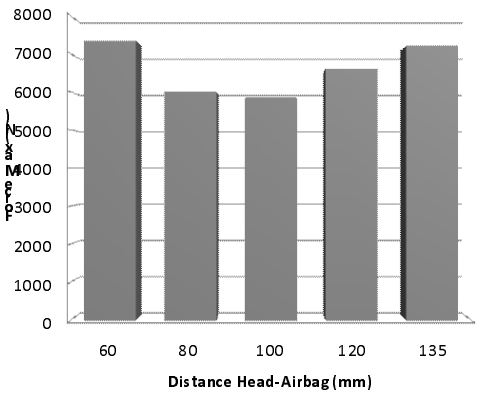

Figure 9. Maximal interaction force calculated for the five head-airbag distances (d=6 cm; d=8 cm; d=10 cm; d=12 cm; d=13,5 cm).

For the five airbag distances simulated the intra-cerebral Von Mises stress calculated (location and time evolution curves) are reported in figure 10. The locations of these maxima are similar in the five cases (at the vertex area). Five bricks were considered to obtain a mean value of the time evolution of Von Mises stress at these maxima location.

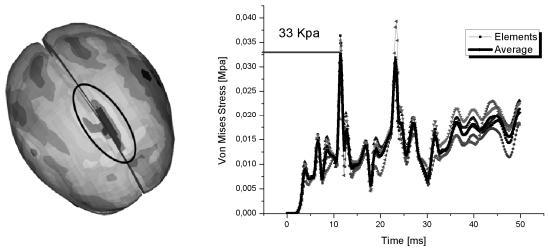

Figure 10. Illustration of the intracerebral Von Mises stress computed for the distance 100 mm (location of these maxima on left and time evolution on right) in frontal impact configuration.

Maxima of Von Mises stress are obtained after the total airbag deployment (after 10ms) and all results are summarized in figure 11.

For the head-airbag distance of about 60mm, an intracerebral Von Mises stress of 59kPa wich is higher than the tolerance limits calculated for a 50% risk of moderate neurological injuries (48kPa) is obtained. It is interesting to observe that the intra-cerebram Von Mises stresses are much more correlated with the head-airbag distance then the interaction force is.

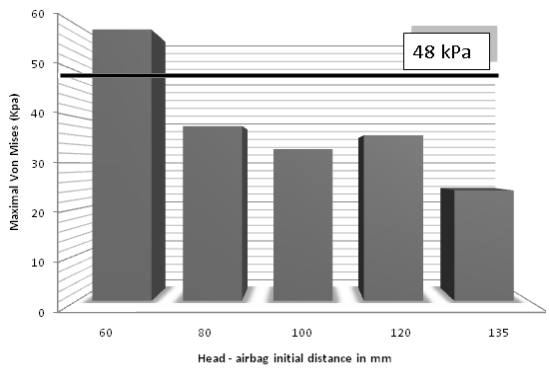

Figure 11. Maxima of intracerebral Von Mises stress computed within for the five head/airbag distances under frontal impact configuration.

Lateral impact

The conditions of the lateral airbag impact are similar to the frontal impact i.e. a free thorax boundary conditions boundary conditions. An overall view of the kinematics under this lateral airbag deployment (d=100 mm) is illustrated in figure 12.

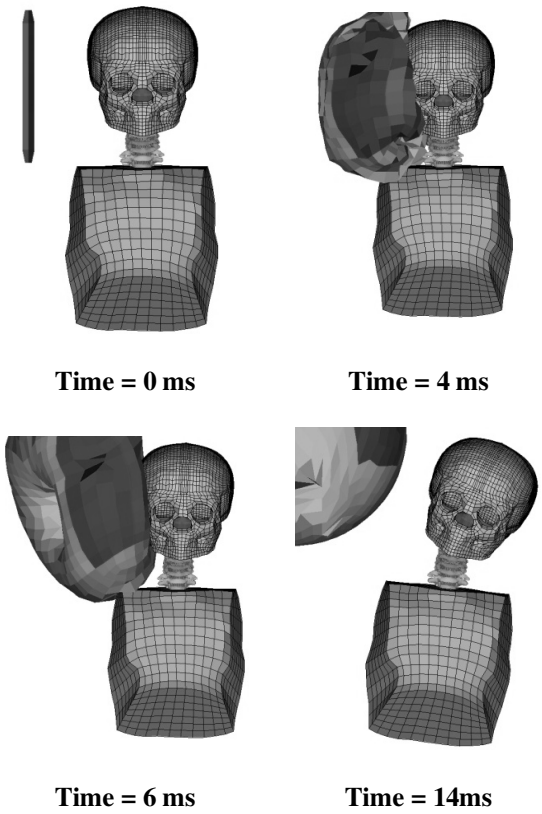

Figure 12. Overall kinematics of the Head FEM under lateral airbag impact.

As for frontal impact configuration no significant correlation between head/airbag distance and maximum interaction force calculated is observed as illustrated in figure 13.

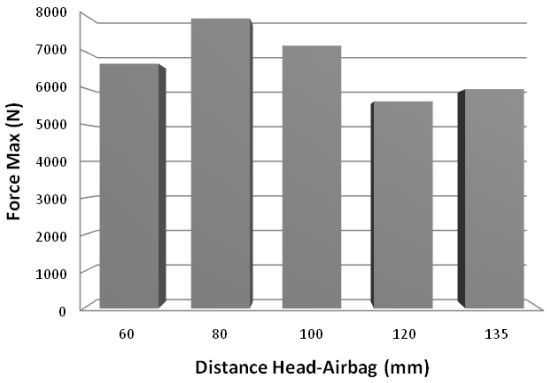

Figure 13. Maximal interaction force calculated for the five head-airbag distances (d=60mm; d=80mm; d=100mm; d=120mm; d=135 mm).

Figure 14 shows the maximum intracerebral Von Mises stress computed (location and time evolution curves) for the five airbag distances in lateral impact configuration. Location of these maxima is similar in the five cases (at the opposite side to the impacted area). Except for the 135 mm distance all simulated cases conduced to the same conclusion i.e. that it exits a risk of moderate neurological injury due to the fact that the intracerebral Von Mises stress calculated exceed tolerance limit fixed to 48kPa.

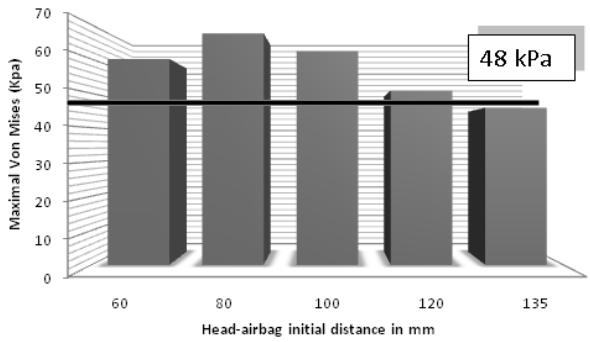

Figure 14 Maxima of intracerebral Von Mises stress computed within the brain for the five head/airbag under lateral impact configuration.

DISCUSSIONS

After the development of a three years old child Head-neck FE model and its use under airbag deployment it's important to define the limitations of this study. A number of limitation exist at biomechanical modeling level were clearly improvement are needed in the future especially as long as neck injury criteria are concerned. The boundary conditions applied aren't the same as in accident condition as the simulations don't take into account the initial velocity of the whole body, the effect of the seatbelt and the initial position influence kinematic's and the injury risk. The main originality of the proposed head-neck-thorax model is to consider a realistic and detailed geometry of the cervical spine and a FE head model who proposed tolerance limits for moderate neurological lesion. It's therefore a step towards numerical tools for the assessment of the child head and neck injury risk under airbag deployment.

CONCLUSIONS

The objective of this study was to assess the injury risk of the child head-neck system under airbag deployment for frontal and lateral configuration.

The presented work is based on a head and neck model of the three year old child developed in earlier studies as well as first head injury criteria. Proposed then is the coupling of the head-neck system to a simplified thorax model in order to assess head injury risk under frontal and lateral airbag deployment. A parametric study on head-airbag distance is finally conduced with following main conclusions.

For the frontal airbag deployment it's shown that there is a low correlation between initial distance and the interaction force. A head injury risk appears only if the initial distance between the airbag and the head is less than 80 mm.

Concerning the lateral airbag deployment configuration a similar conclusion can be made as for the frontal impact i.e. no correlation between the interaction force and the injury risk. However the brain injury risk appears to be much higher as for the frontal impact. For all distances a brain injury risk over 50% has been computed.

Even if a number of limitations exist in this child response simulation under impact first steps have been provided towards numerical tools designed for the assessment of child head-neck injury risk under deployment.

AKNOLEDGMENT

The authors wish to thank TRW for their support.

REFERENCES

Deck C., Willinger R. Improved Head Injury Criteria Based on Head FE Model. Int. J. of Crashworthiness, Vol 13,n°6, pp 667-679 (2008).

Ewing, C., Thomas, D., Patrick, L., Beeler, G. and Smith, M. Dynamic response of the head and neck of the living human to -Gx impact acceleration. Proc. 12th Stapp Car Crash Conference Society of Automotive Engineers, Warrendale, PA Paper 680792, pp. 424-439 (1968)

Ewing, C., Thomas, D., Lustick, L., Muzzy, III W., Willems, G. and Majewski, P. Dynamic response of the human head and neck to +Gy impact acceleration. Proc. 21st Stapp Car Crash Conference,. Society of Automotive Engineers, Warrendale, PA. Paper 770928 pp. 549-586 (1977).

IRTAD (International Traffic Safety Data and Analyse Group) www.irtad.net

Irwin, A. and Mertz, H. J. Biomechanical basis for the CRABI and hybrid III Child dummies, SAE paper 973317 (1997).

Meyer F., Bourdet N., Deck C., Willinger R. Human Neck Finite Element Model Development and Validation against Original Experimental Data. Stapp Car Crash Journal, Vol., pp. 177-206 (2004)

Meyer F., Roth S., Willinger R. Child neck FE model development and validation. Int. J. Human factors Modelling and Simulation. Vol 1, N°2 pp 244-257 (2008)

Roth S., Vappou J., Raul J.S., Willinger R. Child head injury criteria investigation through numerical simulation of real world trauma Computer Methods and Programs in Biomedicine, Volume 93, Issue 1, Pages 32-45 (2008)

Nakahira Y., Furukawa K., Niimi H., Ishihara T., Miki K., Matsuoka F., A combined evaluation method and modified maximum likelihood method for injury risk curves, Proc. of the IRCOBI Conf., (2000), pp. 147-156

Van Der Horst, M. J. (2002): 'Human head neck response in frontal, lateral and rear end impact loading--modeling and validation'. PhD thesis, Technical University of Eindhoven, Eindhoven, The Netherlands

ANALYSIS OF 3D RIGID BODY MOTION USING THE NINE ACCELEROMETER ARRAY AND THE RANDOMLY DISTRIBUTED IN-PLANE ACCELEROMETER SYSTEMS

Erik G. Takhounts
NHTSA
Vikas Hasija
GESAC, Inc
Rolf H. Eppinger
NHTSA (retired)
United States
Paper Number: 09-0402

ABSTRACT

The nine accelerometer array sensor package is used extensively in injury biomechanics research to obtain the rotational acceleration time histories of a rigid body. It has been shown in the past to remain computationally stable while the alternative, the six accelerometer array, becomes unstable in the presence of small inaccuracies in the individually measured accelerations. The nine accelerometer array process achieves its stability by requiring the measurement of three rotational accelerations, thus eliminating the six accelerometer array's dependency on having knowledge of the rigid body's three rotational velocities at each instant in time. The nine accelerometer array's additional three measurements also provide other important benefits: 1. Identifying whether or not any one of the nine translational acceleration measurements is inconsistent with rigid body motion, 2. If an incorrect acceleration is found, determining what the actual time history should be for that case, 3. Use of optimization methodology to obtain the best possible solution for the rigid body motion. This paper presents the derivation of an additional set of constraint equations that a given set of nine linear accelerations must satisfy to be consistent with rigid body motion, demonstrates how an inconsistent acceleration input is discovered, and describes the process by which the true time history of the acceleration is recovered. In addition, optimization methodology is introduced to obtain the best possible solution for a randomly distributed in-plane accelerometer system when errors in measurements are artificially introduced.

INTRODUCTION

The Nine Accelerometer Array Package (NAAP) uses translational accelerations to describe the angular motion of a rigid body. It has been used extensively in injury biomechanics research to obtain human and dummy head 3D kinematics (Hardy et al., 2001, 2007, Takhounts et al., 2003, 2008). This sensor package typically uses nine accelerometers placed in a 3-2-2-2 configuration (Figure 1) to track the motion of a rigid body (Padgaonkar et al., 1975). The advantage of this configuration was shown to be in the stability of the NAAP when compared to the six accelerometer array (Figure 2) which required the knowledge of rotational velocities at each instant of time. This stability advantage of the NAAP is achieved at the expense of measuring three additional translational accelerations (in Figure 1 the three additional accelerations are $\boldsymbol{a}_{2x}$, $\boldsymbol{a}_{3x}$, and $\boldsymbol{a}_{3y}$).

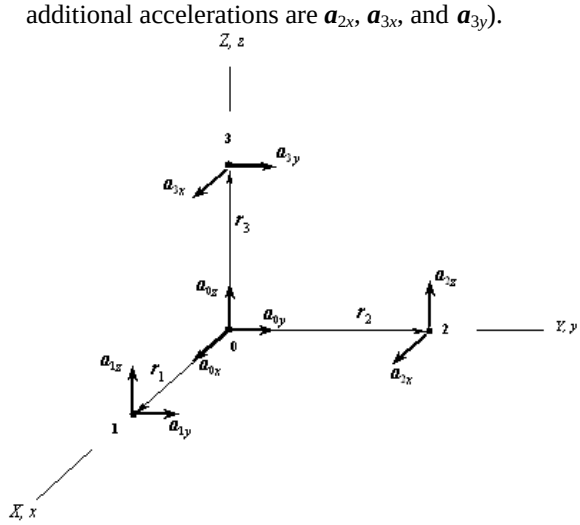

Figure 1. Nine accelerometer array configuration.

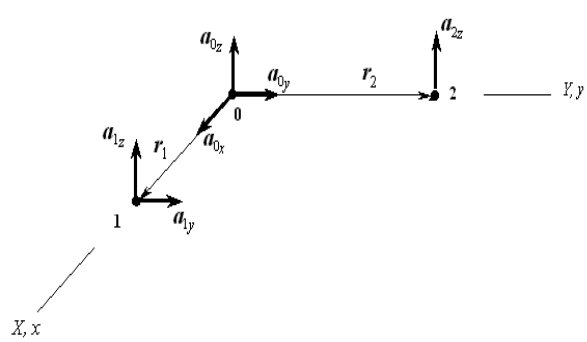

Figure 2. Six accelerometer array configuration.

It will be shown in this paper that these tree additional measurements are not independent and are subject to the rigid body constraints. To do so, first consider a general 3D motion of a rigid body (Figure 3) about a fixed point that is the same as the motion of point *B* measured by the observer located at point *A*.

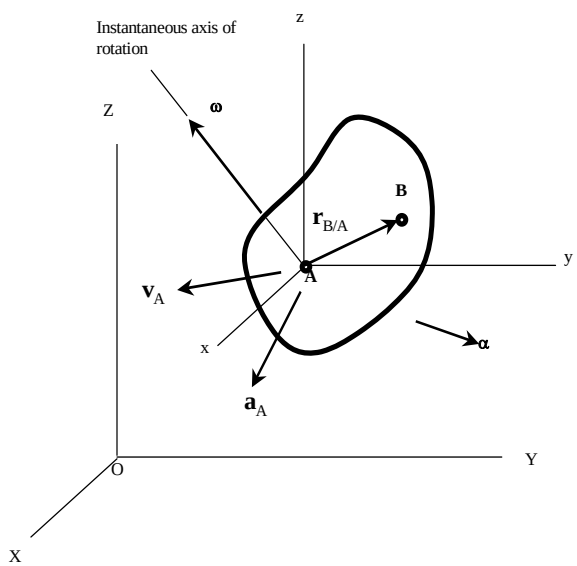

Figure 3. Rigid body subjected to a 3D general motion.

This relative motion occurs about the instantaneous center of rotation and is defined by:

$$\boldsymbol{v}_{B/A} = \boldsymbol{\omega} \times \boldsymbol{r}_{B/A} \tag{1}$$

and

$$\boldsymbol{a}_{B/A} = \boldsymbol{\alpha} \times \boldsymbol{r}_{B/A} + \boldsymbol{\omega} \times (\boldsymbol{\omega} \times \boldsymbol{r}_{B/A}), \tag{2}$$

where $\boldsymbol{v}_{B/A}$ and $\boldsymbol{a}_{B/A}$ are the relative velocity and acceleration of point *B* with respect to point *A*, $\boldsymbol{\omega}$ and $\boldsymbol{\alpha}$ are rotational velocity and acceleration. For translating axes, the relative motions are related to absolute motions by $\boldsymbol{v}_B = \boldsymbol{v}_A + \boldsymbol{v}_{B/A}$ and $\boldsymbol{a}_B = \boldsymbol{a}_A + \boldsymbol{a}_{B/A}$, and the absolute velocity and acceleration of point *B* are determined from the following equations:

$$\boldsymbol{v}_B = \boldsymbol{v}_A + \boldsymbol{\omega} \times \boldsymbol{r}_{B/A} \tag{3}$$

$$\boldsymbol{a}_B = \boldsymbol{a}_A + \boldsymbol{\alpha} \times \boldsymbol{r}_{B/A} + \boldsymbol{\omega} \times (\boldsymbol{\omega} \times \boldsymbol{r}_{B/A}). \tag{4}$$

If the vectors are defined as: $\boldsymbol{a}_A = [a_{Ax}, a_{Ay}, a_{Az}]^T$, $\boldsymbol{a}_B = [a_{Bx}, a_{By}, a_{Bz}]^T$, $\boldsymbol{\alpha} = [\alpha_x, \alpha_y, \alpha_z]^T$, $\boldsymbol{\omega} = [\omega_x, \omega_y, \omega_z]^T$, and $\boldsymbol{r}_{B/A} = [r_x, r_y, r_z]^T$, then equation 4 can be rewritten in the component form:

$$\begin{bmatrix} a_{Bx} \\ a_{By} \\ a_{Bz} \end{bmatrix} = \begin{bmatrix} a_{Ax} \\ a_{Ay} \\ a_{Az} \end{bmatrix} + \begin{bmatrix} \alpha_y r_z - \alpha_z r_y \\ \alpha_z r_x - \alpha_x r_z \\ \alpha_x r_y - \alpha_y r_x \end{bmatrix} + \begin{bmatrix} \omega_x(\omega_y r_y + \omega_z r_z) - r_x(\omega_y^2 + \omega_z^2) \\ \omega_y(\omega_z r_z + \omega_x r_x) - r_y(\omega_z^2 + \omega_x^2) \\ \omega_z(\omega_x r_x + \omega_y r_y) - r_z(\omega_x^2 + \omega_y^2) \end{bmatrix} \tag{5}$$

Equations 5 will be used extensively throughout the paper in deriving both – the closed form constraints equations for the NAAP and the optimization based solution for a randomly distributed in-plane accelerometer system.

METHODOLOGY

NAAP Constraints Equations

Consider the 3-2-2-2 NAAP configuration illustrated in Figure 1 arranged within a rigid body. The accelerations of points 1, 2, and 3 with respect to point 0 can be expressed using equations 5. For points 1 and 0 substitute 1 for *B*, 0 for *A*, $\boldsymbol{r}_{B/A} = \boldsymbol{r}_1 = [r_x, 0, 0]^T$, where r_x is the distance between points 1 and 0:

$$\begin{bmatrix} - \\ a_{1y} \\ a_{1z} \end{bmatrix} = \begin{bmatrix} - \\ a_{0y} \\ a_{0z} \end{bmatrix} + \begin{bmatrix} - \\ \alpha_z r_x \\ -\alpha_y r_x \end{bmatrix} + \begin{bmatrix} - \\ \omega_y \omega_x r_x \\ \omega_z \omega_x r_x \end{bmatrix}. \tag{6}$$

Similarly, for points 2 and 0, substitute 2 for *B*, 0 for *A*, $\boldsymbol{r}_{B/A} = \boldsymbol{r}_2 = [0, r_y, 0]^T$, where r_y is the distance between points 2 and 0:

$$\begin{bmatrix} a_{2x} \\ - \\ a_{2z} \end{bmatrix} = \begin{bmatrix} a_{0x} \\ - \\ a_{0z} \end{bmatrix} + \begin{bmatrix} -\alpha_z r_y \\ - \\ \alpha_x r_y \end{bmatrix} + \begin{bmatrix} \omega_x \omega_y r_y \\ - \\ \omega_z \omega_y r_y \end{bmatrix}. \tag{7}$$

For points 3 and 0, substitute 3 for *B*, 0 for *A*, $\boldsymbol{r}_{B/A} = \boldsymbol{r}_3 = [0, 0, r_z]^T$, where r_z is the distance between points 3 and 0:

$$\begin{bmatrix} a_{3x} \\ a_{3y} \\ - \end{bmatrix} = \begin{bmatrix} a_{0x} \\ a_{0y} \\ - \end{bmatrix} + \begin{bmatrix} \alpha_y r_z \\ -\alpha_x r_z \\ - \end{bmatrix} + \begin{bmatrix} \omega_x \omega_z r_z \\ \omega_y \omega_z r_z \\ - \end{bmatrix}. \tag{8}$$

From equations 7 and 8, α_x is found to be:

$$\begin{cases} \alpha_x = \dfrac{a_{2z} - a_{0z}}{r_y} - \omega_y \omega_z \\ \alpha_x = -\dfrac{a_{3y} - a_{0y}}{r_z} + \omega_y \omega_z \end{cases} \tag{9}$$

Similarly, α_y is found from equations 6 and 8:

$$\begin{cases} \alpha_y = -\dfrac{a_{1z} - a_{0z}}{r_x} + \omega_z \omega_x \\ \alpha_y = \dfrac{a_{3x} - a_{0x}}{r_z} - \omega_z \omega_x \end{cases} \tag{10}$$

and α_z is found from equations 6 and 7:

$$\begin{cases} \alpha_z = \dfrac{a_{1y} - a_{0y}}{r_x} - \omega_x \omega_y \\ \alpha_z = -\dfrac{a_{2x} - a_{0x}}{r_y} + \omega_x \omega_y \end{cases} \tag{11}$$

By adding the paired equations 9, 10, and 11, the three angular accelerations α_x, α_y, and α_z can be expressed as functions of the nine translational accelerations and the arm lengths, i.e.:

$$\begin{cases} \alpha_x = \dfrac{a_{2z} - a_{0z}}{2r_y} - \dfrac{a_{3y} - a_{0y}}{2r_z} \\ \alpha_y = \dfrac{a_{3x} - a_{0x}}{2r_z} - \dfrac{a_{1z} - a_{0z}}{2r_x} \\ \alpha_z = \dfrac{a_{1y} - a_{0y}}{2r_x} - \dfrac{a_{2x} - a_{0x}}{2r_y} \end{cases} \tag{12}$$

Equations 12 are given in Padgaonkar et al. (1975), and currently serve as the basis for derivation of angular motion of a rigid body from a set of nine translational accelerations. Translational accelerations, as shown in equations 12, are usually functions of time. Therefore, angular velocities of the rigid body could be obtained by simply integrating equations 12 with respect to time:

$$\begin{cases} \omega_x(t) = \int_t \alpha_x(t)dt \\ \omega_y(t) = \int_t \alpha_y(t)dt \\ \omega_z(t) = \int_t \alpha_z(t)dt \end{cases} \tag{13}$$

However, by subtracting the paired equations 9, 10, and 11 from each other, another set of equations can be found:

$$\begin{cases} \omega_y\omega_z = \dfrac{a_{2z} - a_{0z}}{2r_y} + \dfrac{a_{3y} - a_{0y}}{2r_z} \\ \omega_z\omega_x = \dfrac{a_{3x} - a_{0x}}{2r_z} + \dfrac{a_{1z} - a_{0z}}{2r_x} \\ \omega_x\omega_y = \dfrac{a_{1y} - a_{0y}}{2r_x} + \dfrac{a_{2x} - a_{0x}}{2r_y} \end{cases} \tag{14}$$

To fully describe a general 3D motion of a rigid body in space and time all nine equations 12 – 14 must be satisfied. This implies that nine measured acceleration in a NAAP configuration are not independent functions of time, but rather are bound by the additional set of equations (14). Let's call these equations – rigid body constraint equations.

To illustrate this point, consider a simple example of pure rotation of a rigid body where:

$$a_{0x}(t) = a_{0y}(t) = a_{0z}(t) = 0, \tag{15}$$

and the remaining six accelerations are identical functions of time:

$$a_{1y}(t) = a_{1z}(t) = a_{2x}(t) = a_{2z}(t) = a_{3x}(t) = a_{3y}(t) = t. \tag{16}$$

Then, equations (12) become:

$$\begin{cases} \alpha_x(t) = \dfrac{t}{2r_y} - \dfrac{t}{2r_z} \\ \alpha_y(t) = \dfrac{t}{2r_z} - \dfrac{t}{2r_x} \\ \alpha_z(t) = \dfrac{t}{2r_x} - \dfrac{t}{2r_y} \end{cases} \tag{17}$$

Integrating these equations (17) with respect to time gives the following angular velocities:

$$\begin{cases} \omega_x(t) = \dfrac{t^2}{4r_y} - \dfrac{t^2}{4r_z} \\ \omega_y(t) = \dfrac{t^2}{4r_z} - \dfrac{t^2}{4r_x} \\ \omega_z(t) = \dfrac{t^2}{4r_x} - \dfrac{t^2}{4r_y} \end{cases} \tag{18}$$

Using equations 18, the products of the angular velocities are found to be:

$$\begin{cases} \omega_y(t)\omega_z(t) = -\dfrac{t^4(r_x - r_y)(r_x - r_z)}{16r_x^2 r_y r_z} \\ \omega_z(t)\omega_x(t) = \dfrac{t^4(r_x - r_y)(r_y - r_z)}{16r_x r_y^2 r_z} \\ \omega_x(t)\omega_y(t) = -\dfrac{t^4(r_x - r_z)(r_y - r_z)}{16r_x r_y r_z^2} \end{cases} \tag{19}$$

However, substituting equations 15 and 16 into 14 directly yields another relationship for the products of the angular velocities:

$$\begin{cases} \omega_y(t)\omega_z(t) = \dfrac{t}{2r_y} + \dfrac{t}{2r_z} \\ \omega_z(t)\omega_x(t) = \dfrac{t}{2r_z} + \dfrac{t}{2r_x} \\ \omega_x(t)\omega_y(t) = \dfrac{t}{2r_x} + \dfrac{t}{2r_y} \end{cases} \tag{20}$$

Comparing equations 19 and 20 and noticing their inequality it can be conclude that the conditions 12, 13, and 14 cannot be satisfied simultaneously if nine translational accelerations are chosen in the arbitrary form of 15 and 16. In other words, in order to satisfy equations 12, 13, and 14, the nine translational accelerations cannot be arbitrary functions of time.

Closed Form Solutions for an Erroneous Channel in NAAP

Suppose it is known that one of the accelerations in Figure 1, e.g. $a_{1y}(t)$, $a_{1z}(t)$, $a_{2x}(t)$, $a_{2z}(t)$, $a_{3x}(t)$, or $a_{3y}(t)$ is not measured properly or missing. Assume first for the sake of simplicity that the accelerations at point 0 $a_{0x}(t)$, $a_{0y}(t)$, and $a_{0z}(t)$ are measured properly. To identify and correct the improperly measured trace

equations 12 – 14 will be used. From the first set of equations (14) the acceleration trace $a_{2z}(t)$ can be expressed as:

$$a_{2z}(t) = 2r_y\left(\omega_y(t)\omega_z(t) - \frac{a_{3y}(t) - a_{0y}(t)}{2r_z}\right) + a_{0z}(t). \quad (21)$$

Using equations 13 for $\omega_y(t)$ and $\omega_z(t)$ and equations 12 for $\alpha_y(t)$ and $\alpha_z(t)$, and substituting them into the equation above for $a_{2z}(t)$ (21), we get:

$$\begin{aligned} a_{2z}(t) &= 2r_y\left\{\int_t \alpha_y(t)dt\int_t \alpha_z(t)dt - \frac{a_{3y}(t)-a_{0y}(t)}{2r_z}\right\} + a_{0z}(t) \\ &= 2r_y\left\{\int_t\left[\frac{a_{3x}(t)-a_{0x}(t)}{2r_z} - \frac{a_{1z}(t)-a_{0z}(t)}{2r_x}\right]dt\int_t\left[\frac{a_{1y}(t)-a_{0y}(t)}{2r_x} - \frac{a_{2x}(t)-a_{0x}(t)}{2r_y}\right]dt \right. \\ &\quad \left. - \frac{a_{3y}(t)-a_{0y}(t)}{2r_z}\right\} + a_{0z}(t) \end{aligned}$$

(22)

In a functional form the above equation can be rewritten:

$$a_{2z}(t) = f[a_{0x}(t), a_{0y}(t), a_{0z}(t), a_{1y}(t), a_{1z}(t), a_{2x}(t), a_{3x}(t), a_{3y}(t), r_x, r_y, r_z]$$

(22a)

It should be observed that the acceleration trace $a_{2z}(t)$ is a function of all the other eight acceleration traces in the array and the distances r_x, r_y, and r_z. This means that if acceleration trace $a_{2z}(t)$ was measured incorrectly, but all the rest traces were correct, the correct $a_{2z}(t)$ can be calculated using equation 22.
Similarly, for the rest accelerations the relationship will be:

$$\begin{aligned} a_{1y}(t) &= 2r_x\left\{\int_t \alpha_x(t)dt\int_t \alpha_y(t)dt - \frac{a_{2x}(t)-a_{0x}(t)}{2r_y}\right\} + a_{0y}(t) \\ &= 2r_x\left\{\int_t\left[\frac{a_{2x}(t)-a_{0x}(t)}{2r_y} - \frac{a_{3y}(t)-a_{0y}(t)}{2r_z}\right]dt\int_t\left[\frac{a_{3x}(t)-a_{0x}(t)}{2r_z} - \frac{a_{1z}(t)-a_{0z}(t)}{2r_x}\right]dt \right. \\ &\quad \left. - \frac{a_{2x}(t)-a_{0x}(t)}{2r_y}\right\} + a_{0y}(t) \end{aligned}$$

(23)

$$\begin{aligned} a_{1z}(t) &= 2r_x\left\{\int_t \alpha_x(t)dt\int_t \alpha_x(t)dt - \frac{a_{3x}(t)-a_{0x}(t)}{2r_z}\right\} + a_{0z}(t) \\ &= 2r_x\left\{\int_t\left[\frac{a_{1y}(t)-a_{0y}(t)}{2r_x} - \frac{a_{2x}(t)-a_{0x}(t)}{2r_y}\right]dt\int_t\left[\frac{a_{2z}(t)-a_{0z}(t)}{2r_y} - \frac{a_{3y}(t)-a_{0y}(t)}{2r_z}\right]dt \right. \\ &\quad \left. - \frac{a_{3x}(t)-a_{0x}(t)}{2r_z}\right\} + a_{0z}(t) \end{aligned}$$

(24)

$$\begin{aligned} a_{2x}(t) &= 2r_y\left\{\int_t \alpha_x(t)dt\int_t \alpha_y(t)dt - \frac{a_{1y}(t)-a_{0y}(t)}{2r_x}\right\} + a_{0x}(t) \\ &= 2r_y\left\{\int_t\left[\frac{a_{2z}(t)-a_{0z}(t)}{2r_y} - \frac{a_{3y}(t)-a_{0y}(t)}{2r_z}\right]dt\int_t\left[\frac{a_{3x}(t)-a_{0x}(t)}{2r_z} - \frac{a_{1z}(t)-a_{0z}(t)}{2r_x}\right]dt \right. \\ &\quad \left. - \frac{a_{1y}(t)-a_{0y}(t)}{2r_x}\right\} + a_{0x}(t) \end{aligned}$$

(25)

$$\begin{aligned} a_{3x}(t) &= 2r_z\left\{\int_t \alpha_z(t)dt\int_t \alpha_x(t)dt - \frac{a_{1z}(t)-a_{0z}(t)}{2r_x}\right\} + a_{0x}(t) \\ &= 2r_z\left\{\int_t\left[\frac{a_{1y}(t)-a_{0y}(t)}{2r_x} - \frac{a_{2x}(t)-a_{0x}(t)}{2r_y}\right]dt\int_t\left[\frac{a_{2z}(t)-a_{0z}(t)}{2r_y} - \frac{a_{3y}(t)-a_{0y}(t)}{2r_z}\right]dt \right. \\ &\quad \left. - \frac{a_{1z}(t)-a_{0z}(t)}{2r_x}\right\} + a_{0x}(t) \end{aligned}$$

(26)

$$\begin{aligned} a_{3y}(t) &= 2r_z\left\{\int_t \alpha_y(t)dt\int_t \alpha_z(t)dt - \frac{a_{2z}(t)-a_{0z}(t)}{2r_y}\right\} + a_{0y}(t) \\ &= 2r_z\left\{\int_t\left[\frac{a_{3x}(t)-a_{0x}(t)}{2r_z} - \frac{a_{1z}(t)-a_{0z}(t)}{2r_x}\right]dt\int_t\left[\frac{a_{1y}(t)-a_{0y}(t)}{2r_x} - \frac{a_{2x}(t)-a_{0x}(t)}{2r_y}\right]dt \right. \\ &\quad \left. - \frac{a_{2z}(t)-a_{0z}(t)}{2r_y}\right\} + a_{0y}(t) \end{aligned}$$

(27)

Each one of the six computed acceleration traces (22 through 27) in the nine accelerometer array can be compared with the corresponding originally measured acceleration trace. If one of the computed traces is not coincident with that originally measured, then the originally measured acceleration trace contains an error, and it should be replaced with the computed one. If more than one of the computed traces is not coincident with the corresponding originally measured traces, then the error could be in one of the three accelerations [$a_{0x}(t)$, $a_{0y}(t)$, or $a_{0z}(t)$], or may be due to more than one of the acceleration traces (or arm lengths) being measured improperly.
To check for an incorrect trace, first let's derive additional equations for the three acceleration traces at point 0: $a_{0x}(t)$, $a_{0y}(t)$, and $a_{0z}(t)$. From the second equation of set 14 and by using relations 12 and 13, $a_{0x}(t)$ can be expressed as:

$$\begin{aligned} a_{0x}(t) &= -2r_z\left\{\int_t \alpha_z(t)dt\int_t \alpha_x(t)dt - \frac{a_{1z}(t)-a_{0z}(t)}{2r_x}\right\} + a_{3x}(t) \\ &= -2r_z\left\{\int_t\left[\frac{a_{1y}(t)-a_{0y}(t)}{2r_x} - \frac{a_{2x}(t)-a_{0x}(t)}{2r_y}\right]dt\int_t\left[\frac{a_{2z}(t)-a_{0z}(t)}{2r_y} - \frac{a_{3y}(t)-a_{0y}(t)}{2r_z}\right]dt \right. \\ &\quad \left. - \frac{a_{1z}(t)-a_{0z}(t)}{2r_x}\right\} + a_{3x}(t) \end{aligned}$$

(28a)

Similarly, from the third equation of set 14:

$$\begin{aligned} a_{0x}(t) &= -2r_y\left\{\int_t \alpha_x(t)dt\int_t \alpha_y(t)dt - \frac{a_{1y}(t)-a_{0y}(t)}{2r_x}\right\} + a_{2x}(t) \\ &= -2r_y\left\{\int_t\left[\frac{a_{2z}(t)-a_{0z}(t)}{2r_y} - \frac{a_{3y}(t)-a_{0y}(t)}{2r_z}\right]dt\int_t\left[\frac{a_{3x}(t)-a_{0x}(t)}{2r_z} - \frac{a_{1z}(t)-a_{0z}(t)}{2r_x}\right]dt \right. \\ &\quad \left. - \frac{a_{1y}(t)-a_{0y}(t)}{2r_x}\right\} + a_{2x}(t) \end{aligned}$$

(28b)

If equations 28a and 28b yield the same result, then all nine traces are self-consistent and no further investigation is required. However, if these equations

don't yield the same result, then the acceleration trace $a_{0x}(t)$ should be expressed as a function of the remaining eight acceleration traces. One of the possible ways to accomplish this is to subtract equation 28b from 28a and solve the newly obtained equation for the velocity $\int_t a_{0x}(t)dt$:

$$\int_t a_{0x}(t)dt = \frac{r_y r_z}{r_y^2 + r_z^2}\left\{-2r_z\int_t\left[\frac{a_{1y}(t)-a_{0y}(t)}{2r_x}-\frac{a_{2x}(t)}{2r_y}\right]dt + 2r_y\int_t\left[\frac{a_{3x}(t)}{2r_z}-\frac{a_{1z}(t)-a_{0z}(t)}{2r_x}\right]dt + \frac{1}{\int_t\left[\frac{a_{2z}(t)-a_{0z}(t)}{2r_y}-\frac{a_{3y}(t)-a_{0y}(t)}{2r_z}\right]dt}\left[-2r_y\frac{a_{1y}(t)-a_{0y}(t)}{2r_x}+2r_z\frac{a_{1z}(t)-a_{0z}(t)}{2r_x}-a_{2x}(t)+a_{3x}(t)\right]\right\}$$

(29)

The equation above allows for the calculation of the acceleration $a_{0x}(t)$ when the other eight accelerations in the nine accelerometer array are known.

Similarly for the acceleration trace $a_{0y}(t)$, from the first equation of set 14:

$$a_{0y}(t) = -2r_z\left\{\int_t \boldsymbol{\alpha}_y(t)dt\int_t \boldsymbol{\alpha}_z(t)dt - \frac{a_{2z}(t)-a_{0z}(t)}{2r_y}\right\} + a_{3y}(t)$$
$$= -2r_z\left\{\int_t\left[\frac{a_{3x}(t)-a_{0x}(t)}{2r_z}-\frac{a_{1z}(t)-a_{0z}(t)}{2r_x}\right]dt\int_t\left[\frac{a_{1y}(t)-a_{0y}(t)}{2r_x}-\frac{a_{2x}(t)-a_{0x}(t)}{2r_y}\right]dt - \frac{a_{2z}(t)-a_{0z}(t)}{2r_y}\right\} + a_{3y}(t)$$

(30a)

And by following the previous method, from the third equation of set 14:

$$a_{0y}(t) = -2r_x\left\{\int_t \boldsymbol{\alpha}_x(t)dt\int_t \boldsymbol{\alpha}_y(t)dt - \frac{a_{2x}(t)-a_{0x}(t)}{2r_y}\right\} + a_{1y}(t)$$
$$= -2r_x\left\{\int_t\left[\frac{a_{2z}(t)-a_{0z}(t)}{2r_y}-\frac{a_{3y}(t)-a_{0y}(t)}{2r_z}\right]dt\int_t\left[\frac{a_{3x}(t)-a_{0x}(t)}{2r_z}-\frac{a_{1z}(t)-a_{0z}(t)}{2r_x}\right]dt - \frac{a_{2x}(t)-a_{0x}(t)}{2r_y}\right\} + a_{1y}(t)$$

(30b)

By subtracting 30b from 30a:

$$\int_t a_{0y}(t)dt = \frac{r_x r_z}{r_x^2 + r_z^2}\left\{-2r_x\int_t\left[\frac{a_{2z}(t)-a_{0z}(t)}{2r_y}-\frac{a_{3y}(t)}{2r_z}\right]dt + 2r_z\int_t\left[\frac{a_{1y}(t)}{2r_x}-\frac{a_{2x}(t)-a_{0x}(t)}{2r_y}\right]dt + \frac{1}{\int_t\left[\frac{a_{3x}(t)-a_{0x}(t)}{2r_z}-\frac{a_{1z}(t)-a_{0z}(t)}{2r_x}\right]dt}\left[2r_x\frac{a_{2x}(t)-a_{0x}(t)}{2r_y}-2r_z\frac{a_{2z}(t)-a_{0z}(t)}{2r_y}+a_{1y}(t)-a_{3y}(t)\right]\right\}$$

(31)

Again, for the acceleration trace $a_{0z}(t)$, from the first equation of set 14 we have:

$$a_{0z}(t) = -2r_y\left\{\int_t \boldsymbol{\alpha}_y(t)dt\int_t \boldsymbol{\alpha}_z(t)dt - \frac{a_{3y}(t)-a_{0y}(t)}{2r_z}\right\} + a_{2z}(t)$$
$$= -2r_y\left\{\int_t\left[\frac{a_{3x}(t)-a_{0x}(t)}{2r_z}-\frac{a_{1z}(t)-a_{0z}(t)}{2r_x}\right]dt\int_t\left[\frac{a_{1y}(t)-a_{0y}(t)}{2r_x}-\frac{a_{2x}(t)-a_{0x}(t)}{2r_y}\right]dt - \frac{a_{3y}(t)-a_{0y}(t)}{2r_z}\right\} + a_{2z}(t)$$

(32a)

and from the second equation of set 14:

$$a_{0z}(t) = -2r_x\left\{\int_t \boldsymbol{\alpha}_z(t)dt\int_t \boldsymbol{\alpha}_x(t)dt - \frac{a_{3x}(t)-a_{0x}(t)}{2r_z}\right\} + a_{1z}(t)$$
$$= -2r_x\left\{\int_t\left[\frac{a_{1y}(t)-a_{0y}(t)}{2r_x}-\frac{a_{2x}(t)-a_{0x}(t)}{2r_y}\right]dt\int_t\left[\frac{a_{2z}(t)-a_{0z}(t)}{2r_y}-\frac{a_{3y}(t)-a_{0y}(t)}{2r_z}\right]dt - \frac{a_{3x}(t)-a_{0x}(t)}{2r_z}\right\} + a_{1z}(t)$$

(32b)

By subtracting 32b from 32a:

$$\int_t a_{0z}(t)dt = \frac{r_x r_y}{r_x^2 + r_y^2}\left\{-2r_y\int_t\left[\frac{a_{3x}(t)-a_{0x}(t)}{2r_z}-\frac{a_{1z}(t)}{2r_x}\right]dt + 2r_x\int_t\left[\frac{a_{2z}(t)}{2r_y}-\frac{a_{3y}(t)-a_{0y}(t)}{2r_z}\right]dt + \frac{1}{\int_t\left[\frac{a_{1y}(t)-a_{0y}(t)}{2r_x}-\frac{a_{2x}(t)-a_{0x}(t)}{2r_y}\right]dt}\left[2r_y\frac{a_{3y}(t)-a_{0y}(t)}{2r_z}-2r_x\frac{a_{3x}(t)-a_{0x}(t)}{2r_z}+a_{2z}(t)-a_{1z}(t)\right]\right\}$$

(33)

The derived above equations 22 through 27, 29, 31, and 33 give the closed form solution for each acceleration trace in a NAAP configuration (Figure 1) as a function of the rest eight traces in the array, thus allowing for correction/calculation of any inaccurate/missing acceleration trace. An example in the Results section illustrates the use of these equations. It should be noted, however, that the closed form solutions above are given under the assumption of one inaccurate trace out of nine. If there are measuring errors in more than one trace then the optimization methodology similar to the one presented below should be utilized.

Optimization Methodology for an In-plane Accelerometer Array Configuration

Consider a rigid body (Figure 4) with a set of translational accelerometers affixed to it at random locations with the known coordinates in a global coordinate system XYZ. For each point in Figure 4 equations similar to equations 5 can be written and solved for angular accelerations $(\alpha_x, \alpha_y, \alpha_z)$. These angular accelerations are then served as the design variables so that the cumulative error given in equation 34 is minimized at each time step between the measured translational accelerations and the

corresponding computed translational accelerations derived from equations 5.

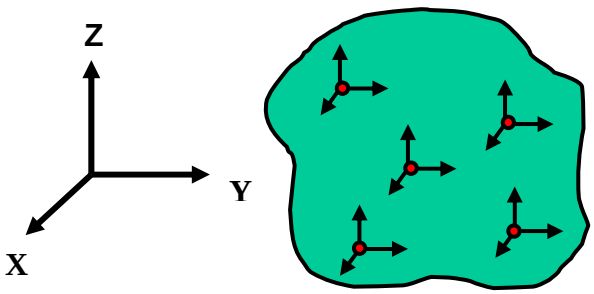

Figure 4. Rigid body with accelerometers affixed to it at random locations.

The objective function (error function) minimized at each time step is defined as:

$$\sqrt{\sum_{i=1}^{n}\left[(a_{ix}^{m}-a_{ix}^{c})^{2}+(a_{iy}^{m}-a_{iy}^{c})^{2}+(a_{iz}^{m}-a_{iz}^{c})^{2}\right]}$$

(34)

where n is the number of points from which the acceleration data is obtained, m is the measured, and c is the computed data. This methodology allows for obtaining 3D angular accelerations that best satisfy all translational acceleration time histories at all given points.

RESULTS

Example of a Closed Form Solution

This example first takes a consistent set of nine accelerations from one of the NHTSA conducted NCAP tests, calculates angular accelerations using only Padgaonkar equations (12), then inputs these angular accelerations into a rigid body finite element model of a human skull (Figure 5) that calculates translational accelerations at the locations similar to those used in NAAP, and then compares the model output with the original measured translational accelerations.

Next, one of the acceleration traces from the initially consistent set of nine accelerations was modified in the manner shown in Figure 6 in which the signal was clipped in half of its original amplitude. The purpose of this was to see the effect of this clipping procedure on the computed translational accelerations output from the model (Figure 7)

Figure 8 shows the results for the original and computed sets of accelerations confirming consistency of the original set, Figure 9 shows the results of all nine traces after one of them was clipped.

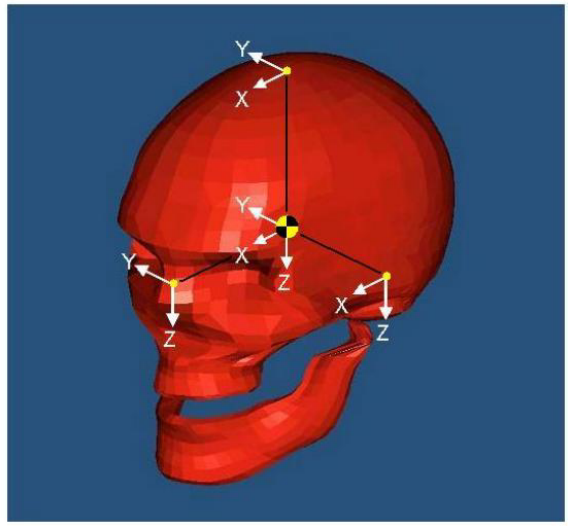

Figure 5. Rigid human finite element skull with accelerometer locations shown.

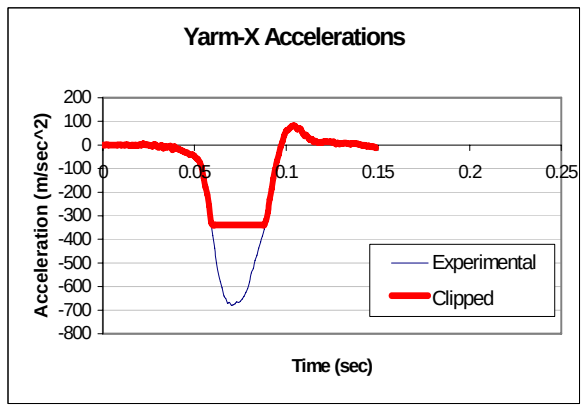

Figure 6. An original and clipped acceleration traces.

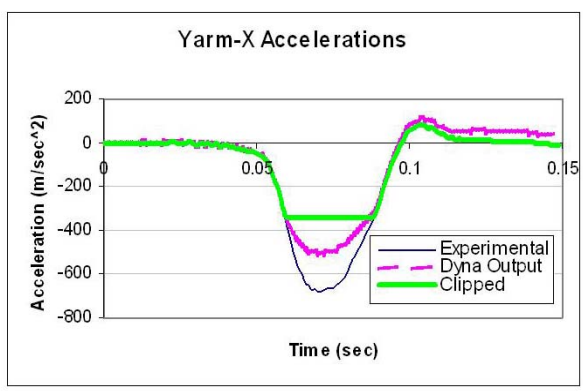

Figure 7. An original (blue), clipped (green), and model output (magenta) acceleration traces.

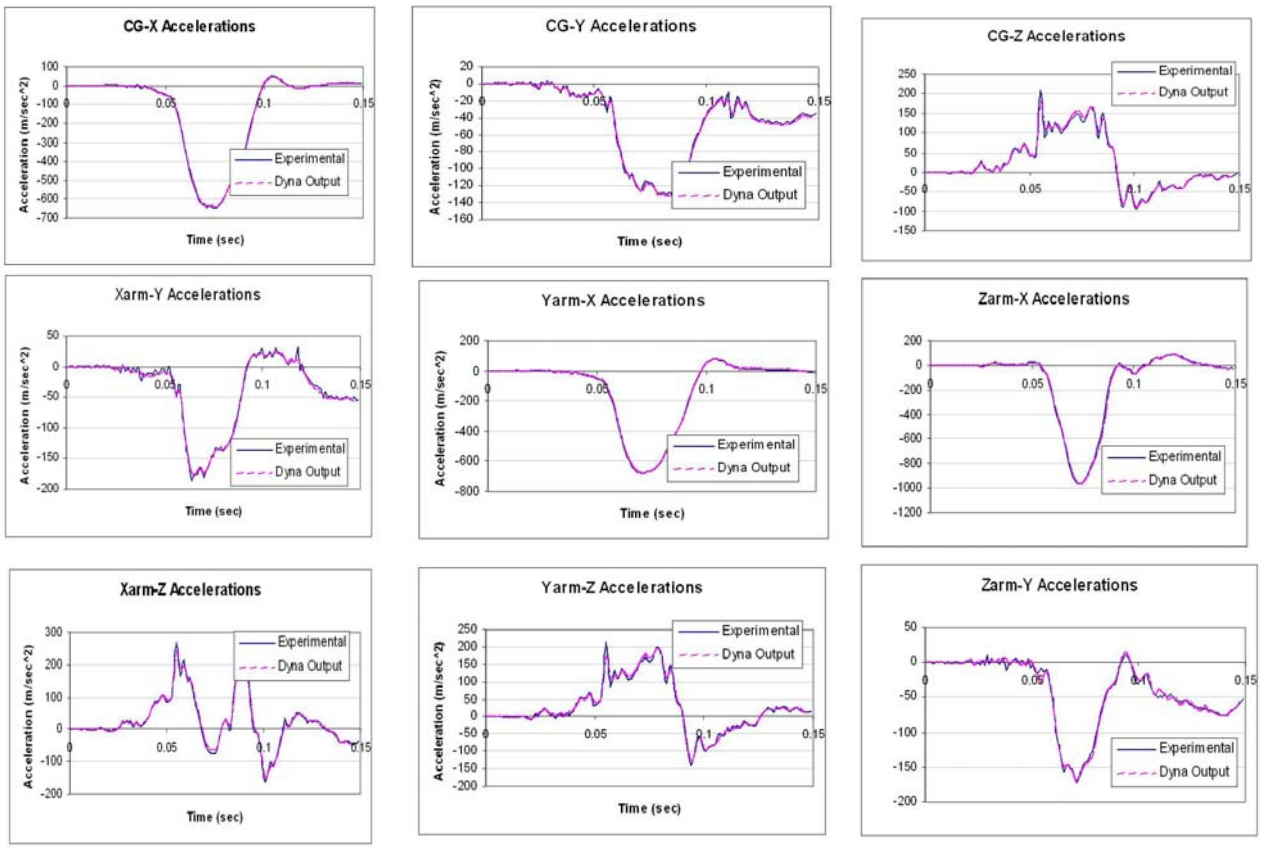

Figure 8. Consistent set of nine accelerations.

It is clear from Figure 9 that by clipping one of the original traces, then calculating angular accelerations using equations 12, and applying them to the finite element model, yields results that are inconsistent with the original set of translational accelerations. Interestingly, as illustrated in Figure 9, almost all of the original traces were affected by clipping only one of them. This illustrates the point that was made previously using equations 15 through 20.

The consistency/inconsistency of nine acceleration traces in NAAP can also be illustrated through the use of constraints equations (14). For a consistent set equations 14 will be satisfied, while opposite is true for an inconsistent set.

Equations 14, however, along with the derived above equations 22 through 27, 29, 31, and 33 can be used to identify and correct the erroneous trace. The procedure for this identification and correction is as follows:

1. Compute α_x, α_y, α_z using original traces and Padgaonkar equations 12,
2. Compute products of angular velocities $\omega_x\omega_y$, $\omega_x\omega_z$, $\omega_y\omega_z$ using rigid body constraint equations 14,
3. Compute each translational acceleration time history as a function of the remaining eight accelerations and radius vectors using equations 22 through 27, 29, 31, and 33,
4. Compare computed and original eight translational accelerations (excluding the one under consideration) and find their cumulative error using equation similar to 34,
5. When the cumulative error is very small, the erroneous trace is found and it should be substituted with it's computed equivalent.

When the described above procedure was applied to the set of nine acceleration traces with one of them clipped, the clipped trace was identified and substituted with its computed equivalent giving results similar to the one shown in Figure 8 with all the traces overlapping each other.

Optimization Methodology Example

Consider a small triangular plate with accelerometers mounted in the manner shown in Figure 10. The small size of the plate is chosen such that it fits into a mouthpiece of a boxer, football or hokey player.

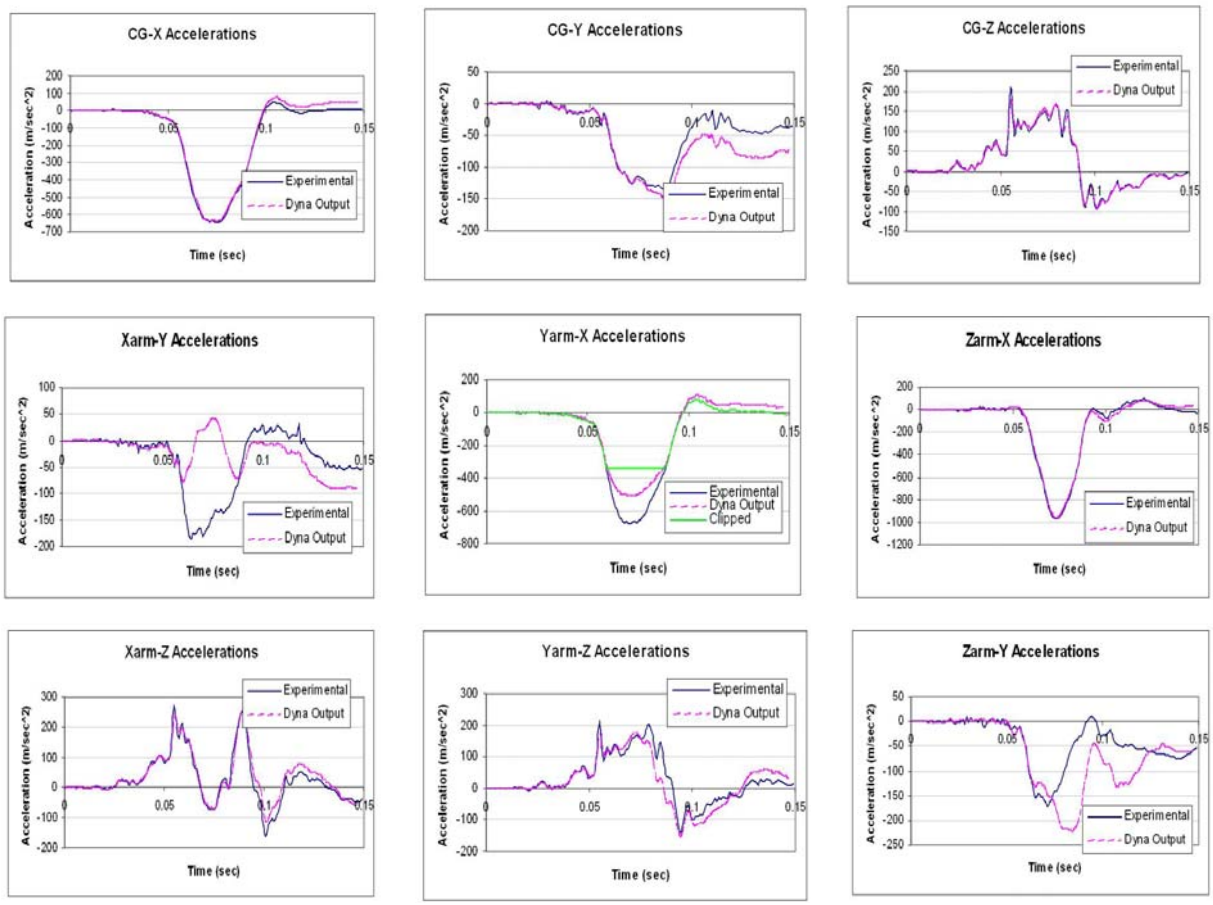

Figure 9. Inconsistent set of nine accelerations (magenta) as compared with the original consistent set (blue).

Using the general equations 5, translational accelerations shown in Figure 10 can be expressed as:

$$\begin{bmatrix} a_{1x} \\ a_{1y} \\ a_{1z} \end{bmatrix} = \begin{bmatrix} a_{2x} \\ a_{2y} \\ a_{2z} \end{bmatrix} + \begin{bmatrix} 0 \\ \alpha_z r_x \\ -\alpha_y r_x \end{bmatrix} + \begin{bmatrix} -r_x\left(\omega_y^2 + \omega_z^2\right) \\ \omega_y\left(\omega_x r_x\right) \\ \omega_z\left(\omega_x r_x\right) \end{bmatrix} \quad (35)$$

$$\begin{bmatrix} a_{2x} \\ a_{2y} \\ a_{2z} \end{bmatrix} = \begin{bmatrix} a_{1x} \\ a_{1y} \\ a_{1z} \end{bmatrix} - \begin{bmatrix} 0 \\ \alpha_z r_x \\ -\alpha_y r_x \end{bmatrix} - \begin{bmatrix} -r_x\left(\omega_y^2 + \omega_z^2\right) \\ \omega_y\left(\omega_x r_x\right) \\ \omega_z\left(\omega_x r_x\right) \end{bmatrix} \quad (36)$$

$$\begin{bmatrix} a_{3x} \\ a_{3y} \\ a_{3z} \end{bmatrix} = \begin{bmatrix} a_{1x} \\ a_{1y} \\ a_{1z} \end{bmatrix} + \begin{bmatrix} -\alpha_z r_y \\ \alpha_z \frac{1}{2} r_x \\ \alpha_x r_y - \alpha_y \frac{1}{2} r_x \end{bmatrix} + \begin{bmatrix} \omega_x\left(\omega_y r_y\right) - \frac{1}{2} r_x\left(\omega_y^2 + \omega_z^2\right) \\ \omega_y\left(\omega_x \frac{1}{2} r_x\right) - r_y\left(\omega_z^2 + \omega_x^2\right) \\ \omega_z\left(\omega_x \frac{1}{2} r_x + \omega_y r_y\right) \end{bmatrix}$$

(37)

where α_x, α_y, α_z are angular accelerations of the plate, ω_x, ω_y, ω_z are angular velocities, and r_x, r_y, r_z are distances between points 1, 2, and 3 in the directions X,Y, and Z respectively.

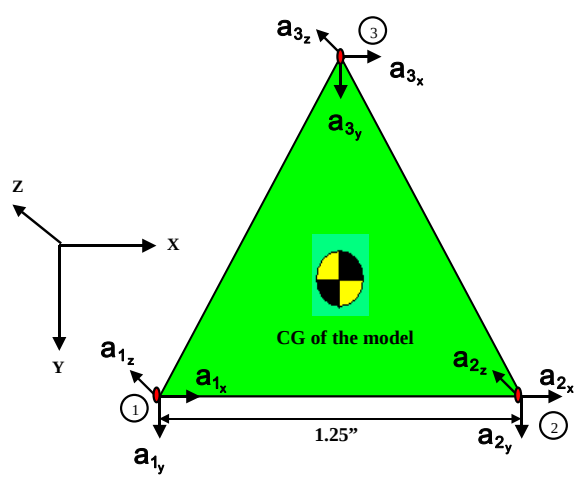

Figure 10. Small triangular plate setup with nine accelerometers fixed at points 1, 2, and 3.

Using numerical finite element model of the rigid triangular plate an arbitrary 3D motion was applied to

generate the nine consistent traces. Figure 11 shows comparison of the angular accelerations from the finite element model with those obtained using optimization (equations 35 – 37, and 34 as an objective function).

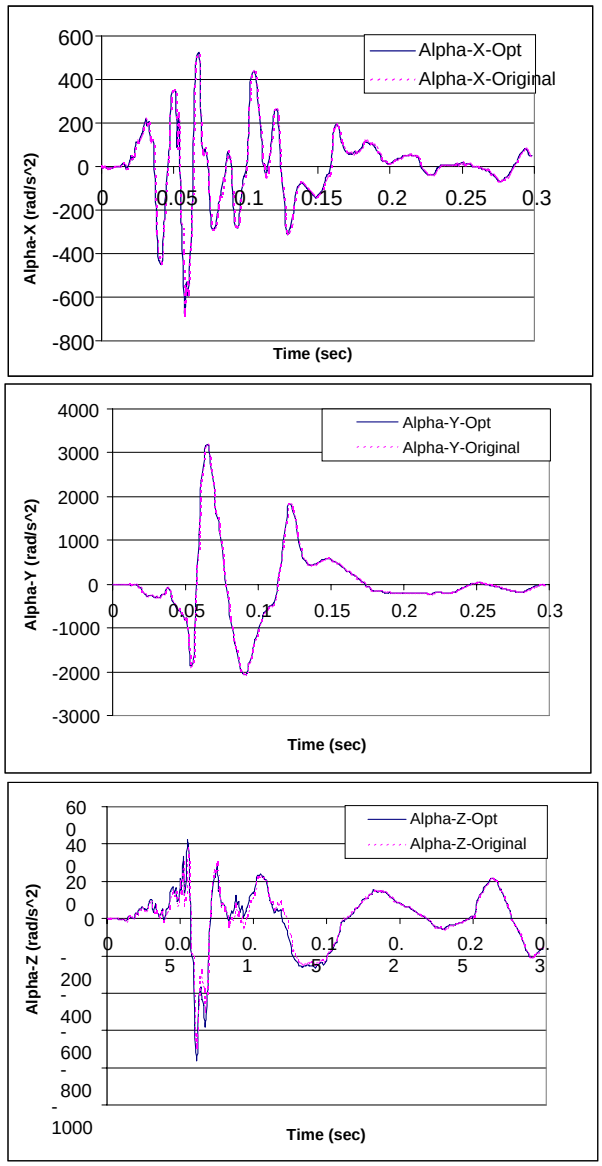

Figure 11. Original versus optimized angular accelerations.

Assume now that there is a 3% cross-axis sensitivity error for each tri-axial accelerometer located at points 1, 2, and 3 in Figure 10. This error can be expressed as:

$$\begin{aligned} a_{ix} &= a_{ix} + 0.03a_{iy} + 0.03a_{iz} \\ a_{iy} &= a_{iy} + 0.03a_{ix} + 0.03a_{iz} \\ a_{iz} &= a_{iz} + 0.03a_{ix} + 0.03a_{iy} \end{aligned} \qquad i = 1 \text{ to } 3. \qquad (38)$$

When the new (erroneous) accelerations (38) are used in place of the old traces obtained from finite element simulation and the optimization procedure, described above, applied to this new set of accelerations, the resulting angular accelerations are identical to those shown in Figure 11.

This procedure demonstrates the applicability of the optimization methodology to recover proper set of acceleration traces when some of the channels are contaminated with random errors. The closed form solution for this hypothetical situation is not currently available.

DISCUSSION

This paper demonstrates some of the limitations in the use of NAAP when only Padgaonkar equations (12) are considered. In particular, if one or more of the accelerometers in the array are not measured properly, the resulting kinematics of a rigid body is substantially affected because these errors are present in the computed angular accelerations. To correct for these possible errors, two methods were derived in this paper and their use was demonstrated.

The first method – the closed form solution - uses additional constraint equations (14) to express each accelerometer in the array as a function of the other eight. The computed and original translational accelerations can then be compared, erroneous acceleration identified, and replaced. This method is limited to the cases when one of the acceleration traces is incorrect. It was also demonstrated that nine accelerations in the NAAP are not independent of each other, but rather bound by the rigid body constraints. This is somewhat intuitive because a rigid body has six degrees of freedom and any additional measure beyond six must be governed by an additional constraint. In the case of NAAP, three additional accelerations are governed by three additional constraints – equations 14.

The second method – the optimization method – uses angular accelerations as design variables for the objective function set to minimize the differences/errors between the measured and computed translational accelerations. This method, although not as elegant as the first one, can be used when multiple channels of accelerations in NAAP or any other configuration are not measured properly.

Both methods can be used by the biomechanical laboratories to analyze and gain confidence in the measures of angular kinematics of human or dummy heads.

CONCLUSIONS

The paper presents two methodologies to analyze angular kinematics of a rigid body when an array of translational accelerometers is used as the motion sensing device. It was demonstrated that:

- Nine accelerometer measures in NAAP are not independent, but rather constrained,
- The constraint equations can be derived and used to identify and correct an erroneous acceleration trace using a closed form solution method,
- The closed form solution method is limited to one erroneous accelerometer trace in the array,
- Optimization methodology can be utilized to correct errors in multiple channels of translational accelerometers.

REFERENCES

[1] Hardy, W.N., Foster, C., Mason, M., Yang, K., King, A., Tashman, S., 2001, ”Investigation of head injury mechanisms using neutral density technology and high-speed biplanar X-ray”. Stapp Car Crash Journal 45. pp. 337-368.

[1] Hardy, W.N., Mason, M., Foster, C.D., Shah, C.S., Kopacz, J.M., Yang, K.H., King, A.I., 2007, ”A study of the Response of the Human Cadaver Head to Impact”. Stapp Car Crash Journal 51, pp. 17-80.

[3] Takhounts, E.G., Eppinger, R.H., Campbell, J.Q., Tannous, R.E., Power, E.D., Shook, L.S., 2003, “On the Development of the SIMon Finite Element Head Model”. Stapp Car Crash Journal 47, pp. 107-133.

[4] Takhounts, E.G., Hasija, V., Ridella, S.A., Tannous, R.E., Campbell, J.Q., Malone, D., Danelson, K., Stitzel, J., Rowson, S., Duma, S, 2008, “Investigation of Traumatic Brain Injuries Using the Next Generation of Simulated Injury Monitor (SIMon) Finite Element Head Model.” Stapp Car Journal 52, pp 1 – 32.

[5] Pagaonkar, A.J., Krieger, K.W.., and King, A.I, 1975. “Measurement of angular acceleration of a rigid body using linear accelerometers”. Journal of Applied Mechanics, pp. 552-556.

BIOFIDELITY OF THE WORLDSID SMALL FEMALE REVISION1 DUMMY

Andre Eggers
Britta Schnottale
Federal Highway Research Institute, BASt
Germany
Bernard Been
Kees Waagmeester
First Technology Safety Systems Europe
The Netherlands
David Hynd
Jolyon Carroll
TRL limited
United Kingdom
Luis Martínez
University Institute for Automobile Research, Polytechnic University of Madrid (UPM-INSIA)
Spain
Paper Number 09-0420

ABSTRACT

In the EC FP6 Integrated Project Advanced Protection Systems, APROSYS, the first WorldSID small female prototype was developed and evaluated by BASt, FTSS, INRETS, TRL and UPM-INSIA during 2006 and 2007. Results were presented at the ESV 2007 conference (Been *et al.*, 2007). With the prototype dummy scoring a biofidelity rating higher than 6.7 out of 10 according to ISO/TR9790, the results were very promising. Also opportunities for further development were identified by the evaluation group.

A revised prototype, Revision1, was subsequently developed in the 2007-2008 period to address comments from the evaluation group. The Revision1 dummy includes changes in the half arms and the suit (anthropometry and arm biomechanics), the thorax and abdomen ribs and sternum (rib durability), the abdomen/lumbar area and the lower legs (mass distribution). Also a two-dimensional chest deflection measurement system was developed to measure deflection in both lateral and anterior-posterior direction to improve oblique thorax loading sensitivity. Two Revision1 prototype dummies have now been evaluated by FTSS, TRL, UPM-INSIA and BASt. The updated prototype dummies were subjected to an extensive matrix of biomechanical tests, such as full body pendulum tests and lateral sled impact tests as specified by Wayne State University, Heidelberg University and Medical College of Wisconsin.

The results indicated a significant improvement of dummy biofidelity. The overall dummy biofidelity in the ISO rating system has significantly improved from 6.7 to 7.6 on a scale between 0-10. The small female WorldSID has now obtained the same biofidelity rating as the WorldSID mid size male dummy. Also repeatability improved with respect to the prototype. In conclusion the recommended updates were all executed and all successfully contributed in achieving improved performance of the dummy.

INTRODUCTION

Side impact is still one of the predominant causes of serious or fatal road accidents. A recent study analysing the national accident datasets of the UK, France and Sweden showed that side impacts typically represent 33% of all fatalities in these countries (Thomas *et al.*, 2009).

For evaluation and improvement of new and advanced occupant protection technologies anthropometric test dummies specifically designed for side impact testing have proven to be very useful. However, several different types of side impact dummies exist, which are used in various regulations and consumer tests.

The introduction of a family of worldwide harmonised side impact dummies to be used for vehicle safety development could contribute to an increased efficiency of vehicle safety development by enabling safety system designers to focus on a single set of objectives.

In a first step to address the need for worldwide harmonised side impact dummies the WorldSID 50% adult male was developed. Newland *et al.* (2005) showed, based on analysis of worldwide accident data, the importance of having also a small adult female test device for assessment of vehicle safety available. According to Newland's study done within IHRA, the proportions of male and female severely or fatally injured occupants in vehicle-to-vehicle crashes were either similar or slightly predominated by females (up to 60%) in some regions.

To address this need a prototype of a small female WorldSID was developed within the European FP6 project APROSYS to complete the family of worldwide harmonised side impact dummies with similar design, instrumentation and functional handling.

In order to accurately predict injuries of human occupants based on tests with these dummies biofidelity is crucial. The biofidelity of the WorldSID small female prototype was assessed earlier and reported by Been *et al.* (2007). The biofidelity of the prototype was already very good. Taking into account recommendations from prototype testing an updated version, the Revision1, was developed.
The objective of the study reported in this paper was to repeat the tests for biofidelity assessments and to analyse the effects of the dummy updates. The modifications, which were made based on recommendations from the prototype testing, are explained. The results of the biofidelity tests are presented and compared to the results of the prototype evaluation.

SMALL FEMAL REVISION1: DUMMY MODIFICATIONS

The dummy requirements and design specifications of the small female WorldSID prototype dummy were described in detail by Been *et al.* (2007). Therefore in this paper only modifications of Revision1 will be explained below.

Anthropometry

Recommendations were given to increase the abdomen mass and reduce the lower leg mass by the same amount of 1.2 kg total (Martínez et al., 2007). New tibia bones were installed, with the mass of each tibia reduced by 0.6 kg; the abdomen was ballasted with a high density metal lumbar bracket. Further mass increase in the thorax and abdomen was achieved with 2D IR-Traccs and the addition of damping material on the ribs. The WorldSID small female Revision1 dummy now represents the target body segment mass distribution and overall mass (see Table 1. In this table it should be noted that the difference in sub-total body segment comes from the shoe. The shoe is part of the foot and dummy and the sub-total. In the anthropometry reference the shoe is outside the sub-total an included only in the total. Further small differences may occur due to the fact that anthropometric section planes sometimes do not match dummy sub-assemblies.
The half arm length was increased by 40 mm to get closer to the human target length. However it was decided not to increase the arm length fully to the length of the human target to stay clear from the iliac wing. An arm contact on the iliac wing during testing would cause the arm to bridge between the shoulder and the iliac wing and so reducing the loads on the thorax and abdomen ribs. The total arm length from the shoulder joint to the bottom of the half arm is 240 mm. The small female anthropometric dummy target gleno-humeral joint to elbow joint distance is 255 mm.

Table 1.
Mass comparison Revision1 to target

Body segment [kg]	Target (Schneider et al. 1983)	WorldSID 5F Rev1
Head	3.70	3.66
Neck	0.60	0.54
Thorax including half arms and 2D IR-Traccs	15.23	15.81
Abdomen	1.61	1.33
Pelvis	6.98	6.98
Upper legs	11.83	11.83
Lower legs, feet & shoes	6.00	6.61
Sub Total	**45.94**	**46.75**
Suit	1.52	1.52
Pair of shoes	0.64	-
Total	**48.10**	**48.27**

Instrumentation

The major update in instrumentation was the integration of a two-dimensional chest deflection measurement system to measure deflection in both lateral and anterior-posterior direction. The calculation of deformation components in the different plane was possible by additional angular sensors in the thorax and abdomen ribs. More details on the design and performance of this 2D IR-Traccs can be found in the ESV paper by Been *et al.* (2009).
During this test series the two dummies were not fully instrumented as not enough sensors were available for full instrumentation at this stage.
The instrumentation of the WorldSID 5th female dummies as it was used in most of the tests reported in this paper is given in Table 2.

Table 2.
Instrumentation of WorldSID small female Rev1

Segment	Parameter	Nr.
Head	Acceleration ($a_{x,y,z}$)	3
Neck	Upper loads ($F_{x,y,z}$, $M_{x,y,z}$)	6
Shoulder	Loads ($F_{x,y,z}$)	3
	Deflection (δ_y)	1
Thorax/Abdomen	T1 acceleration ($a_{x,y,z}$)	3
	T12 acceleration ($a_{x,y,z}$)	3
	Rib deflection (δ_y)	5
	Rib acceleration (a_y)	5
	Rib rotation(φz)	5
Pelvis	Pubic loads (F_y)	1
	Acceleration ($a_{x,y,z}$)	3
Femur	Femoral neck load ($F_{x,y,z}$)	3
	Femur load ($F_{x,y,z}$ $M_{x,y,z}$)	6

EVALUATION METHODOLOGY

Biofidelity evaluation method

As a basis for evaluation of the biofidelity of the WorldSID 5th female Revision1 the response requirements as specified in ISO Technical Report TR9790 (ISO, 1997) for lateral biofidelity were scaled for 5th female according the formulas specified by Irwin *et al.* (2002).

To achieve similar force plate interaction with the small female dummy as the original PMHS test set up, the force plates in the sled test conditions were scaled according to the method prescribed by Ferichola *et al.* (2007). ISO Technical Report 9790 includes a large set of dynamic biofidelity performance specifications for the head, neck, shoulders, thorax, abdomen and pelvis of a 50th percentile side impact dummy.

In this study a subset of the ISO test conditions was conducted, selected on the basis of the highest weighting factor. Some of the tests described in the ISO Technical Report 9790 were not performed because of a high risk of damaging the dummy.

In contrary to the prototype test, normalisation was not applied for the Revision1 tests for the assessment in ISO TR9790. Normalisation is not prescribed for ISO corridors, as the dummy is considered to perfectly represent the target anthropometry pertaining to the corridors.

In addition full body sled tests of the NHTSA configuration were conducted to evaluate the dummy against PMHS tests of Yoganandan *et al.* (2005). The NHTSA sled test conditions are not part of the ISO TR9790 biofidelity test conditions and rating system. ISO/TC22/SC12/WG5 is currently working on adopting the NHTSA sled test conditions in ISO TR9790 for the mid size male anthropometry and apply the ISO method for corridor construction to the data set. NHTSA applies a biofidelity rating using Cumulative Variance (Rhule *et al.*, 2002) on this data set. The NHTSA test conditions are part of the NHTSA biofidelity requirements to assess the response of Side Impact Dummies of the mid-size male anthropometry. Yoganandan *et al.* (2005) derived small female responses from the NHTSA sled test database by mass scaling to small female anthropometry. This data set is likely to be adopted by NHTSA for evaluation of small female side impact dummies. The data set has response corridors for external load as well as dummy internal acceleration and deflection.

The biofidelity assessment of rib deflection was done by a comparison of chest band data from the PMHS tests (Figure 2) to calculated dummy signals. The 2D deflection sensor of the small female WorldSID, 2D IR-Tracc, allows calculating the displacement of the ribs in the X-Y (transversal) plane of the dummy from the compression and rotation angle of the IR-Tracc (for details see Been *et al.*, 2009). Two parameters could be useful for assessment of rib deflection, the parameter 'Calculated Y displacement' and 'R resultant displacement' (Figure 1). As illustrated in Figure 2 the calculated Y displacement could be a good match with what was originally measured in the PMHS with the chest bands. The resultant deflection R might be an overestimation of the rib deflection with respect to the original data, getting larger with more forward or rearward displacement in the dummy's chest. For the biofidelity evaluation of the chest deflection response of the dummy, the resultant displacement and calculated lateral displacement Y were both applied for comparison with Yoganandan (2005) PMHS data.

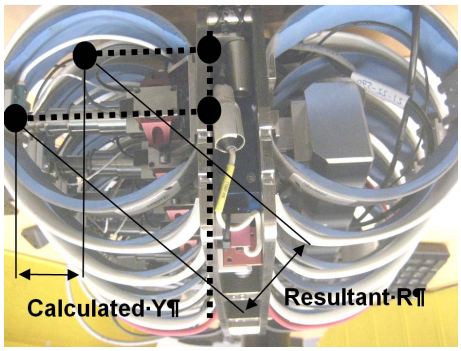

Figure 1: Deflection parameters R and Y calculated from deflection and angle measured with 2D IR-Traccs.

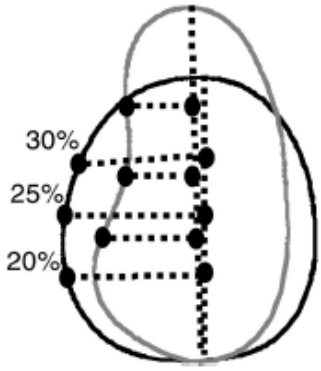

Figure 2: Computation method half-thorax deflection from PMHS testing instrumented with chest band. Source: Yoganandan, (2005).

Repeatability

ISO/TC22/SC12/WG produced a paper on how to assess repeatability and reproducibility of a dummy (ISO, 2004). Repeatability is defined as the variations in measured responses of a single dummy that is subjected to a set of identical tests. Reproducibility is defined as the variations in measured responses of two or more dummies of the same design that are subjected to sets of identical tests. The document describes the calculation methods and acceptance levels for assessing repeatability and reproducibility of a dummy design.

Requirement: Repeatability CV ≤ 7%: repeat tests with the same dummy N times, then the standard deviation (σ) divided by the average of selected measurements should not exceed 7%.
Requirement: Reproducibility CV ≤ 10%: repeat tests with different dummies, then the standard deviation divided by the average of selected measurements should not exceed 10%.

Test matrix

Like in the test programme with the prototype dummy not the complete set of ISO TR9790 tests was performed. Also some of the NHTSA sled test configurations (e.g. high velocity, thorax offset) had to be omitted due to high risk in terms of dummy damage.
Also not all test configurations reported by Been *et al.* (2007), which were done with the prototype dummy were repeated with the Revision1 dummy due to time restrictions and the need to limit the risk to the dummy. The test matrix relevant for biofidelity and repeatability evaluation of this study is provided in Table 3.

Table 3.
Test matrix WorldSID 5th Revision1 for evaluation of biofidelity and repeatability

Test type	Test configuration	No. of tests	Biofidelity assessment				
			Head	Shoulder	Thorax	Abdomen	Pelvis
Drop tests	200 mm rigid lateral head drop	4	x				
	376 mm forehead rigid drop	2	x				
Pendulum Tests	4.5 m/s, shoulder	3		x			
	HSRI, 4.3 m/s, lateral, thorax	3			x		
	WSU, 4.3 m/s, lateral, thorax	3			x		
	WSU, 4.3 m/s, oblique, thorax	3			x		
	WSU, 6.0 m/s, oblique, thorax	3			x		
	6.0 m/s, pelvis	4					x
	8.0 m/s, pelvis	3					x
Sled tests	WSU, 6.8 m/s, rigid wall	3				x	x
	WSU, 8.9 m/s, padded foam	3		x	x	x	x
	WSU, 8.9 m/s, paper honeycomb	3		x	x	x	x
	Heidelberg, 6.8 m/s, rigid wall	3			x		
	NHTSA/MCW, 6.7 m/s padded flat wall	5			x	x	x
	NHTSA/MCW, 6.7 m/s rigid flat wall	3			x	x	x
	NHTSA/MCW, 6.7 m/s padded pelvis offset	4			x	x	x
	NHTSA/MCW, 6.7 m/s rigid pelvis offset	3			x	x	x

RESULTS

In the following the results regarding biofidelity and repeatability will be shown per body segment.

Head

The head biofidelity was evaluated by drop testing according ISO TR9790 with 200 mm lateral drop and a 376 mm drop on the forehead. ISOTR9790 prescribes a resultant linear acceleration on the non struck side of the head on a lateral axis passing through the head centre of gravity (CG). No such instrumentation is available, as the WorldSID accelerometer is located at the head centre of gravity. The numbers given in Table 4 are obtained by calculation of the resultant linear acceleration on the non struck side of the head from the accelerations at head CG and rotational acceleration. The frontal drop test results of 2005 were slightly below the corridor. The tests were repeated with two heads of the same build level. The results are given in Table 4. Both heads now pass the frontal as well as the lateral biofidelity corridors. The prototype failed the frontal test. The overall biofidelity of the head is now 10. The results have increased about 8 g for the lateral tests and about 15 G for the frontal tests. The results show an excellent repeatability. The coefficient of variation is 2.5% or less for all accelerations.

Table 4.
Results head drop tests

Condition	Revision1		Prototype		Corridor
	Resultant acc. [g]		Resultant acc. [g]		
	CoG	non struck	CoG	non struck	
Lateral	127	152	120	139.5	107-161
Lateral	126	151	119	135.9	
Lateral	128	151	-	-	
Lateral	132	154	-	-	
Frontal	261	NA	244	NA	250-300
Frontal	260	NA	236	NA	

Neck

The biofidelity tests for the neck component were conducted with the prototype dummy. The neck was not changed for the Revision1 prototype and the tests were not repeated. Based on recommendations (Been *et al.*, 2007), new corridors were developed based on a new scaling method. This method and pertaining corridors shall be submitted to ISO/TC22/SC12/WG5 for consideration, however strictly speaking ISO only have published 50th percentile male response corridors (ISO, 1997).
In this report the new head-neck corridors were applied to the prototype responses. The head neck response of the Revision1 dummy may slightly have changed due to the changes in the shoulder and half arm. It is anticipated that the T1 acceleration would increase due the increased stiffness of the arm and the sternum, providing more support from the entire thorax in this test. The results are given in Table 5. The results in this table deviate from those published by Meijer *et al.* (2008). When these tests were conducted, the results of the first test were not satisfactory. The test set-up was slightly changed to obtain better shoulder interaction with the impact

panel of the sled. Therefore the results of the first test were omitted in the current report. Further the peak horizontal acceleration was rounded from 11.9 to 12, bringing the response just into the corridor. The conclusions from the reference report are taken over in this report.

From the comparison of the dummy responses and the new corridors the following dummy measures are proposed to further improve the head-neck responses:

1. The head flexion angle may be reduced by installing stiffer neck buffers in the lateral position. This will reduce the head angle and may improve the rating.
2. The neck twist response may be improved by replacing the rear square neck buffers with a circular one, which is similar to the ones used in lateral positions. The twist motion may be doubled by this measure, with a potential to approach the lower boundary of 32° and increasing the score from 0 to 5. The change will have no significant effect on the lateral response.
3. Human necks are more flexible in neck extension (backward bending) then in flexion. The frontal response has not been validated so far, but a change to the rear neck buffer will not affect the frontal response. It is recommended to assess frontal biofidelity according to Mertz OC angle moment relationship (Mertz and Patrick, 1971).

It is recommended to apply above mentioned changes and repeat neck test 1 with Revision1 updated dummy to review its response to the newly develop corridors.

Table 5.
Head-neck responses and biofidelity rating prototype dummy in new corridors

						Boundary			Ratings				Biofidelity	
Body region	Ui	Impact condition	Vij	Measurement	Wijk	Lower	Upper	Unit	test 1	test 2	test 3	Average	Impact	**Test**
Neck	6	7.2 g sled	7	Peak horizontal Acc T1	5	12	18	G	5	10		7.5	37.5	
test 1		impact		Peak hor. Displ. T1/sled	5	38	51	mm	5	5		5.0	25	
		NBDL		Peak hor. Displ. head cg/t1	8	116	145	mm	5	5		5.0	40	
				Peak vert. Displ. Head CG/T1	6	57	84	mm	10	10		10.0	60	
				Time of max head excursion	5	0.142	0.157	s	5	5		5	25	
				Peak lateral Acc head cg	5	9	12	G	10	10		10	50	
				Peak vertical Acc head cg	5	9	11	G	10	10		10	50	
				Peak flexion angle	7	44	59	deg	5	5		5	35	
				Peak twist angle	4	-32	-45	deg	0	0		0.0	0	
				Peak OC lateral bending moment	non ISO	26	43	Nm	5	5		5.0		
				Peak OC torsion twist moment	non ISO	10	17	Nm	5	5		5.0		
					50								323	**6.5**

Shoulder

The biofidelity of the shoulder response was evaluated by three pendulum tests and six WSU type sled test of two different configurations.

Figure 3 shows the impact force which is not completely inside the corridor. The shoulder deflection (Figure 4) is within the corridor for the pendulum test and also the NBDL sled test results were improved. In the WSU 8.9 m/s padded sled impact (Figure 5) the shoulder and thorax beam force is inside the corridors for two tests and in one test the response is very close to scoring 10 points.

Table 6 gives the biofidelity rating of the individual shoulder tests. Overall shoulder biofidelity has significantly improved from 5.0 to 7.4 and meets the target of ISO BR>6.5, good biofidelity.

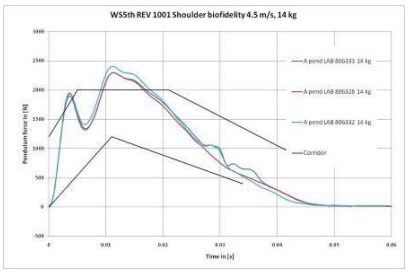

Figure 3. Shoulder impact force, 4.5 m/s, 14 kg.

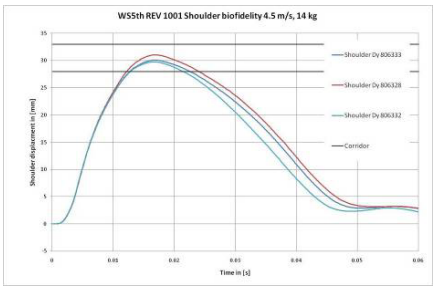

Figure 4. Shoulder deflection, 4.5 m/s, 14 kg shoulder impact.

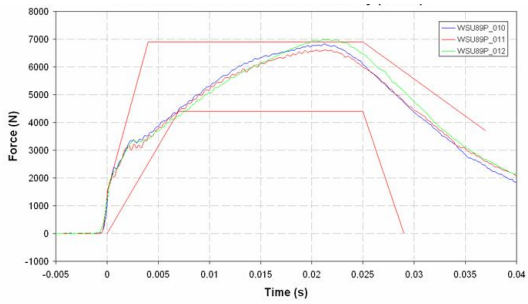

Figure 5. WSU 8.9 m/s, padded foam, shoulder and thorax forces.

Table 6.
ISO TR9790 biofidelity score for shoulder tests

Body region	Ui	Impact condition	Vij	Measurement	Wijk	Lower	Upper	Unit	test 1	test 2	test 3	Average	Impact	Test	Test condi	Body region
Shoulder	5	4.5 m/s	6	Pendulum force-time	8	force time corridor			5	5	5	5.0	40			
test 1		APR		Pendulum Force		1.2	2	kN								
		pendulum		Peak shoulder deflection	6	28	33	mm	10	10	10	10.0	60			
					14								100	**7.1**	42.9	
test 2		7.2 G sled	5	Peak horizontal Acc T1	6	15	22	G		5	10	7.5	45			
		sled		Peak hor. Displ. T1/sled	6	38	51	mm		5	5	5.0	30			
		NBDL			12								75	**6.3**	31.3	
test 4		8.9 G	7	shoulder + thoracic plate force	9	force time corridor			10	10	5	8.3	75			
		WSU sled				4.4	6.9	kN								
		23 PSI padded			9								75	**8.3**	58.3	
			18												132	**7.4**

Thorax

To assess the thorax biofidelity of the WorldSID 5th female Revision1 prototype dummy, four different pendulum and seven sled test configurations were conducted.

Thorax: Pendulum Tests - Thorax Test set-up similarly to the original WSU tests are shown in Figure 6 and Figure 7.
Figure 6 shows the force responses of the 4.3 m/s WSU lateral thorax pendulum test. The responses are close to the upper corridor limit. In the 6.0 m/s test the peak force is above the upper limit of the corridor and the duration of the response is shorter than that of the corridor (Figure 7).

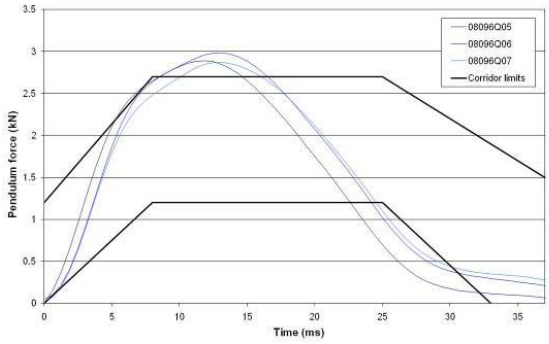

Figure 6. 4.3 m/s, 14 kg, pendulum force responses using lateral WSU setup, ISO corridor

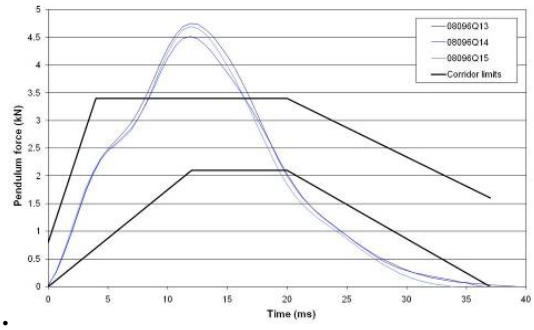

Figure 7. 6.0 m/s, 14 kg, pendulum force response, ISO corridor

Thorax: Sled Tests - Thorax plate forces from Heidelberg sled tests are shown in Figure 8 and Figure 9. Peak forces are shown in Table 7. Even though the plate force response just goes out of the corridor, the general shape better looks more similar to the corridor. However, according to the ISO rating the prototype showed a better performance. The repeatability was good in this test as the CV values in Table 7 show.
Figure 10 shows the shoulder plus thorax response from WSU sled tests along with the ISO corridors. In one test the forces were completely within the corridor, in the other two tests the signals were almost completely within the limits. Compared to the prototype tests, the biofidelity of thorax plate forces in this test configuration have been improved considerably.

Table 7.
Peak thorax plate force results

		Biofidelity target		Prototype results		Revision1 results	
		Lower limit (kN)	Upper limit (kN)	Peak values (kN)	Coefficient of variation (%)	Peak values (kN)	Coefficient of variation (%)
Thorax plate force	EEVC normalisation	7.2	12.1	7.9	4.9	10.5	4.3
				8.0		9.9	
				8.7		9.7	
	ISO normalisation	3.7	12.4	8.0	4.9	10.6	4.3
				8.1		10.0	
				8.8		9.8	

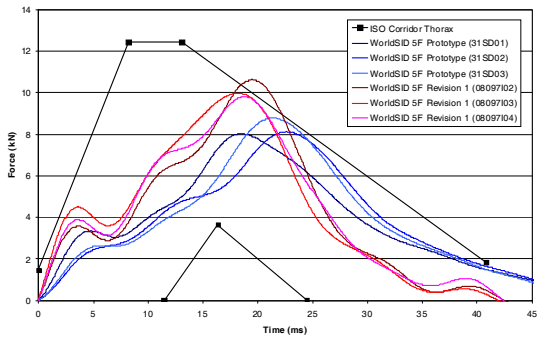

Figure 8. Heidelberg. 6.8 m/s ,Thorax force plates - ISO corridors

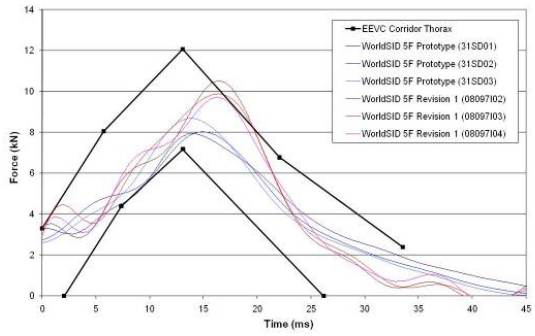

Figure 9. Heidelberg, 6.8 m/s, Thorax force plates - EEVC corridors

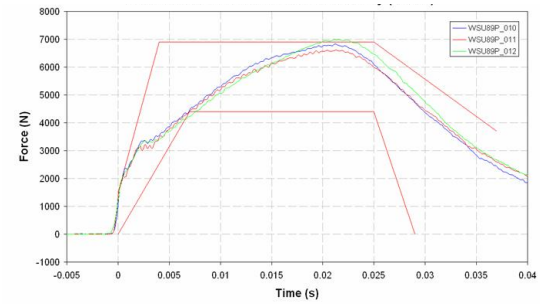

Figure 10. WSU, padded 8.9 m/s – Shoulder plus thorax beam force

<u>Thorax: Biofidelity Rating According to ISO</u>
The thorax biofidelity rating is given in Table 8. The thorax rating is significantly improved from 5.6 for the prototype to 6.9 for the Revision1 prototype and meets the target of ISO BR>6.5 good biofidelity. The external load responses of the Revision1 prototype dummy are generally within or just outside the upper corridors of the ISO. The ISO biofidelity rating of 6.9 for the thorax is considered to be quite good.

<u>Thorax: Yoganadan/NHTSA Sled Tests</u> - In the Yoganandan test series there is a variation of 4 test conditions, padded and rigid flat and offset wall and for each condition a large amount of test parameters (9) to consider (acceleration 1st and 12th vertebra and pelvis, load wall force thorax, abdomen and pelvis and deflection upper, middle and lower ribs). Therefore not all responses are shown in this report. Only a limited number of relevant responses are shown in the figures below. The biofidelity of rib deflection was evaluated as described above based on the calculated resultant and calculated lateral deflection (Figure 1).
Figure 11 to Figure 12 show the two different calculated deflection parameters for the 1st thoracic rib in the sled configuration padded flat with the PMHS corridors. In Figure 13 for comparison the measured lateral deflection of the prototype dummy in this configuration in shown.
The calculated lateral deflection (Figure 11) is close to the lower corridor which indicates only moderate biofidelity. The biofidelity in the prototype was slightly better (Figure 13). The calculated resultant deflection (Figure 12) shows the best biofidelity.
These finding would indicate that the dummy chest might be too stiff. Thus the use of the resultant rib deformation which is overestimating the real deformation could compensate the too stiff dummy chest, and finally provide a more biofidelic output.

Table 8.
Thorax biofidelity rating for Revision1 prototype

						Boundary			Ratings				Biofidelity			
Body region	Ui	Impact condition	Vij	Measurement	Wijk	Lower	Upper	Unit	test 1	test 2	test 3	Average	Impact	Test	Test condi	Body region
Thorax	10	4.3 m/s	9	Pendulum force	9	force time corridor				5	8.3	6.7	59.9			
test 1		HSRI				1.2	2.7	kN								
		pendulum		Peak T4 Y acc.	7	acc. time corridor				5	5	5.0	35			
					16	**10**	**18**	**G**					94.9	**5.9**	53.4	
test 2		6.0 m/s	9	Pendulum force	9	force time corridor				5	10	7.5	67.5			
		WSU/GML				2.1	3.4	kN								
		pendulum			9								67.5	**7.5**	67.5	
test 5		6.8 m/s	7	Thorax plate force	8	force time corridor			10	10	5	8	66.7			
		Heidelberg				3.7	12.4	kN								
		rigid sled		peak T1 Y acc.	7	100	149	G	5	0	5	3.3	23.3			
				peak T12 Y acc.	7	87	131	G	5	5	5	5.0	35			
				peak rib acc.	6	78	122	G	5	5	5	5.0	30			
					28								155	**5.5**	38.8	
test 6		8.9 m/s	7	shoulder + thoracic plate force	9	force time corridor			10	10	5	8	75			
		WSU				4.4	6.9	kN					0			
		sled		Peak lateral displacement of T12	5	65.0	88.0		10	10	10	10	50			
		23 PSI padded			14								125	**8.9**	62.5	
			32												222	**6.9**

The plots of deflection calculated parameters of the other thoracic ribs and other sled configurations are not shown in this report. However, the tendency was similar, which can also be seen in the biofidelity rating based on the cumulative variance. This was done for all configurations and all parameters and is shown at the end of the result section in Table 16.

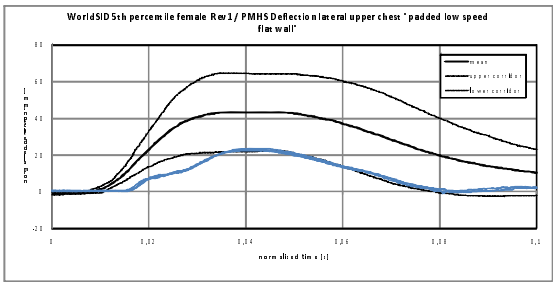

Figure 11. Padded Flat Wall 6,7 m/s; WS5F Rev1; Lateral measured deflection of 1st Thoracic rib.

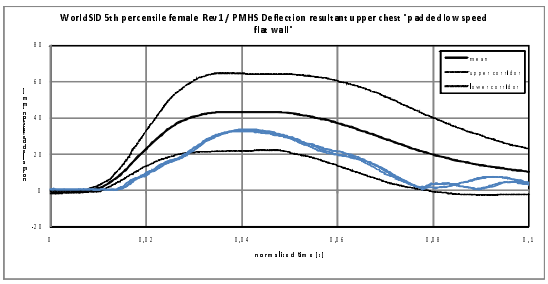

Figure 12. Padded Flat Wall 6,7 m/s; WS5F Rev1; Resultant measured deflection of 1st Thoracic rib.

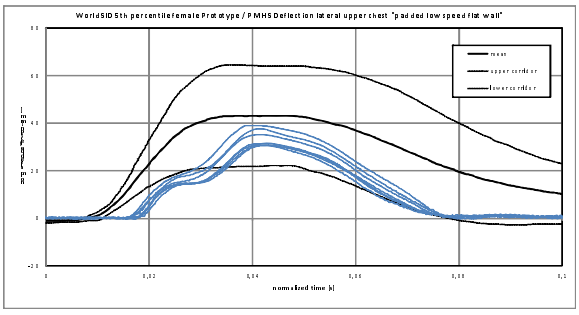

Figure 13. Padded Flat Wall 6,7 m/s; WS5F Prototype; Lateral measured deflection of 1st Thoracic rib.

The thoracic plate forces of the four different sled configurations are shown in Figure 14 to Figure 17. The forces are close to the mean PMHS curve except for the padded pelvis offset configuration where the curve is closer to the lower corridor. The results show excellent biofidelity, which improved compared to the prototype.

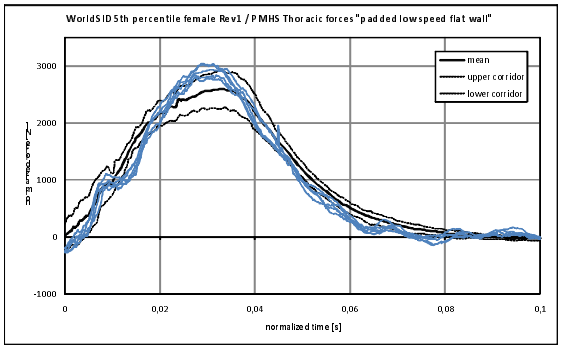

Figure 14. Padded flat, 6.8 m/s, thorax plate forces.

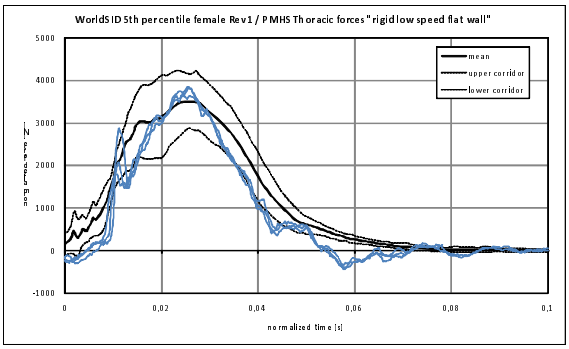

Figure 15. Rigid flat, 6.8 m/s, thorax plate forces.

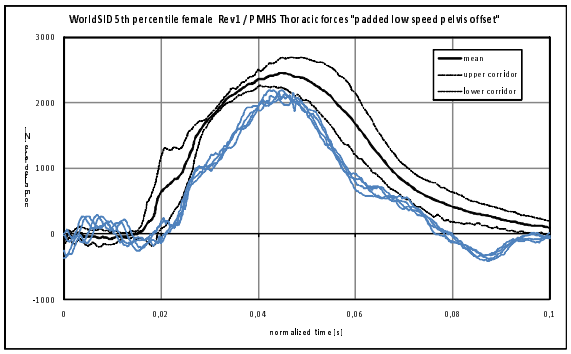

Figure 16. Padded pelvis offset, 6.8 m/s, thorax plate forces.

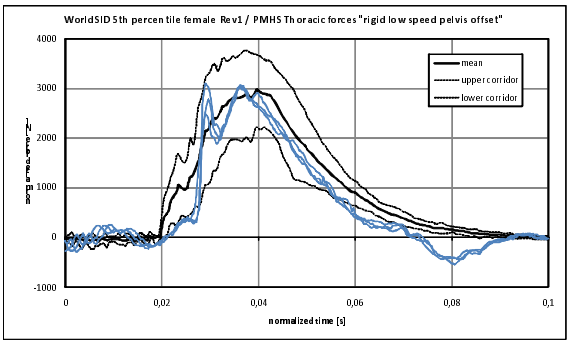

Figure 17. Rigid pelvis offset, 6.8 m/s, thorax plate forces.

Abdomen

The abdomen biofidelity for the Revision1 WorldSID 5th was evaluated based on seven different sled conditions (three WSU and four NHTSA).

<u>Abdomen: WSU Sled Results</u> - The results obtained in the rigid and padded tests are shown in Figure 18 and Figure 19 along with the proposed corridor. In the rigid configuration the response was too stiff and peak duration too short. This resulted in the maximum values slightly being above the upper corridor and all three curves cut the lower boundary. In the padded configuration the dummy response was in good agreement with the corridors. The dummy rigid test response lies within one corridor width out of the proposed corridor which leads to a biofidelity score of 5 according to the ISO TR9790 rating system. The padded test result lies entirely within the corridor and scores a 10.

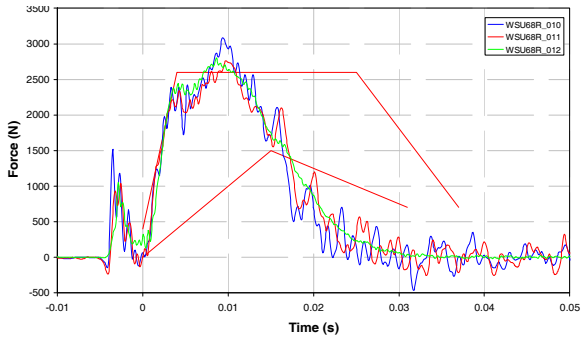

Figure 18. Abdominal forces, WSU, rigid, 6.8 m/s.

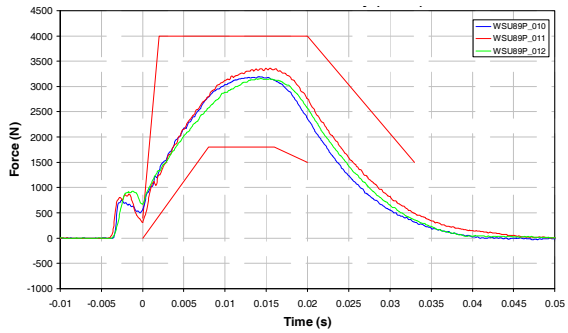

Figure 19. Abdominal forces, WSU, 8.9 m/s, padded

The overall ISO TR9790 Abdomen rating remained the same at a high level of 8.5 based on 2 out of 5 test conditions; see Table 9. The responses were slightly better than the prototype dummy, but it is not reflected in the rating.

<u>Abdomen: NHTSA/Yoganandan Sled Tests</u> - The plots concerning abdomen biofidelity (T12 acceleration and plate forces) are not shown here. However, the biofidelity rating is provided at the end of the result section (Table 15 to Table 17).
The responses for lower spine acceleration and abdomen force are generally close to or within the corridors, which is in good correspondence with the ISO biofidelity rating.
The load wall forces are within the corridors for all configurations showing excellent biofidelity. The biofidelity of the abdomen load wall forces was already very good for the prototype and improved further with the Revision1 dummy.

Table 9.
ISO TR9790 biofidelity score for abdomen tests based on 2 out of 5 test conditions

						Boundary			Ratings				Biofidelity			
Body region	Ui	Impact condition	Vij	Measurement	Wijk	Lower	Upper	Unit	test 1	test 2	test 3	Average	Impact	Test	Test condi	Body region
Abdomen	8	6.8 m/s	3	Abdominal plate force	9	force time corridor			5	5	5	5.0	45			
test 3		WSU				1.5	2.6	kN								
		rigid sled			9								45	**5.0**	15	
test 5		8.9 m/s	7	Abdominal plate force	9	force time corridor			10	10	10	10	90			
		WSU sled				1.8	4	kN								
		23 PSI padded			9								90	**10**	70	
			10												85	**8.5**

Pelvis

The biofidelity of the small female WorldSID pelvis was extensively evaluated based on full body lateral pendulum test and sled tests of WSU, Heidelberg and NHTSA configuration.

Pelvis: Pendulum Tests - The biofidelity of pelvis impact forces has been improved (Figure 20 and Figure 21). It should be noted that these tests were conducted with a 14 kg pendulum and scaled to the required 10.1 kg pendulum mass, by applying mass scaling methods. At 6 m/s the pendulum forces are just within the lower corridor and at 8.3m/s the response moves outside the upper corridor. The 8.3m/s test was conducted using an additional pendulum accelerator with elastic bungee cord. It was not possible to run pendulum tests at higher speeds, due to limitation of the ceiling height of the building. The linear trend indicates that at 10m/s the response would still be within the 5 points boundary. Please keep in mind that the energy in this test, conducted with 14 kg pendulum at 8.3 m/s (482 J), is close to the energy of a 10.1 kg test at 10 m/s (510 J). The 8.3 m/s-14 kg test is considered to be representative for the 10.1 kg-10 m/s condition at the high end of the scale. The repeatability of the pelvis is excellent in pendulum test conditions.

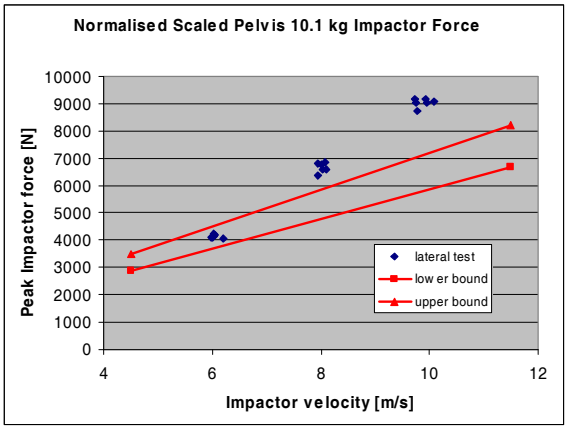

Figure 20. Prototype: Peak scaled* 10.1 kg pendulum pelvis impact force, normalised.

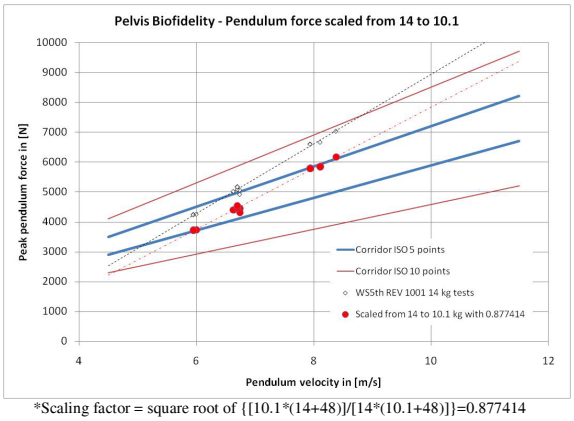

Scaling factor = square root of {[10.1(14+48)]/[14*(10.1+48)]}=0.877414

Figure 21. Revision1: Peak scaled* 10.1 kg pendulum pelvis impact force not normalised

Pelvis: Heidelberg Tests - Three Heidelberg conditions are applicable for the pelvis rigid sled at 6.8 and 8.9 m/s and padded 8.9 m/s sled test. The high speed tests were not conducted with the Revision1 prototype to reduce the risk of damage to the dummy and negative consequences for the completion of the test program. In the biofidelity rating the prototype responses were used for the high velocity tests, as nothing was changed in the pelvis between prototype and Revision1. The Revision1 response in the 6.8 m/s Heidelberg test was significantly stiffer than the prototype dummy (Figure 22 and Figure 23). As there were no changes to the pelvis, this is a little difficult to explain. The mass was increased in the abdomen area, but this is effectively decoupled from the pelvis by a lateral shearing lumbar. The lower legs were made lighter, but could not have influenced the pelvis responses significantly.
The repeatability of the responses from the Heidelberg sled test was very high and showed an improvement compared to the prototype (Figure 8).

Pelvis: WSU Sled Tests - Figure 24 and Figure 25 show the pelvis beam forces from the WSU sled tests. Although the forces leave the upper corridor the biofidelity has improved with respect the prototype dummy, because the peak values are lower compared to the prototype dummy.

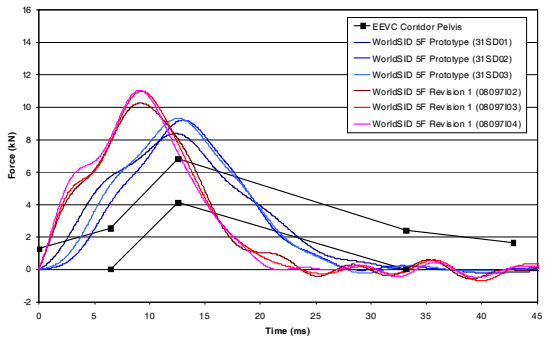

Figure 22. EEVC normalised pelvis plate force, 7.6 m/s rigid wall test condition

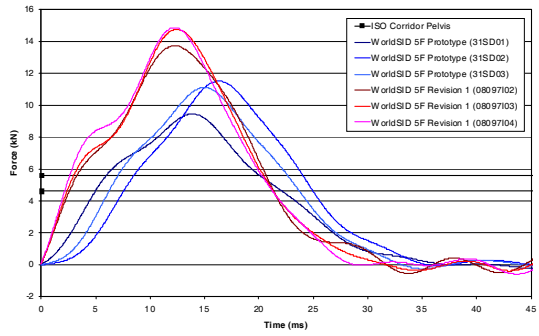

Figure 23. ISO normalised pelvis plate force, 7.6 m/s rigid wall test condition

Table 10.
Heidelberg sled test: Peak pelvis plate force results

		Biofidelity target		Prototype results		Revision1 results	
		Lower limit (kN)	Upper limit (kN)	Peak values (kN)	Coefficient of variation (%)	Peak values (kN)	Coefficient of variation (%)
Pelvis plate force	EEVC normalisation	4.1	6.8	8.4 9.2 9.3	5.6	10.3 11.0 11.0	4.0
	ISO normalisation	4.6	5.6	9.4 11.5 11.1	10.3	13.7 14.8 14.8	4.3

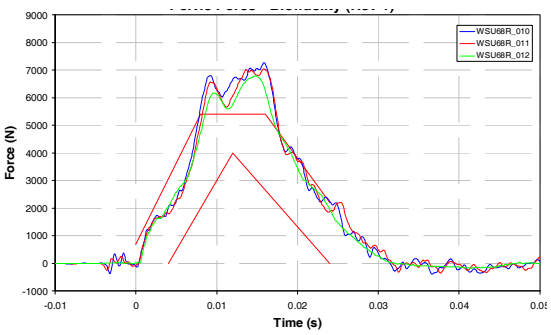

Figure 24. WSU, 6.8 m/s, rigid, ISO normalised pelvis force

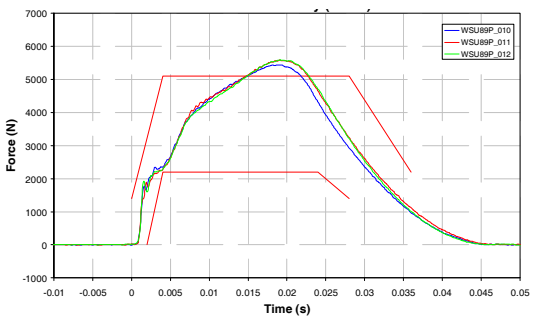

Figure 25. WSU, 8.9 m/s, padded foam, ISO normalised pelvis force

<u>Pelvis Biofidelity Rating</u> - The overall biofidelity pelvis responses according to the rating scheme of ISO TR9790 are summarised in Table 11.

The results of the high speed Heidelberg tests were taken over from the prototype dummy. Generally the response of the pelvis improved, except for the 6.8m/s Heidelberg test. However, in most cases the response changes were not large enough to highly increase (or diminish) the biofidelity rating of the pelvis. Nevertheless the overall pelvis biofidelity rating of the Revision1 dummy has improved with respect to the prototype from 5.6 to 6.5 and now meets the body segment target of 'good' biofidelity (BR $\geq$ 6.5).

The main contributor to the improved rating is the 10 m/s pendulum result. Please keep in mind that the score is not based on an actual test result at 10 m/s, but on the trend obtained from lower velocity tests. Also keep in mind that the energy in this test, conducted with 14 kg pendulum at 8.3 m/s (482 J), is close to the energy of a 10.1 kg test at 10 m/s (510 J). The 8.3 m/s-14 kg test is considered to be representative for the 10.1 kg-10 m/s condition. Indeed the trend of improved biofidelity is also indicated by the other test conditions. Also note that this score is based on a sub set of seven out of thirteen specified test conditions. However, the tests with the highest weighting factors were included in this sub set.

Table 11.
ISO TR9790 biofidelity score for WorldSID 5th female Revision1 pelvis tests

						Boundary			Ratings				Biofidelity			
Body region	Ui	Impact condition	Vij	Measurement	Wijk	Lower	Upper	Unit	test 1	test 2	test 3	Average	Impact	Test	Test condi	Body region
Pelvis	8	4.5 m/s	8	Pendulum force	9	2.9	3.5	kN	10	10	10	10	90			
test 1		10.14 kg impact			9								90	**10**	80	
test 2		11.5 m/s	9	Pendulum force	9	6.7	8.2	kN	5	5	5	5	45			
		10.14 kg impact			9								45	**5**	45	
test 7		6.8 m/s	8	Peak pelvic force	9	4.6	5.6	kN	0	0	0	0	0			
		Heidelberg		Peak pelvic acc.	7	78	95	G	5	5	5	5	35			
		rigid sled			16								35	**2.2**	17.5	
test 8		8.9 m/s	7	Peak pelvic force	8	16.2	19.1	kN	10	10	10	10	80			
		Heidelberg		Peak pelvic acc.	7	118	143	G	5	5	5	5	35			
		rigid sled			15								115	**7.7**	53.7	
test 9		8.9 m/s	8	Peak pelvic force	9	8.4	9.8	kN	10	10	10	10	90			
		Heidelberg		Peak pelvic acc.	8	75	93	G	5	5	5	5	40			
		padded sled			17								130	**7.6**	61.2	
test 10		6.8 m/s	3	Peak pelvic force	9	force time corridor			5	5	5	5	45			
		WSU				4	5.4	kN								
		rigid sled		Peak pelvic Y acc.	7	105	142	G	5	5	5	5	35			
					16								80	**5.0**	15	
test 13		8.9 m/s	7	Peak pelvic force	9	force time corridor			10	10	10	10	90			
		WSU				2.2	5.1	kN								
		23 PSI padded		Peak pelvic Y acc.	7	80	110	G	5	5	5	5	35			
		sled			16								125	**7.8**	54.7	
			50												327	**6.5**

Pelvis: NHTSA/Yoganandan Sled Tests - Because of the large amount of test parameters to consider not all responses are shown in this paper. Pelvis plate forces of the four tested configurations are shown in Figure 26 through Figure 30. All responses are within or close to the corridors showing increased biofidelity for all configurations. Only in the configuration rigid - pelvis offset, the forces leave the upper and lower corridor indicating a slightly worse biofidelity compared to the prototype.

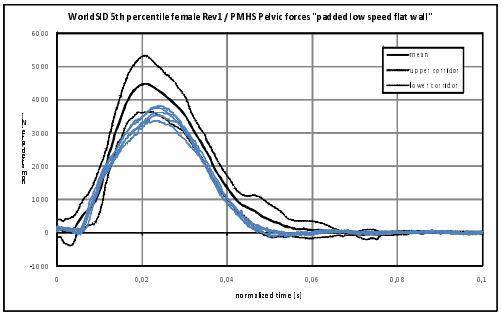

Figure 26. Revison 1, Padded, flat wall, 6.8 m/s, pelvis plate forces.

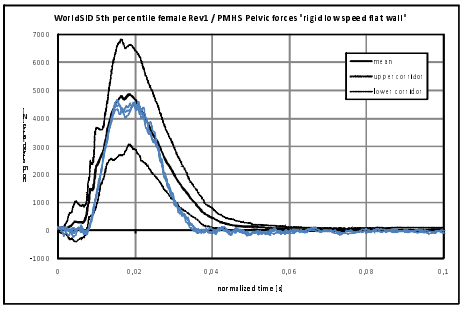

Figure 27. Figure 28: Revison 1, Rigid, flat wall, 6.8 m/s, pelvis plate forces.

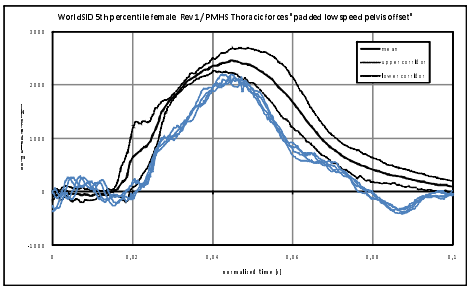

Figure 29. Revison 1, Padded, pelvis offset, 6.8 m/s, pelvis plate forces.

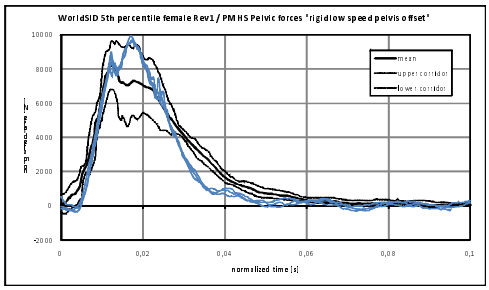

Figure 30. Revison 1, Rigid, pelvis offset, 6.8 m/s, pelvis plate forces.

Overall Biofidelity

ISO Rating - The body segment and full dummy biofidelity rating for the WorldSID 5th female prototype dummy according to the ISO TR9790 requirements (ISO, 1997) is given in Table 13. The

rating scheme used for biofidelity classification according to ISO TR9790 is given in Table 12.
The result is based on a sub-set of high weighted test conditions and is a good indication of the dummy's biofidelity. The overall Biofidelity rating is significantly improved with respect to the prototype dummy. With an overall score of 7.6 the rating of the WorldSID small female revised prototype meets the Biofidelity of her parent, the pre-production version WorldSID 50th percentile male dummy (ISO, 2004). Moreover, there are no longer definitive weak segments, as all body segments meet the target of BR ≥ 6.5.

Table 12.
ISO TR9790 biofidelity classification

Biofidelity Classification	BR (Calculated Biofidelity Rating)
Excellent	8.6 ≤ B < 10
Good	6.5 ≤ B < 8.6
Fair	4.4 ≤ B < 6.5
Marginal	2.6 ≤ B < 4.4
Unacceptable	0.0 ≤ B < 2.6

Table 13.
ISO TR9790 biofidelity rating of WorldSID small female Revision1 and prototype and WorldSID mid size male pre production version

WorldSID Biofidelity rating ISO TR9790			
	Small Female		Mid size male
	Revision1	Prototype	Pre-production
Head	10	10	10
Neck	6.5	4.9	5.6
Shoulder	7.4	5	7.1
Thorax	6.9	5.6	8.3
Abdomen	8.5	8.5	7.8
Pelvis	6.5	5.6	6.1
Overall rating	7.6	6.7	7.6

EEVC Assessment - Thorax and pelvis responses from sled tests were assessed according the EEVC biofidelity corridors (Roberts *et al.*, 1991). For pelvis evaluation also responses from sled tests using a pelvis plate similar to WSU size and shape were applied to the EEVC corridors.

Thorax: The WorldSID 5th female Revision1 prototype dummy shows a good biofidelity and was improved with respect to the prototype. The thorax response was more rigid and better representing the human response; however one out of three of the test results exceeded the EEVC corridor. The high speed test was not repeated with the Revision1 prototype due to the risk at damage.

Pelvis: The Heidelberg pelvis plate responses suggest that the pelvis became stiffer with the Revision1 prototype. However no changes were made to the pelvis. In the low speed sled tests with pelvis plates of WSU shape and size the pelvis response is almost entirely within the corridor, with a little exceedence of the upper corridor. The low-speed test condition is likely to be more representative of modern vehicle door velocity and is therefore the more important requirement to meet.

NHTSA Biofidelity Rating - The results of the sled tests have been analysed and compared to the test corridors of the PMHS tests which have been conducted by the Medical College of Wisconsin (Yoganandan *et al.* 2005).

Table 14.
NHTSA Biofidelity Classification

Perfect:	BR = 0
Excellent:	BR between 0 and 1,0
Good:	BR Between 1 and 2
Moderate	2 < BR <3
Poor:	BR higher than 3

The biofidelity rating method used is the 'Cumulative Variance' by Rhule *et al.* (2002). The green shading in the table indicates that the responses were entirely within the corridor and would score excellent biofidelity; yellow and orange shadings indicate that responses are farther outside the corridor for a longer duration. Larger numbers indicate a larger deviation from the corridors.
The accelerations of lower spine and pelvis were slightly worse in the Revision prototype (Table 15). Especially the biofidelity of T12 acceleration clearly decreased in the offset tests, which should be investigated further. However, most responses were still within moderate classification.

Table 15.
Mean BR values of accelerations

		Prototype	Revision 1
Configuration	Acceleration	Mean BR values	
Padded Flat	Lower Spine (T12)	0,3	0,5
	Sacrum	2,7	3,4
Padded Pelvis Offset	Lower Spine (T12)	2,4	5,2
	Sacrum	2,3	2,8
Rigid Flat	Lower Spine (T12)	1,0	0,8
	Sacrum	3,0	4,1
Rigid Pelvis Offset	Lower Spine (T12)	1,7	3,1
	Sacrum	0,9	1,1

The chest deflections, as already mentioned above, were all improved for all test configurations, when considering the 2D IR-Tracc calculated parameter of resultant rib displacement (Table 16). Applying the parameter calculated lateral displacement for biofidelity calculation, resulted in a similar or slightly worse rating compared to the prototype.

The plate forces from the load wall are an indicator for the external biofidelity of the dummy. The NHTSA sled test results with the prototype already showed an excellent external biofidelity of the small female WorldSID (Table 17). The rating in the Revision1 tests improved even further. Now all forces show an excellent biofidelity except pelvis force in the flat padded and the thorax force in the padded pelvis offset test.

Table 16.
Mean BR values of rib deflections (Revision1 lateral and resultant deflection)

		Prototype	Revision 1	Revision 1
		Mean BR values		
	Deflection	Lateral	Lateral	Resultant
Padded Flat	Upper Chest (Thorax Rib 1)	0,8	1,1	0,6
	Mid Chest (Thorax Rib 3)	3,0	3,8	2,0
	Lower Chest (Abdomen Rib 2)	5,6	4,6	3,6
Padded Pelvis Offset	Upper Chest (Thorax Rib 1)	5,8	5,8	3,0
	Mid Chest (Thorax Rib 3)	5,8	5,4	3,5
	Lower Chest (Abdomen Rib 2)	6,2	6,0	5,5
Rigid Flat	Upper Chest (Thorax Rib 1)	1,6	3,1	1,4
	Mid Chest (Thorax Rib 3)	5,2	5,4	2,6
	Lower Chest (Abdomen Rib 2)	4,2	2,9	1,9
Rigid Pelvis Offset	Upper Chest (Thorax Rib 1)	0,6	0,5	0,3
	Mid Chest (Thorax Rib 3)	9,4	10,1	3,7
	Lower Chest (Abdomen Rib 2)	1,4	1,5	1,5

Table 17.
Mean BR values of load wall plate forces

		Prototype	Revision 1
Configuration	Plate Forces	Mean BR values	
Padded Flat	Thorax	0,4	0,9
	Abdomen	0,7	0,7
	Pelvis	0,5	1,3
Padded Pelvis Offset	Thorax	2,8	3,4
	Abdomen	0,5	0,4
	Pelvis	2,7	0,6
Rigid Flat	Thorax	1,0	0,6
	Abdomen	0,3	0,7
	Pelvis	0,4	0,2
Rigid Pelvis Offset	Thorax	0,6	0,4
	Abdomen	1,6	0,8
	Pelvis	0,5	1,0

Repeatability

Repeatability was already good for the prototype, as reported by Been *et al.* (2007). Generally for the Revision1 test houses indicated improved repeatability. A factor in improved repeatability is advanced experience of test houses in seating of the dummy and running the tests repeatably.
In almost all tests done in the test series with the Revision1 dummies an improvement of repeatability was noted. Now all responses meet the criterion of CV less than 7%. In the pendulum and drop tests CV of the majority of measured responses were even below 3% indicating an excellent repeatability.

CONCLUSIONS AND RECOMMENDATIONS

Two WorldSID small female Revision1 prototype side impact dummies were extensively evaluated and tested to verify compliance of the dummy to its requirements and to see if the changes in the revised prototype brought about the expected improvements.
The anthropometry was improved resulting in a good correspondence of the Revision1 dummy with its requirements of body segment mass distribution.
The overall dummy biofidelity in the ISO rating system has significantly improved from 6.7 to 7.6 on a scale between 0-10. The small female WorldSID has obtained the same biofidelity rating as the WorldSID mid size male dummy. The small female dummy also meets the individual body segments targets of 'good biofidelity'. In this respect the small female dummy outclasses the 50th percentile male dummy, which does not achieve 'good biofidelity' for all body segments. The improved biofidelity was confirmed in the NHTSA/Yoganandan sled test conditions and rating system.
The recommendations regarding durability handling were implemented and showed an improvement in this test series. Also repeatability was improved with respect to the prototype. The repeatability generally exceeds the requirement of CV better than 7% and a CV better than 3% was achieved with pendulum and drop tests, which is considered excellent.
It can be concluded that the recommended updates were all executed and were all successful in achieving the expected outcome. The APROSYS project laid solid foundation for further activities. The WorldSID small female dummy is ready for use and further assessment by research parties and vehicle manufacturers worldwide.

Recommendations

To optimise the head-neck responses to the new targets, some measures are recommended: 1) Reduced head flexion angle by installing stiffer neck buffers in the lateral position; 2) Increase the neck twist response by replacing the rear square neck buffers with a circular ones top and bottom; 3) Assess frontal biofidelity according to Mertz OC angle moment relationship (Mertz and Patrick, 1971) Repeat the head neck tests in the NBDL sled test condition.
It is recommended that a harmonised biofidelity rating system is developed, combining benefits of various systems (EEVC, ISO and NHTSA) that have been developed. Furthermore the effect of not normalizing responses should be examined in detail.
It is recommended to improve damping material bonding, if possible.
The reliability of the IR-Traccs needs to be further improved. A further validation of the dummy oblique thorax response with available human response data is also recommended.

ACKNOWLEDGEMENTS

This work was supported through funding from: the European Commission, UK Department for Transport, the Federal Highway Research Institute (BASt) and Community of Madrid through the SEGVAUTO programme (S-0505/DPI-0329). In-dummy data acquisition system: DTS; donor sensors for 2nd dummy: ACEA. Staff of test laboratories, BASt, FTSS, TRL and UPM-INSIA.

REFERENCES

Been B.W., Meijer R., Bermond F., Bortenschlager K., Hynd D., Martinez L. and Ferichola,G. 2007. "WorldSID small female side impact dummy specifications and prototype evaluation." Proceedings of the 20th Enhanced Safety of Vehicles (ESV) Conference, Lyon, France.

Been B.W., Waagmeester C.W., Trosseille X., Hynd. D., Carroll J. 2009." WorldSID small female two-dimensional chest deflection sensors and sensitivity to oblique impact". ESV 2009. Paper number: 09-0418

Ferichola G., Guerra L.J., Garcia A. 2007. "INSIA-WSU Barrier Scaling To 5th Percentile", APROSYS Technical Report AP SP52 0055.

ISO TC22/SC12/WG 5. 2004. "Road vehicles — Design and performance specifications for the WorldSID 50th percentile male side impact dummy — Part 1: Terminology and rationale.", ISO 15830 International Standard.

ISO.1997. "Road vehicles - anthropomorphic side impact dummy - lateral response requirements to assess the biofidelity of the dummy." ISO TR 9790 ISO/TC22/SC12/WG5 Document N455 Rev4 May 1997

Newland, C. 2005. "International Harmonised Research Activities Side Impact Working Group Status Report.", ESV 2005 IHRA status report on behalf of the IHRA Side Impact Working Group. conference paper 05-0460

Martínez L., Ferichola G., García A., Guerra L.J. 2007. "WorldSID 5th female prototype Anthropometry assessment", APROSYS Technical Report AP SP52 0040-B.

Meijer R., Wisgerhof R., Wismans J., Been B.W. 2009. 'Scaling Head-Neck Response Data And Derivation Of 5th Percentile Female Side Impact Dummy Head & Neck Response Requirements In NBDL Test Condition', International Journal of Crashworthiness, Special Issue Advanced Protection Systems (APROSYS): Part 2.

Mertz H.J. 2004. "Calculation Methods & Acceptance Levels for Assessing Repeatability and Reproducibility (R & R)". ISO/TC22/SC12/WG5 Document N751.

Mertz H.J., Patrick L.M. 1971. „Strength and Response of the Human Neck." Proceedings of the 15th Stapp Car Crash Conference, pp 207-255. Society of Automotive Engineers, New York.

Rhule H., Brunner J., Bolte J., Donnelly B., Maltese M., Eppinger R. 2002. "Development of a New Biofidelity Ranking System for Anthropomorphic Test Devices." Stapp Car Crash Journal, Vol. 46 (November 2002).

Roberts A., Lowne R., Beusenberg M. and Cesari D. 1991. "Test procedures for defining biofidelity targets for lateral impact test dummies." 13th International Conference on Enhanced Safety of Vehicles, Paris, France: US Dept of Transport, National Highway Traffic Safety Administration, 91-S8-W-18, 956-967.

Schneider L.W., Robbins D.H, Pflüg M.A., Snyder R.G. 1983. "Development Of Anthropometrically Based Design Specifications For An Advance Adult Anthropomorphic Dummy Family." Final Report DOT-HS-806-715 NHTSA (UMTRI).

Thomas P., Welsh R., Langerrand E., Vallet G., Otte D., Strandroth J. 2009 "Priorities for Enhanced Side Impact Protection in Regulation 95 Compliant Cars" ESV 2009. Paper number: 09-0156.

Yoganandan N. and Pintar F.A. 2005. "Deflection, Acceleration, and Force Corridors for Small Females in Side Impacts." Traffic Injury Prevention, 6:379–386, 2005.

DYNAMIC RESPONSE OF HEAD UNDER VEHICLE CRASH LOADING

Mariusz Ziejewski, Ph.D.
Ghodrat Karami, Ph.D.
Department of Mechanical Engineering and Applied Mechanics
North Dakota State University
Fargo, ND 8105-5285
William W. Orrison Jr., M.D., M.BA
Eric H. Hanson, M.D., M.P.H.
Advanced Medical Imaging and Genetics Division of Neuroradiology
Touro University College of Osteopathic Medicine
Las Vegas, NV
Paper Number 09-0432

ABSTRACT

In this paper, a three-dimensional (3-D) nonlinear finite element (FE) method is used in association with the Articulated Total Body (ATB) biodynamics method, to study the human brain response under dynamic loading. The FE formulation includes the detailed model of the skull, brain, cerebral-spinal fluid (CSF), dura mater, pia mater, falx and tentorium membranes. The brain is modeled as viscoelastic material, whereas, a linear elastic material model is assumed for all other tissue components. Proper contact and compatibility conditions between different components are assumed. Instead of direct contact, inertial load resulting from the acceleration and deceleration of the head mass system is implemented. The ATB biodynamic package is used to simulate real vehicle impact scenarios, and to extract the six translation and rotation acceleration data at the center of the mass of the head component. These six-degrees of freedom (6-DOF) kinematic descriptions are used to represent the inflicted inertial loadings. The magnetic resonance imaging (MRI) outcomes, from two incidents with head impact, are compared with the biomechanical FE simulations to present the model capabilities. To examine and verify the material parameters used in FE formulations, experiments are conducted on a simulated brain material made from silicon dielectric gel. The results support that the combination of the FE deformation analysis and the ATB rigid body model is an effective method in head impact analysis and traumatic brain injury (TBI) identification.

Keywords: head impact, traumatic brain injury (TBI), Articulate Total Body (ATB) Model, dynamic analysis, three-dimensional (3-D) finite element (FE) model

INTRODUCTION

Every year vehicle crashes cause over a million fatalities and a hundred million injuries worldwide [1]. In the United States (U.S.), traffic accidents have been the leading cause of death for the age groups of 1 to 34, in recent years [2]. In European countries, 45,000 fatalities and 1.5 millions injuries were reported in 1995 [3]. The societal and economic annual cost of traffic accidents is estimated to be $200 million in the U.S. [4], and over $160 million in European countries [5].

Due to the devastating consequences of traumatic brain injury (TBI), crash analysis and head injury biomechanics are important fields in biomedical research. The head is routinely identified as the body part most frequently involved in life-threatening injuries in vehicular collisions [6]. In theU.S., approximately 2 million cases of TBI are recorded each year [7]. About one third of the hospitalized victims suffer from permanent disability [8]. Most of these victims undergo injury associated physical and psychological distress with a resulting high societal burden and cost. Although many injury protection devices, such as safety belts, airbags and helmets, have been developed and improved, traffic accidents are still responsible for most TBI cases [9]. Crash analysis of head injury biomechanics focuses on head impact and injury mechanisms that are very important in the development of effective TBI prevention and minimization strategies.

In an attempt to better understand head injury mechanisms, both clinical and laboratory studies have been conducted for decades. Mathematical models have been acknowledged as increasingly valuable tools in crash analysis. Sophisticated three-dimensional (3-D) finite element analysis (FEA) and rigid body biodynamic methods can be used to study impact injury events and the associated biomechanical response of the human head. The rigid

body model is used to determine the gross dynamics and movements of a subject's head with the results introduced in finite elements (FEs) to determine local brain deformation. Complex geometry and constitutive models of multiple materials can also be employed under dynamic loading conditions. Combining these methods of analysis is time saving and improves effectiveness of the analysis [10].

The Articulated Total Body (ATB) Model, employed here for dynamic analysis of the body, is a validated 3-D rigid-body biodynamic model. This method has been successfully used by the Air Force Research Laboratory (AFRL) and other organizations for crash simulation and the prediction of gross human body response in crash dynamic environments. The ATB Model is quite general in nature and can be used to simulate the dynamic response of a wide range of physical problems approximated as a system of connected, or free, bodies and is not limited to crash dummy, or human, applications [11].

A 3-D FE brain dynamic analysis under impact is also employed in this paper. In a previous publication [12] the researchers reported the suitability of material modeling under frontal head impact scenarios. In this paper, the combination of FE and the articulated rigid body (ARB) dynamics is used to simulate and examine brain behavior under direct impact to the occipital portion of the head.

FE MODELING

The geometrical data for the development of the FEs of the human head, modeled here, represents a modification of existing geometric data obtained, and previously published, by Horgan [13]. A 3-D simulation, with multiple material model and load conditions, is then created. Altair Hyperwork 7.0 (Altair Engineering, Troy, Michigan) was used for FE pre-processing modeling and data post-processing.

The ATB modeling facilities are used to perform biodynamic simulation and to extract the head kinematic data under vehicle impact. These combined six degrees of freedom (6-DOF) acceleration data are used in the FE model for head response simulation. The 3-D FE model takes into account the detailed structure of the human head anatomy including the brain, falx and tentorium, cerebral spinal fluid (CSF), dura mater, pia mater, skull and scalp. The brain, CSF and skull are modeled as first-order eight nodded brick elements. The falx, tentorium, dura, pia and scalp are modeled as four-nodded membrane, or shell elements, with uniform thickness. Figures 1 and 2 show the 3-D FE model of these components.

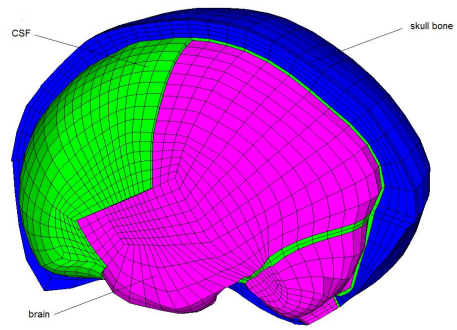

Figure 1. The right half model of brain CSF and skull bone.

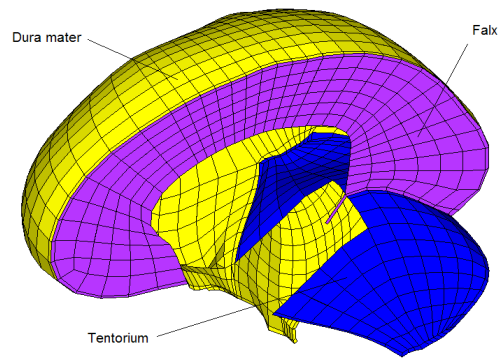

Figure 2. The right half model of dura mater, falx and tentorium.

The general-purpose 3-D nonlinear FE code LS-DYNA is used as the solver. The main solution methodology is based on explicit time integration using the central difference method differentiating scheme. The explicit method is computationally efficient due to the small time steps in this problem to assure the convergence and stability of the solutions. The entire duration of the crash analysis is typically 10-200 ms and small time steps are required, therefore, and are suitable for a converged and accurate solution procedure [14].

Using a Lagrangian formulation [15], the time-dependent finite deformation of continuum material can be expressed in terms of convected coordinates X_j, and time t:

$$x_i = \phi_i(X_j, t) \quad (1.)$$

where ϕ_i is the mapping function between the reference configuration and the current configuration.

The equation of motion (balance of momentum) describing continuum deformation states that:

$$\frac{\partial P_{ji}}{\partial X_j} + \rho_0 b_i = \rho_0 \ddot{u}_i \quad (2.)$$

where P_{ij} is the nominal stress, b_i is the body force density, ρ_0 is the density in the reference configuration, u_i is the displacement of a material point and $\ddot{u}_i$ is the acceleration. By integrating the equation of motion over the reference configuration, we have:

$$\int_{\Omega_0} \delta u_i \left(\frac{\partial P_{ji}}{\partial X_j} + \rho_0 b_i - \rho_0 \ddot{u}_i \right) d\Omega_0 = 0 \quad (3.)$$

Applying the derivative product formula, and the divergence theorem:

$$\underbrace{\int_{\Omega_0} \left(\delta u_i \rho_0 \ddot{u}_i \right) d\Omega_0}_{\delta w^{kin}} + \underbrace{\int_{\Omega_0} \left(\delta (\frac{\partial u_i}{\partial X_j}) P_{ji} \right) d\Omega_0}_{\delta w^{int}} - \underbrace{\int \delta u_i \rho_0 b_i d\Omega_0 - \sum_{i=1}^{n_{SD}} \int_{\Gamma_{t_i}^0} \delta u_i \bar{t}_i^0 d\Gamma_0}_{\delta w^{ext}} = 0$$

(4.)

where δw^{int} δw^{ext} and δw^{kin} are, respectively, virtual internal work, virtual external work and virtual inertial work. The surface tractions are denoted by $\bar{t}_i^0$ denotes the surface tractions and SD is the number of space dimensions. By discretizing the domain into a Lagrangian mesh of FEs, where the geometry and field variables are described in terms of shape functions $N_I(X)$, the stationary form of the equations is finally written in the simple form of the balances of inertia forces (mass matrix times acceleration) , internal and external forces as:

$$M_{ijIJ} \ddot{u}_{jJ} + f_{iI}^{\text{int}} - f_{iI}^{ext} = 0, \quad \text{with}$$

$$M_{ijIJ} = \delta_{ij} \int_{\Omega_0} \rho_0 N_I N_J d\Omega_0, \quad f_{iI}^{\text{int}} = \int_{\Omega_0} \frac{\partial N_I}{\partial X_j} P_{ji} d\Omega_0 \quad \text{and} \quad f_{iI}^{ext} = \int_{\Omega_0} N_I \rho_0 b_i d\Omega_0 + \int_{\Gamma_{t_i}^0} N_I \bar{t}_i^0 d\Gamma_0$$

(5.)

where the upper-case indices stand for the node number and the lower-case indices stand for the directions number. The time rate equations part of the equation (5) can be solved using the central difference explicit time integration method. For this purpose, the time domain is divided into a sequence of time steps and the solution is sought with the marching in time.

MATERIAL CONSTITUTIVE MODEL

The FE analysis of head impact biomechanics is usually based on small deformations of elastic, or viscoelastic, material. The assumptions of linearity, homogeneity and isotropy are used for the head tissues in this work (see Table 1). The linear elastic material model is used for the skull, scalp, dura mater, pia mater, falx and tentorial membranes. A linear elastic model is also used for the CSF. Low shear modulus and high bulk modulus were used to simulate incompressibility. Fluid option is used for the CSF linear solid elements, in which the deviatoric stress is eliminated for fluid like behavior.

Table 1.
Tissue structure and finite element model

Tissue	Anatomical structure 50th perc. male	Constitutive model	Finite element model	# of Elements
Scalp	5-7mm thick	Linear elastic	6 mm thick shell element	2064
Skull	195mm length, 155mm breadth 225 mm height 4-7 mm thick	Linear elastic	Solid element	8256
Dura, falx, tentorium	1 mm thick	Linear elastic	1 mm thick membrane element	2622
Pia	1 mm thick	Linear elastic	1 mm thick membrane element	2786
CSF		Low shear modulus, high bulk modulus incompressible	1.3 mm thick solid element	2874
Brain	165 mm length 140mm transverse diameter	Homogeneous linear viscoelastic material	Solid element	7318

A linear viscoelastic material model is used for the brain tissue. The shear relaxation behavior is described by the Maxwell model as:

$$G(t) = G_\infty + (G_0 - G_\infty)e^{-\beta t} \quad (6.)$$

where G_0 is the short term shear modulus, G_∞ is the long term shear modulus, and β is the decay factor. Table 2 shows the material properties used in the FE model.

Brain Substitute Material

Since it is not feasible to use actual brain tissue in collision simulation, it is necessary to find a suitable modeling material. The material should be viscoelastic and have a complex modulus similar to brain tissue when subjected to shear strain.

Studies from different species (human, porcine, bovine) and from different parts of the brain (white matter, cerebrum, brainstem) have consistently demonstrated that the viscoelastic properties of brain tissue fall into a predictable range [16-26]. Silicone dielectric gel (specifically Dow Corning Sylgard 527 A&B) has been demonstrated to have viscoelastic properties approaching those of actual brain tissue and has gained widespread acceptance as a physical substitute for brain tissue [16, 25-28]. It is worth noting, however, that the gel exhibits a lesser degree of dynamic deformation because the phase angel of the gel material increases at a greater rate with respect to frequency than does brain tissue at frequencies above 1 Hz. This means that the gel exhibits greater viscous damping than brain tissue at finite strains. In other words, the gel material provides an accurate estimate of the response of brain tissue to oscillatory shear strains below 1 Hz in frequency and a conservative estimate above 1 Hz. The gel is, therefore, an excellent alternative for benchmarking studies [16, 25].

The suitability of silicone dielectric gel is confirmed through the independent testing in this research using the accepted technique of measuring the complex modulus of brain tissue by applying an oscillating shear strain and measuring the resulting strain and the phase shift between input stress and output strain. Testing is conducted using an Advanced Rheometric Expansion System (ARES) Rheometer (LS714306), from TA Instruments, in the University of Minnesota's Rheological Measuring Laboratory (serial no. 199815770). Figure 3 shows the results of this testing, along with results published by Brands, et al. [16], which includes their tests of the same gel material, the results of their testing with several samples of porcine brain tissue and other findings in the literature, which include several human brain tissue samples.

Table 2.
The head tissue material parameters used in the finite element model

Tissue	**Young's mod.** (GPa)	**Density** (kg/mm^3)	**Poisson's ratio**
Skull	8	1.21×10^{-6}	0.22
Dura mater	0.0315	1.13×10^{-6}	0.45
Dura tentorium	0.0315	1.13×10^{-6}	0.45
Dura falx	0.0315	1.13×10^{-6}	0.45
Pia mater	0.0115	1.13×10^{-6}	0.45
Scalp	0.0167	1.0×10^{-6}	0.42

Tissue	**Young's mod.** (GPa)	**Bulk mod.** (GPa)	**Shear mod.** (GPa)	**Density** (kg/mm^3)	**Poisson's ratio**	**Static shear mod.** (GPa)	**Dynamic shear mod.** (GPa)	**Decay const.** (ms^{-1})
Brain	667×10^{-6}	2.19		1.04×10^{-6}	0.49999635	5.28×10^{-5}	1.68×10^{-5}	0.4
CSF	667×10^{-6}	2.19	5.0×10^{-7}	1.004×10^{-6}				

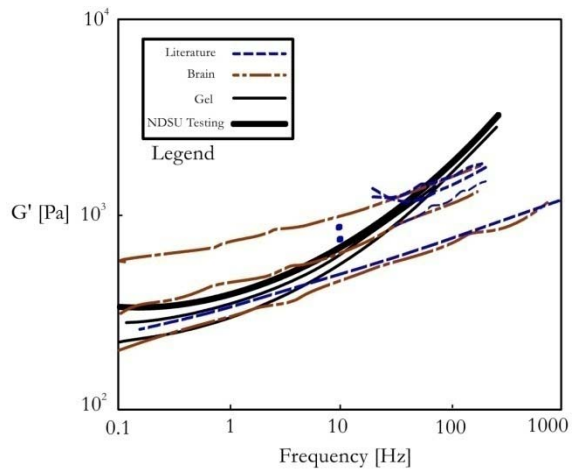

Figure 3. Our (NDSU) independent testing of storage modulus of silicone dielectric gel over a range of frequencies in addition to results for gel and several samples of brain tissue originally reported in Brands et al. [16]. Literature data includes porcine cerebrum [18, 20], porcine brainstem [21], calf cerebrum [19], human cerebrum [22], and human white matter [23].

BOUNDARY CONDITIONS

The free-boundary condition is defined as the junction of the neck and the head in the model. This means that there is no constraint effect at the head-neck joint, since for short duration impacts, such as 6 ms in Nahum's frontal impact [29], the neck does not influence the dynamic response of the head. Further, in inertial loading analysis, the 6-DOF kinematic description is sufficient and no extra boundary conditions are required.

According to the anatomical structure and physiology of the human head, the interfaces between the scalp and skull, the skull and dura, as well as the brain and pia, are modeled as a tied surface-to-surface contact definition. The interface between the dura, tentorium and falx is defined as a tied node-to-surface contact model as these components physically adhere to each other. A tied contact algorithm is preferred for the brain-membrane interfaces because it transfers loads in both compression and tension; only loads in compression, however, are transferred in a penalty contact algorithm, so a gap will be created in the contrecoup region where tensile loading is possible in frontal impact. [30]

Due to the presence of CSF, and the fact that the relative motion between the skull and brain during impact has been observed [30], the interfaces between the dura, pia, falx, tentorium and CSF are modeled as an automatic surface-to-surface sliding contact with a friction coefficient of 0.2, as previously reported [31]. This contact definition is also appropriate for the simulation of CSF fluid behavior by linear solid element methods.

HEAD RESPONSE ANALYSIS UNDER VEHICLE CRASH LOADINGS

Head impact against padded, or rigid, surfaces is a common and important source of loading to the human brain. In the modeling presented here, an ATB biodynamic package is used to reconstruct impact scenarios of a real vehicle. Six translation and rotation acceleration data are extracted at the center of gravity (CG) of the head. Since the combined acceleration data reflects the head kinematics, restraint system interaction and head/neck reaction forces during the impact events, these DOF kinematic descriptions can be used to replicate the angular and translational acceleration momentum and resulting inertial loads experienced by the head tissue system in the dynamic conditions of a vehicle crash [32]. The head kinematic data from the ATB is then applied to the FE model to replicate the head biodynamic response in car crash cases. Finally, the mechanical response outputs are compared with the magnetic resonance imaging (MRI) observations of brain tissue injury to validate the simulation methodology.

ATB Simulation

The ATB computer program is a 3-D, rigid-body dynamic crash simulator developed jointly by the National Highway Traffic Safety Administration (NHTSA) and Armstrong Aerospace Medical Research Laboratory at Wright-Patterson Air Force Base (AMRL/WPAFB) to predict human body dynamics during events such as automobile collisions, pilots' ejections and other hazardous events [33]. The Generator of Body Data (GEBOD) preprocessing program is used to generate the necessary input parameters for ATB, including geometric and mass properties of various body segments and locations and range of motion characteristics of joints [34]. This system can be used to predict both human and manikin body motion, as well as to provide injury assessment. ATB is used here to simulate the actual incidents and to determine the motion of the head for further FE simulation in cases for which MRI data is also available.

Case I: This case represents a rear end collision simulation. A tested impact scenario is based on a simulated human male subject weighing 79.3 kg (175

lbs) with a height of 1.8 meters (71 inches). The subject is positioned with a head separation of 7.5 cm (3 in) and a head rotation of 30º to the left at the time of impact, striking the headrest with a head angulation of 70º yaw, 0º pitch and 0º roll.

The impact scenario consists of a rearward acceleration resulting in a change in velocity of approximately 12.9 km/h (8mph). The translational and rotational accelerations, in three directions, are shown in Figures 3 and 4.

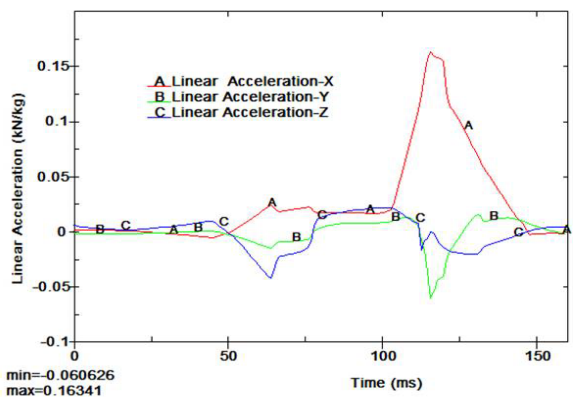

Figure 4. Translation accelerations in inertial coordinate

Case II: The second analysis is performed for a direct head impact in the occipital area. In this case, a female who was 1.5 meters (61 inches) tall and weighing between 54-59 kg, (120-130 lbs), loses her balance and strikes a rigidly attached wooden structure with the back of her head. At the time of impact, her head velocity is approximately 6.5 meters per second (4 mph). The translational and rotational accelerations, in three directions, are shown in Figures 5 and 6.

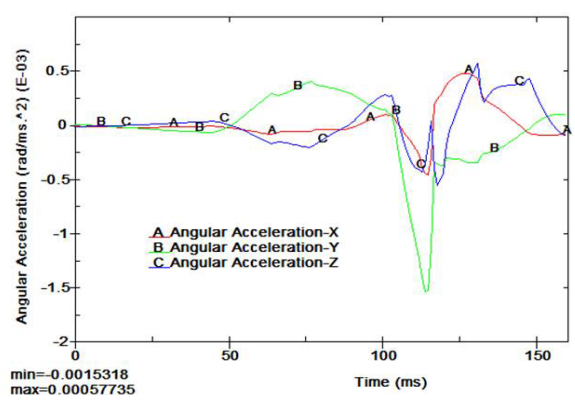

Figure 5. Rotational accelerations in inertial coordinate

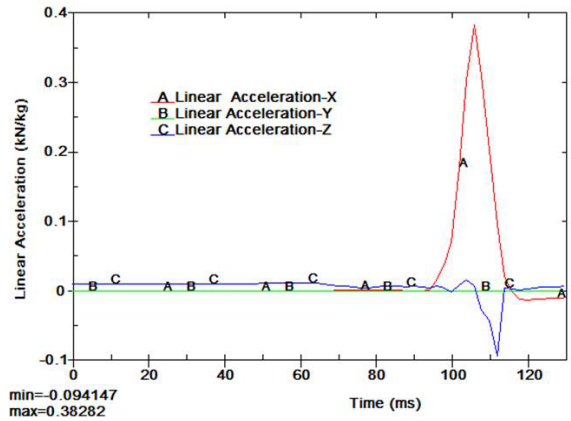

Figure 6. Translation accelerations in inertial coordinate

FEA of Inertial Loading Response

The FE head model and material model are used to analyze the inertial loading response of brain under these two scenarios. The translational accelerations from ATB simulation are applied at the center of mass of the head model, which is rigidly connected to the skull to introduce the loading to the entire system. The skull solid elements are defined as solid body to apply the rotational accelerations. Because head soft tissue injuries are known to occur without large deformations of the skull, the rigid skull assumption is reasonable for the analysis of soft tissue response under dynamic loading [32].

The Mechanical Response and Soft Tissue Injury

Brain soft tissue injuries result from the combination of many biomechanical factors such as the material nature of brain tissue, anatomic structure of head and brain tissue, kinematics and other constraints. Basically, the brain deforms when exposed to rapid momentum change due to direct impact forces, or non-contact forces, transferred through the neck as a result of the velocity differences between the head and human body.

Brain tissue is resistant to the dilatational deformation and hydrostatic stress due to the high bulk modulus. Due to the low shear modulus, however, the internal anatomical structure of the head-brain complex and the angular kinematic loading under impact conditions, brain tissue injury, such as, diffuse axonal injury (DAI), may be developed from shear deformation and shear stress [32].

Figure 7 compares the FE solutions for maximum shear stress distribution with the MRI observations of

brain tissue injury for case I at 114 ms, the peak time of the impact for the case. In Figures 8 and 9, the FE solutions for the variation of maximum shear stress and maximum shear strain in the brain, from 114 ms to 116 ms, are shown.

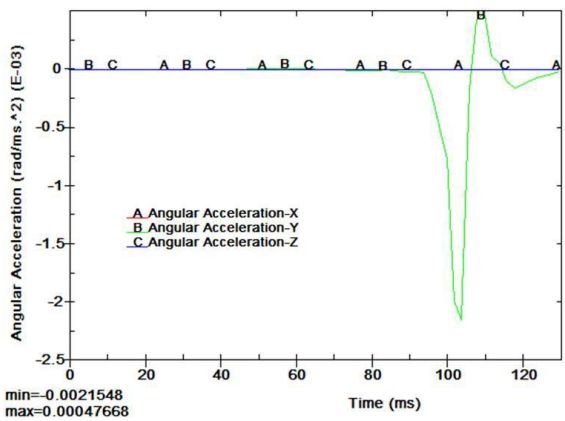

Figure 7. Rotational accelerations in inertial coordinate

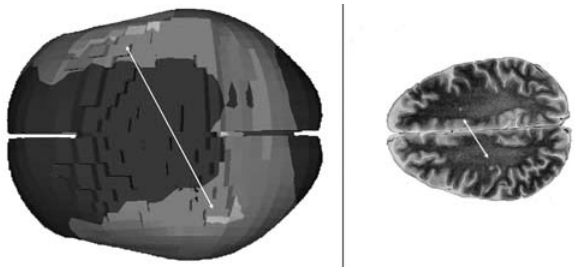

Figure 8. Case I brain shear injury MPI and maximum shear stress at 114ms (top-horizontal view)

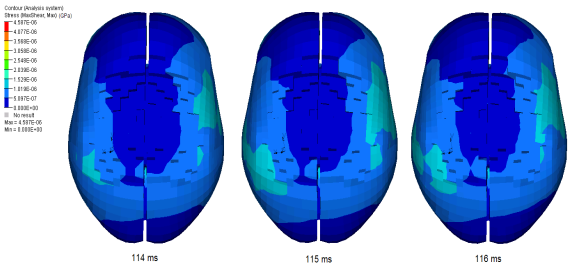

Figure 9. Case I brain maximum shear stress (top-horizontal view)

The MRI data for the cases are from patients referred for clinical evaluation and were obtained following informed consent under IRB approval. The red arrows in the Figures indicate the sites of maximum shear stress and observed shear injury of brain tissue. In Figures 10- 12, the maximum shear stress distribution is compared with the MRI brain tissue injury for case II at the peak impact time of 105ms from different view directions. In Figures 13, 14 and 15, a maximum shear stress variation of the brain from 104 *ms* to 106ms is shown from different view directions for this case.

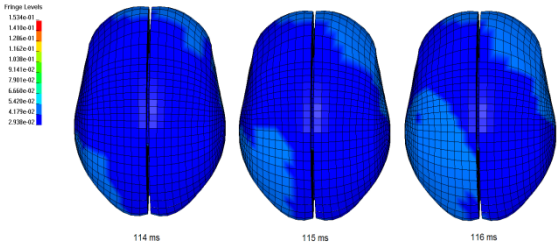

Figure 10. Case I brain maximum shear strain (top horizontal view)

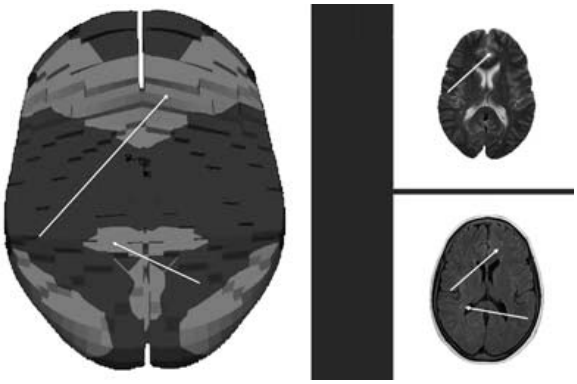

Figure 11. Case II brain shear injury MPI and maximum shear stress at 105ms (top-horizontal view)

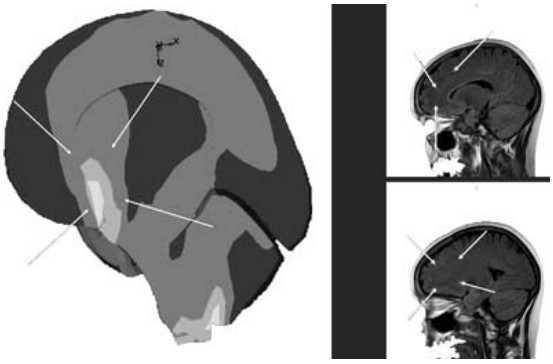

Figure 12. Case II brain shear injury MPI and maximum shear stress at 105ms (mid-sagittal view)

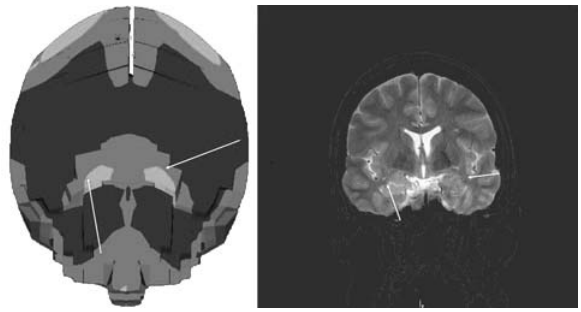

Figure 13. Case II brain shear injury MPI and maximum shear stress at 105 ms (coronal view)

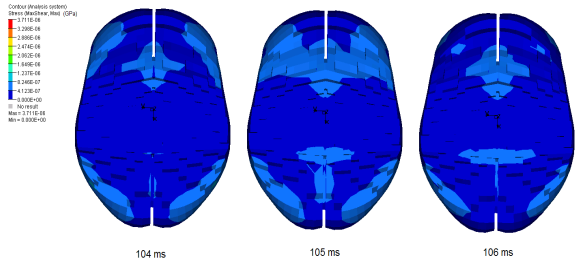

Figure 14. Case II brain maximum shear stress (top-horizontal view)

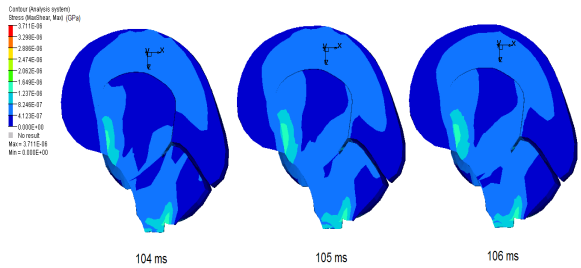

Figure 15. Case II brain maximum shear stress (mid-sagittal view)

Discussion

A good correlation between the internal injury sites and high shear stress regions is demonstrated. The FE head model accurately identifies and predicts locations of internal brain injury associated with blunt trauma as validated here. The maximum angular acceleration experienced by the head is 1532 rad/s^2 in case I, and 2155 rad/s^2 in case II.

These accelerations are in the range of the published values known to cause TBI in the human brain [35-36]. The type, magnitude, duration and direction of acceleration loads all play important roles in brain injury mechanisms.

CONCLUSIONS

The combination of FE deformation analysis and an ATB rigid body model is an effective method in head impact analysis and TBI identification. More real accident simulations can be done to test the accuracy and the validity range of the head model. Parametric analysis of crash simulations can be done to study the brain injury mechanism.

Acknowledgement: The authors appreciate the support from the Fargo-Moorhead Area Foundation in the completion of this work.

REFERENCES

1. Davy W.A. Brands, "Predicting Brain Mechanics during Closed Head Impact: Numerical and Constitutive Aspects", Technische Universiteit Eindhoven, Eindhoven, 2002.

2. WISQARS (2001): "Leading Causes of Death Report, 1998", in Web-based Injury Statistics Query and Reporting System (WISQARS), *Centers for Disease Control and Prevention*, Word Wide Web Page: http://webapp.cdc.gov/sasweb/ncipc/leadcaus.html.

3. *European Transport Safety Council* (1997): A strategic Road Safety Plan for the European Union, Brussels, Belgium.

4. Blincoe LJ, Seay AG, Zaloshnja E, et al. "The Economic Impact of Motor Vehicle Crashes", 2000. Washington, DC: *National Highway Traffic Safety Administration*; May 2002. Report DOT HS 809 446.

5. *European Transport Safety Council* (1999): Exposure Data for Travel Risk Assessment.

6. *European Transport Safety Council* (1993): Report in Motorcycle Safety, European Experimental Vehicles Committee Ad-Hoc Group.

7. Kraus, J.F., McArthur, D.L., "Epidemiologic Aspects of Brain Injury", *Neurol. Clin.*, 14, pp. 435-450, 1996.

8. Brooks, C.A., Gabella B, Hoffman R, Sosin D, and G. Whiteneck (1997): "Traumatic brain injury: designing and implementing a

population-based follow-up system", *Arch Phys Med Rehabil*, 78(8): S26-S3.

9. Davy W.A. Brands, "Predicting Brain Mechanics during Closed Head Impact: Numerical and Constitutive Aspects", Technische Universiteit Eindhoven, Eindhoven, 2002.

10. M. Ziejewski, Jie Song, "Assessment of Brain Injury Potential in the Development of Children's Helmets using Rigid Body Dynamics and Finite Element Analysis", Department of Mechanical Engineering, North Dakota State University.

11. Huaining Cheng, Annette L. Rizer, Articulated Total Body Model Version V User's Manual, *United States Air Force Research Laboratory*, February 1998.

12. Li, D., Ziejewski M., Karami G., Brain Material Properties and Analysis of Head Impact *J. of Biomechanics*, 2005 (submitted)

13. T.J.Horgan, M.D. Gilchrist, "The Creation of Three-dimensional Finite Element Models for Simulating Head Impact Biomechanics", *International Journal of Crashworthiness*, Vol. 8, No. 4, pp 353-366, 2003.

14. Jesse S. Ruan, Chun Zhou, Tawfik B. Khalil and Albert I. King, "Techniques and Applications of Finite Element Analysis of the Biomechanical Response of the Human Head to Impact", *CRC Press LLC*, 2001.

15. "LS-DYNA Theoretical Manual", *Livermore software Technology Corporation*, May 1998.

16. Brands, D.W.A., Bovendeerd, P.H.M., Peters, G.W.M., Wismans, J.S.H.M., Paas, M.H.J.W., and J.L.M.J. van Bree (1999): "Comparison of the dynamic behavior of brain tissue and two model materials", *Stapp Car Crash Conference Proceedings*, SAE paper 99SC21, pp. 313-320.

17. Arbogast, K.B. and S.S. Margulies (1998): "Material characterization of the brainstem from oscillatory shear tests", *Journal of Biomechanics*, vol. 31, pp. 801-807.

18. Thibault, K.L. and S.S. Margulies (1998): "Age-dependent material properties of the porcine cerebrum: effect on pediatric inertial head injury criteria", *Journal of Biomechanics*, vol. 31, pp. 1119-1126.

19. Peters, G.W.M., Meulman, J.H., and A.A.H.J. Sauren (1997): "The applicability of the Time/Temperature Superposition Principle to brain tissue", *Biorheology*, vol. 34 (2), pp. 127-138.

20. Thibault, K.L. and S.S. Margulies (1996): "Material properties of the developing porcine brain", *Proceedings of the International IRCOBI Conference on Biomechanics of Impact*, Dublin, pp. 75-85.

21. Arbogast, KB. and S.S. Margulies (1997): "Regional differences in mechanical properties of the porcine central nervous system", *Stapp Car Crash Conference Proceedings*, SAE paper 973336, pp. 293-300.

22. McElhaney, J.H., Melvin, J.W., Roberts, V.L., and H.D. Portnoy (1972): "Dynamic characteristics of the tissues of the head", *Symposium Perspectives in Biomedical Engineering*, pp. 1-8.

23. Fallenstein, G.T., Hulce, V.D., and J.W. Melvin (1969): "Dynamic mechanical properties of human brain tissue", *Journal of Biomecahnics*, vol. 2, pp. 217-226.

24. Bilston, L.E., Liu, Z. and N. Phan-Thien (1997): "Linear viscoelastic properties of bovine brain tissue in shear", *Biorheology*, vol. 34 (6), pp. 377-385.

25. Brands, D.W.A., Bovendeerd, P.H.M., Peters, G.W.M., and J.S.H.M. Wismans (2000): "The large shear strain dynamic behavior of in-vitro porcine brain tissue and a silicone gel model material", *The Stapp Journal*, vol. 44, pp. 249-260.

26. Viano, D., Aldman, B., Pape, K., van Hoof, J., and H. von Holst (1997): "Brain kinematics in physical model tests with translational and rotational acceleration", *International Journal of Crashworthiness*, vol. 2 (2), pp. 191-205.

27. Ivarsson, J., Viano, D.C., Lövsund, P., and B. Aldman (2000): "Strain relief from the cerebral ventricles during head impact: experimental studies on natural protection of the brain", *Journal of Biomechanics*, vol. 33. pp. 181-189.

28. Meaney, D.F., Ross, D.T., Winkelstein, B.A., Brasko, J., Goldstein, D., Bilston, L.B., Thibault, L.E., and T.A. Gennarelli (1994): "Modification of the cortical impact model to produce axonal injury in the rat cerebral cortex", *Journal of Neurotrauma*, vol. 11 (5), pp. 599-612.

29. Remy Willinger, Ho-Sung Kang, and Baye Diaw, "Three-Dimensional Human Head Finite Element Model Validation against Two Experimental Impacts", *Annals of Biomedical Engineering*, Vol. 27, pp. 403-410, 1999.

30. Svein Kleiven, Hans von Holst, "Review and Evaluation of Head Injury Criteria", *Proc. RTO Specialist Meeting*, the NATO's Research and Technology Organization (RTO), Koblenz, Germany, 19-23 May 2003.

31. Miller, R.T., Margulies, S.S., Leoni, M., et al., "Finite Element Modeling Approaches for Predicting Injury in an Experimental Model of Severe Diffuse Axonal Injury", Proc. 42nd Stapp Car Crash Conf., SAE paper, No. 983154, SAE, pp. 155-166, 1998.

32. Frank, P. DiMasi, Rolf H. Eppinger, and Faris A. Bandak, "Computational Analysis of Head Impact Response under Car Crash Loadings", *SAE paper*, No. 952718, Society of Automotive Engineers, pp. 425-438, 1995.

33. Cheng, H., Obergefell, L. Rizer, A., 1994. Generator of body data (GEBOD) manual. Armstrong Laboratory Report N0. AL/CF-TR-1994-0051.

34. Cheng, H., Rizer, L., Obergefell, L., 1998. Articulated total body model volume V user's manual. Air Force Research Laboratory Report No. AFRL-HE-WP-TR-1998-0015.

35. Pellman E., D. Viana, A. Tucker, et al., "Concussion in Professional Football: Reconstruction of Game Impacts and Injuries" *Neurosurgery* Vol. 53, No. 4, October 2003.

36. Omaya AK, "Biomechanics of Head Injury: Experimental Aspects" *The Biomechanics of Trauma*, Chapter 13, 1985

Development of Response Corridors for the Compressive Stiffness of the Male and Female Arm in Lateral Loading

Andrew Kemper and Stefan Duma
Virginia Tech – Wake Forest, Center for Injury Biomechanics
United States of America
Paper Number 09-0506

ABSTRACT

The biofidelity of side impact ATDs is crucial in order to accurately predict injury of human occupants. Although the arm serves as a load path to the thorax, there are currently no biofidelity response requirements for the isolated arm. The purpose of the study was to characterize the compressive stiffness of male and female upper arms in lateral loading and to develop corresponding biofidelity stiffness corridors. This was accomplished by performing a series of pendulum tests on sixteen isolated upper arms, obtained from four male and four female cadavers, at impact velocities of approximately 2 m/s and 4 m/s. The upper arms were oriented vertically with the medial side placed against a rigid wall in order to simulate loading during a side impact automotive collision. The force versus deflection response data was normalized to that of a 50th percentile male or a 5th percentile female and then response corridors were developed. For both impact rates the cadaver arms exhibited a considerable amount of deflection under very low force, i.e. toe region, before the any substantial increase in force. The deflection at which the force began to increase substantially was found to be similar to the average difference in thickness between the initial and compressed volunteer arm thickness measurements for both the 5th percentile female and 50th percentile male. Although the response of the SID-IIs arm was similar in shape to that of the female cadaver arms for both impact rates, the SID-IIs arm did not exhibit a considerable toe region and therefore did not fall within the response corridors for the 5th percentile. The results of the current study could lead to an improvement in the overall biofidelity of side impact ATDs by providing valuable data necessary to validate the compressive response of ATD arm independent of the global response.

INTRODUCTION

Approximately 8,000 automobile occupants are killed and 24,000 seriously injured each year in automotive side impact collisions [2]. For all types of side impact collisions the second leading source of fatality, next to head injuries, is chest injuries (29%) [2]. The development of anthropometric test dummies (ATDs) specifically designed for side impact testing has helped automotive safety engineers evaluate and improve new and evolving occupant protection technologies. One such dummy is the SID-IIs, which represents the 5th percentile human female. Accurate biofidelity for side impact ATDs, such as the SID-IIs, is crucial in order to accurately predict injury of human occupants. A recent area of concern is the biofidelity of the arm of side impact ATDs. There have been several studies that have investigated the tolerance of the upper extremity in three-point bending and side airbag deployments [1, 2, 3, 4, 5, 6, 8]. However, the characterization of the compressive stiffness of the arm has been limited [9, 10]. Given that the arm serves as a load path to the thorax, the response characteristics of the upper extremity can influence the thoracic response in side impact test dummies. Although there are biofidelity evaluations for the global response of the side impact ATD arm and thorax combined, there are currently no biofidelity evaluations with respect to the compressive characteristics of the isolated arm. Therefore, the purpose of the study was to characterize the stiffness of the male and female upper arm in lateral compressive loading and to develop corresponding biofidelity stiffness corridors.

METHODS

A total of 18 pendulum impacts were performed on 9 matched arms, 5 female and 4 male obtained from fresh previously frozen post mortem human subjects (PHMS). The arms were obtained from 9 fresh previously frozen human cadavers, 5 female and 4 male (Table 1). In addition, a total of 4 pendulum impacts were performed on the standard arm of the Sid-IIs dummy using the same experimental setup to provide means of comparison.

Table 1: Subject Information.

Subject ID	Gender (F/M)	Age (yrs)	Mass (kg)	Height (cm)
Cadaver 1	Female	72	64	165
Cadaver 2	Female	77	55	160
Cadaver 3	Female	87	82	173
Cadaver 4	Female	76	70	157
Cadaver 5	Female	73	100	170
Cadaver 6	Male	76	44	170
Cadaver 7	Male	62	60	178
Cadaver 8	Male	67	105	183
Cadaver 9	Male	71	105	188

Experimental Setup

The primary component of the test setup was a 14 kg pendulum with a rigid 152 mm diameter impacting surface (Figure 1). The impactor was supported by 8 steel cables in order to provide smooth pendulum travel with no rotation or translation. The pendulum was instrumented with a single axis accelerometer (Endevco 7264B, 2000 G, San Juan Capistrano, CA). The arm was then placed against a polyethylene backing surface, which was mounted to a rigid aluminum plate. The reaction force was measured using a single axis load cell (Interface 1210AF-22,240 N, Scottsdale, AZ) mounted to a rigid wall with the use of a rigid aluminum plate. The data acquisition system and high-speed video were triggered with the use of a contact strip placed on the soft tissue of each arm at the point of initial impactor contact.

The arms were oriented vertically and suspended with a rope tied around the head of the humerus (Figure 2). The superior skin and muscle of the arm were held taught by with the use of sutures and string attached to the suspending rope. The arms were positioned so that the center of the impactor was in-line with the humerus bone. Special care was taken to ensure that only the main shaft of the humerus was in front of the polyethylene backing surface. In order to provide a comparison to the response of the dummy arm, matched tests were performed on the arm of the SID-IIs dummy (Figure 2).

The arms were randomly divided into two groups, where each group contained one specimen, right or left arm, from each of the 9 matched pairs. The first group was subjected to a 2.0 m/s impact (20.3 cm drop height). The second group was subjected to a 4.0 m/s impact (81.5 cm drop height). Pre-test measurements were taken of each test specimen to document anthropometrical data of the arms with soft tissue attached (Table A1). The thickness and circumference of each specimen was measured after the specimen was positioned on the experimental test setup. Post-test measurements were taken of each test specimen to document anthropometrical data of the humerus bone (Table A2).

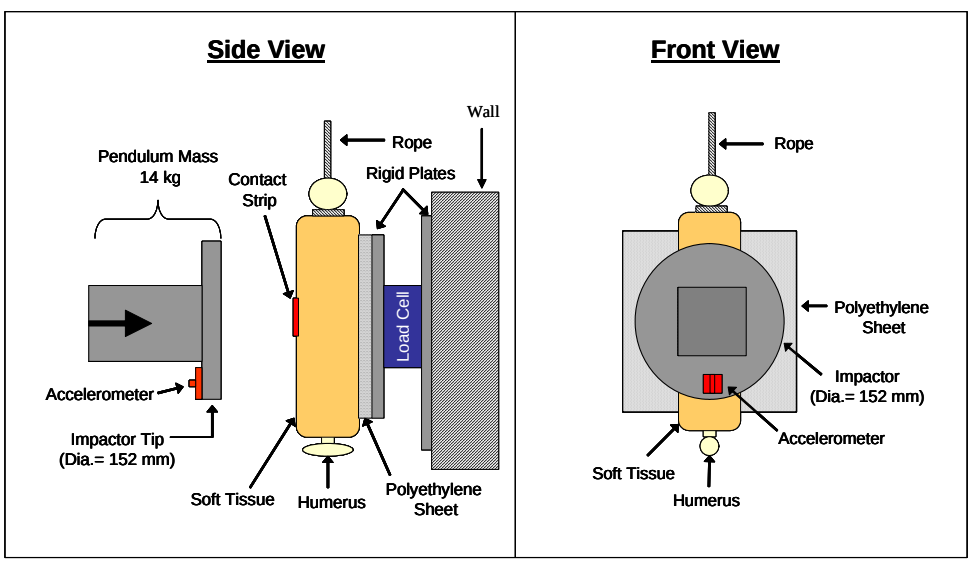

Figure 1: Pendulum impact experimental test setup.

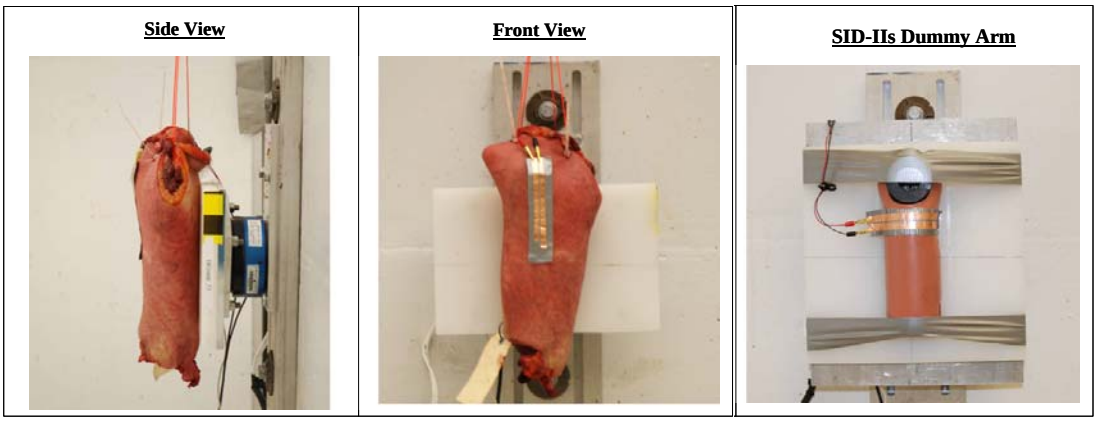

Figure 2: Cadaver and SID-IIs arm positioning.

Data Acquisition and Processing

All data was recorded at a sampling frequency of 30,000 Hz (Iotech WBK16, Cleveland, OH) and filtered to Channel Filter Class (CFC) 600. The impactor force was calculated as the product of impactor acceleration and impactor mass, 14 kg. High-speed video (Phantom V9.1, Vision research) was recorded at a sampling rate of 2000 Hz at a resolution of 864 x 1000 pixels (Figure 4). The camera was positioned to obtain video perpendicular to the impact direction. The positions of the impactor targets were tracking using Phantom software. In order to obtain medial-lateral deflection, the position of the impactor at the point of initial contact from subtracted from the impactor position at each point in time

Volunteer Measurements

In order to obtain a indication of the toe region of the arm due to medial-lateral compression, the upper arms of 16 male, approximately 50th percentile, and 4 female, approximately 5th percentile female, volunteers were measured (Figure 3, and Table 2). To measure the thickness of the arm in the vertical position, a flat plate was inserted between the body and the arm of a standing volunteer. The volunteer was asked to relax their muscles and maintain contact between the plate and elbow joint with the arm hanging vertically in a relaxed position. The thickness was measured with a combination square, perpendicular to the plate, and from the plate to the midpoint of the arm. A second thickness measurement was taken by compressing the arm to a tolerable limit. This measurement was taken to give an indication of the toe region that would result from compressing the soft tissue.

Initial Thickness (No Compression) **Compressed Thickness** (Compressed to a Tolerable Level)

Figure 3: Arm thickness measurements taken on a volunteer.

Table 2: Average arm thickness measurements for 20 volunteers.

Gender	Number of Subjects	Average Age (yrs)	Mass Range (kg)	Average Initial Thickness	Average Compressed Thickness	Average Difference b/w Initial and Compressed
Male	16	21	68 -84	78.5	45.4	33.1
Female	4	19	42 -52	66.3	36.5	29.8

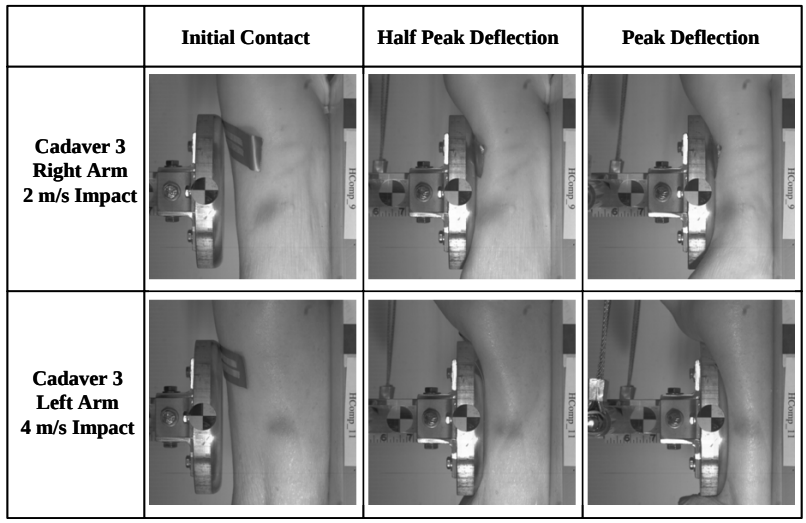

Figure 4: High speed video stills used to determine medial-lateral deflection.

Data Scaling

In order to minimize the variations in subject response due to individual geometry and inertial properties, the force and deflection were scaled to the response of a standard subject. A number of different standard scaling techniques were evaluated: Eppinger et al. (1984); Mertz (1984); ISO/TR-9790:1999. However, the scaling the procedure detailed by Eppinger et al. (1984) was found to be the most effective [12, 13, 14]. The scaling factors are defined below (Equations 1-3). In the scaling factor equations, m_i is the mass of the cadaver, m_s is the mass of a standard subject. The mass of the standard 5th percentile female is 46.9 kg, and the mass of the standard 50th percentile male is 76 kg [15]. The scaling factors used to normalize the response of each cadaver arm are reported in Table 3.

Table 3: Scaling Factors.

Subject ID	Gender	Scaling Factors	
		Deflection (Rx)	Force (Rf)
Cadaver 1	F	0.90	0.82
Cadaver 2	F	0.95	0.90
Cadaver 3	F	0.83	0.69
Cadaver 4	F	0.87	0.76
Cadaver 5	F	0.78	0.60
Cadaver 6	M	1.20	1.44
Cadaver 7	M	1.08	1.18
Cadaver 8	M	0.90	0.81
Cadaver 9	M	0.90	0.81

$$\lambda = \left(\frac{m_s}{m_i}\right)^{1/3} \qquad \text{Eqn (1)}$$

$$Force_{scaled}(t) = \lambda^2 * Force_{imp}(t) \qquad \text{Eqn (2)}$$

$$Deflection_{scaled}(t) = \lambda * Deflection(t) \qquad \text{Eqn (3)}$$

RESULTS

The non-scaled force versus deflection responses of each arm were plotted for each loading rate (Figures 5, 8, 11, and 14). The scaled force versus deflection responses of each arm were plotted for each loading rate (Figures 6, 9, 12, and 15). In addition, the average difference in thickness between the initial and compressed volunteer arm thickness was plotted along with the scaled data.

Arm Stiffness Response Corridors

Force versus deflection response corridors were developed using the characteristic average approach for both male and female arm responses at each impact rate (Figures 7, 10, 13, and 16) [11]. The upper bound corresponds to the positive standard deviation in force vs. the negative standard deviation in deflection. The lower bound corresponds to the negative standard deviation in force vs. the positive standard deviation in deflection.

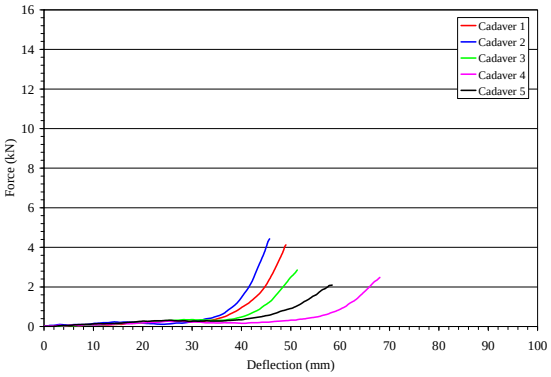

Figure 5: Female arm force vs. deflection responses- 2 m/s.

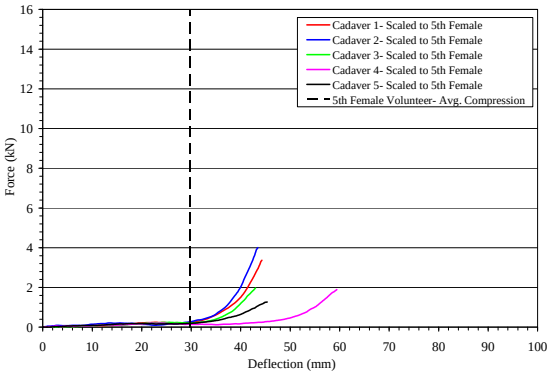

Figure 6: Scaled female arm force vs. deflection responses - 2 m/s.

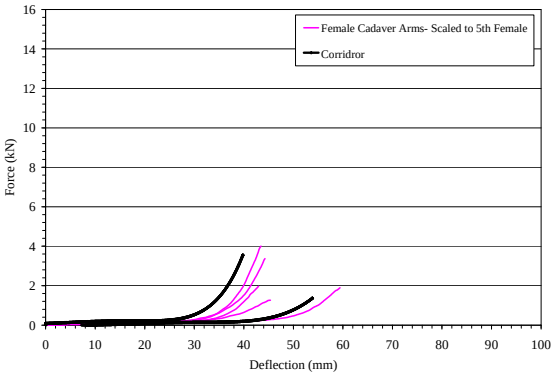

Figure 7: Scaled female arm force vs. deflection response corridors - 2 m/s.

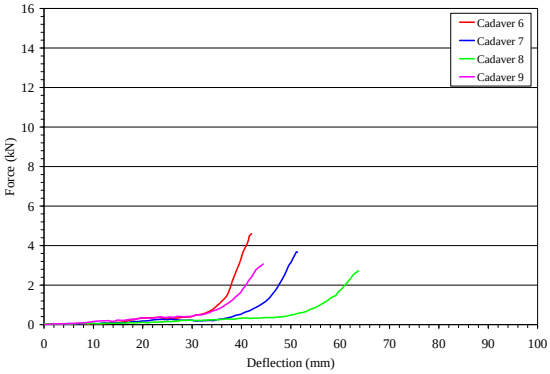

Figure 8: Male arm force vs. deflection responses - 2 m/s.

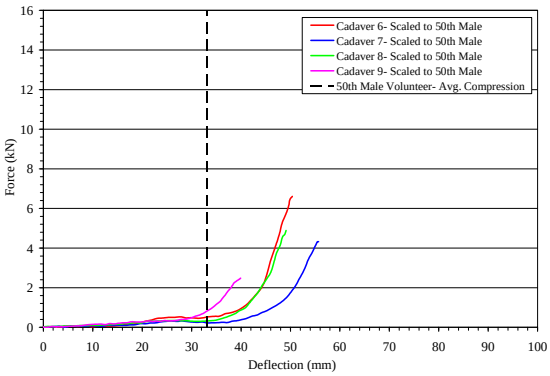

Figure 9: Scaled male arm force vs. deflection responses - 2 m/s.

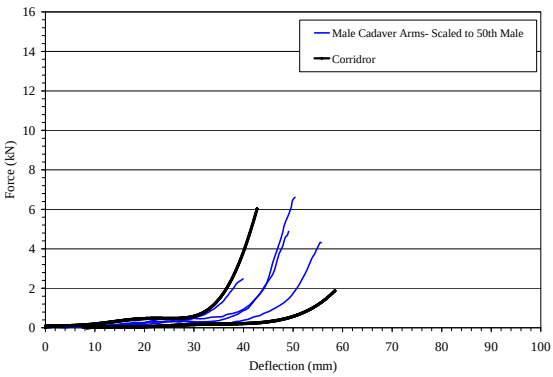

Figure 10: Scaled male force vs. deflection response corridors - 2 m/s.

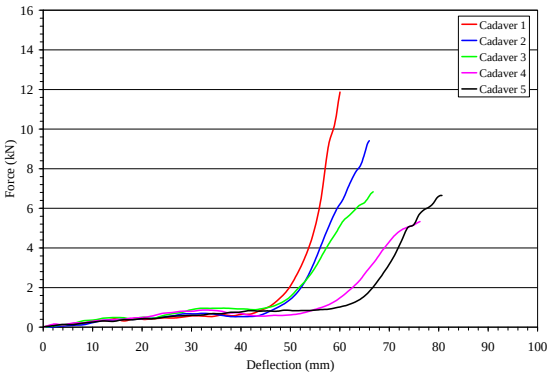

Figure 11: Female arm force vs. deflection responses - 4 m/s.

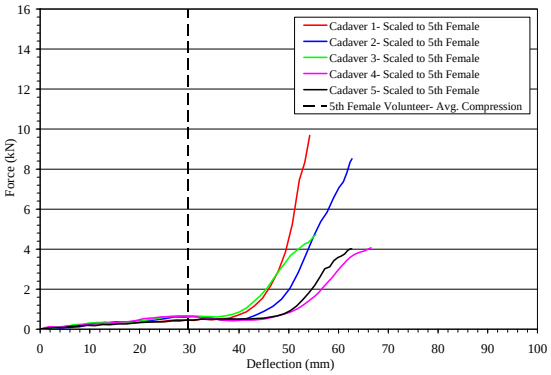

Figure 12: Scaled female arm force vs. deflection responses - 4 m/s.

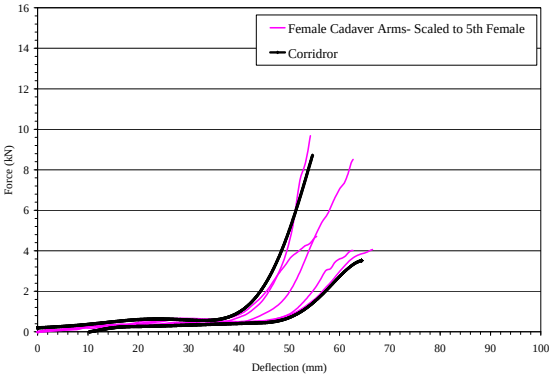

Figure 13: Scaled female force vs. deflection response corridors - 4 m/s.

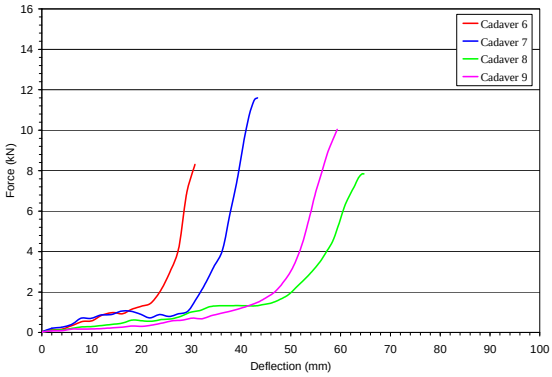

Figure 14: Male arm force vs. deflection responses - 4 m/s.

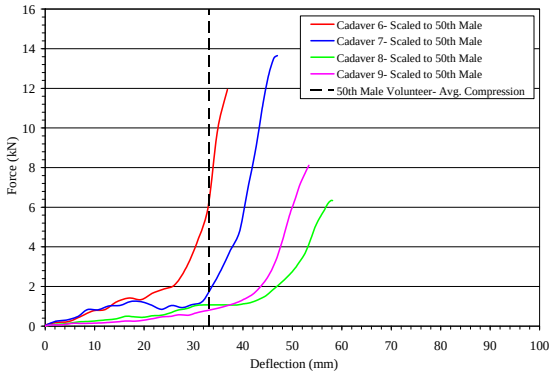

Figure 15: Scaled Male arm force vs. deflection responses - 4 m/s.

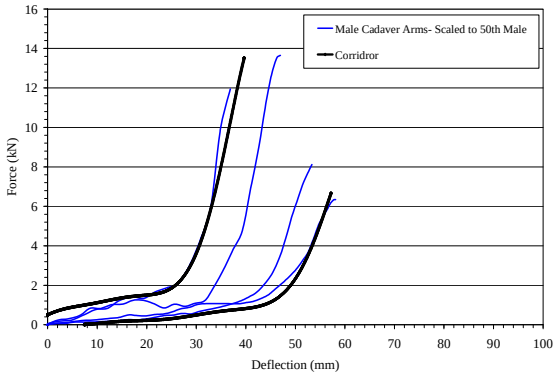

Figure 16: Scaled male force vs. deflection response corridors - 4 m/s.

Scaled Female vs. SID-IIS Response

The SID-IIs dummy arm did not exhibit a considerable toe region before the any substantial increase in force. For means of comparison, the scaled force versus deflection responses of the female arms were plotted along with the responses of the Sid-IIs dummy arms for both loading rates (Figures 17 and 18). The comparison clearly shows that the response of the SID-IIs does not lie within the response corridors for the 5th percentile female due to a lack of any considerable toe region.

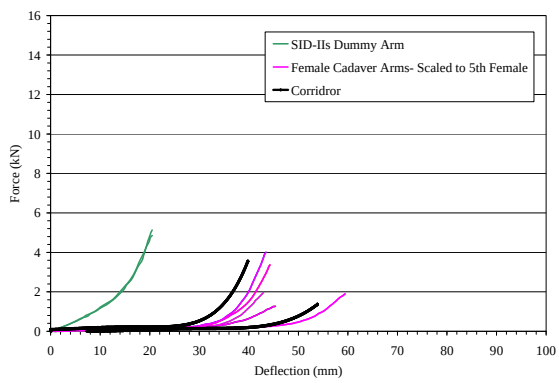

Figure 17: SID-IIS versus scaled female force vs. deflection responses- 2 m/s.

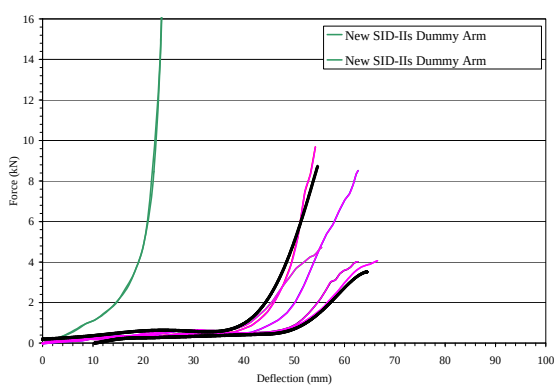

Figure 18: SID-IIS versus scaled female force vs. deflection responses- 4 m/s.

DISCUSSION

Although, the scaling the procedure detailed by Eppinger et al. (1984) was found to be the most effective method out of the standard scaling methods evaluated in the current study, this method is based on total subject mass and does not account for the differences in the ratio of arm mass to total body mass or arm thickness Given that the arm in constrained by the backing surface, the changes in the thickness of the soft tissue between subjects dominates the changes in the force versus deflection response between subjects. Therefore, an alternate scaling method based solely on arm thickness is proposed here. This method assumes that the material properties of the soft tissue do not change between subjects, but the amount, or thickness, of the tissue does. The scaling factors based on arm thickness alone are defined below (Equations 1-6, Table 4). In the scaling factor equations, t_i is the medial lateral arm thickness of the cadaver, t_s is the medial lateral arm thickness of a standard subject. The medial lateral arm thickness of the standard 5th percentile female is 67 mm, and the medial lateral arm thickness of the standard 50th percentile male is 86 mm [15].

$$\lambda_t = \left(\frac{t_s}{t_i}\right) \qquad \text{Eqn (4)}$$

$$Force_{scaled}(t) = \lambda_t * Force_{imp}(t) \qquad \text{Eqn (5)}$$

$$Deflection_{scaled}(t) = \lambda_t * Deflection(t) \qquad \text{Eqn (6)}$$

Table 4: Scaling Factors Based on Maximum Arm Thickness.

Subject ID	Gender	Impact Speed	Scaling Factor
Cadaver 1	F	2 m/s	0.86
		4 m/s	0.77
Cadaver 2	F	2 m/s	0.83
		4 m/s	0.71
Cadaver 3	F	2 m/s	0.65
		4 m/s	0.63
Cadaver 4	F	2 m/s	0.55
		4 m/s	0.54
Cadaver 5	F	2 m/s	0.58
		4 m/s	0.52
Cadaver 6	M	2 m/s	1.19
		4 m/s	1.54
Cadaver 7	M	2 m/s	0.93
		4 m/s	1.16
Cadaver 8	M	2 m/s	0.78
		4 m/s	0.79
Cadaver 9	M	2 m/s	0.97
		4 m/s	0.88

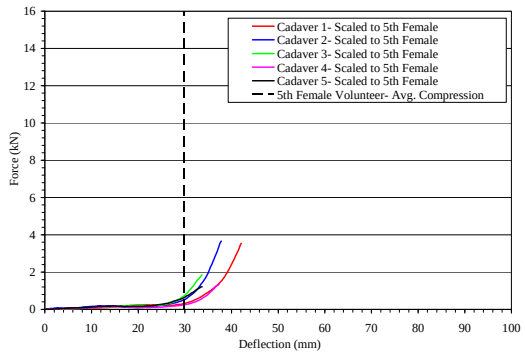

Figure 19: Scaled female arm force vs. deflection responses based on thickness- 2 m/s.

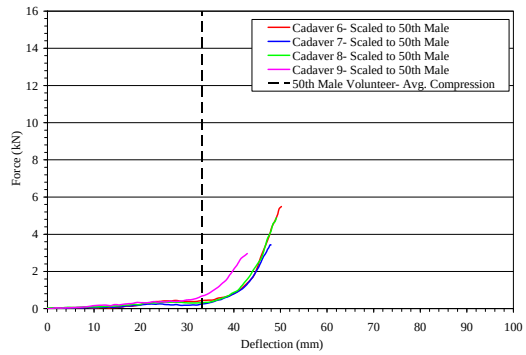

Figure 21: Scaled male arm force vs. deflection responses based on thickness - 2 m/s.

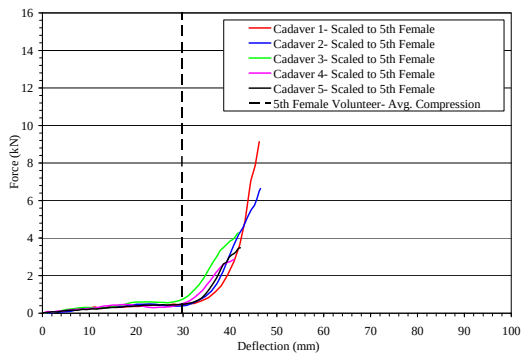

Figure 20: Scaled female arm force vs. deflection responses based on thickness - 4 m/s.

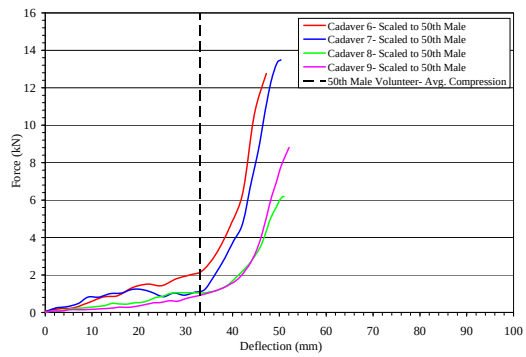

Figure 22: Scaled male arm force vs. deflection responses based on thickness - 4 m/s.

CONCLUSIONS

The study presents results from 18 medial-lateral pendulum impacts performed on 9 human arm matched pairs with a 14 kg pendulum at 2 m/s or 4 m/s. Force versus deflection response corridors were developed for both the 50th percentile male and the 5th percentile female arm response at each impact rate. In addition, 4 pendulum impacts performed on a Sid-IIs dummy arm using the same experimental setup for means of comparison. For both impact rates the cadaver arms exhibited a considerable amount of deflection under very low force, i.e. toe region, before the any substantial increase in force. The deflection at which the force began to increase substantially was found to be similar to the average difference in thickness between the initial and compressed volunteer arm thickness measurements for both the 5th percentile female and 50th percentile male. Although the response of the SID-IIs dummy arm was similar in shape to that of the female cadaver arms for both impact rates, the SID-IIs dummy arm did not exhibit a considerable toe region before the any substantial increase in force. Therefore, the SID-IIs response force vs. deflection response did not lie within the response corridors for the 5th percentile female. The results of the current study could lead to an improvement in the overall biofidelity of side impact ATDs by providing valuable data necessary to validate the compressive response of side impact ATD arms independent of the global ATD response.

ACKNOWLEDGMENTS

The authors wish to acknowledge Toyota Motor Corporation for providing the funding for this research.

REFERENCES

[1] Bass, C., Duma, S., Crandall, J., Morris, R., Martin, P., Pilkey, W., Hurwitz, S., Khaewpong, N., Eppinger, R., Sun, E. (1997) The interaction of airbags with upper

extremities. Proc. 41st Stapp Car Crash Conference, Society of Automotive Engineers. Warrendale, PA. 41: 101-110.

[2] Cavanaugh J., Zhu Y., Haung Y., and King A. (1993) Injury and response of the thorax in side impact cadaveric tests. Proc. 37th Stapp Car Crash Conference, Society of Automotive Engineers. Warrendale, PA. 37:199-221.

[3] Duma, S., Crandall, J., Hurwitz, S., Pilkey, W. (1998) Small female upper extremity interaction with a deploying side airbag. Proc. 42nd Stapp Car Crash Conference, Society of Automotive Engineers. Warrendale, PA. 42: 47-63.

[4] Duma, S., Schrieber, P., McMaster, J., Crandall, J., Bass, C., Pilkey, W. (1999) Dynamic injury tolerances for long bones of the female upper extremity. Journal of Anatomy, 194: 463-471.

[5] Duma, S., Boggess, B., Bass, C., Crandall, J. (2003) Injury risk functions for the 5th percentile female upper extremity. SAE Paper No. 010166. Society of Automotive Engineers, Warrendale, PA.

[6] Duma, S., Hansen, G., Kennedy, E., Rath, A., Mcnally, C., Kemper, A., Smith, E., Brolinson, P., Stizel, J., Davis, M., and Bass, C., (2004) Upper extremity interaction with a helicopter side airbag: injury criteria for dynamic hyperextension of the female elbow joint. *Stapp Car Crash Journal*, 48.

[7] Eppinger, R., Marcus, J., and Morgan, R. (1984) Development of dummy and injury index for NHTSA's thoracic side impact protection research program. SAE Paper No. 840885. Society of Automotive Engineers, Warrendale, PA.

[8] Kallieris, D., Rizzetti, A., Mattern, R., Jost, S., Priemer, P., Unger, M. (1997) Response and vulnerability of the upper arm through side airbag deployment. SAE Paper No. 973323. Society of Automotive Engineers, Warrendale, PA.

[9] Kanno, Y., Jamal, S., Yang, K., King, A. (1993) Mathematical modeling of human thoracic responses with and without arms during side impact. Crashworthiness and Occupant Protection in Transportation Systems. Vol. 169, ASME.

[10] Kemper, A., McNally, C., and Duma, S. (2008) Biofidelity of an Original and Modified SID-IIs Upper Extremity: Matched Cadaver and Dummy Compression Tests. Biomedical Sciences Instrumentation Symposium. 44.

[11] Lessely, D. Crandall, J., Shaw, G., Kent, R., and Funk, J. (2004) A Normalization Technique for Developing Corridors from Individual Subject Responses. Society of Automotive Engineers, Warrendale, PA. 2004-01-0288.

[12] Eppinger, R., Marcus, J., and Morgan, R. (1984) Development of dummy and injury index for NHTSA's thoracic side impact protection research program. Society of Automotive Engineers, Warrendale, PA.

[13] International Standards Organization (ISO) Road vehicles– Anthropometric side impact dummy- Lateral impact response requirements to assess the biofidelity of the dummy, ISO/TR 9790:1999(E).

[14] Mertz, H. (1984) A Procedure for normalizing impact response data. Society for AutomotiveEngineers, Warrendale, PA.

[15] Schneider, L., Robbins. D., Pflueg M, and Snyder, R. (1983) Development of anthropometrically based design specifications for an advanced adult anthropomorphic dummy family. Contract No. DTNH22-80-C-07502, University of Michigan Transportation Research Institute, Ann Arbor.

APPENDIX

Table A1: Cadaver arm pre-test anthropometric measurements.

Subject ID	Right/Left Arm	Arm Measurements with Soft Tissue				
		Arm Mass	Medial-Lateral Thickness		Circumference	
			[center of plate]	[maximum]	[center of plate]	[maximum]
		(g)	(mm)	(mm)	(cm)	(cm)
Cadaver 1	Right	1480	69.0	78.0	22.5	26.5
	Left	1320	80.0	87.0	23.5	26.0
Cadaver 2	Left	1450	81.0	81.0	25.5	27.0
	Right	1550	85.0	95.0	26.0	27.0
Cadaver 3	Right	2335	95.0	103.0	32.5	33.0
	Left	2355	102.0	107.0	31.0	34.0
Cadaver 4	Left	2900	115.0	122.0	35.0	36.0
	Right	3430	116.0	125.0	37.5	39.5
Cadaver 5	Right	2980	112.0	116.0	37.5	38.5
	Left	3445	115.0	128.0	37.5	43.5
Cadaver 6	Right	1445	55.0	72.0	18.5	21.5
	Left	1185	51.0	56.0	17.5	19.5
Cadaver 7	Left	2020	72.0	92.0	25.0	30.0
	Right	2060	68.0	74.0	25.0	28.0
Cadaver 8	Right	2995	93.0	110.0	34.0	37.0
	Left	3035	98.0	109.0	34.0	37.5
Cadaver 9	Left	2300	80.0	89.0	31.0	33.5
	Right	2385	77.0	98.0	30.5	35.5

Table A2: Cadaver arm post-test anthropometric measurements.

Subject ID	Right/Left Arm	Humerus Bone Measurements				
		Total Length	Length of Main Shaft	Midpoint Diameter		Circumference
				[medial-lateral]	[anterior-posterior]	[midpoint]
		(cm)	(cm)	(cm)	(cm)	(cm)
Cadaver 1	Right	32.0	21.0	2.22	1.80	6.50
	Left	32.0	21.0	2.22	1.88	6.50
Cadaver 2	Left	32.5	20.5	2.03	2.06	6.75
	Right	33.0	21.0	2.03	2.18	6.50
Cadaver 3	Right	32.5	21.5	1.93	1.84	6.25
	Left	32.5	21.0	1.91	1.88	6.25
Cadaver 4	Left	31.0	20.0	2.22	2.16	7.50
	Right	31.0	20.0	2.22	2.17	7.50
Cadaver 5	Right	31.5	22.0	2.13	2.16	7.00
	Left	31.5	22.0	1.92	2.16	7.00
Cadaver 6	Right	35.5	22.0	2.10	2.39	7.00
	Left	35.5	22.0	1.75	2.79	7.00
Cadaver 7	Left	33.5	22.0	2.41	2.54	8.00
	Right	34.0	22.5	2.50	2.54	8.25
Cadaver 8	Right	36.0	24.0	2.41	2.35	7.50
	Left	36.0	23.5	2.41	2.35	7.25
Cadaver 9	Left	35.0	21.0	2.06	2.25	7.50
	Right	34.5	22.0	2.13	2.03	7.50

OOP AIR BAG TESTS WITH THE FIFTH PERCENTILE FEMALE THOR AND HYBRID III DUMMIES

Peter G. Martin
Matthew Craig
Stephen Ridella
National Highway Traffic Safety Administration
U.S. Department of Transportation
Washington, D.C., USA

Paul Rigby
Philemon Chan
L-3/Jaycor
San Diego, CA, USA

Paper Number 09-0546

ABSTRACT

The THOR-05F is a new anthropomorphic test device with many notable features, including a biofidelic neck design with built-in lordosis that segregates load paths within the cervical spine. Static air bag deployment tests were carried out with the dummy positioned in the NHTSA-1 (chin on module) driver Out-Of-Position (OOP) configuration. A set of late-model two-stage air bag modules were used in a total of forty tests, including reference tests conducted with the 5th percentile female Hybrid III dummy. All of the modules were driver-side units, and each was contained within its own steering wheel assembly. Half of the modules were configured to deploy more aggressively. All bags were observed to deploy asymmetrically, resulting in a substantial twist of the head about the z-axis of the THOR-05F neck, and a high corresponding Mz upper neck moment. The THOR-05F demonstrated its ability to discriminate air bag aggressiveness, especially in its upper neck tension measurements which was the most predominant upper neck load. Compared to Hybrid III, the THOR-05F neck showed less tendency to go into extension. The upper neck moment (My) and shear (Fx) were much lower in magnitude than those of the Hybrid III 5th. Head accelerations were similar to those produced by the Hybrid III 5th.

INTRODUCTION

The THOR 5th percentile female dummy is a new anthropomorphic test device (ATD) with many notable features, including a biofidelic neck design with built-in curvature that segregates load paths within the cervical spine. This ATD is very similar to the THOR-NT 50th percentile male archetype which has seen wide interest since its release in 2003. Both dummies were developed by NHTSA for advancing the study of biomechanical phenomena and the development of new injury criteria supported by other efforts in human volunteer tests, cadaver tests and modeling. The new fifth percentile female has been called informally THOR-05F during the development process.

Figure 1. Fifth percentile female THOR-05F ATD.

The development of the THOR-05F was initially presented at international conferences in 2003. A paper was presented at the ESV conference, titled "Design requirements for a fifth percentile female version of the THOR ATD" which discussed the scaled biomechanical corridors that were developed for evaluating the biofidelity of the new dummy [Shams, 2003]. This was followed by a paper at the 2003 Stapp Conference titled, "Design and development of a THOR based small female crash test dummy" that summarized the development work and the initial biofidelity testing [MacDonald, 2003].

The THOR-05F dummy was designed using the anthropometric data developed for the 5th percentile female [Robbins, 1983] and biomechanical requirements derived from scaling the responses of the 50th male [Shams, 2003]. While many of the mechanical components of the THOR-NT 50th male were scaled according to the appropriate anthropometric data, a number of improved design features have been introduced in the THOR-05F.

THOR neck technology – Multiple load paths

The study herein focuses on the performance of air bags as measured within the THOR-05F's head/neck complex. As with the 50th percentile male THOR-NT, the neck has distinct sub-assemblies reflecting a design premise that human necks are loaded along multiple paths, and that loads are borne by both ligamentous tissues and musculature. Loads that pass through a human neck are presumed to include those borne by "external" musculature only (represented in THOR by the two cable sub-assemblies), and those borne by both "internal" muscles and ligaments (represented in THOR by the molded neck sub-assembly and the pin joint/nodding block sub-assembly).

The THOR design philosophy also presumes that human neck injuries occur when ligamentous tissues become overloaded. Hence, a THOR injury criterion will be based on its upper neck load cell alone, which is mounted to the neck rather than in the head (as with the Hybrid III). Forces measured in the load cells attached to THOR's anterior and posterior cables represent "external" non-injurious loads borne by musculature alone (and not ligamentous tissues). These load cell measures are contemplated as reference measures only, and may not be directly linked to an injury criterion.

THOR-05F Beta neck construction.

Unlike the THOR-NT 50th male, the THOR-05F incorporates the "Beta neck" design (Fig. 2). This neck features built-in lordosis and is more anthropometrically correct than the standard THOR-NT neck. The Beta neck concept was originally developed for the 50th male version of THOR [Huang, 2003]. Due to cost considerations, the prototype was constructed by gluing (rather than molding) the rubber pucks to the aluminum plates. But failures due to debonding prevented the Beta neck design from ever being verified for inclusion with the release of the standard THOR-NT.

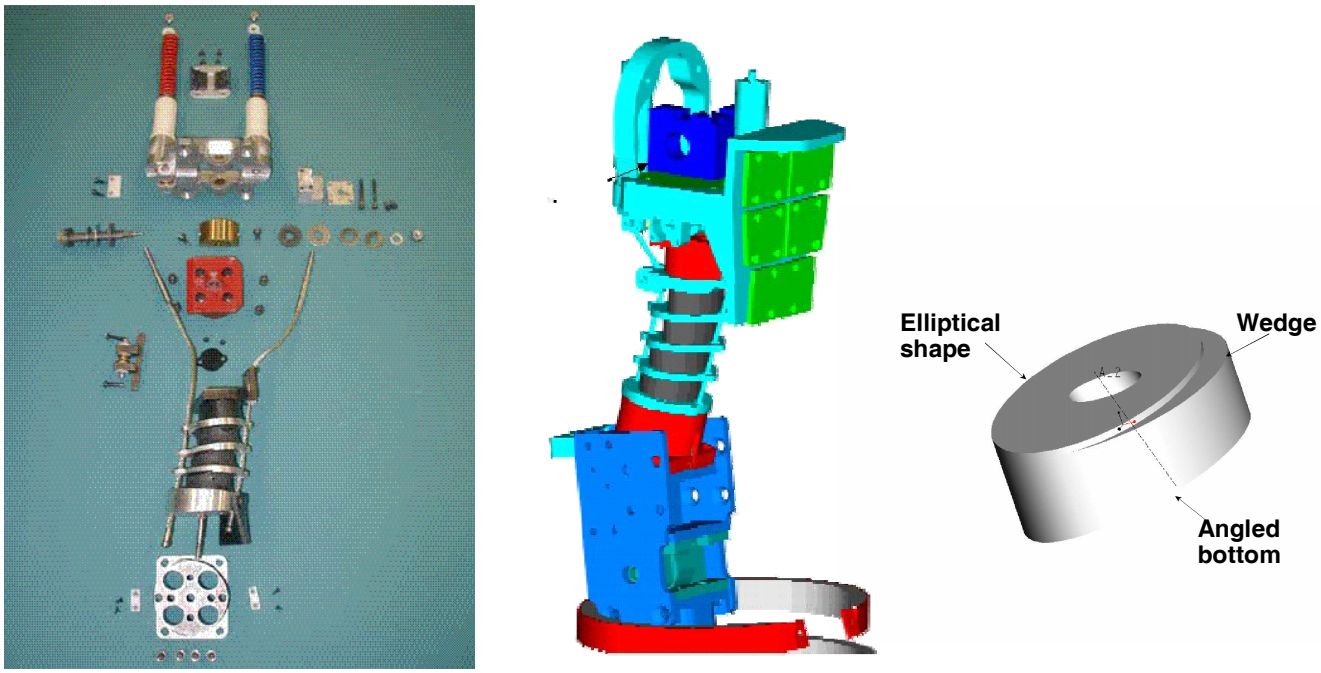

a. THOR-05F Beta neck components

b. THOR-05F Head/neck system on spine.

c. Beta neck's wedge-shaped rubber puck (one of four).

Figure 2. THOR-05F Beta neck system and components.

Thus, further development of the basic Beta neck has been carried out in conjunction with the experimental THOR-05F. By using standard scaling techniques, a new, smaller Beta neck was designed for the THOR-05F. To overcome the debonding problem, the new neck has been injection molded. In addition to the core design concept of multiple load paths that is represented in the standard THOR-NT neck, the Beta neck includes the following principal design features.

Four Pucks and Offset Geometry. The four-puck neck agrees with the length between the human occipital condyles and the first thoracic vertebra (OC-T1 length) derived from volunteer tests and the T1 is located at a well-defined rigid position. As a result, the new neck is offset from the top to the bottom. The gradual offset design is different from the THOR-NT and Hybrid III one-step change, and the Beta neck resembles the curvature of the human neck structure.

Elliptical Puck Shape. The shape of the pucks in the neck is elliptical. In order to have different responses in flexion and extension, the two bottom pucks are wedge shaped (Fig. 2c). The wedged pucks result in higher stiffness in extension at larger bending angles than in flexion. The current material for the puck is Neoprene with 75A durometer.

Cam/Rubber Mechanism for the OC Joint. The head-to-neck joint in the dummy is meant to mimic the neck segment between the OC and the second cervical vertebra in the human. A metal cam/rubber mechanism is used for the design of the OC joint in the 5th percentile female neck. The rubber shape is used to control the characteristics of OC to provide a more biofidelic moment-angle property at the OC joint.

Central Compliant Rubber Bushing. The main purpose of this design is to allow the neck to extend in the longitudinal direction (z-axis), in much the same way a human neck will react during impact. The rubber bushing is located within the lower neck load cell. The central cable will push to compress the rubber during motion and develop the z-axis extension.

This paper presents results of laboratory tests with the THOR-05F using driver-side air bags which reveal unique characteristics of the THOR-05F response. When exposed to a static air bag deployment in the NHTSA-1 OOP position, the THOR-05F provides new insights into cervical spine loading. The THOR-05F also provides a new perspective on discriminating air bag aggressiveness. As the THOR-05F is a relatively new dummy, this paper also serves to provide an evaluation of the dummy's functionality, durability, and repeatability under well controlled conditions. The focus of the evaluation is on the all-new Beta neck. For reference, the responses of the THOR-05F dummy are compared to those of Hybrid III 5th percentile female under the same air bag deployment conditions.

METHODS

All tests were carried out with the dummy positioned in the NHTSA-1 (chin on module) driver OOP position. A set of late-model two-stage air bag modules installed within a steering wheel assembly were used in a total of forty tests, including reference tests conducted with the 5th percentile female Hybrid III dummy. All steering wheels/air bag modules were obtained directly from an air bag supplier and were not adulterated in any way after receipt. All of the modules were driver-side units, and each was contained within its own steering wheel assembly. All bags contained two 15-cm tethers. Half of the modules were configured by the supplier to deploy more aggressively (described below as "normal" and "aggressive") and the stage-two firing times were experimentally varied.

Air bag Modules – Normal and Modified. Two types of driver air bags were used under two deployment conditions. The first type was an actual fleet air bag for a late model sedan (i.e., "Normal" bag) with a reverse-rolled cushion at the six and twelve o'clock positions. The second type was a modification of the first (i.e., "Modified" bag). It was folded using an accordion pattern at the six and twelve o'clock positions in lieu of the reverse rolls of the "Normal" bag. Generally, an accordion fold is easier to unravel and inflate, producing a more aggressive thrust. The different bag folding patterns are also shown in Fig. 3.

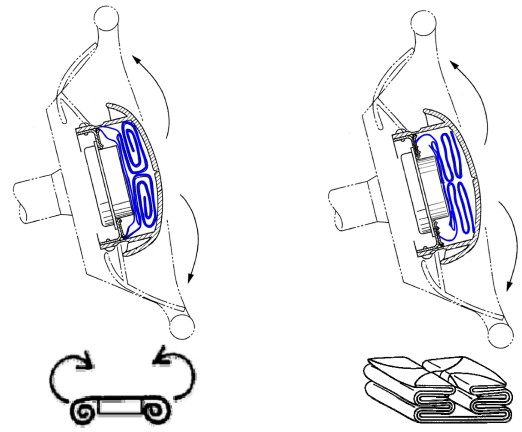

Figure 3. Air bag fold patterns: (Left) "Normal" reverse roll bag; (Right) "Modified" accordion bag.

Also, the gas diffuser/deflector was removed from the second type to provide a more aggressive deployment. A diffuser/deflector is a small, tethered patch of cloth covering the inflator which fills with gas like a parachute and diffuses the gas (Fig. 4).

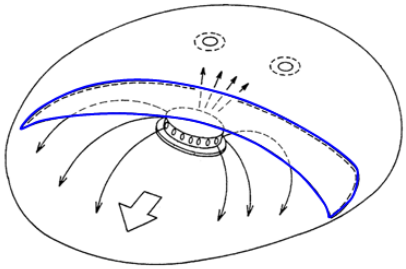

Figure 4. Typical gas diffuser within an air bag.

The second type of bag was supplied for the experimental purposes herein. While accordion folds are used widely in production, and not all production bags have diffusers, it is not known whether the particular "modified" bag employed herein is used in any fleet vehicles.

NHTSA-1 Setup: Benign vs. Aggressive. All forty tests were carried out with the dummy positioned in the standard NHTSA-1 position (chin on module) in accordance with the seating procedure of Federal Motor Vehicle Safety Standard (FMVSS) No. 208, "Occupant crash protection," (Part 571.208). The position of the dummy was accurately controlled using fixed position markers on the seat and the adjustable neck positioning arm for each test. The transducers used in THOR-05F and Hybrid III included accelerometers, load cells, displacement string potentiometers, and rotary potentiometers.

All signals were recorded using a digital data acquisition system with a sampling rate of 10 kHz. A high-speed digital camera recorded the air bag-dummy interaction at 1000 frames per second. Signal conditioning, filtering, and recording techniques complied with the SAE J211 standard [1995].

Two variations of the steering wheel module were imposed in order to produce a "benign" deployment and an "aggressive" deployment. For the benign setup, the two air bag stages were initiated 30 msec apart and the steering wheel angle was set at 68° from horizontal. For the aggressive setup, air bag stages were initiated simultaneously, which provided a more aggressive deployment than sequential firing. Moreover, the steering wheel angle was set at 60° from horizontal. This promoted more of an upward deployment than the 68° setup. As such, it tended to produce higher ATD neck forces and moments.

The choice of steering wheel angle is representative of typical passenger cars in the U.S. fleet. The 68° angle is typical of a production sedan such as that in which the modules tested herein are intended to be installed. The 60° angle is not uncommon in larger vehicles like pickup trucks and SUVs.

Additionally, a shield was installed behind steering wheel to prevent the air bag from slipping under and behind the steering wheel rim during inflation, which reduces repeatability. The shield fit behind the steering wheel so as to not interfere with the air bag deployment.

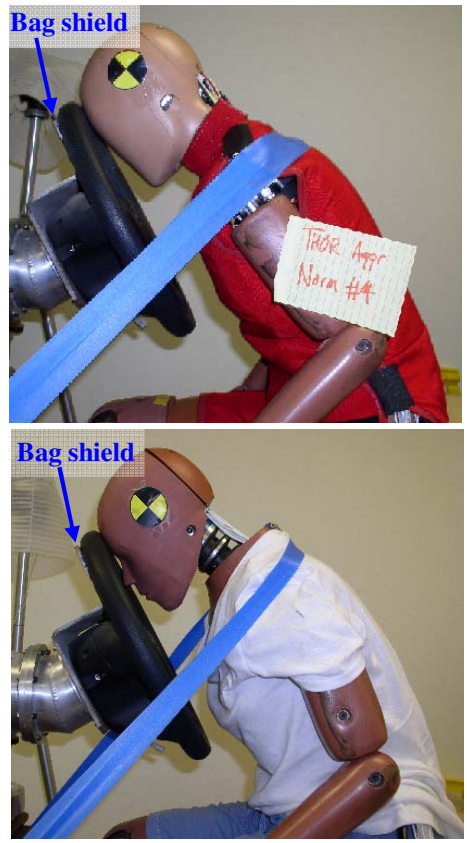

Figure 5. THOR-05F (top) and Hybrid III (bottom) in the NHTSA-1 Aggressive Setup (steering wheel angled upward).

Test Matrix. A series of forty full-deployment air bag impact tests were carried out. Two ATD units were used: the prototype THOR-05F and a Hybrid III 5th percentile female. Both units passed through standard dummy certification tests (head drop, head/neck pendulum swings, chest impacts) just prior to the air bag series. The forty tests were carried out on an "on again, off again" basis that extended over 40 weeks. Tests were typically run in batches of three to five tests per batch. During the "on again"

periods, a one-hour test-to-test delay was imposed to allow full dummy recovery. No re-certifications or part replacements occurred at any time during the 40-week period.

Five repeat tests were performed for each test condition, as indicated in Table 1. Head/neck load time-history data comparison was performed for each air bag model. Air bag inflation repeatability and variability for each model was confirmed and analyzed using the high-speed video recordings. Data analysis focused primarily on trend comparisons in the head/neck region. Data for five repeat tests for each case were averaged for time-history trend comparison. Values of Head Injury Criterion based on the 15-ms time interval (HIC_{15}) were also computed.

Table 1. Test matrix

Setup Position	Normal Air bag		Modified Air bag	
	THOR-05F	Hybrid III	THOR-05F	Hybrid III
Benign	5	5	5	5
Aggressive	5	5	5	5

Comparing THOR-05F with Hybrid III. As stated earlier, the THOR-05F has a unique neck construction in which muscles and osteoligamentous structures are represented by separate mechanical components (Fig. 2). The primary structural component of the THOR-05F neck is the segmented molded rubber column which is designed based on the responses of the human cervical spine. A six-axis load cell is placed at the top of this component to directly measure the loads at the head/neck pin joint, which represents human occipital condyles. In the results presented herein, all upper neck loads refer to the OC pin joint location. Cable elements representing the anterior and posterior neck musculature also bear loads. Cross-sectional loads refer to loads including the front and rear cable loads with respect to the head coordinate system.

The Hybrid III does not account for separate load paths; its neck load cell measurements correspond to "cross-sectional" neck loads. Unlike the THOR-05F, the Hybrid III upper head/neck load cell is installed in the head above the OC pin joint and measures the load in the head coordinate system. The upper head/neck moment, My, measured by the upper head/neck load cell is translated to the OC level by subtracting the moment obtained by multiplying the shear force Fx by the height of the load cell above the OC from the moment data measured by the load cell.

To facilitate comparison with the Hybrid III, the THOR-05F instrumentation allows one to compute its "cross-sectional load" by accounting for the cable loads. The dummy also has a rotary potentiometer that measures rotation of the head with respect to the neck. Using data from this potentiometer, one may translate THOR-05F's cross-sectional neck loads to the head coordinate system for direct comparison with the Hybrid III.

RESULTS

All THOR-05F neck results presented hereafter are "ligamentous" loads of the upper neck at the level of the head/neck pin joint (representing the human occipital condyles) unless otherwise specified. As such, these loads are derived from the upper neck load cell only, and do not include the contributions of the front and rear cables. Furthermore, since the upper neck load cell is mounted atop the neck and beneath the head/neck pin joint, the THOR-05F neck load vectors correspond to a local upper neck coordinate system. This is the way the neck data are expected to be used for injury assessment.

For the Hybrid III, the upper neck load cell is contained within the head and is mounted on the head instrument plane. Thus, all Hybrid III loads reported herein represent the total cross-sectional loads and the load vectors correspond to a local upper neck coordinate system. The Hybrid III head rotates very little with respect to the neck due to the engagement of its nodding blocks. On the other hand, the THOR-05F head/neck pin joint offers much less resistance so that the head may rotate as much as +/- 40 degrees before its nodding blocks engage fully. Thus, the directions of the upper neck load cell force vectors of the THOR-05F and Hybrid III can vary substantially.

Repeatability and variability. The dummy response in tests with the normal air bags proved to be more repeatable than in tests with the modified bags for both the THOR-05F and Hybrid III. Figure 6 shows the averages of the THOR-05F and Hybrid III upper neck tension (Fz) and upper neck flexion/extension moment (My) for the benign setups (Figs. 6a and b) and the aggressive setups (Figs. 6c and d). The shaded areas represent one standard deviation about the mean. The Fz and My measures, which are typically used to define injury risk, are used for comparison herein. However, the other ATD channels, including head acceleration measurements, indicate the similar findings.

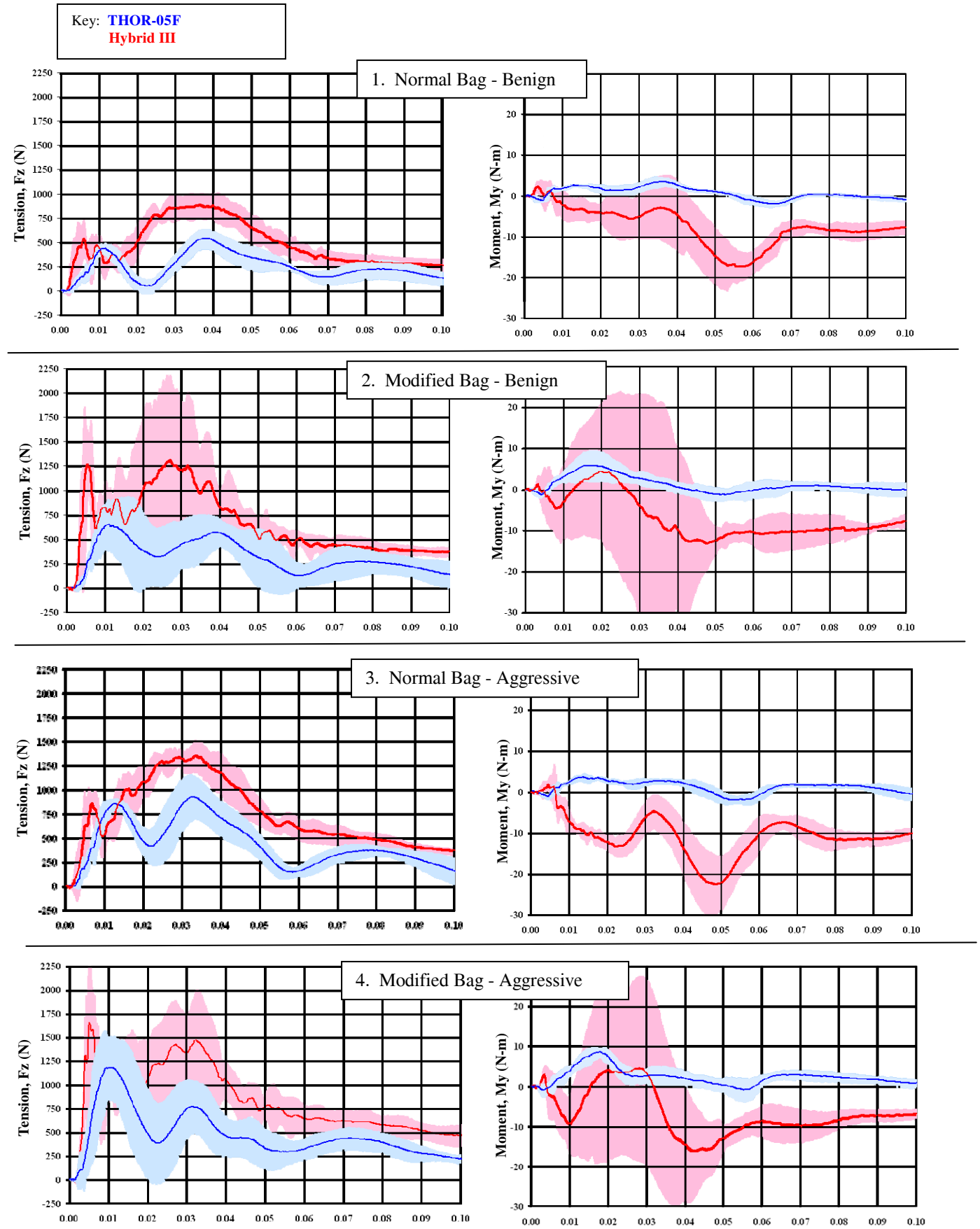

Figure 6. THOR-05F and Hybrid III time-histories (sec). Average upper neck tension (Fz) and flexion/extension moment (My) for the four test conditions. The shaded areas represent +/- 1 standard deviation.

All plots in Fig. 6 indicate a tighter shaded area – and greater repeatability – for the normal bags. When comparing the tests run under the benign vs. aggressive setups, the relative repeatability appears to be about the same for each dummy. As shown in Fig. 6, the repeatability of the Hybrid III upper neck is on a par with the THOR. An assessment of repeatability is discussed in the next section.

THOR-05F and Hybrid III comparison. Consider the THOR-05F vs. the Hybrid III in the "Normal Bag/Aggressive Setup" condition. This condition is the best of the four to compare the two, because it involves a relatively repeatable air bag with a strong deployment with relatively high measurements. Upper neck tension Fz, shear Fx, and moment My are compared since they represent the primary measurements of the current NHTSA injury criteria (Fig. 7).

In both the THOR-05F and Hybrid III, upper neck Fz force is generally positive, indicating that the neck is in tension for both dummies (Fig. 6). This tensile force is a combined effect of the external air bag load and the centrifugal rearward rotation of the head. However, the Hybrid III recorded a much stronger upper neck extension (negative My) and a higher upper neck shear force (negative Fx) than THOR-05F (Fig. 7). Other dissimilarities are discussed below.

For the THOR-05F, the upper neck load data shown in the figures above all indicate a fairly consistent response typified by the relatively repeatable "Normal Bag/Aggressive Setup" condition. In general, the neck tension (Fz) was the predominant load, with very low moment (My) and shear (Fx). The low My is attributable to the THOR-05F head/neck junction where the pin joint offers little resistance (and sustains low moments) to relative head-to-neck rotation of up to 30 deg. Even so, the potentiometer that captured this rotation indicated that the rotation was never greater than 10 degrees in any of the tests.

What little upper neck moment and shear that was present in the THOR-05F indicates that the air bag pushed the chin backwards and downwards, which generated a negative upper head/neck shear force (negative Fx) and positive flexion moment (positive My) at about 20 ms. The THOR-05F neck did not go into extension until well after bag separation.

The general response of the Hybrid III differs from the THOR-05F. Under the "Normal Bag/Aggressive Setup" condition, high-speed video data showed the air bag became trapped under the Hybrid III chin and pushed it upwards. The neck was shown to be in extension with a slight bend to the neck column as the dummy separated from the bag. This condition produced the negative My (extension) moments apparent in the data. It also generated a corresponding negative upper neck shear Fx due to the bag being lodged between the chin and the neck. This was consistent for all five tests.

For the "Modified Bag/Aggressive Setup" condition, however, the above condition was only apparent in one of the five Hybrid III repeat tests. Other repeat tests resulted in a response closer to that of the THOR-05F in which the neck was initially placed into flexion.

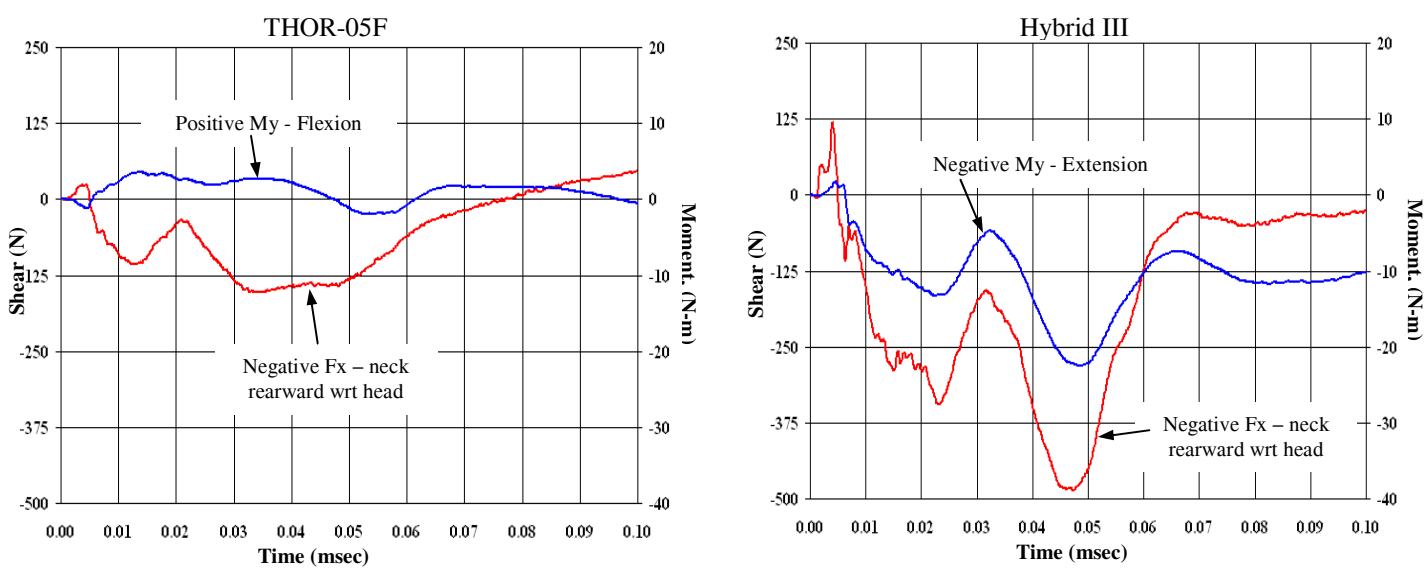

Fig. 7. Average upper neck shear (Fx) and flexion/extension (My) comparison for THOR-05F (left) and Hybrid III (right), normal bag, aggressive setup.

Injury metrics for various air bags. Table 2 provides the critical injury assessment values for human spine tolerance of a fifth percentile female and corresponding injury reference values for the Hybrid III. For the human, compression force, flexion moment, and extension moment were derived from tests on female post-mortem human subjects [Nightingale 1997; Nightingale, 2002]. Tensile force was derived from the male failure values reported by Chancey [2003] and scaled by 0.63 per the "equal stress, equal velocity" model scaling convention for geometrically similar models.

Table 2. 5th percentile female: critical values for upper neck, M_Y and F_Z.

	Human	HIII
Compression, F_C (N)	2020	2520
Tension, F_T (N)	1580	2620
Flexion, M_F (Nm)	29	155
Extension, M_E (Nm)	52	67

While the THOR-05F is designed to mimic the human neck, it is probably stiffer than the human spine. Though the increased stiffness has not been quantified, it is likely that some adjustment of the human cervical spine tolerance values will be necessary before they can be used as injury reference values in the THOR-05F. Thus, the human threshold values as presented herein are to be used for reference only.

Of the four test conditions with the THOR-05F, the "Modified Bag/Aggressive Setup" condition is the only one where the critical value for neck tension given in Table 2 was exceeded. The axial tension force Fz exceeded the human critical value of 1580 N shown in Table 2 in one of the five repeat tests. This air bag also produced the highest inflation pressure in tank test reports provided by the air bag supplier. Compared to the others, this setup also produced the largest upper neck moment which was dominated by extension throughout the entire bag-dummy interaction process (Fig. 6).

Values of HIC_{15} were also computed for each test. All forty air bag tests (both dummies, all test conditions) produced HIC_{15} values well below the threshold value of 700. As with the upper neck measurements, the "Modified Bag/Aggressive Setup" produced the highest HIC_{15} values (Fig. 8).

Air bag discrimination. Both the THOR-05F and the Hybrid III identified the "Modified Bag/Aggressive Setup" as the most threatening condition and the "Normal Bag/Benign Setup" as the least threatening condition. This finding was expected, as these two setup conditions and modifications to the bags were put in place in an attempt to facilitate this outcome. So, it is reassuring that the outcome was confirmed by both dummies. Though both the THOR-05F and Hybrid III found the "Modified Bag/Aggressive Setup" to be most threatening, the distinction for the Hybrid III was not as clear cut, where the highest two average Nij bars in Fig. 8 are almost even.

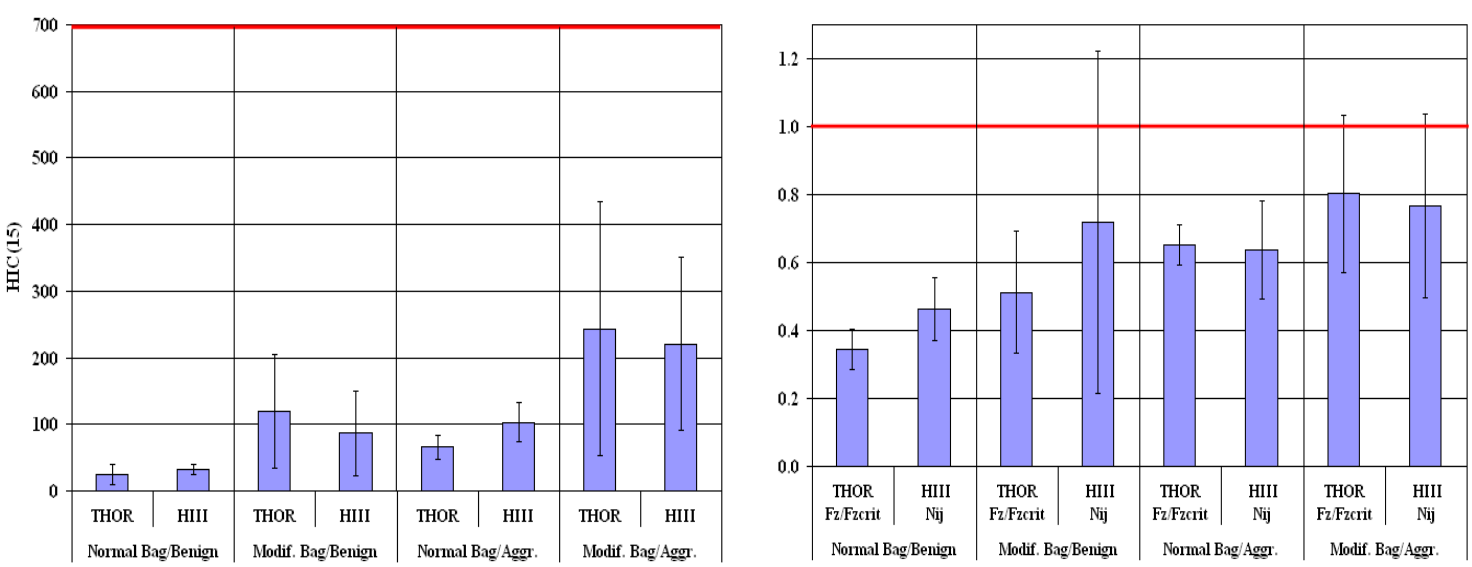

Figure 8. Average of Head Injury Criteria (HIC15) (left) and upper neck measurements (right) for the four test conditions. Error bars represent one standard deviation.

The distinction between "Normal Bag/Aggressive Setup" vs. "Modified Bag/Benign Setup" as the 2nd- or 3rd-most threatening is less apparent. It depends on which dummy and which injury metric is used. Using neck tension Fz as an arbitrator, the THOR-05F identified "Normal Bag/Aggressive Setup" as the more threatening of the two, but when HIC is used "Modified Bag/Benign Setup" is more threatening. The Hybrid III indicated the exact opposite conditions as the most threatening when Nij and HIC are considered. However, the high variability associated with the modified bag renders this comparison non-conclusive, as can be shown in Fig. 8 where the error bars associated with "Modified Bag/Benign Setup" are extremely large.

Deployment asymmetry. An asymmetric air bag deployment was observed in all forty deployments. Asymmetry was also observed in a series of deployments with no dummy present. These deployments were carried out to assure that the asymmetry was due to the air bag module alone and not an artifact of dummy positioning (Fig. 9).

As shown earlier, both versions of the air bags were tucked within the module using pleats on the right and left sides and folded (accordioned or reversed rolled) top and bottom. As the bag escaped from the module, the upper fold was observed to unravel and inflate well before the lower fold. This condition was observed for both normal and modified bags, and for both the simultaneous and sequential firings. The asymmetry, however, was more prominent in the modified bags.

When a dummy was present, the asymmetrical deployment of the first fold tended to produce a lateral thrust to the dummy resulting in a significant y-acceleration to the head with an Fy-force and Mx-moment at the upper neck. By the time the dummy was moving away from the bag, the second fold was just beginning to unravel and inflate. This "second punch" effectively spun the head about the neck z-axis by more than 90° producing an appreciable upper neck Mz moment (Fig. 10).

The THOR-05F and Hybrid III showed similar behavior in this regard. However, differences in overall body kinematics between the THOR-05F and the Hybrid III were revealed in the high-speed video. The THOR-05F exhibited much greater lateral head rotation and overall lateral body movement (Fig. 11).

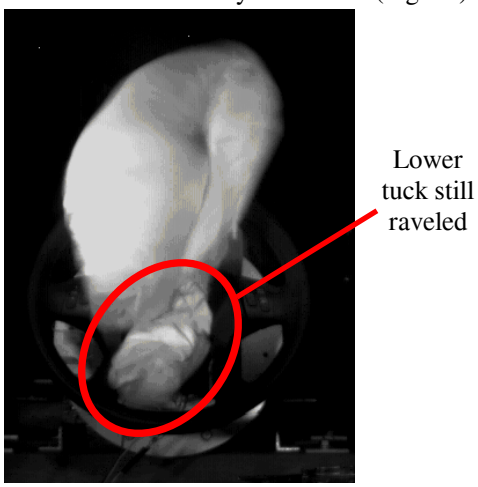

Figure 9. Asymmetric air bag deployment. Left side unravels and inflates before right.

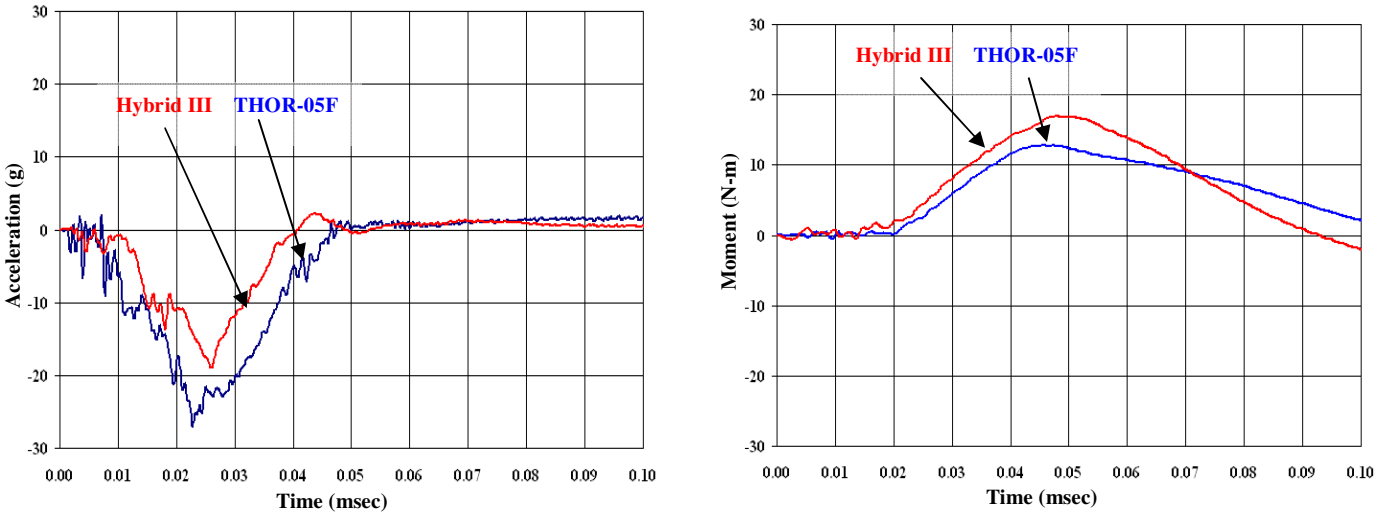

a. Head CG-y Acceleration

b. Upper Neck Mz moment

Figure 10. THOR-05F vs. Hybrid III for "Modified Bag/Aggressive Setup" condition: Average head CG-y acceleration (left) and upper neck moment (right).

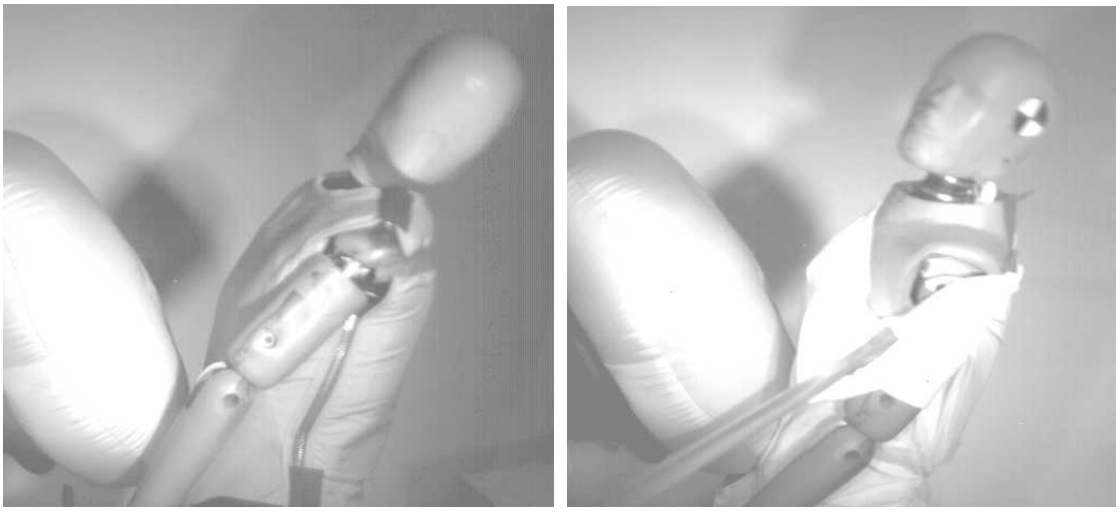

a. THOR-05F b. Hybrid III

Figure 11. THOR-05F vs. Hybrid III for "Modified Bag/Aggressive Setup" condition: head position at bag separation.

Cross-sectional vs "Ligamentous" comparison. For the THOR-05F, the total cross-sectional Fz is about 10% higher than the OC Fz, which means the front and rear neck cables have only a small contribution to the upper neck tension force. This also means that most of the load is borne by the "ligamentous" spine, which is significant from an injury assessment standpoint. The cable loads have more of a contribution to the total cross-sectional My moment, given the relatively low upper neck load cell moment, but the overall moment is still relatively low (only about 10 Nm maximum). This trend is consistent for all test conditions. This further confirms the intended capability of the THOR-05F neck design to distinguish the musculature from the ligamentous load by transferring load around the neck column via the cables.

Durability and functionality. There were no reports of durability or functionality problems with the THOR-05F during the 40-week test interval.

DISCUSSION

The present study herein has shown that the head/neck complex of the THOR-05F dummy is capable of capturing the detailed air bag load effects due to the variability of bag inflation on the occupant head and neck in OOP conditions. The test data obtained confirmed the expected performance of the THOR-05F head/neck complex design.

From an overall air bag assessment standpoint, both the THOR-05F and the Hybrid III identified the same test conditions as being the most threatening and the least threatening to the risk of an upper neck injury (where the most threatening condition produced responses near or above given injury risk assessment values). Both dummies indicated that the head injury risk was well below the HIC_{15}=700 reference value for all test conditions. Both dummies also identified the asymmetry of the deployments, and both recognized the "modified" bags to be less repeatable.

There were, however, some differences in responses between the two dummies. In the THOR-05F, neck tension was the predominant upper neck load. The upper neck moment and shear were much lower in magnitude than that of the Hybrid III. Compared to the Hybrid III, the THOR-05F neck had less tendency to go into extension. Hybrid III neck measurements also exhibited a sharp initial spike – most likely due to the relatively rigid head-to-neck coupling – that was not present in the THOR-05F signals.

Repeatability/Asymmetry. The tests herein indicate that both the asymmetry of the air bag deployments and the removal of the gas diffuser contributed to dummy response variability. This precludes a full assessment of THOR-05F repeatability. A valid repeatability assessment requires well-controlled air bag inflation and symmetric deployment. Such an assessment was performed previously on the 50th male THOR-NT using fleet air bags that deployed symmetrically and were folded in a conventional accordion pattern. These tests produced highly repeatable bag inflation and dummy responses [Li, 2007]. Such tests are necessary to fully assess the repeatability of the THOR-05F.

On the other hand, all Hybrid III tests under the "Normal Bag/Benign Setup" (the condition most

similar to an actual NHTSA vehicle compliance test) resulted in injury metrics well below injury thresholds. Therefore, it is likely that the range of the "Normal" fleet bag inflation variability is within the manufacturer's acceptable limits. (Note: the steering wheel-mounted bag blocker utilized herein – while providing a more aggressive deployment – probably produced more repeatable results than would actual fleet tests with no blocker since variability associated with the bag lodging behind the steering wheel rim was avoided.)

Assuming that the THOR-05F can be shown to be repeatable under truly identical test conditions, the variability of the test data herein may serve well in the assessment of air bag risk. For a given neck measurement under a given test condition, both the THOR-05F and the Hybrid III show some amount of variation. But the magnitude of the measure – and the amount of variation – depends on the dummy. Therefore, the acceptable limits that an air bag manufacturer places on inflation could depend on which dummy is used to develop the bag.

Caveats and Limitations. The experimental tests were carried out on a single air bag design and a modification of that design. All bags had similar capacities. Repeat tests for each test condition were limited to five. In addition, only driver air bags were tested and only at one OOP position. Nonetheless, the general observations made above on the THOR-05F upper neck Fz predominance, low My, and no extension are all consistent with prior OOP tests conducted with the 50th male THOR-NT using different air bags. Thus, the observations are true to form with the general THOR neck technology, and not an artifact of the particular air bags and test setups described herein.

The forty tests performed herein are not standard regulatory tests but rather scientific studies for the evaluation of the THOR-05F dummy. Moreover, the use of a non-standard steering wheel bag blocker is not representative of a production vehicle.

Nonetheless, the tests where the 1st and 2nd stages were fired sequentially with a 30 ms time lag represents a possible "low-level" deployment scenario that may exist in production vehicles. Additionally, the tests herein where both stages were fired simultaneously are representative of a possible "high-level" deployment that may also be seen in production vehicles.

Future Work. Previous work has been performed on the 50th percentile male THOR-NT showing favorable biofidelity of the head/neck complex. These tests include a comparison of THOR-NT loads against muscle and occipital condyle loads measured in tests run by the Medical College of Wisconsin (MCW) using post mortem human subjects [Pintar, 2005]. A favorable comparison of the THOR-NT neck response against a human model was also demonstrated by Duke University [Dibb, 2006]. Similar biofidelity evaluations have not yet been carried out on the new THOR-05F's Beta neck.

It should be noted that there are no injury criteria defined for the THOR-05F dummy, nor are there standard OOP positions defined for using the THOR-05F dummy. The present work was intended to understand air bag load paths to the neck in OOP conditions so that well-defined OOP positions for the THOR-05F dummy can be established and injury criteria may be developed in the future. This should probably include a lateral bending criteria.

SUMMARY

• Neck tension in the THOR-05F was the most critical load, with most passing through the ligamentous spine and very little load borne by musculature. This result contributes to the understanding of how injurious air bag load paths are imparted to the neck of humans in OOP conditions.

• Compared to Hybrid III, the THOR-05F neck shows less tendency to go into extension. The upper neck moment (My) and shear (Fx) were much lower in magnitude than those of the Hybrid III. Head accelerations were similar to those produced by the Hybrid III 5th.

• The THOR-05F demonstrated its ability to discriminate air bag aggressiveness, especially in its upper neck tension measurements.

• The THOR-05F response to the asymmetric deployments resulted in a substantial twist of the head about the z-axis of the neck, and a high corresponding Mz upper neck moment. This indicates that an ATD biofidelity requirement and an injury criterion may need to be investigated to assess the threat of injury for such a response.

• The THOR-05F produced relatively repeatable measurements and proved to be durable. It performed smoothly throughout the test series and was generally user-friendly.

• The THOR-05F's distinct neck assembly provides a new perspective on loading of the cervical spine and application of injury tolerances. It also prompts a

new requirement for neck injury reference values specific to the THOR-05F.

DATA AVAILABILITY

All reports and data, including time-history traces, videos, and still photos from the tests described herein may be downloaded by accessing NHTSA's online Biomechanics Database at: http://www-nrd.nhtsa.dot.gov/database/nrd-51/bio_db.html. Reports include descriptions of the test set-ups and instrumentation. Data channels collected on both dummies, but not reported herein, include linear and angular head acceleration, chest deflection, and chest acceleration. Additionally, the THOR-05F recorded lower neck loads and upper spine acceleration.

ACKNOWLEDGEMENTS

This research effort was sponsored by the National Highway Traffic Safety Administration (NHTSA) through a Joint Cooperative Research Agreement with the US Army Medical Research and Materiel Command under contract W81XWH-06-C-0051.

REFERENCES

1. Robbins, D. (1993), "Development of Anthropometrically Based Design Specifications for an Advanced Adult Anthropometric Dummy Family.," Volumes 1 & 2. DOT-HS-806-716, 717, National Highway Traffic Safety Administration, Washington DC.

2. SAE J211 (1995) "Instrumentation for Impact Test," SAE Surface Vehicle Recommended Practice, Society of Automotive Engineers, Warrendale, PA, March 1995.

3. Nightingale, R.W., McElhaney, J.H., Camacho, D.L., Winkelstein, B.A., Myers, B.S.(1997), "The dynamic responses of the cervical spine: the role of buckling end conditions and tolerance in compressive impacts," 41st Stapp Car Crash Conference Proceedings, 451-471

4. Nightingale, R.W., Winkelstein, B.A., Knaub, K.E., Myers, B.S. (2002), "Comparative bending strengths and structural properties of the upper and lower cervical spine," Journal of Biomechanics 35 (6), 725-732.

5. Chancey, V.C., Nightingale, R.W., Van Ee, C.A., Knaub, K.E., Myers, B.S. (2003), "Improved estimation of human neck tensile tolerance: reducing the range of reported tolerance using anthropometrically correct muscles and optimizing physiologic initial conditions, " Stapp Car Crash Journal 47, 135-154.

6. Shams, T., Huang, T., Rangarajan, N., Haffner, M. (2003), "Design requirements of a fifth percentile female version of the THOR ATD," Paper Number 421, 18th International Technical Conference on Enhanced Safety of Vehicles, U.S. DOT.

7. Huang, T.J, Shams, T., Rangarajan, N., Haffner, M., Eppinger, R. (2003), Development of an advanced 50th percentile male head/neck system for application to crash test dummies," Paper Number 425, 18th International Technical Conference on Enhanced Safety of Vehicles, U.S. DOT.

8. J. McDonald, T. Shams, N. Rangarajan, D. Beach, T. Huang, J. Freemire, M. Artis, Y. Wang , M. Haffner (2003), "Design and development of a THOR based small female crash test dummy," Stapp Car Crash Journal, V47.

9. Pintar, FA, Yoganandan N, and Baisden J. (2005) "Characterizing occipital condyle loads under high-speed head rotation," Stapp Car Crash Journal, V49:33-47.

10. Dibb, A.T., Nightingale, R.W., Chancey, V.C., Fronheiser, L.E., Tran, L., Ottaviano, D., Myers, B.S., (2006) "Comparative Structural Neck Response of the THOR-NT, Hybrid-III, and Human in Combined Tension-Bending and Pure Bending," Stapp Car Crash Journal, 50:567-581.

11. Lu, Z, Chan, P. C., Martin, P.G., Ridella S. (2007), "OOP air bag tests using the THOR-NT", Paper Number 07-0293, 21st International Technical Conference on the Enhanced Safety of Vehicles, U.S. DOT.

12. National Highway Traffic Safety Administration, U.S. Department of Transportation, Motor Vehicle Safety Standard No. 571.208.

TEST PROGRAM TO DEFINE OBLIQUE CHEST LOADING IN SIDE IMPACT

Frank Pintar
John Humm
Narayan Yoganandan
Medical College of Wisconsin
Milwaukee, WI, USA

Peter G. Martin
National Highway Traffic Safety Administration
U.S. Department of Transportation
Washington, D.C., USA
Paper No. 09-0557

ABSTRACT

Near side impact crashes – especially pole impacts – have the potential to induce antero-lateral oblique loads to the chest. Current side impact dummies and most laboratory experimental studies have been designed to assess direct lateral impacts. A recent analysis of real world crashes indicated that the human chest experiences oblique loading in side impact crashes – in particular crashes into narrow objects. This paper describes the development of a new sled test program to determine the oblique impact response of the human and to evaluate dummy biofidelity in an oblique mode of loading. The program involves the use of chestbands on dummies in full-scale vehicle tests accompanied by sled tests with unembalmed post mortem human subjects (PMHS). Sled tests are run under varying load wall conditions with a buck configured specially to mimic dummy loading seen in the vehicle tests. The chestbands provide comparative measures of thoracic deformation. Ultimately, the chestband measures will help establish the instrumentation requirements of an ATD for use in a side impact test with a significant oblique component. Additionally, this work could help introduce more biofidelic injury metrics for side impact ATDs.

INTRODUCTION

Side impact crashes often produce more serious injuries and a higher percentage of fatalities than frontal crashes despite a lower overall incidence rate (NHTSA Traffic Safety Facts, 2007). Vehicle to vehicle configurations as well as single vehicle crashes are common. Current federal motor vehicle safety standards address both of these crash types. Most single vehicle side crashes result when the driver loses control and collides with a fixed object. Often the fixed object is a pole or tree. A study using US DOT National Automotive Sampling System (NASS) and Fatality Analysis Reporting System (FARS) data indicated that the overall distribution by crash delta-V of vehicle-to-vehicle side impacts was approximately equal to narrow object impacts (Zaouk et al, 2001).

A more recent investigation of the NHTSA Crash Injury Research Engineering Network (CIREN) database examined side pole crashes in more detail. The CIREN data was used to determine injury mechanisms and associated injuries related to the pole impact location on the vehicle. It was determined that the most devastating injury patterns occurred when the center of the pole impact was between the center of the wheelbase and 25 cm forward of the center of the wheelbase (Figure 1) (Pintar, et al, AAAM, 2007). For this location of maximum damage, greater than 60% of occupants sustained AIS 3+ injuries to head, chest, and pelvis body regions. This particular location was also responsible for a unique chest injury pattern that produced unilateral rib fractures and lung contusions. It was hypothesized that this injury pattern was induced by oblique loads to the chest through the intruding door wherein the center of the intrusion was slightly forward of the occupant torso.

PURPOSE

Since the findings from the CIREN study on narrow object side impacts indicated that the most devastating injuries were sustained with a pole impact to a certain small area of the vehicle, this type of impact was investigated in more detail. The CIREN study concluded that because the chest injuries in these occupants were largely unilateral (closest to impact), and due to the shape of the door intrusion profile, the intruding door induced an oblique load to the antero-lateral portion of the occupant's chest. This was also verified in many vehicles by twisted seatbacks indicating asymmetric loading.

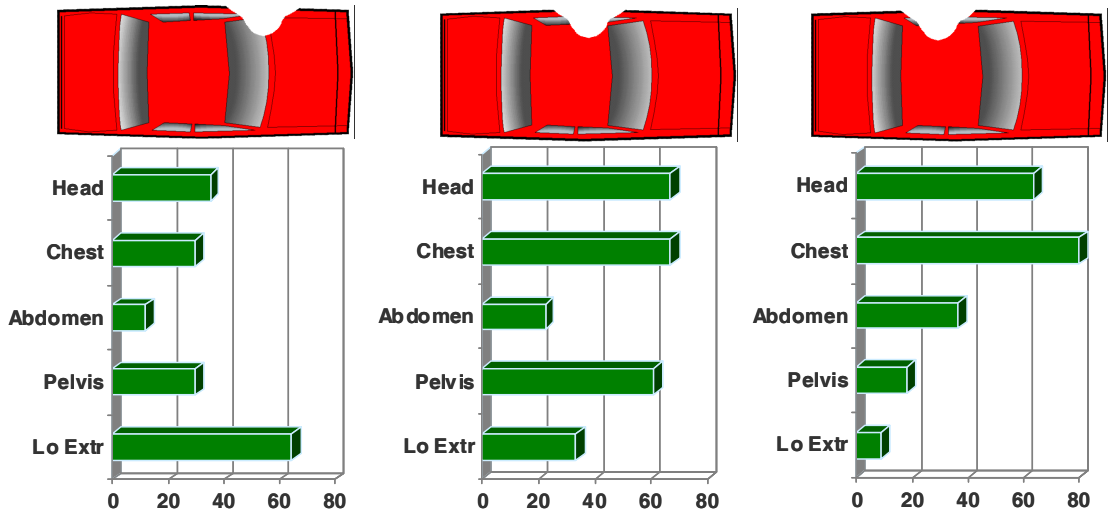

Figure 1. CIREN study results indicating percentage of occupants in side pole crashes with AIS 3+ injuries by body region categorized by location of vehicle damage. Note the middle bar chart depicts greater than 60 percent of occupants sustained head, chest, and pelvis injuries when the narrow object struck the vehicle between the center of the wheelbase and 25 cm forward of center.

This hypothesis is being pursued in the testing program described herein. The desire is to replicate the real world loading conditions in a laboratory sled test procedure. The real world results are first reproduced in full-vehicle side pole crash tests. Injury patterns in the vehicle crash test are then verified for similarity with those found in the CIREN study occupants.

Thereafter, the loading mechanisms can be defined in more detail. The chestband instrumentation is used to describe the magnitude and shape of oblique chest loading. Accelerometer signals from different parts of the torso are used to define the relative timing of the loading to the body regions. The goal of the sled test protocol is to replicate the shape of the chestband contours and the relative timing of the body region loads observed in the vehicle crash tests.

The ultimate goal of the test program is to use the sled test protocol to conduct multiple tests defining injury metrics for oblique chest loading and dummy biofidelity response requirements (Table 1). The sled test protocol is desirable because it provides a well-defined, highly repeatable environment in which specialized instrumentation may be applied to fully evaluate biomechanical response and injury tolerance. This paper describes how the full vehicle crash tests are used to develop the sled testing protocol.

METHODS

The initial methodology for the two experimental test series – the full-vehicle tests and the sled tests – is described below. Preliminary results are given to provide data being used to generate final protocols.

To determine the degree of oblique loading to the chest, a series of full-scale vehicle tests with both ATDs and PMHS have been conducted. Using passenger cars and sport-utility vehicles (SUV), tests have been carried out to observe the pattern of oblique loads in an actual vehicle environment. These tests define the temporal thorax deformations through the use of chestbands The crash tests also define the relative timing between shoulder, thorax, abdomen, and pelvis during the impacting event. A sled buck has been designed with angled load plates that induced antero-lateral oblique loads to the occupant similar to those seen in the vehicle tests.

Subjects. All tests are carried out with post mortem human subjects (PMHS) and with different types of dummies. In accordance with standards set forth by MCW's Institutional Review Board, unembalmed PMHS are procured, medical records evaluated, and screened for HIV, and Hepatitis A, B, and C. Anthropomorphic data and pretest x-rays are obtained and chestbands are affixed according to procedures established by (Pintar et al., 1997). Specimens are dressed in tight-fitting leotards, and a mask covers the head/face.

Table 1. Relationships between studies that define entire program.

Type of Study	Purpose	Outcome	Note
53 CIREN Occupants in narrow-object side impacts	Define real world injury patterns	Location for damage corresponding to worst case injury pattern	
Full-Vehicle Crash tests with PMHS	Reproduce damage and trauma at location defined in CIREN cases.	PMHS provides injury pattern, relative timing of body regions loaded, and chest deformation patterns	Need relative timing for different types of vehicles
Sled tests with PMHS and Dummy occupants	Reproduce vehicle crash test chest deformation patterns and relative timing of loading to body regions.	Biofidelity requirements and injury criteria for oblique side impact loading	Design load wall to match loading conditions seen in vehicle crash

The PMHS are examined for injury with a complete autopsy following the test. Anthropomorphic test devices (ATD) or dummies, are also used. ATDs are being used to conduct preliminary evaluations of sled buck design to ensure that the goals of the design are being met. It is important to conduct matching tests with ATDs to determine if the sled buck design and overall test protocol are producing consistent results. For example, an obliquely oriented load wall has been evaluated by varying the angles of impact, and the timing of contact between thorax, abdomen, and pelvis have been evaluated by varying the extent of pelvic plate offset. ATDs provide a consistent, repeatable output to determine if sled changes have an effect. In this way, PMHS tests are only completed after the protocol has been validated with ATDs.

Subject Instrumentation. In all tests a standard set of instrumentation is used. Each of the human surrogates is instrumented with head, T1, T12, and sacrum triaxial accelerometer packages (Figure 2). In addition, a nine-accelerometer package (NAP) is used to derive head angular accelerations. For the dummies, an internal NAP system from the dummy manufacturer is used, and for the PMHS, a custom-designed pyramid NAP (PNAP) is mounted as described and validated previously (Yoganandan et al., 2006). Rib and sternum accelerometers are also mounted directly to the subject.

Each surrogate is instrumented with a 59-channel chestband device to record chest deflection contours. Each chestband uses 59 strain gauge bridges located around the band to measure the local curvature; curvatures are interpreted and combined over the length of the band at a given time point to produce a total contour of the chest. The contours are computed throughout the event to capture chest shape change. Local deformation at any point along the contour can be calculated with respect to a reference point.

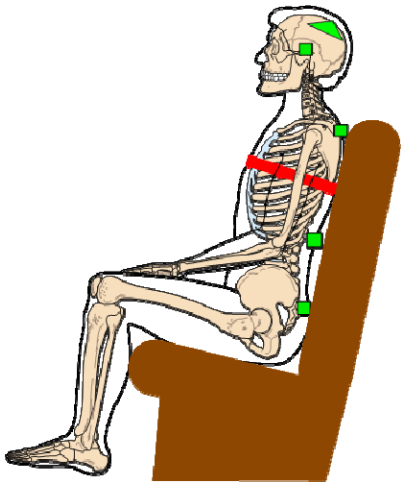

Figure 2: Each PMHS and dummy was instrumented with triaxial accelerometer packages (squares) at the head, T1, T12, and sacrum. In addition, a nine-accelerometer package (triangle) was fixed to the head to derive angular accelerations. Chestbands were also included to determine the nature of the oblique loads to the thorax.

Fitting subjects with Chestband: Since the internal ATD instrumentation is uni-lateral and measures only one location per rib level, matched-pair tests conducted using ATDs are also instrumented with chestbands (Figure 3). On the PMHS, the chestband

is placed just under the axilla such that rib-4 laterally is directly under the chestband; on the dummies the chestband is placed over the upper rib (Pintar et al., 1997).

The accelerometers at T1, T12, and pelvis are triaxial and are used to determine relative timing of the sequence of loading that occurs to the upper thorax, abdomen, and pelvis. To secure the triaxial packages to the PMHS, custom designed mounting blocks that allow for screws into the lamina or pedicle of the vertebrae are used. The rise time of the each of the y-axis accelerometer responses is used to assess the time at which each body segment is loaded by the sled plates. This same instrumentation package is used in both the full-vehicle tests and the sled tests so comparisons can be made.

Customized software has been written to provide flexibility in choosing where to measure the chest deformations. The custom software also allows a choice of reference points so that chestband deformations can be compared to dummy internal deflection sensor measures. A series of contours can be animated to show the change in deformation throughout the test. The chestband is a versatile research tool that provides direct measures of chest deflection in both PMHS and ATDs. It provides the best known method of relating chest deformations and patterns with injury in the PMHS. This, in turn, can be used to derive injury criteria for specific ATDs as the same measures in matched-pair tests can be used to equate injury risk to a biomechanical metric.

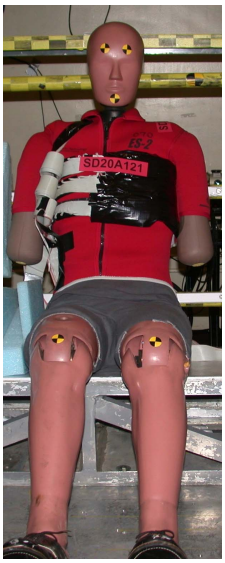

Figure 3: ES-2re dummy thorax fitted with a chestband over each of the three ribs.

Processing of Chestband Contour Data. To examine the chestband contour results, the data is processed using RbandPC software and customized post-processing software developed in-house as follows. First, contours are calculated at every millisecond from chestband curvature signals using RBandPC software (Version 3.0, Conrad Technologies Incorporated, Washington, DC, USA, available from NHTSA) and pretest measurements of the specimen (Pintar et al., 1996). The local coordinate system is defined by using the two gauges closest to the posterior tip of the spinous process at the appropriate level of the thorax. Gauges closest to the spinous process, sternum, and the most lateral points on the left and right sides of the specimen are identified by palpation and recorded, including measurements of left to right chest breadth and sternum to spinous process depth.

On each contour, one-half of the chest deflection is computed. The origin is identified at each contour time step by determining the point one-half the chest breadth distance from the spine along a vector from the spine to the sternum. Distances from each point on the contour to the origin are computed at every time step, and the initial length is defined as the distance in the pre-test contour (approximately 100 milliseconds before impact). The maximum deflection is computed by finding the point on the contour which yields the greatest change from its initial length (Figure 4).

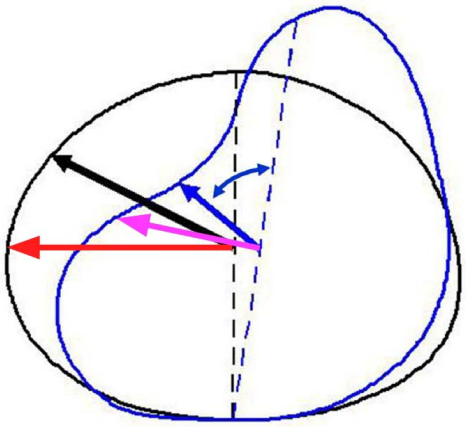

Figure 4: Chestband Contour Plots depicting location of maximum deflection (Black/Blue arrows) and location where deflection would mimic a dummy internal sensor (red arrows).

This method, called the "forced-angle" response, is slightly different than what has been used in the past (Maltese, et al 2002). Previous methods calculated deformations along a line perpendicular to the center

line between spine and sternum. The forced-angle method uses a fixed point of reference just as a dummy chest deflection measurement device is anchored at a fixed point at the spine box. From this fixed reference point one can force an angle (90 degrees) to mimic how an ATD would measure the deformation, or one can allow the algorithm to pick the angle at which the maximum deformation occurs. This permits either direct comparison with dummy internal measures or defines the location where the maximum deflection could be detected if an internal measurement device would be appropriately located.

Full-Scale Vehicle Tests

Full-scale vehicle crash tests have been conducted at 32 km/h into a 10-inch diameter pole. The test matrix is indicated in Table 2. The goal of this test series is to reproduce similar injury patterns to those seen in the real-world CIREN cases (i.e., skull fractures, unilateral (left) rib fractures, and a pelvis or lower limb fractures.) Additionally, these tests are used to establish the relative timing of body segment contact for different types of vehicles and to see if the timing is appreciably different between vehicle types. The ES-2re and the NHTSA-SID-H3 dummy are being used to help define the relative timing of body segments more clearly between vehicle types and to serve as a verification of the PMHS testing.

Table 2:
Test matrix for full-vehicle side impact crash tests into a pole.

Vehicle type	Occ. type	Speed (km/h)	Test conducted
Small Car	PMHS	32	To be completed
Small Car	ES-2re	32	1996 Merc Mystique
Small Car	SID-H3	32	1994 Toyota Corolla
Mid-size Car	PMHS	32	1993 Dodge Intrepid
Mid-size Car	ES-2re	32	1990 Audi 100
Mid-size Car	SID-H3	32	1999 Ford Taurus
SUV	PMHS	32	1995 Jeep Cherokee
SUV	ES-2re	32	1989 Jeep Cherokee
SUV	SID-H3	32	To be completed

The results from the previously published CIREN data have been used to design the test conditions of the vehicle crash tests to induce maximum head and chest loads to the test occupants. The CIREN results summarized in Figure 1 demonstrate that the location of intrusion on the vehicle that produced serious injuries to multiple body regions was between the center of the wheelbase and 25 cm forward of the center.

With respect to the occupant, this location was translated as the center of the pole aligned with a point 10 cm forward of the occupant H-point. The vehicles chosen to this point for testing have been those available from the local discard lot that did not have any structural anomalies. The vehicles did not have side airbag systems which helped to better distinguish the timing of when the occupant contacted the intruding door with different portions of the body.

In tests conducted thus far, the principal direction of force was 285 degrees, or 15 degrees off a direct 9 o'clock impact to the driver. The vehicles were instrumented with a tri-axial center of gravity (CG) accelerometer and door accelerometers in front and rear aspects recording in the lateral direction.

Sled Tests

The sled buck design is being used that allows for direct experimental investigations into human injury criteria that may differ from existing direct lateral injury criteria. It also allows for matched-pair testing of PMHS and ATDs to obtain biofidelity criteria and assess dummy responses. Such a sled buck is intended to be generic enough not to represent a particular vehicle and yet produces the type of loading environment that the human experiences in the actual crash environment. The sled buck design should also demonstrate experimental repeatability and be easily reproduced in computational modeling studies.

<u>Previous Sled Configuration</u>. In the past, a high degree of success has been achieved experimentally by defining the near side impact pulse as primarily a change in velocity between the door and the occupant (Kalieris, original Heidelberg setup, Pintar Stapp side impact, Maltese, et al, 2002). Thus, a generic rigid wall was designed in these early experiments to mimic the average overall dimensions of a vehicle door but to also facilitate load wall sensors defining loading to various body regions. The results of using this load wall arrangement facilitated injury criteria development including the Thoracic Trauma Index (TTI) and maximum chest compression (Cmax) as injury indicators in dummies used in regulatory tests. Such a sled design has also been amenable to assessing the effects of padding and even offers the inclusion of airbag technology.

Initial Sled Configuration. The first attempt at a sled buck design was to alter the previous configuration to incorporate an oblique loading vector to the chest.

The design included a Teflon-covered seat and minimally supported back such that the occupant would slide across the seat during the application of the sled pulse and would contact the rigid wall at the predefined velocity setting. This laboratory sled buck was designed with the intention of matching the full-vehicle test results as closely as possible. The main goal of the initial design was to mimic the relative timing of body contact with the load wall (vehicle door).

Using the full-scale vehicle test data as a reference, the onset of acceleration in the direction of sled travel (Y-axis) for T1 (thorax), T12 (abdomen), and sacrum (pelvis) accelerometers was assessed. The sled load wall design was initially selected to match the previous design used during 90º side loading evaluations of the various side impact ATDs described earlier (Maltese et al, 2002; Yoganandan et al, 2002). The load wall is composed of four distinct load plates: one each at levels of the subject's thorax, abdomen, pelvis and legs. Force transducers on the plates measure loads imposed by the test subject. The load plates may all be fixed along the same vertical plane, or one may be positioned closer to the subject (and offset from the other plates) so that it bears more of the initial load.

In the 15º full-vehicle pole tests, it was observed that the door intrusion and subject position produced a door-to-subject interaction angle that was actually sharper than 15º. Thus, the original test setup has been modified so that the upper (thorax) and middle (abdomen) load plates contact the test subject obliquely (i.e., the load vector has both lateral and frontal components) rather than strictly laterally as in previous tests (Figure 5).

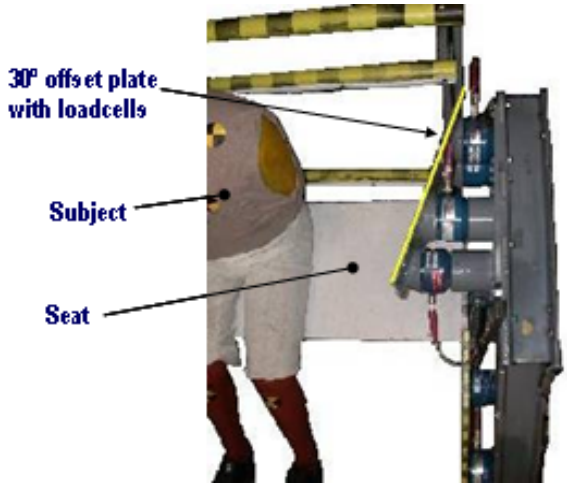

Figure 5. Sled buck load wall demonstrating oblique orientation of load plates.

The desired effect is achieved by positioning individual load plates at angles relative to the deceleration vector. The pelvic load plate is not angled to allow the lower limbs to move freely in the vector direction. It is felt that if the pelvic plate is angled there will be the potential to induce an artificial fulcrum point which would not only induce trauma to the occupant, but also alter the body motion of the upper torso.

The load plates are also offset from each other such that contact timing with body segments may be altered. To date, a series of ATD and PMHS sled tests have been performed using various load wall set-ups to mimic the range of oblique loading experienced in actual full-scale vehicle tests. Once the testing is complete, the results of the PMHS and ATD tests will be compared to examine the biofidelity of the ATD thorax under oblique loading.

RESULTS

Full-Vehicle Pole Tests. To date, two PMHS have been completed in full-vehicle crash tests; one in a mid-size car and another in an SUV. Analysis of the video from the experiments demonstrated that as the pole deformed the vehicle, the body continues moving in the direction of travel. As the door deformation proceeded, the focal intrusion just anterior to the occupant torso produced an angular intrusion and loading on to the anterolateral area of the chest. It appeared that the chest was loaded by the intruding door and squeezed into the seatback.

The autopsy results indicated that both PMHS had a skull fracture; accelerometer traces demonstrated head contact with the pole. Each PMHS also had extensive left sided rib fractures as well as lower limb trauma (Table 3). With just these two PMHS it was demonstrated that the trauma produced in these crash tests was very similar to the trauma recorded in the real world CIREN cases where the pole intrusion was in the same location on the vehicle. There was AIS=3+ trauma in head, chest, and pelvis or lower extremity regions.

The experiments demonstrated that the chest in this crash configuration does experience oblique loading. The chestband contours demonstrated that the anterolateral aspect of the thorax was loaded so severely that the chestband experienced a kink as the PMHS was squeezed between the door and the seatback (Figure 6).

Table 3. Injuries documented in the PMHS tests in full-vehicle crashes.

Test Configuration	Head Injury	Thorax Injury	Pelvis/Lower Extremity Injury
PMHS in Mid-Size Car	Left zygoma and Basilar skull fractures MAIS=3	> 3 rib fractures left side and clavicle fracture MAIS=3	Displaced/comminuted left femur, pelvic ramus fracture MAIS=3
PMHS in SUV	Bilateral orbital wall fractures, linear and Basilar skull fractures MAIS=3	> 3 rib fractures left side with flail chest, clavicle fracture MAIS=4	Pubic symphasis, sacro-iliac joint, unstable rami fractures MAIS=3

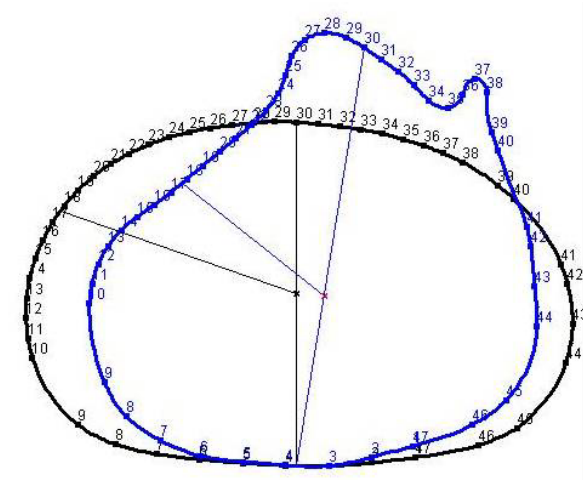

Figure 6: Chestband contour of PMHS in full-vehicle side pole impact test.

Sled Tests. PMHS tests have been completed with both 30 and 20 degree angled plates. Examples of chestband contours from PMHS tests run in both configurations are demonstrated in Figure 7. From these results it appears that the 30 degree load wall configuration mimics the chestband contour shapes and location of maximum deflection from the full-vehicle test configuration slightly better than the 20 degree sled test.

In order to address the question of body segment timing, the measures from the Y-axis accelerometers at T1, T12, and pelvis have been examined. The 30-degree load wall on the sled was adjusted such that the offset distance between the thorax and abdomen plates compared to the pelvis and leg plates was 5 cm, 7.5 cm, or 10 cm. The NHTSA-SID dummy was tested in all three configurations and compared to a full-scale vehicle test run also with the NHTSA-SID.

The body accelerations of all four of these tests are compared in Figure 8. As far as the timing of the signals, it is apparent that the 5 cm sled test comes closest to the timing in the vehicle test. The accelerometer signals from two PMHS full-vehicle tests are shown in Figure 9. It is apparent from these traces that the relative timing of the body segments in the full-vehicle pole test is such that the pelvis is contacted first with the torso lagging somewhat.

DISCUSSION

A test program to characterize the extent of oblique loading in side impact is being established. From the examination and analysis of more than 50 CIREN real world cases it is hypothesized that oblique chest loading occurs in side pole crashes when the pole impact site is just forward of the occupant torso. This scenario produces severe head, chest and lower extremity injuries and is characterized by unilateral rib fracture patterns and lung contusions. This scenario is reproduced in a laboratory setting by orienting the center of the pole 10 cm forward of the H-point of the occupant. Chestband contours document the extent of oblique chest loading in PMHS occupants.

Using the full-vehicle tests as a guide, a unique sled test has been designed to mimic the oblique chest loading. A series of PMHS and dummy tests have revealed that a 30 degree oblique load to the thorax and abdomen of the occupant, offset by about 5 cm from the pelvis and leg load wall reproduces the relative timing of body segment loading. These settings will be further verified in future experiments with additional dummies and PMHS.

It is also apparent that because human anthropometry varies considerably, the sled load wall plates should be designed to adjust to such variations. In other words, a fixed thorax plate on the sled may impact one PMHS at the rib-5 level and a second PMHS at the rib-2 level. The future design of the load plates will take into account such variations in PMHS anthropometry so that direct comparisons of shoulder, thorax, abdomen, and pelvic loads can be made between dummies of different sizes and PMHS of different sizes.

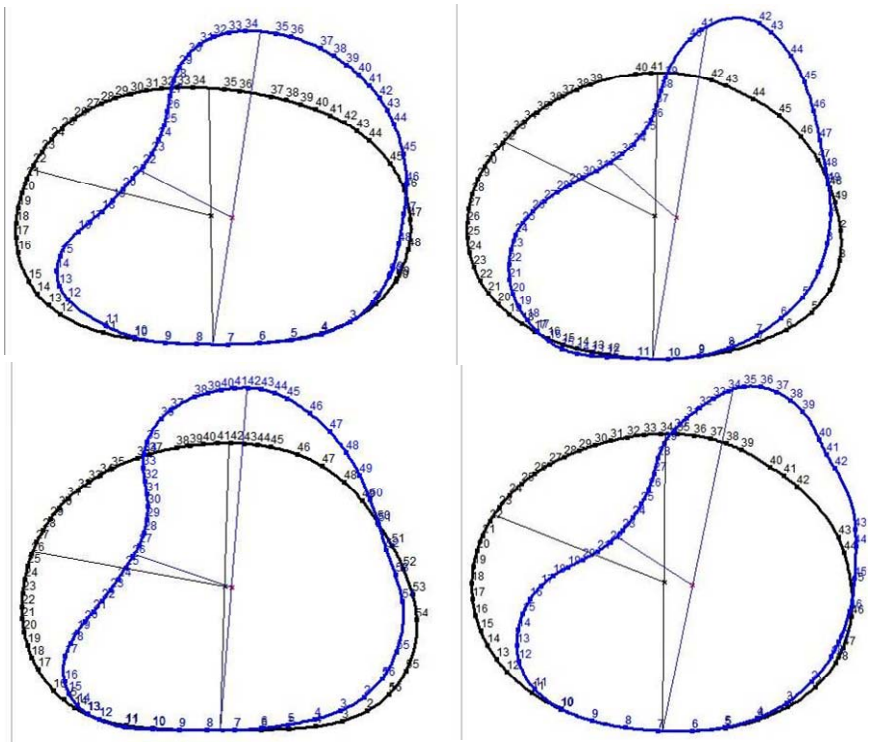

Figure 7. PMHS chestband contours from 20-degree (left) and 30-degree (right) sled tests. Note that direction of maximum deflection is closer to vehicle test (figure 6) for 30-degree tests than for 20-degree tests.

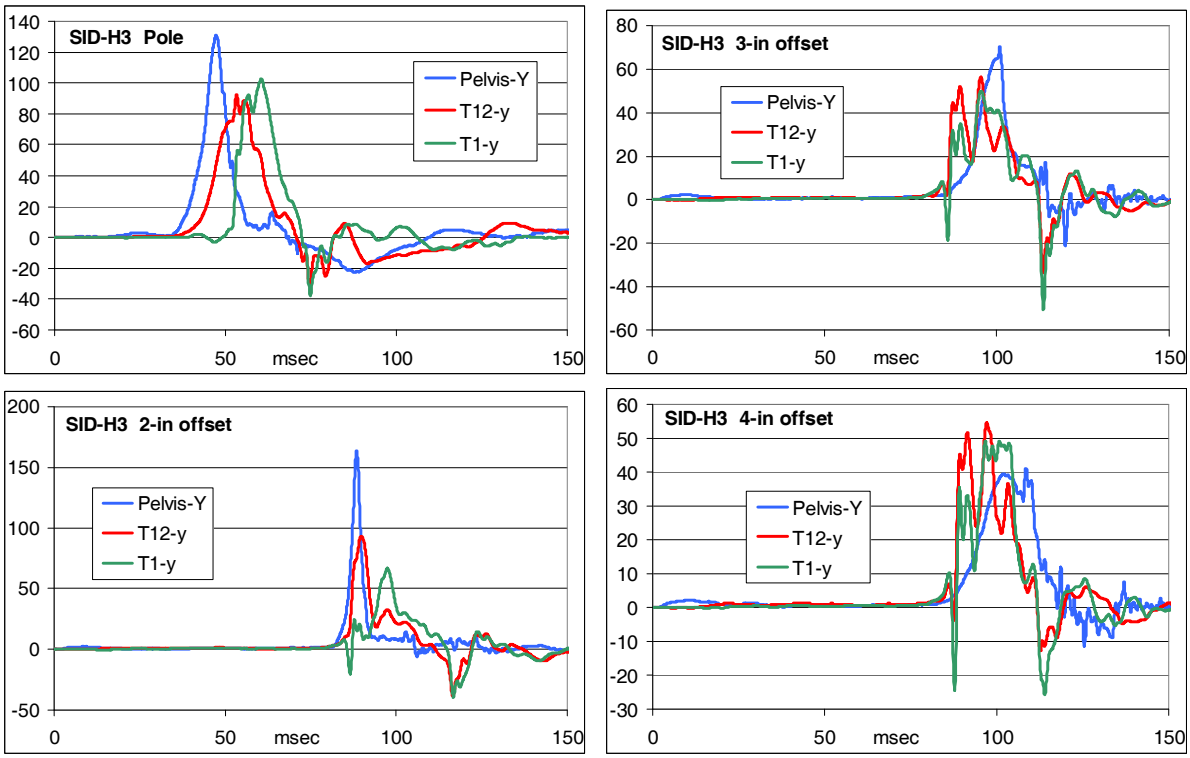

Figure 8. Accelerometer Y-axis traces from a SID-H3 dummy run in a full-vehicle pole test (up-left), 5 cm offset sled test (lo-left), 7.5 cm offset sled test (up-right), and 10 cm offset sled test (lo-right). Note the relative timing of the acceleration signals is most similar between the pole test and the 5 cm offset sled test.

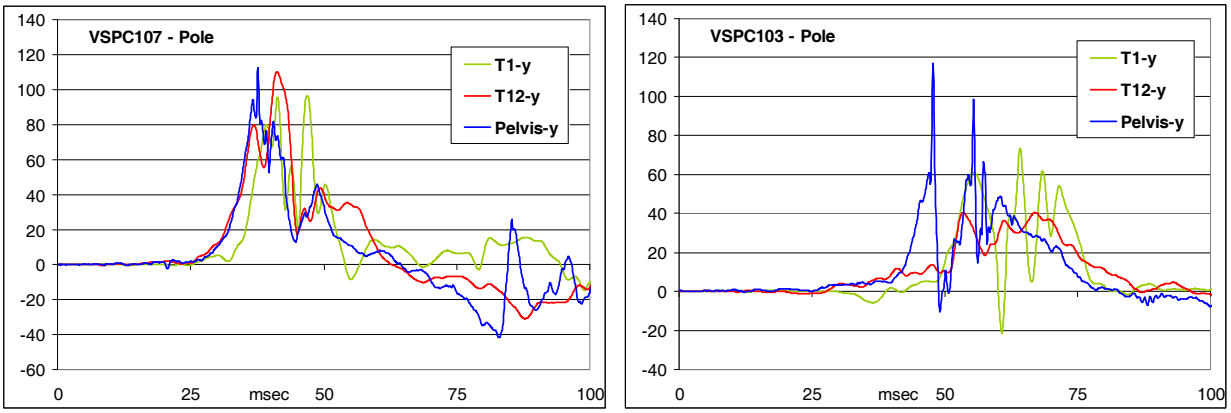

Figure 13: Accelerometer Y-axis traces from PMHS runs in full-vehicle pole tests.

In future efforts, the degree of oblique loading in full-scale vehicle tests and in subsequent sled tests will be further characterized using the chestband contours. These contours can be used in conjunction with the "slice" model to identify the minimum number of chestband points (and their locations) that are needed to sufficiently characterize thorax deformation as described in Campbell et al, 2005. In this manner, the "slice" model may be used to assess ATD instrumentation requirements for measuring oblique thorax loads. The model also provides many valuable insights used in the design, development, and evaluation of restraint systems. And in a sufficiently biofidelic and properly instrumented ATD, the "slice" measurements, which include measures of stress and strain, can conceivably be used as a means to assess injury potential.

The configuration of the tests described earlier represents a worst-case scenario. The level of oblique loading seen in other types of full-scale vehicle crash tests is probably lower than that prescribed herein. Nonetheless, it may be used as a benchmark for ATD use in any sort of developmental tests where the oblique component rises beyond those seen in actual full-scale vehicle crash tests. Under oblique loads such as those imposed by the 30-degree load wall, it is likely that additional ATD measurement locations will need to be monitored in order to accurately record the oblique loading response. Development of such a system for measuring dummy chest deflections in multiple locations optically is already on the market. The RibEye measurement system is currently being evaluated by the NHTSA as a potential improvement to dummy chest deflection measures.

Human injuries: oblique vs. lateral. Contents of the human thoracic ribcage and abdomen are complex, multifunctional, three-dimensional, and, from a biomechanical and material property perspective, heterogeneous. An oblique impact, at the same severity and to the same level of the chest, engages the same internal organ differently, compared to the pure lateral vector. For example, at the upper thoracic region, the pure lateral vector directly loads regions dorsal to the subclavian artery while an oblique vector at 30-degree applies impact forces to ventral arterial regions engaging the common carotid artery and brachiocephalic vein. The former vector introduces postero-anterior load transfer to these tissues, in contrast to anteroposterior load transfer by the oblique vector. The ribcage is loaded with direct compression at its most lateral region by the pure loading vector.

This is in contrast to the angulated compression at the anterolateral region by the oblique vector. The anterior regions of the thoracic vertebral body sustains lateral shear in the pure loading case, whereas it resists a force angled towards the right pedicle in the oblique case. At an inferior level, while the aorta is protected by the stomach in the pure lateral loading vector, in the oblique vector case, the major vessel is protected by the relatively smaller left lobe of the liver and its articulations (Yoganandan et al, 1996). Similar regional load transfer mechanisms are apparent as the impact vector traverses caudally. Purely anatomic considerations with respect to the impact vector in addition to functional and constitutive differences are responsible for the mechanisms of load transfer, tissue injury, and biomechanics (Yoganandan et al, 2000).

The direct 90 degree lateral loading on the struck side indcue deformations of the ribcage initiating from the region of peak skeletal curvature. In contrast, an obliquely oriented vector induces antero-lateral compression of the ribcage on the struck side, and the impact force is thus transferred via a combined shear and compression mechanism at the initiating region. Frontal impact-induced chest injuries with belt-only versus combined airbag and belt loadings have used this type of concept for determining load transfer to the skeletal structures and soft tissues and delineating injury mechanisms (Pintar et al, 2007; Pintar et al, 2008). The added shear component in the oblique side impact vector places demand on soft tissue structures housed within the ribcage. The hoop tension resulting as a consequence of the compressive deformation on the antero-lateral region superimposed with the tangential component is the primary difference in the internal load-sharing mechanism between the two modes of impact. These factors may explain the more aggressive nature of the oblique than the pure lateral vector; a finding recently observed in cases examined by CIREN; narrow object and oblique impacts imparting more severe injuries than pure side impacts (Yoganandan et al, 2003; Yoganandan et al, 2008). This recent study reported that oblique impacts produced more unilateral fractures along with ipsilateral soft tissue trauma.

Anthropomorphic Test Devices. Several types of anthropometric test devices (ATDs) have been developed for use in standardized side impact testing. They include 50th percentile male versions of the EuroSID, the WorldSID, and the NHTSA-SID, and versions of the SID-IIs 5th percentile female dummy. While all four dummies are distinct from one another, they all provide calibrated responses to impacts from the near side. In each case, the dummy has a rib cage that consists of spring steel ribs of one form or another, and lateral displacement is measured by linear displacement transducers mounted between the ribcage and thoracic spine.

As an example of ATD instrumentation, consider a rib module of the ES-2 version of the EuroSID, shown in Figure 14. The ES-2 has three such thoracic rib modules, each with a linear slide and damper mounted inside a steel band. A single-degree-of-freedom potentiometer measures rib displacements. This instrumentation is typical of all four dummies in that they all measure rib displacement along a single axis.

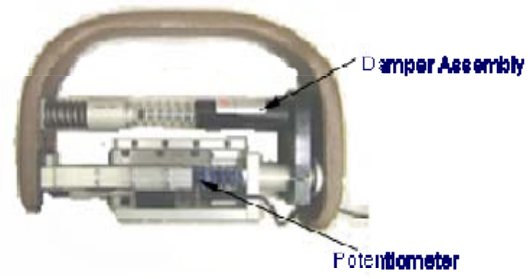

Figure 14: ES-2 Rib Module

The problem of detecting oblique loads in an ATD may not require an exact knowledge of where the loading vector is directed. There are emerging deformation-sensing instrumentation systems that allow for multiple points of measurement. Unlike the chestband, which is secured to the outside of the torso, these systems allow for internal measures at multiple points and in multiple directions. The advanced THOR-NT has four different sensors called CRUX potentiometers that measure the X, Y, and Z-directions of motion of that point on the rib cage. The RibEye LED optical system measures two or three directions of movement of up to 12 locations mounted on the internal aspects of a dummy rib cage (Yoganandan et al, 2009 ESV). Although these systems are more complex than a single potentiometer and may require some degree of understanding of what to do with the output, they are potentially the solution to measurement of oblique chest loads in ATD. The results of the current test program will produce the necessary correlations between PMHS and dummy measures when the loading vector to the chest is from the anterolateral direction.

SUMMARY

This paper summarizes an ongoing plan of research designed to characterize human response in oblique side impacts. The goal of this work is to establish the degree of oblique thoracic loading within post-mortem human subjects and ATDs with the aim of determining differences and possible enhancements of available test dummies and injury criteria. This is accomplished through the use of a new sled test protocol with varying load walls in which human subjects and ATDs are fitted with chestbands to provide comparative measures of thoracic deformation. The chestband measures also help establish the instrumentation requirements of an ATD for use in a side impact test with a significant oblique component. Additionally, this work may help

introduce more biofidelic injury metrics for side impact ATDs in oblique loading environments.

The goal of this work is to establish the degree of oblique loading and biofidelity responses in a side impact environment through the use of chestband contours, and sled tests with varying load walls. In addition, this research will help establish the instrumentation requirements of an ATD used in side impact tests that may have a significant oblique component.

ACKNOWLEDGEMENTS

This research was supported in part by the US DOT NHTSA cooperative research program DTNH22-07-H-00173 and by the Department of Veterans Affairs Research. We gratefully acknowledge Mark Meyer and the rest of the Neuroscience Research Laboratories staff in the conduct of the experiments.

REFERENCES

Campbell JQ, Takhounts EG, Martin PG, Eppinger RH, Nguyen T, Tannous RE, On the development of a theoretically based, statistically justified, thoracic injury criterion, The 19th International Technical Conference on the Enhanced Safety of Vehicles (ESV) - Washington D.C. June 6-9, 2005.

Maltese MR, et al (2002), Response Corridors of Human Surrogates in Lateral Impacts, Stapp Car Crash Journal, Vol. 46, November 2002.

Pintar, F. A., Yoganandan, N., Sances, A., Eppinger, R., 1996. Instrumentation of Human Surrogates for Side Impact. In: Proceedings of the Stapp Car Crash Conference, Albuquerque, NM, 29-42.

Pintar, F. A., Yoganandan, N., Hines, M. H., Maltese, M. R., McFadden, J., Saul, R., Eppinger, R., Khaewpong, N. and Kleinberger, M. (1997), Chestband analysis of human tolerance to side impact. 41st Stapp Car Crash Conference, Lake Buena Vista, FL.

Pintar, F.A., D.J. Maiman, and N. Yoganandan. Occupant dynamics and injuries in narrow-object side impact. in Experimental Safety of Vehicles. 2007. Lyon, France.

Pintar, F.A., N. Yoganandan, and D.J. Maiman, Injury mechanisms and severity in narrow offset frontal impacts. Annu Proc Assoc Adv Automot Med, 2008. 52: p. 185-9.

Traffic Safety Facts 2007, Report DOT HS 810 631, National Highway Traffic Safety Administration, Washington DC.

Yoganandan, N., et al. Thoracic biomechanics with air bag restraint. in Stapp Car Crash Conf. 1993. San Antonio, TX.

Yoganandan, N., et al., Mechanisms of thoracic injury in frontal impact. J Biomech Eng, 1996. 118(4): p. 595-7.

Yoganandan, N., et al., Patterns of abdominal injuries in frontal and side impacts. Annu Proc Assoc Adv Automot Med, 2000. 44: p. 17-36.

Yoganandan N, Pintar F, Gennarelli TA (2002), Biofidelity evaluation of recent side impact dummies, 2002 IRCOBI Conference, Munich Germany, September 2002.

Yoganandan, N. and F.A. Pintar, Deflections from two types of Human Surrogates in Oblique Side Impacts. Annu Proc Assoc Adv Automot Med, 2008. 52: p. 301-13.

Zaouk AK, Eigen AM, Digges KH (2001), Occupant injury patterns in side crashes, Paper 2001-01-0723, Society of Automotive Engineers, Warrendale, PA, 2001